



HAL
open science

Global Climate

Robert Dunn, F. Aldred, Nadine Gobron, John Miller, Kate Willett, M. Ades,
Robert Adler, Richard, Allan, Rob Allan, J. Anderson, et al.

► **To cite this version:**

Robert Dunn, F. Aldred, Nadine Gobron, John Miller, Kate Willett, et al.. Global Climate. Bulletin of the American Meteorological Society, 2021, 102 (8), pp.S11-S142. 10.1175/BAMS-D-21-0098.1 . hal-04846883

HAL Id: hal-04846883

<https://hal.science/hal-04846883v1>

Submitted on 5 Jan 2025

HAL is a multi-disciplinary open access archive for the deposit and dissemination of scientific research documents, whether they are published or not. The documents may come from teaching and research institutions in France or abroad, or from public or private research centers.

L'archive ouverte pluridisciplinaire **HAL**, est destinée au dépôt et à la diffusion de documents scientifiques de niveau recherche, publiés ou non, émanant des établissements d'enseignement et de recherche français ou étrangers, des laboratoires publics ou privés.



Distributed under a Creative Commons Attribution 4.0 International License

STATE OF THE CLIMATE IN 2020

GLOBAL CLIMATE

R. J. H. Dunn, F. Aldred, N. Gobron, J. B. Miller, and K. M. Willett, Eds.



Special Online Supplement to the *Bulletin of the American Meteorological Society* Vol.102, No. 8, August, 2021

[doi:10.1175/BAMS-D-21-0098.1](https://doi.org/10.1175/BAMS-D-21-0098.1)

Corresponding author: Robert Dunn / robert.dunn@metoffice.gov.uk

©2021 American Meteorological Society

For information regarding reuse of this content and general copyright information, consult the [AMS Copyright Policy](#).

STATE OF THE CLIMATE IN 2020

Global Climate

Editors

Jessica Blunden
Tim Boyer

Chapter Editors

Freya Aldred
Peter Bissolli
Howard J. Diamond
Matthew L. Druckenmiller
Robert J. H. Dunn
Catherine Ganter
Nadine Gobron
Gregory C. Johnson
Tim Li
Rick Lumpkin
Ademe Mekonnen
John B. Miller
Twila A. Moon
Ahira Sánchez-Lugo
Ted A. Scambos
Carl J. Schreck III
Sharon Stammerjohn
Richard L. Thoman
Kate M. Willett

Technical Editor

Andrea Andersen

BAMS Special Editor for Climate

Michael A. Alexander

American Meteorological Society

Cover credit:

Caption: Spring leaf emergence at Harvard Forest, Petersham, MA, USA, exemplified by the Witness Tree (Mapes 2017), a century-old red oak (*Quercus rubra*). Image courtesy of the PhenoCam Network.

Mapes, L.M. *Witness Tree: Seasons of Change with a Century-Old Oak*. Bloomsbury USA, New York. 240 pp.

Global Climate is one chapter from the *State of the Climate in 2020* annual report and is available from <https://doi.org/10.1175/BAMS-D-21-0098.1> Compiled by NOAA's National Centers for Environmental Information, *State of the Climate in 2020* is based on contributions from scientists from around the world. It provides a detailed update on global climate indicators, notable weather events, and other data collected by environmental monitoring stations and instruments located on land, water, ice, and in space.

The full report is available from <https://doi.org/10.1175/2021BAMSStateoftheClimate.1>.

How to cite this document:**Citing the complete report:**

Blunden, J. and T. Boyer, Eds., 2021: "State of the Climate in 2020". *Bull. Amer. Meteor. Soc.*, **102** (8), Si–S475, <https://doi.org/10.1175/2021BAMSStateoftheClimate.1>.

Citing this chapter:

Dunn, R. J. H., F. Aldred, N. Gobron, J. B. Miller, and K. M. Willett, Eds., 2021: Global Climate [in "State of the Climate in 2020"]. *Bull. Amer. Meteor. Soc.*, **102** (8), S11–S141, <https://doi.org/10.1175/BAMS-D-21-0098.1>.

Citing a section (example):

Tye, M. R., S. Blenkinsop, M. G. Bosilovich, M. G. Donat, I. Durre, A. J. Simmons, and M. Ziese, 2021: Land-based precipitation extremes [in "State of the Climate in 2020"]. *Bull. Amer. Meteor.*, **102** (8), S57–S60, <https://doi.org/10.1175/BAMS-D-21-0098.1>.

- Ades, M.**, European Centre for Medium-Range Weather Forecasts, Reading, United Kingdom
- Adler, Robert**, CMNS-Earth System Science Interdisciplinary Center, University of Maryland, College Park, Maryland
- Aldred, F.**, Met Office Hadley Centre, Exeter, United Kingdom
- Allan, Richard, P.**, Department of Meteorology and National Centre for Earth Observation, University of Reading, Reading, United Kingdom
- Allan, Rob**, Met Office Hadley Centre, Exeter, United Kingdom
- Anderson, J.**, Department of Atmospheric and Planetary Science, Hampton University, Hampton, Virginia
- Argüez, Anthony**, NOAA/NESDIS National Centers for Environmental Information, Asheville, North Carolina
- Arosio, C.**, University of Bremen, Bremen, Germany
- Augustine, John A.**, NOAA/OAR Earth System Research Laboratory, Boulder, Colorado
- Azorin-Molina, C.**, Centro de Investigaciones sobre Desertificación – Spanish National Research Council, Moncada (Valencia), Spain; and Regional Climate Group, Department of Earth Sciences, University of Gothenburg, Gothenburg, Sweden
- Barichivich, J.**, Instituto de Geografía, Pontificia Universidad Católica de Valparaíso, Valparaíso, Chile
- Beck, H. E.**, GloH2O, Almere, the Netherlands
- Becker, Andreas**, Global Precipitation Climatology Centre, Deutscher Wetterdienst, Offenbach, Germany
- Bellouin, Nicolas**, University of Reading, Reading, United Kingdom
- Benedetti, Angela**, European Centre for Medium-Range Weather Forecasts, Reading, United Kingdom
- Berry, David I.**, National Oceanography Centre, Southampton, United Kingdom
- Blenkinsop, Stephen**, School of Engineering, Newcastle University, Newcastle-upon-Tyne, United Kingdom
- Bock, Olivier**, Université de Paris, Institut de physique du globe de Paris, CNRS, IGN, F-7500 Paris, France
- Bodin, X.**, Laboratoire EDYTEM, CNRS/Université Savoie Mont-Blanc, Le Bourget-du-Lac, France
- Bosilovich, Michael G.**, Global Modeling and Assimilation Office, NASA Goddard Space Flight Center, Greenbelt, Maryland
- Boucher, Olivier**, Sorbonne Université, Paris, France
- Buehler, S. A.**, Meteorologisches Institut, Centrum für Erdsystem-und Nachhaltigkeitsforschung (CEN), Fachbereich Erdsystemwissenschaften, Universität Hamburg, Hamburg, Germany
- Calmettes, B.**, Collecte Localisation Satellites (CLS), Ramonville Saint-Agne, France
- Carrea, Laura**, Department of Meteorology, University of Reading, Reading, United Kingdom
- Castia, Laura**, NOAA Climate Prediction Center, College Park, Maryland
- Christiansen, Hanne H.**, Geology Department, University Centre in Svalbard, Longyearbyen, Norway
- Christy, John R.**, The University of Alabama in Huntsville, Huntsville, Alabama
- Chung, E.-S.**, Korea Polar Research Institute, Incheon, South Korea
- Coldewey-Egbers, Melanie**, DLR (German Aerospace Center) Oberpfaffenhofen, Wessling, Germany
- Cooper, Owen R.**, Cooperative Institute for Research in Environmental Sciences, University of Colorado, Boulder, Colorado; NOAA Chemical Sciences Laboratory, Boulder, Colorado
- Cornes, Richard C.**, National Oceanography Centre, Southampton, United Kingdom
- Covey, Curt**, Lawrence Livermore, National Laboratory, Livermore California
- Cretaux, J.-F.**, CNES/LEGOS, UMR5566, Université de Toulouse, Toulouse, France
- Crotwell, M.**, Cooperative Institute for Research in Environmental Sciences, University of Colorado, Boulder, Colorado; NOAA/OAR Global Monitoring Laboratory, Boulder, Colorado
- Davis, Sean M.**, NOAA Chemical Sciences Laboratory, Boulder, Colorado
- de Jeu, Richard A. M.**, VanderSat B.V., Haarlem, The Netherlands
- Degenstein, Doug**, University of Saskatchewan, Saskatoon, Saskatchewan, Canada
- Delaloye, R.**, Department of Geosciences, University of Fribourg, Fribourg, Switzerland
- Di Girolamo, Larry**, University of Illinois at Urbana-Champaign, Illinois
- Donat, Markus G.**, Barcelona Supercomputing Centre, Barcelona, Spain
- Dorigo, Wouter A.**, TU Wien - Vienna University of Technology, Vienna, Austria
- Dunn, Robert J. H.**, Met Office Hadley Centre, Exeter, United Kingdom
- Durre, Imke**, NOAA/NESDIS, National Center for Environmental Information, Asheville, North Carolina
- Dutton, Geoff S.**, Cooperative Institute for Research in Environmental Sciences, University of Colorado, Boulder, Colorado; NOAA/OAR Global Monitoring Laboratory, Boulder, Colorado
- Duveiller, Gregory**, European Commission, Joint Research Centre, Ispra, Italy; currently at the Max Planck Institute for Biogeochemistry, Jena, Germany
- Elkins, James W.**, NOAA/OAR Global Monitoring Laboratory, Boulder, Colorado
- Fioletov, Vitali E.**, Environment and Climate Change Canada, Toronto, Canada
- Flemming, Johannes**, Copernicus Department, European Centre for Medium-Range Weather Forecasts, Reading, United Kingdom
- Foster, Michael J.**, Cooperative Institute for Meteorological Satellite Studies, Space Science and Engineering Center, University of Wisconsin-Madison, Madison, Wisconsin
- Frith, Stacey M.**, Science Systems and Applications, Inc., Lanham, Maryland; NASA Goddard Space Flight Center, Greenbelt, Maryland
- Froidevaux, Lucien**, Jet Propulsion Laboratory, California Institute of Technology, Pasadena, California
- Garforth, J.**, Woodland Trust, Grantham, United Kingdom
- Gentry, Matthew**, Cooperative Institute for Research in Environmental Sciences, University of Colorado, Boulder, Colorado; NOAA/OAR Global Monitoring Laboratory, Boulder, Colorado
- Gobron, Nadine**, European Commission, Joint Research Centre, Ispra, Italy
- Gupta, S. K.**, Science Systems and Applications, Inc. (SSAI), Hampton, Virginia
- Hahn, S.**, TU Wien - Vienna University of Technology, Vienna, Austria
- Haimberger, Leopold**, Department of Meteorology and Geophysics, University of Vienna, Vienna, Austria
- Hall, Brad D.**, NOAA/OAR Global Monitoring Laboratory, Boulder, Colorado
- Harris, Ian**, National Centre for Atmospheric Science (NCAS), University of East Anglia, Norwich, United Kingdom; Climatic Research Unit, School of Environmental Sciences, University of East Anglia, Norwich, United Kingdom
- Hemming, D. L.**, Met Office Hadley Centre, Exeter, United Kingdom; Birmingham Institute of Forest Research, Birmingham University, Birmingham, United Kingdom
- Hirschi, M.**, ETH Zürich, Zürich, Switzerland
- Ho, Shu-pen (Ben)**, Center for Satellite Applications and Research, NOAA, College Park, Maryland
- Hrbacek, F.**, Department of Geography, Masaryk University, Brno, Czechia
- Hubert, Daan**, Royal Belgian Institute for Space Aeronomy (BIRA-IASB), Brussels, Belgium

Editor and Author Affiliations (alphabetical by name)

- Hurst, Dale F.**, Cooperative Institute for Research in Environmental Sciences, University of Colorado Boulder, Boulder, Colorado; NOAA/OAR Global Monitoring Laboratory, Boulder, Colorado
- Inness, Antje**, Copernicus Department, European Centre for Medium-Range Weather Forecasts, Reading, United Kingdom
- Isaksen, K.**, Norwegian Meteorological Institute, Oslo, Norway
- John, Viju O.**, EUMETSAT, Darmstadt, Germany
- Jones, Philip D.**, Climatic Research Unit, School of Environmental Sciences, University of East Anglia, Norwich, United Kingdom
- Junod, Robert**, Earth System Science Center (ESSC), University of Alabama in Huntsville, Huntsville, Alabama
- Kaiser, J. W.**, Satellite-based Climate Monitoring Unit, Deutscher Wetterdienst, Offenbach am Main, Germany
- Kaufmann, V.**, Institute of Geodesy, Working Group Remote Sensing and Photogrammetry, Graz University of Technology, Graz, Austria
- Kellerer-Pirklbauer, A.**, Institute of Geography and Regional Science, Cascade - The Mountain Processes and Mountain Hazards Group, University of Graz, Graz, Austria
- Kent, Elizabeth C.**, National Oceanography Centre, Southampton, United Kingdom
- Kidd, R.**, Earth Observation Data Centre (EODC), Vienna, Austria
- Kim, Hyungjun**, Moon Soul Graduate School of Future Strategy, Korea Advanced Institute of Science and Technology (KAIST), Daejeon, South Korea
Institute of Industrial Science, The University of Tokyo, Tokyo, Japan
- Kipling, Z.**, European Centre for Medium-Range Weather Forecasts, Reading, United Kingdom
- Koppa, A.**, Hydro-Climate Extremes Lab (H-CEL), Ghent University, Ghent, Belgium
- Kraemer, B. M.**, IGB Leibniz Institute for Freshwater Ecology and Inland Fisheries, Berlin, Germany
- Kratz, D. P.**, NASA Langley Research Center, Hampton, Virginia
- Lan, Xin**, Cooperative Institute for Research in Environmental Sciences, University of Colorado, Boulder, Colorado; NOAA/OAR Global Monitoring Laboratory, Boulder, Colorado
- Lantz, Kathleen O.**, NOAA/OAR Earth System Research Laboratory, Boulder, Colorado
- Lavers, D.**, European Centre for Medium-Range Weather Forecasts, Reading, United Kingdom
- Loeb, Norman G.**, NASA Langley Research Center, Hampton, Virginia
- Loyola, Diego**, DLR (German Aerospace Center) Oberpfaffenhofen, Wessling, Germany
- Madelon, R.**, CESBIO (Université Toulouse 3, CNES, CNRS, INRAE, IRD), Toulouse, France
- Mayer, Michael**, University of Vienna, Vienna, Austria and European Centre for Medium-Range Weather Forecasts, Reading, United Kingdom
- McCabe, M. F.**, Division of Biological and Environmental Sciences and Engineering, King Abdullah University of Science and Technology, Thuwal, Saudi Arabia
- McVicar, Tim R.**, CSIRO Land and Water, Canberra, Australian Capital Territory; Australian Research Council Centre of Excellence for Climate Extremes, Sydney, New South Wales, Australia
- Mears, Carl A.**, Remote Sensing Systems, Santa Rosa, California
- Merchant, Christopher J.**, Department of Meteorology, University of Reading, Reading, United Kingdom
- Miller, John B.**, NOAA/OAR Global Monitoring Laboratory, Boulder, Colorado
- Miralles, Diego G.**, Hydro-Climate Extremes Lab (H-CEL), Ghent University, Ghent, Belgium
- Moesinger, L.**, TU Wien – University of Technology, Vienna, Austria
- Montzka, Stephen A.**, NOAA/OAR Global Monitoring Laboratory, Boulder, Colorado
- Morice, Colin**, Met Office Hadley Centre, Exeter, United Kingdom
- Mösinger, L.**, TU Wien – University of Technology, Vienna, Austria
- Mühle, Jens**, Scripps Institution of Oceanography, University of California, San Diego, La Jolla, California
- Nicolas, Julien P.**, European Centre for Medium-Range Weather Forecasts, Reading, United Kingdom
- Noetzi, Jeannette**, WSL Institute for Snow and Avalanche Research SLF, Davos-Dorf, Switzerland
- Noll, Ben**, National Institute of Water and Atmospheric Research (NIWA), New Zealand
- O’Keefe, J.**, The Harvard Forest, Harvard University, Petersham, Massachusetts
- Osborn, Tim J.**, Climatic Research Unit, School of Environmental Sciences, University of East Anglia, Norwich, United Kingdom
- Park, T.**, NASA Ames Research Center, Moffett Field, California; Bay Area Environmental Research Institute, Moffett Field, California
- Pasik, A. J.**, TU Wien – Vienna University of Technology, Vienna, Austria
- Pellet, C.**, Department of Geosciences, University of Fribourg, Fribourg, Switzerland
- Pelto, Maury S.**, Nichols College, Dudley, Massachusetts
- Perkins-Kirkpatrick, S. E.**, University of New South Wales, Canberra, Australia
- Petron, G.**, Cooperative Institute for Research in Environmental Sciences, University of Colorado, Boulder, Colorado; NOAA/OAR Global Monitoring Laboratory, Boulder, Colorado
- Phillips, Coda**, Cooperative Institute for Meteorological Satellite Studies, Space Science and Engineering Center, University of Wisconsin-Madison, Madison, Wisconsin
- Po-Chedley, S.**, Program for Climate Model Diagnosis and Intercomparison, Lawrence Livermore National Laboratory, Livermore, California
- Polvani, L.**, Columbia University, New York, New York
- Preimesberger, W.**, TU Wien – Vienna University of Technology, Vienna, Austria
- Rains, D. G.**, Hydro-Climate Extremes Lab (H-CEL), Ghent University, Ghent, Belgium
- Randel, W. J.**, National Center for Atmospheric Research, Boulder, Colorado
- Rayner, Nick A.**, Met Office Hadley Centre, Exeter, United Kingdom
- Rémy, Samuel**, HYGEOS, Lille, France
- Ricciardulli, L.**, Remote Sensing Systems, Santa Rosa, California
- Richardson, A. D.**, School of Informatics, Computing, and Cyber Systems and Center for Ecosystem Science and Society, Northern Arizona University, Flagstaff, Arizona
- Robinson, David A.**, Rutgers University, Piscataway, New Jersey
- Rodell, Matthew**, Hydrological Sciences Laboratory, NASA Goddard Space Flight Center, Greenbelt, Maryland
- Rodríguez-Fernández, N. J.**, CESBIO (Université Toulouse 3, CNES, CNRS, INRAE, IRD), Toulouse, France
- Rosenlof, K.H.**, NOAA Chemical Sciences Laboratory, Boulder, Colorado
- Roth, C.**, University of Saskatchewan, Saskatoon, Canada
- Rozanov, A.**, University of Bremen, Bremen, Germany
- Rutishäuser, T.**, Institute of Geography and Oeschger Center, University of Berne, Berne, Switzerland
- Sánchez-Lugo, Ahira**, NOAA/NESDIS National Centers for Environmental Information, Asheville, North Carolina
- Sawaengphokhai, P.**, Science Systems and Applications, Inc. (SSAI), Hampton, Virginia

Editor and Author Affiliations (alphabetical by name)

- Scanlon, T.**, TU Wien – University of Technology, Vienna, Austria
- Schenzinger, Verena**, Medical University of Innsbruck, Innsbruck, Austria
- Schlegel, R. W.**, Sorbonne Université, CNRS, Villefranche-sur-mer, France
- Sharma, S.**, York University, Toronto, Ontario, Canada
- Shi, Lei**, NOAA/NESDIS, National Centers for Environmental Information, Asheville, North Carolina, United States
- Simmons, Adrian J.**, European Centre for Medium-Range Weather Forecasts, Reading, United Kingdom
- Siso, Carolina**, Cooperative Institute for Research in Environmental Sciences, University of Colorado, Boulder, Colorado, USA, and NOAA/OAR Global Monitoring Laboratory, Boulder, Colorado
- Smith, Sharon L.**, Geological Survey of Canada, Natural Resources Canada, Ottawa, Canada
- Soden, B. J.**, University of Miami Rosenstiel School of Marine and Atmospheric Science (RSMAS), Key Biscayne, Florida, United States
- Sofieva, Viktoria**, Finnish Meteorological Institute (FMI), Helsinki, Finland
- Sparks, T. H.**, Poznań University of Life Sciences, Poznań, Poland
- Stackhouse, Jr., Paul W.**, NASA Langley Research Center, Hampton, Virginia
- Steinbrecht, Wolfgang**, German Weather Service (DWD), Hohenpeissenberg, Germany
- Stengel, Martin**, Deutscher Wetterdienst, Offenbach, Germany
- Streletskiy, Dimitri A.**, George Washington University, Washington, D.C.
- Sun-Mack, Sunny**, Science Systems and Applications, Inc. (SSAI), Hampton, Virginia
- Tans, P.**, NOAA/OAR Global Monitoring Laboratory, Boulder, Colorado
- Thackeray, S. J.**, Centre for Ecology and Hydrology, Lancaster, United Kingdom
- Thibert, E.**, Université Grenoble Alpes, INRAE, UR ETGR, Grenoble, France
- Tokuda, D.**, Institute of Industrial Science, The University of Tokyo, Tokyo, Japan
- Tourpali, Kleareti**, Aristotle University, Thessaloniki, Greece
- Tye, Mari R.**, National Center for Atmospheric Research, Boulder, Colorado
- van der A, Ronald**, Royal Netherlands Meteorological Institute (KNMI), DeBilt, The Netherlands
- van der Schalie, Robin**, VanderSat B.V., Haarlem, The Netherlands
- van der Schrier, Gerard**, Royal Netherlands Meteorological Institute, De Bilt, The Netherlands
- van der Vliet, M.**, VanderSat B.V., Haarlem, The Netherlands
- van der Werf, Guido R.**, Faculty of Science, Vrije Universiteit Amsterdam, Amsterdam, Netherlands
- Vance, A.**, Met Office Hadley Centre, Exeter, United Kingdom
- Vernier, Jean-Paul**, National Institute of Aerospace/NASA Langley Research Center, Hampton, Virginia
- Vimont, Isaac J.**, Cooperative Institute for Research in Environmental Sciences, University of Colorado Boulder, and NOAA/OAR Global Monitoring Laboratory, Boulder, Colorado
- Vömel, Holger**, Earth Observing Laboratory, National Center for Atmospheric Research, Boulder, Colorado
- Vose, Russell S.**, NOAA/NESDIS, National Center for Environmental Information, Asheville, North Carolina
- Wang, Ray**, Georgia Institute of Technology, Atlanta, Georgia
- Weber, Markus**, University of Bremen, Bremen, Germany
- Wiese, David**, Jet Propulsion Laboratory, California Institute of Technology, Pasadena, California
- Wilber, Anne C.**, Science Systems and Applications, Inc. (SSAI), Hampton, Virginia
- Wild, Jeanette D.**, NOAA/NWS, Climate Prediction Center, College Park, Maryland; ESSIC/University of Maryland, College Park, Maryland
- Willett, Kate M.**, Met Office Hadley Centre, Exeter, United Kingdom
- Wong, Takmeng**, NASA Langley Research Center, Hampton, Virginia
- Woolway, R. Iestyn**, European Space Agency Climate Office, ECSAT, Harwell Campus, Didcot, United Kingdom
- Yin, Xungang**, NOAA/NESDIS, NOAA National Centers for Environmental Information, Asheville, North Carolina
- Zhao, Guangyu**, University of Illinois at Urbana-Champaign, Illinois
- Zhao, Lin**, School of Geographical Sciences, Nanjing University of Information Science & Technology, Nanjing, China
- Zhou, Xinjia**, Global Science and Technology, Inc., Greenbelt, Maryland
- Ziemke, Jerry R.**, Goddard Earth Sciences Technology and Research, Morgan State University, Baltimore, Maryland; NASA Goddard Space Flight Center, Greenbelt, Maryland
- Ziese, Markus**, Global Precipitation Climatology Centre, Deutscher Wetterdienst, Offenbach am Main, Germany
- Zotta, R. M.**, TU Wien – University of Technology, Vienna, Austria

Editorial and Production Team

- Allen, Jessica**, Graphics Support, Cooperative Institute for Satellite Earth System Studies, North Carolina State University, Asheville, North Carolina
- Andersen, Andrea**, Technical Editor, Innovative Consulting Management Services, LLC, NOAA/NESDIS National Centers for Environmental Information, Asheville, North Carolina
- Hammer, Gregory**, Content Team Lead, Communications and Outreach, NOAA/NESDIS National Centers for Environmental Information, Asheville, North Carolina
- Love-Brotak, S. Elizabeth**, Lead Graphics Production, NOAA/NESDIS National Centers for Environmental Information, Asheville, North Carolina
- Misch, Deborah J.**, Graphics Support, Innovative Consulting Management Services, LLC, NOAA/NESDIS National Centers for Environmental Information, Asheville, North Carolina
- Riddle, Deborah B.**, Graphics Support, NOAA/NESDIS National Centers for Environmental Information, Asheville, North Carolina
- Veasey, Sara W.**, Visual Communications Team Lead, Communications and Outreach, NOAA/NESDIS National Centers for Environmental Information, Asheville, North Carolina

2. Table of Contents

List of authors and affiliations	S14
a. Overview	S19
b. Temperature	S26
1. Global surface temperature	S26
2. Lake surface water temperature.....	S28
3. Land and marine temperature extremes	S31
4. Tropospheric temperature.....	S34
5. Stratospheric temperature and winds	S37
Sidebar 2.1: Night marine air temperature	S39
c. Cryosphere	S42
1. Permafrost thermal state.....	S42
Sidebar 2.2: Rock glacier kinematics.....	S44
2. Northern Hemisphere continental snow cover extent.....	S46
3. Alpine glaciers.....	S47
4. Lake ice	S48
d. Hydrological cycle	S51
1. Surface humidity	S51
2. Total column water vapor	S53
3. Upper tropospheric humidity.....	S55
4. Precipitation	S56
5. Land-based precipitation extremes.....	S57
6. Lake water levels.....	S60
7. Cloudiness.....	S61
8. River discharge and runoff.....	S63
9. Groundwater and terrestrial water storage.....	S65
10. Soil moisture.....	S67
11. Monitoring global drought using the self-calibrating Palmer Drought Severity Index	S68
12. Land evaporation	S70
e. Atmospheric circulation	S71
1. Mean sea level pressure and related modes of variability	S71
2. Land and ocean surface winds.....	S73
3. Upper air winds.....	S77

2. Table of Contents

f. Earth radiation budget	S79
1. Earth radiation budget at top-of-atmosphere	S79
2. Mauna Loa apparent transmission	S82
g. Atmospheric composition	S83
1. Long-lived greenhouse gases.....	S83
2. Ozone-depleting substances.....	S87
3. Aerosols	S89
4. Stratospheric ozone	S92
5. Stratospheric water vapor	S95
6. Tropospheric ozone.....	S98
7. Carbon monoxide	S101
h. Land surface properties	S103
1. Land surface albedo dynamics.....	S103
2. Terrestrial vegetation dynamics.....	S104
3. Biomass burning.....	S106
4. Phenology of primary producers	S108
Sidebar 2.3: Long-term monitoring of vegetation state through passive microwave satellites.....	S110
Acknowledgments	S113
Appendix 1: Chapter 2 – Acronyms.	S116
Appendix 2: Supplemental Materials	S119
References	S128

*Please refer to Chapter 8 (Relevant datasets and sources) for a list of all climate variables and datasets used in this chapter for analyses, along with their websites for more information and access to the data.

2. GLOBAL CLIMATE

R. J. H. Dunn, F. Aldred, N. Gobron, J. B Miller, and K. M. Willett, Eds.

a. Overview—R. J. H. Dunn, F. Aldred, N. Gobron, J. B Miller, and K. M. Willett

For reasons other than the climate, 2020 was an extraordinary year. The COVID-19 pandemic has affected almost all of us, changing the lives of many people around the globe. While the economic disruption associated with COVID-19 led to modest estimated reductions of 6–7% (e.g., le Quere et al. 2020; Friedlingstein et al. 2020; BP Statistical Review of the World Energy 2021) in global anthropogenic carbon dioxide (CO₂) emissions, atmospheric CO₂ levels continued to grow rapidly—a reminder of its very long residence time in the atmosphere and the challenge of reducing atmospheric CO₂. As we show in this chapter, the climate has continued to respond to the resulting warming from these increases in CO₂ and other greenhouse gases such as methane and nitrous oxide, which also experienced record increases in 2020.

The year 2020 was one of the three warmest since records began in the mid-to-late 1800s, with global surface temperatures around 0.6°C above the 1981–2010 average, despite the El Niño–Southern Oscillation progressing from neutral to La Niña conditions by August (see section 4b). Lower tropospheric temperatures matched those from 2016, the previous warmest year. Meanwhile, stratospheric temperatures continued to cool as a result of anthropogenic CO₂ increases. Along with the above-average surface temperatures, an unprecedented (since instrumental records began) geographic spread of heat waves and warm spells occurred. Antarctica observed its highest temperature on record (18.3°C) at Esperanza in February. In August, Death Valley, California, reported the highest temperature observed anywhere on Earth since 1931 (preliminary value of 54.4°C).

Consequently, many permafrost measurement sites experienced their highest temperatures on record; Northern Hemisphere (NH) snow cover was below the 51-year average and the fourth-least extensive on record. Glaciers in alpine regions experienced their 33rd consecutive year of negative mass balance and 12th year of average losses of more than 500 mm depth. On average, NH lakes froze over 3 days later and thawed 5.5 days earlier than the 1981–2010 average during the 2019/20 winter, which was the third-shortest ice cover season since 1979/80.

The atmosphere responded to higher temperatures accordingly by holding more water. Total column water vapor was high relative to the 1981–2010 average, ranging from 0.75 to 1.06 mm over ocean and 0.58 to 0.94 mm over land, but did not reach the record values of 2016. At the surface, specific humidity over oceans was at record high levels (0.23 to 0.41 g kg⁻¹) and was well above average over land (0.14 to 0.36 g kg⁻¹). Conversely, relative humidity was well below average over land (–1.28 to –0.68 %rh), continuing the long-term declining trend. Precipitation increased compared to 2019, driven largely by land values, but there were few exceptional extreme precipitation events, coupled with below-average cloudiness over most of the land. More lakes showed positive water level anomalies than 2019, and in East Africa, Lake Victoria's level rose by over a meter due to a wet long-rains season. Soil moisture and terrestrial water storage showed stronger regional variations than in previous years, with East Africa and India being especially moist. Global drought area continued to increase for most of the year, reaching a peak in October, with the third-highest global land area experiencing extreme drought according to the Palmer Drought

Severity Index (6.8%). Despite progression to a neutral Indian Ocean dipole (IOD) this year, from a strongly positive IOD in 2019 (see section 4h), the western Indian Ocean and East Africa showed above-average hydrological cycle anomalies generally, including upper tropospheric humidity.

Greenhouse gas levels continued to rise, with the three primary greenhouse gases, CO₂, CH₄, and N₂O, all reaching their highest levels in at least 800,000 years. Radiative forcing from the long-lived greenhouse gases also reached a new record level of 3.2 W m⁻², with CO₂ being responsible for a large majority of the total. Tropospheric ozone, another greenhouse gas (although shorter lived and not well-mixed throughout the atmosphere), continued a modest upward trend, which was dominated by trends over and downwind of Asia. Stratospheric ozone, on the other hand, exhibited unusually large negative anomalies, especially in the Arctic and Antarctic. These large ozone depletions resulted mainly from stable polar vortices despite continued reduction in equivalent effective stratospheric chlorine, as calculated from tropospheric values of ozone-depleting substances.

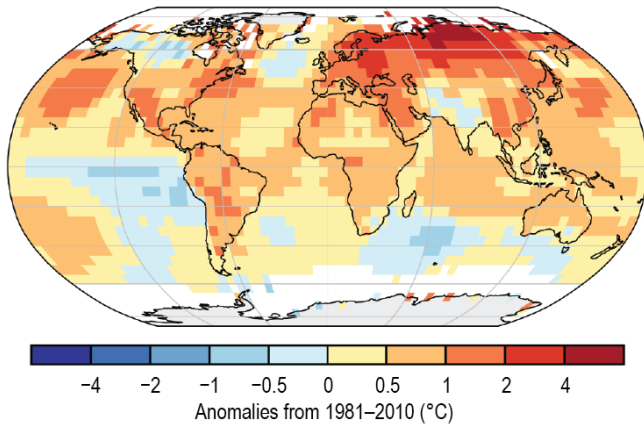
COVID-19 impacts on the troposphere, at least at large spatial scales, were not readily apparent in 2020 anomalies. Modest anthropogenic CO₂ emissions reductions of perhaps 6–7% were too small to be identified on a background of large interannual CO₂ variability driven by the terrestrial biosphere. Carbon monoxide (CO) and aerosol optical depth anomalies could also not be clearly tied to COVID-19-related emissions reductions. However, significant CO and aerosol anomalies related to large fires in southeastern Australia, the western United States, and Siberia were evident.

The warmer temperatures were also felt in the biosphere, with an earlier start of season, later end of season, and hence, longer growing season as measured by the normalized difference vegetation index, for example, the United Kingdom had the earliest “first leaf” of the Pedunculate oak in a 20-year series. Anomalies of vegetation productivity reached a record positive peak in the NH. Overall, 2020 saw one of the lowest fire years in the record but regionally some locations experienced extreme fire activity, notably southeastern Australia, the Siberian Arctic, and western United States, as noted above.

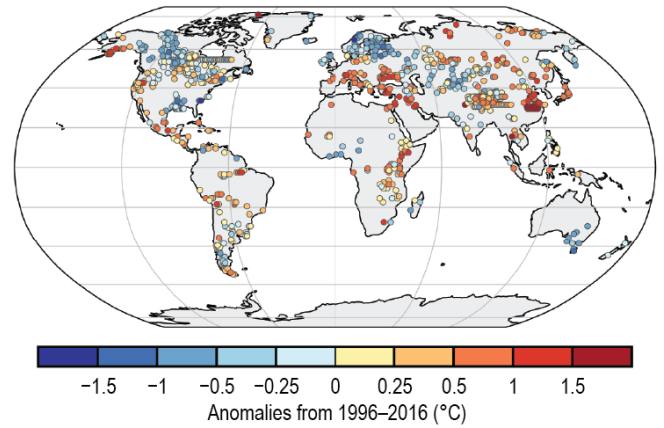
Three new measurements are included as sidebars in this year’s report. Night marine air temperature (NMAT) provides a useful independent comparison against sea surface temperature datasets to explore ongoing warming over oceans. Available NMAT observations (and marine humidity) have declined from around 7000 Voluntary Observing Ships in the 1980s to around 1000 at present, severely endangering our monitoring ability. Extending our cryosphere coverage, rock glacier kinematics, which is linked to the state of the permafrost, shows speeds in 2020 in the European Alps close to the maximum recorded. Increasing our monitoring of the biosphere, the final sidebar outlines the use of passive microwave satellite measurements for determining the vegetation properties via the amount of attenuation (the vegetation optical depth).

Time series and anomaly maps for many of the variables in this chapter are shown in Plates 1.1 and 2.1, respectively.

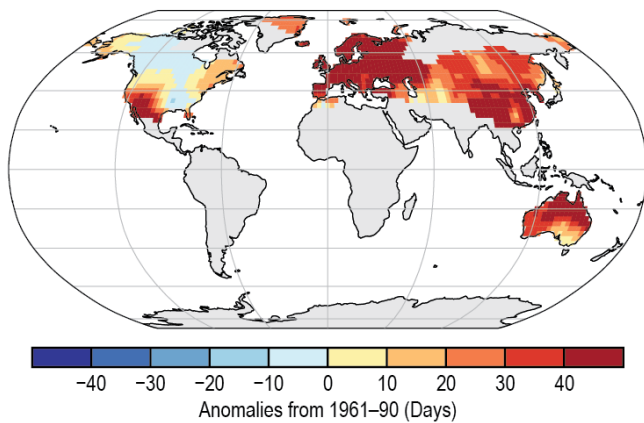
(a) Surface Temperature



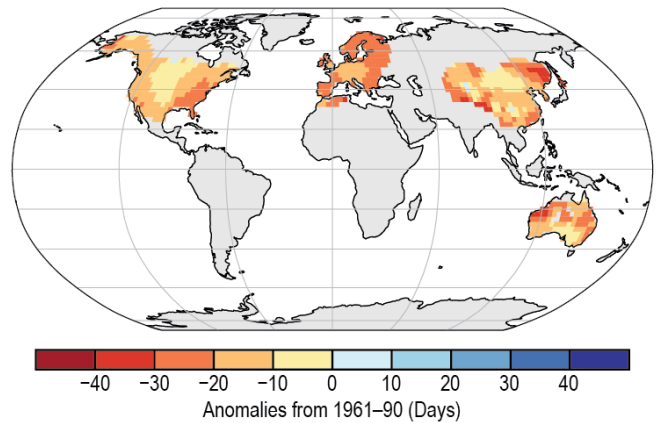
(b) Lake Temperatures



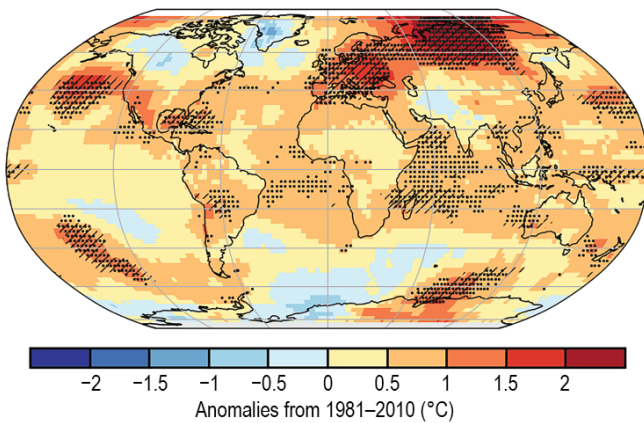
(c) Warm Days



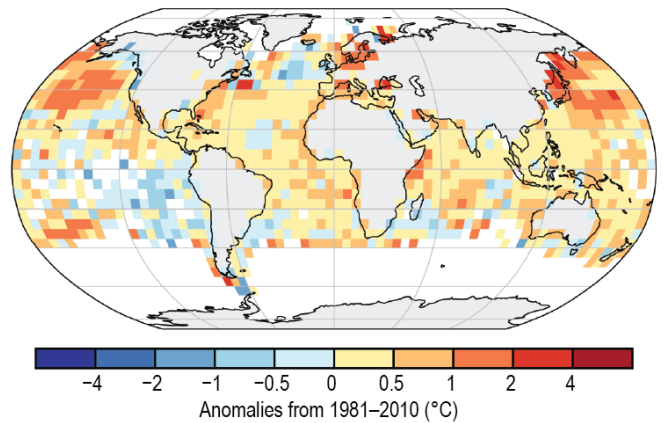
(d) Cool Nights



(e) Lower Tropospheric Temperature



(f) Night Marine Air Temperature



(g) Surface Specific Humidity

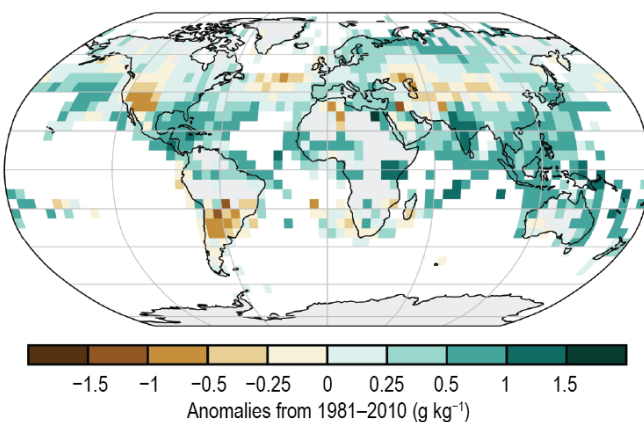
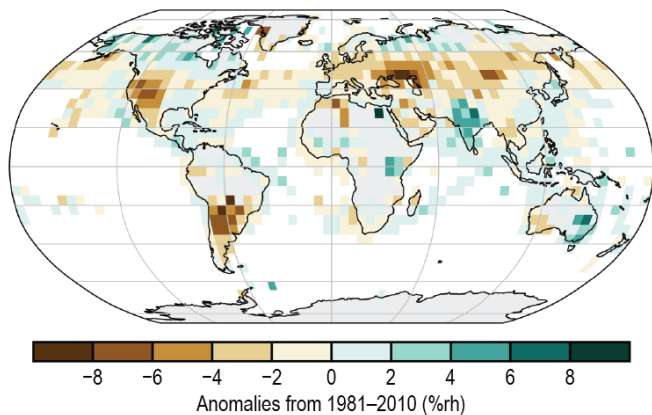
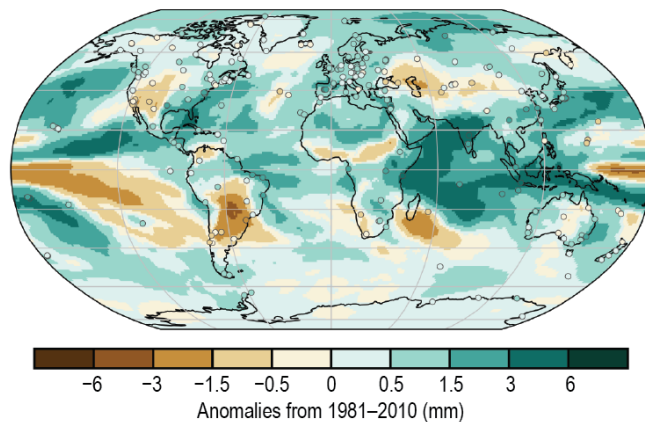


Plate 2.1. (a) NOAA NCEI Global land and ocean surface annual temperature anomalies (°C); (b) Satellite-derived lake surface water temperature anomalies (°C); (c) GHCNDEX warm day threshold exceedance (TX90p); (d) GHCNDEX cool night threshold exceedance (TN10p); (e) Average of RSS and UAH lower tropospheric temperature anomalies (°C). Hatching (stippling) denotes regions in which 2020 was the warmest year on record for UAH (RSS); (f) CLASSmat night marine air temperature anomalies (°C); (g) HadISDH surface specific humidity anomalies (g kg⁻¹);

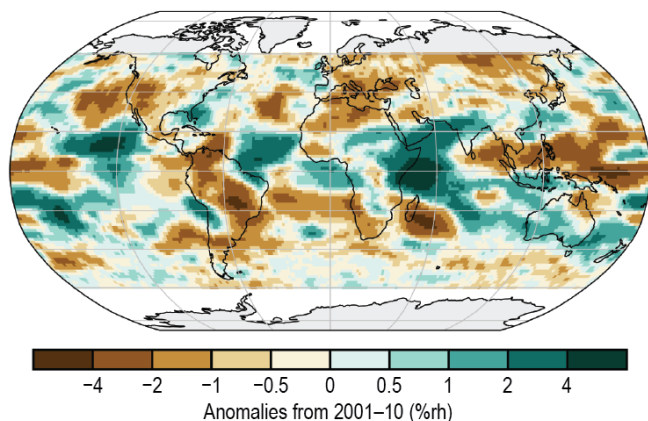
(h) Surface Relative Humidity



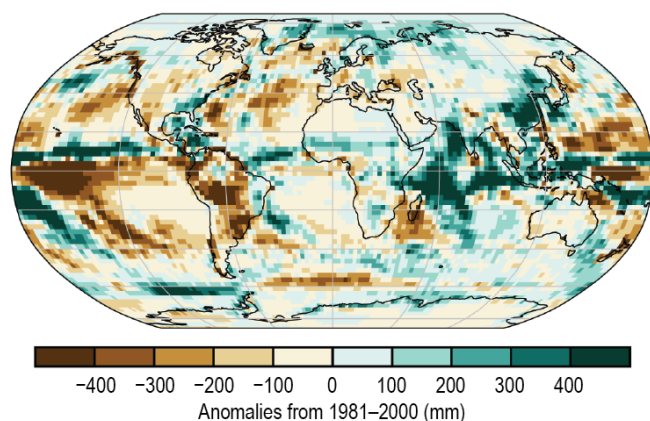
(i) Total Column Water Vapor



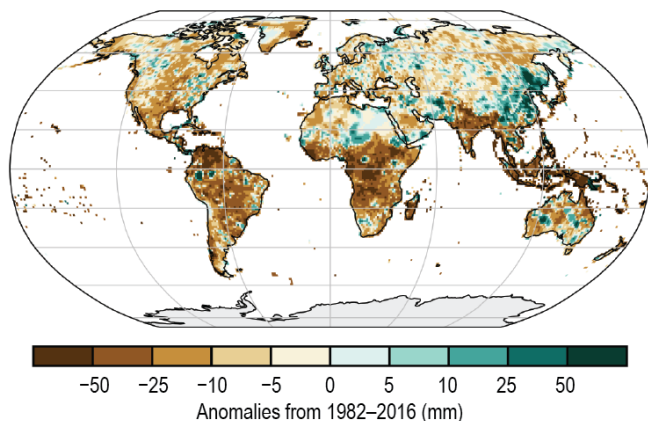
(j) Upper Tropospheric Humidity



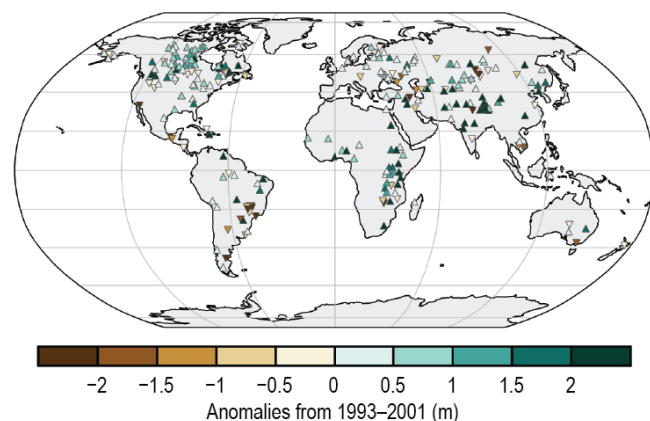
(k) Precipitation



(l) Rx1day Anomalies



(m) Lake Water Level



(n) Cloudiness

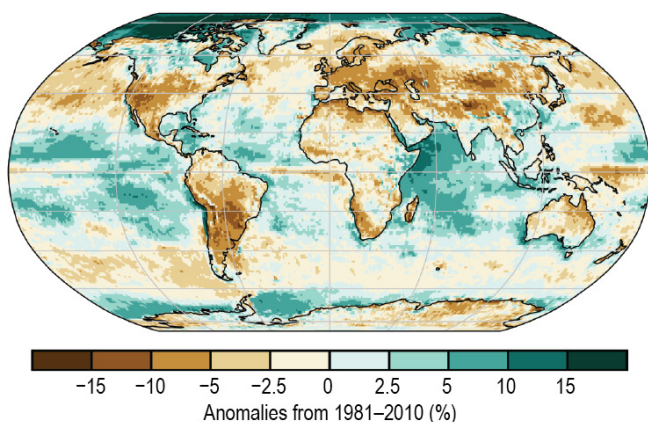
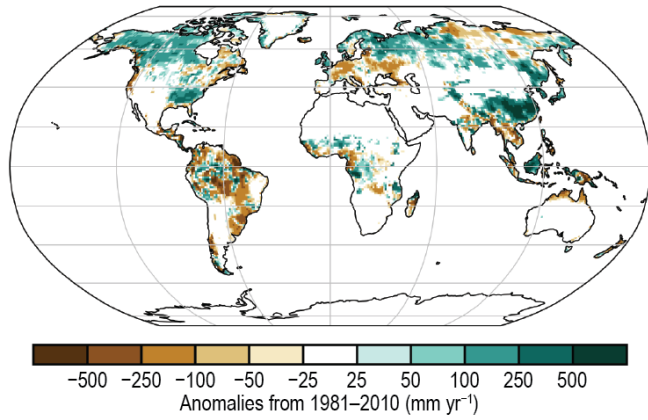
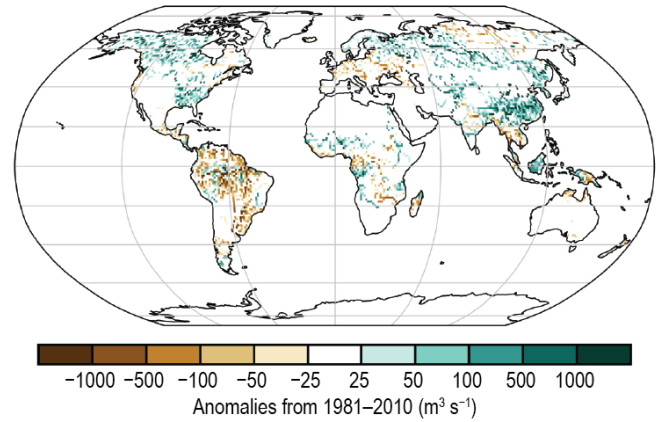


Plate 2.1. (cont.) (h) HadISDH surface relative humidity anomalies (%rh); (i) ERA5 TCWV anomalies (mm). Data from GNSS stations are plotted as filled circles; (j) "All sky" microwave-based UTH anomalies (%rh); (k) GPCP v2.3 annual mean precipitation anomalies (mm yr⁻¹); (l) GPCP maximum 1-day (Rx1day) annual precipitation anomalies (mm); (m) Lake water level anomalies (m); (n) PATMOS-x/AVHRR+HIRS global cloudiness anomalies (%);

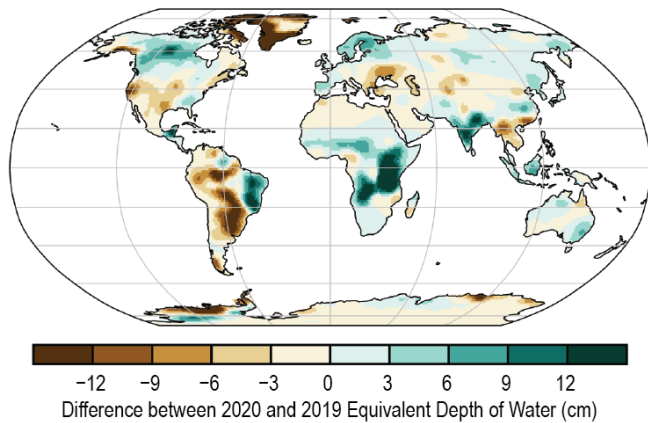
(o) Runoff



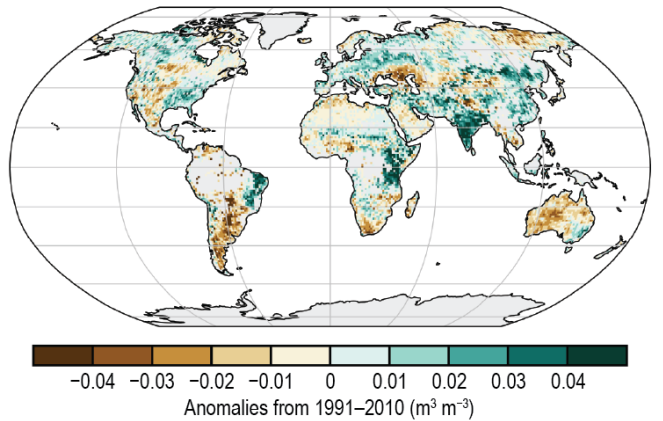
(p) River Discharge



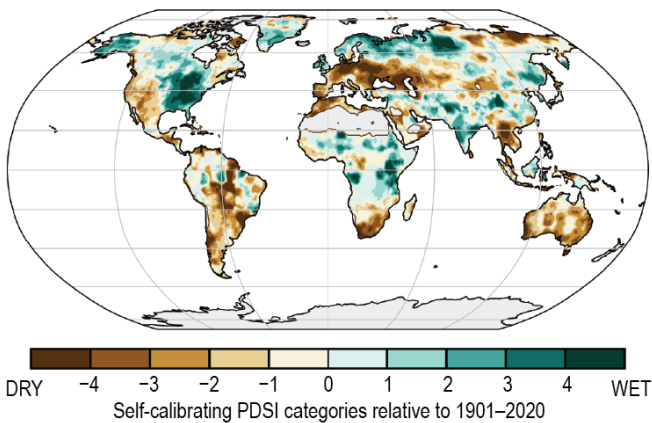
(q) Terrestrial Water Storage



(r) Soil Moisture



(s) Drought



(t) Land Evaporation

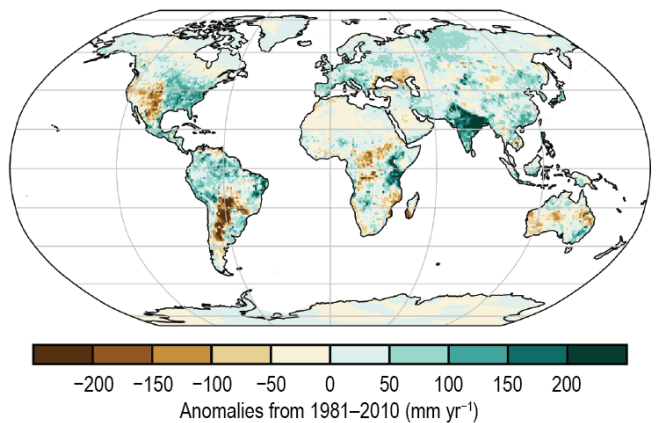
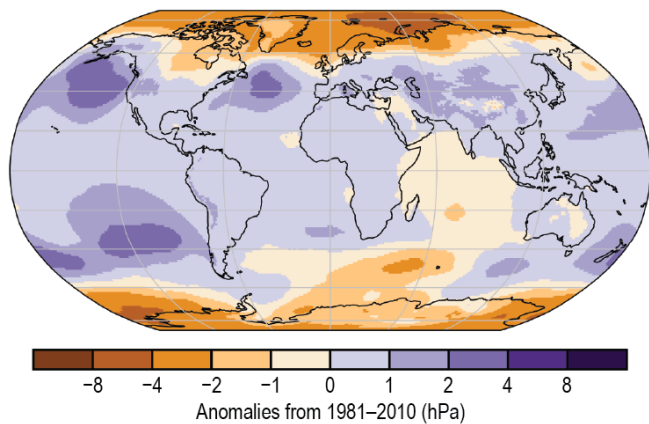
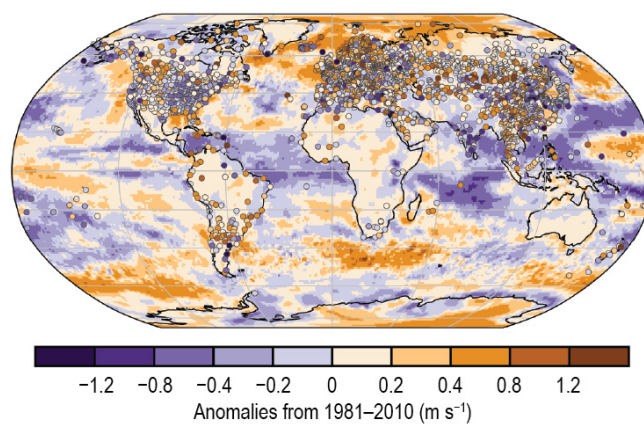


Plate 2.1. (cont.) (o) ELSE (Ensemble Land State Estimator) global distribution of runoff anomalies (mm yr^{-1}); (p) ELSE global distribution of river discharge anomalies ($\text{m}^3 \text{s}^{-1}$); (q) GRACE and GRACE-FO difference in annual-mean terrestrial water storage between 2019 and 2020 (cm); (r) ESA CCI average surface anomalies ($\text{m}^3 \text{m}^{-3}$); (s) Mean scPDSI for 2020. Droughts are indicated by negative values (brown), wet episodes by positive values (green); (t) GLEAM land evaporation anomalies (mm yr^{-1});

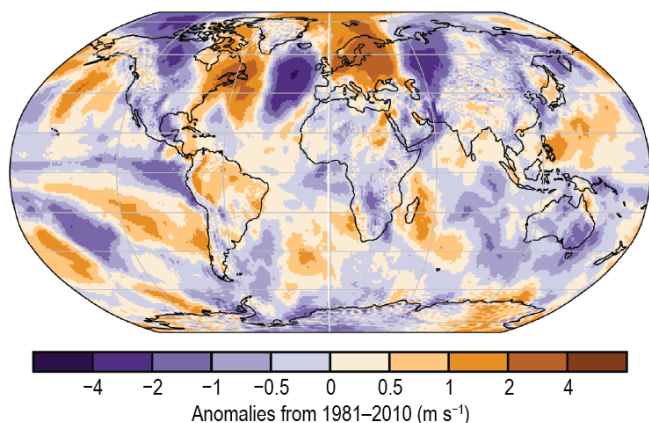
(u) Sea Level Pressure



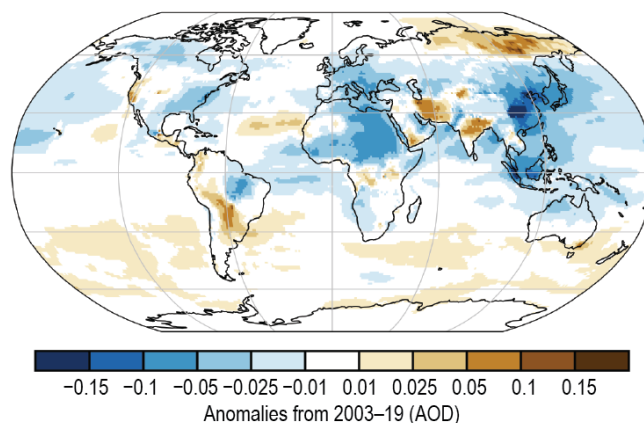
(v) Surface Winds



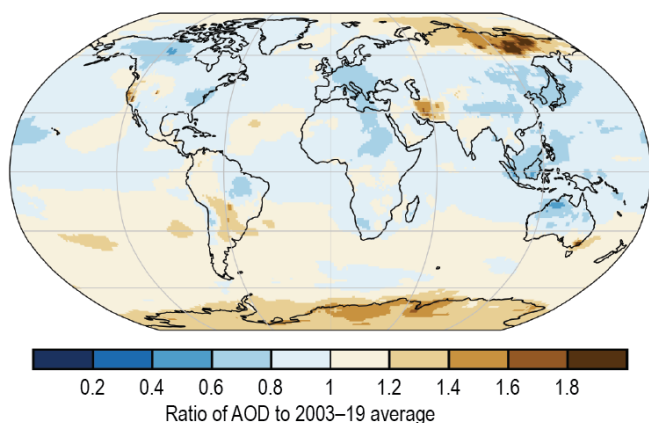
(w) Upper Air (850-hPa) Northward Winds (SOND)



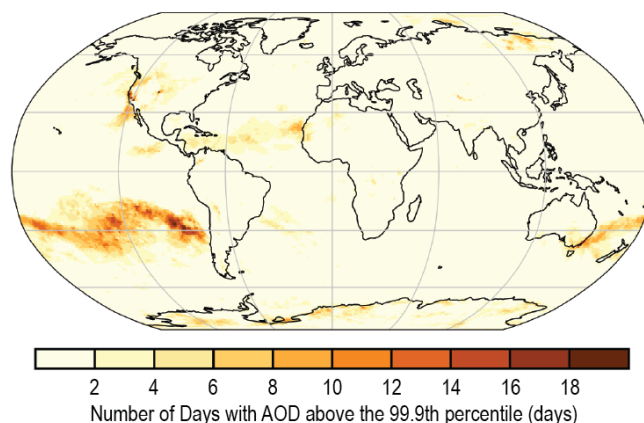
(x) Total Aerosol



(y) AOD Ratio



(z) Extreme Aerosol Days



(aa) Stratospheric (Total Column) Ozone

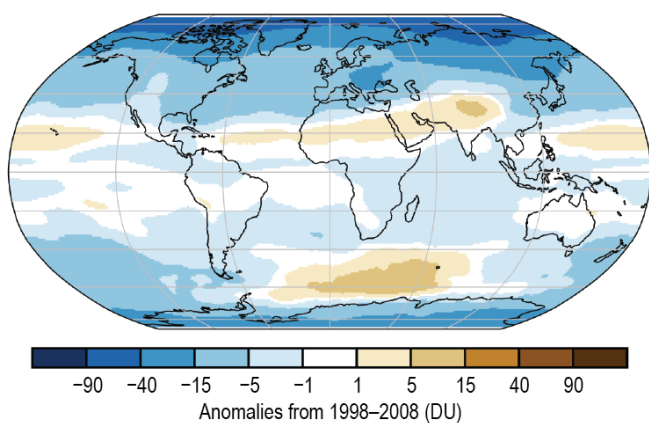
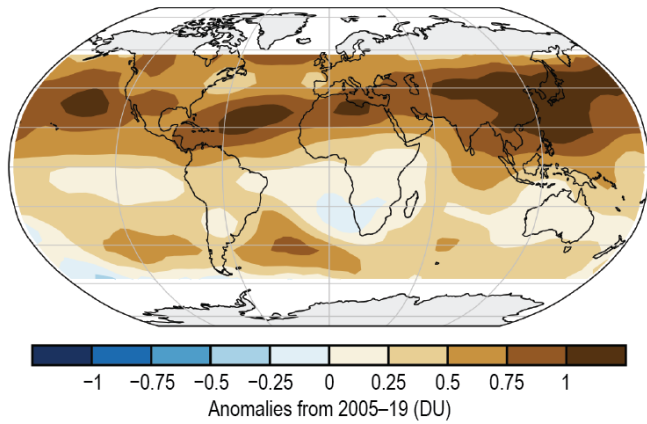
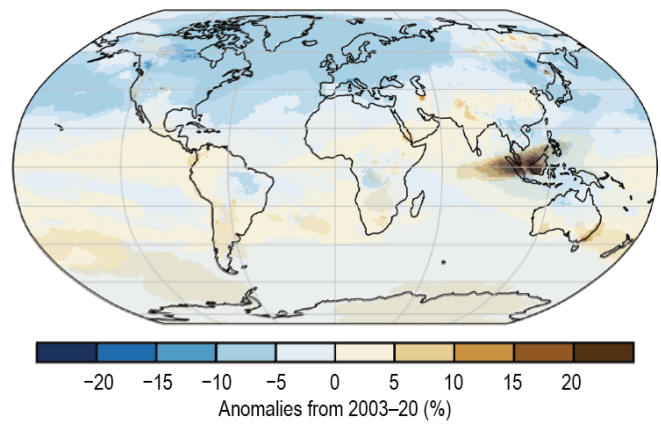


Plate 2.1. (cont.) (u) ERA5 surface pressure anomalies (hPa); (v) Surface wind speed anomalies (m s^{-1}) from the observational HadISD3 dataset (land, circles), the MERRA-2 reanalysis output (land, shaded areas), and RSS satellite observations (ocean, shaded areas); (w) ERA5 Sep–Dec average 850-hPa northward wind speed anomalies (m s^{-1}); (x) Total aerosol optical depth (AOD) anomalies at 550 nm; (y) Ratio of total AOD at 550 nm in 2020 relative to 2003–19; (z) Number of days with AOD above the 99.9th percentile; (aa) GOME2 total column ozone anomalies (DU; using GOME, SCIAMACHY, GOME-2A and -2B [GSG]);

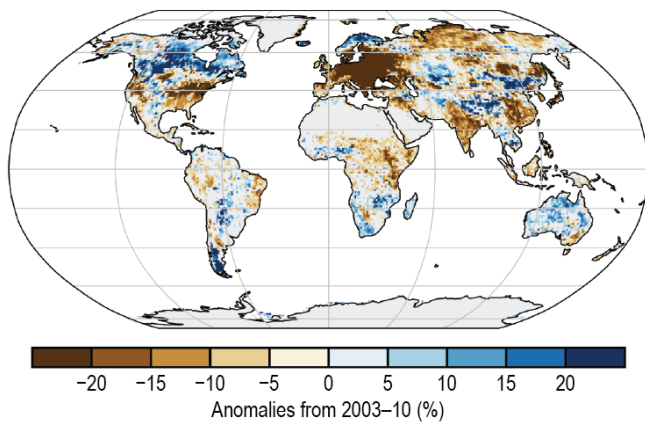
(ab) OMI/MLS Tropospheric Column Ozone



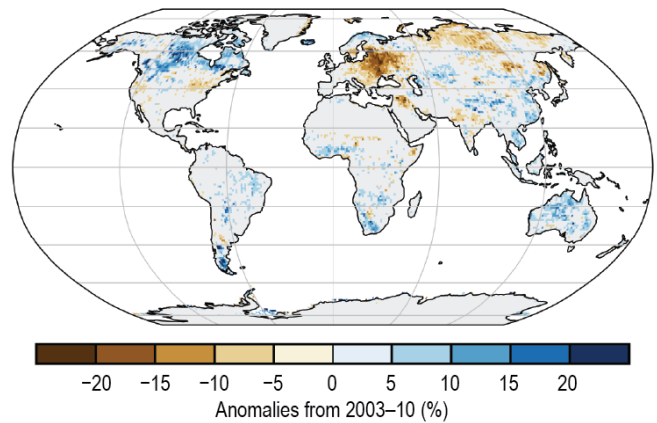
(ac) Carbon Monoxide



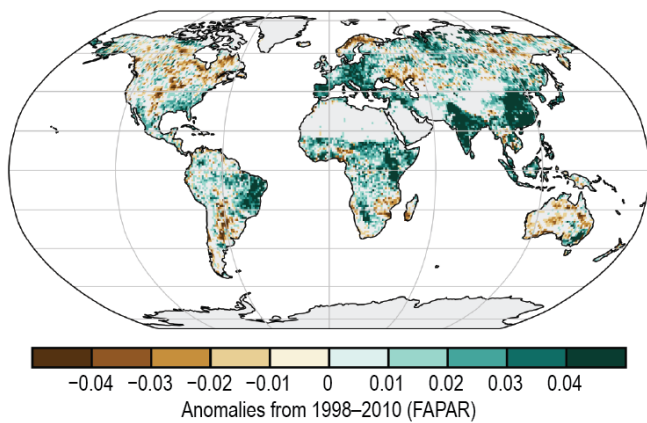
(ad) Land Surface Albedo in the Visible



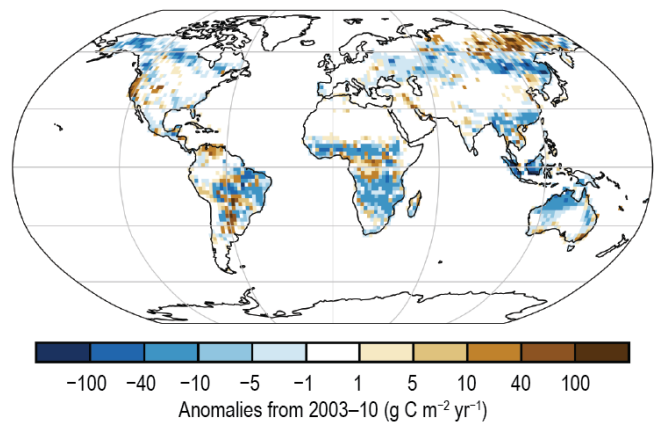
(ae) Land Surface Albedo in the Near-Infrared



(af) Fraction of Absorbed Photosynthetically Active Radiation



(ag) Carbon Emissions from Biomass Burning



(ah) Vegetation Optical Depth

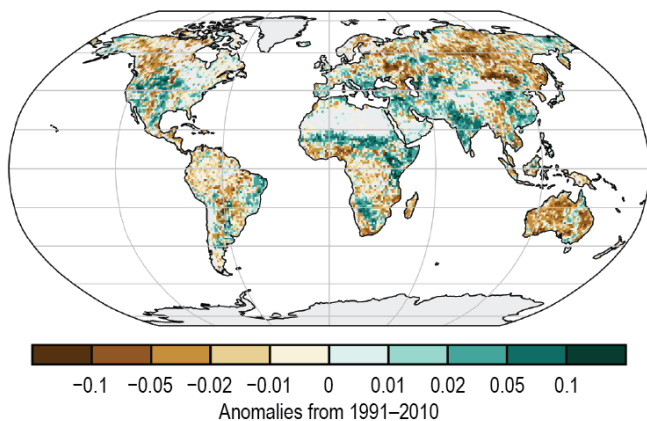


Plate 2.1. (cont.) (ab) OMI/MLS tropospheric ozone column anomalies for 60°S-60°N (DU); (ac) CAMS reanalysis total column CO anomalies (%); (ad) Land surface visible broadband albedo anomalies (%); (ae) Land surface near-infrared albedo anomalies (%); (af) FAPAR anomalies; (ag) GFAS1.4 carbonaceous emission anomalies ($\text{g C m}^{-2} \text{yr}^{-1}$) from biomass burning; (ah) VODCA Ku-band VOD anomalies.

b. Temperature

1) *Global surface temperature*— A. Sánchez-Lugo, C. Morice, J. P. Nicolas, and A. Argüez

The year 2020 was one of the three warmest years since global records began in the mid-to-late 1800s, with a global land and ocean surface temperature 0.54° – 0.62°C above the 1981–2010 average, according to five global temperature datasets (Table 2.1). These datasets consist of three independent global in situ surface temperature analyses (NASA-GISS, Lenssen et al. 2019; HadCRUT5, Morice et al. 2021; NOAA GlobalTemp, Zhang et al. 2019) and two global atmospheric reanalyses (ERA5, Hersbach et al. 2020; JRA-55, Kobayashi et al. 2015). Depending on the dataset, 2020 was either the warmest year on record, 2020 was tied with 2016 as the warmest on record, 2020 was the second-warmest year on record, or 2020 was the third-warmest (Fig. 2.1).

The year began in El Niño–Southern Oscillation (ENSO)-neutral conditions, transitioning to La Niña by August (see section 4b for details). The global monthly temperature anomalies were high throughout 2020, with each month from January through November ranking among the five warmest for each respective month across all datasets. December had the smallest temperature anomaly of the year. Despite the slightly cooler end to the year, this was the warmest non-El Niño year on record, surpassing 2017 by 0.07° – 0.11°C . Furthermore, the five datasets agree that the last 7 years (2014–20) were the seven warmest years on record.

Even though each dataset might differ slightly on the yearly rankings and anomalies, it is worth noting that these differences are small and that, overall, temperature anomalies for each dataset are in close agreement. The three global in situ surface temperature analyses assessed here are derived from air temperatures observed at weather stations over land and sea surface temperatures (SSTs) observed from ships and buoys. The differences between each analysis are mainly due to how each methodology treats areas with little to no data and how each analysis accounts for changes in measurement methods (for more details see Kennedy et al. 2010; Hansen et al. 2010; Huang et al. 2015; Sánchez-Lugo et al. 2017). The global average surface temperature has increased at an average rate of $0.08^{\circ}\text{C decade}^{-1}$ since 1880 with a rate more than twice as high since 1981 (0.19° – $0.20^{\circ}\text{C decade}^{-1}$, depending on the dataset).

Unlike the global in situ surface temperature analyses, global atmospheric reanalyses use a weather prediction model to combine information from a range of satellite, radiosonde, aircraft, and other in situ observations to reconstruct historical weather and climate across the whole globe. These characteristics give reanalyses a unique ability to produce globally-complete temperature fields in a physically consistent manner; however, these datasets can also suffer from regional model biases and the effects of changes in the observation network over time (Simmons et al. 2017, 2021). Nonetheless, surface temperatures from reanalyses should be consistent with in situ analyses in regions of good observational coverage. One of the reanalyses used here, ERA5, provides data from 1950 onward, but because of lower confidence in its surface temperature data prior to 1967 (Simmons et al. 2021), only data from 1967 onward are shown. In addition, temperatures

Table 2.1. Temperature anomalies ($^{\circ}\text{C}$) and uncertainties (where available) for 2020 with respect to the 1981–2010 base period. Where uncertainty ranges are provided, temperature anomalies correspond to the central values of a range of possible estimates. Uncertainty ranges represent a 95% confidence interval. Note that for HadCRUT5, land values were computed using the CRUTEM 5.0.1.0 dataset (Osborn et al. 2021), ocean values were computed using the HadSST4.0.0.0 dataset (Kennedy et al. 2019), and global land and ocean values used the HadCRUT5.0.1.0 dataset (Morice et al. 2021).

Global	NASA-GISS ($^{\circ}\text{C}$)	HadCRUT5 ($^{\circ}\text{C}$)	NOAA GlobalTemp ($^{\circ}\text{C}$)	ERA5 ($^{\circ}\text{C}$)	JRA-55 ($^{\circ}\text{C}$)
Land	+0.97	+0.85 \pm 0.13	+0.95 \pm 0.14	+0.99	+0.88
Ocean	+0.37	+0.42 \pm 0.07	+0.39 \pm 0.16	+0.47	+0.41
Land and Ocean	+0.60 \pm 0.05	+0.57 \pm 0.08	+0.54 \pm 0.15	+0.62	+0.54

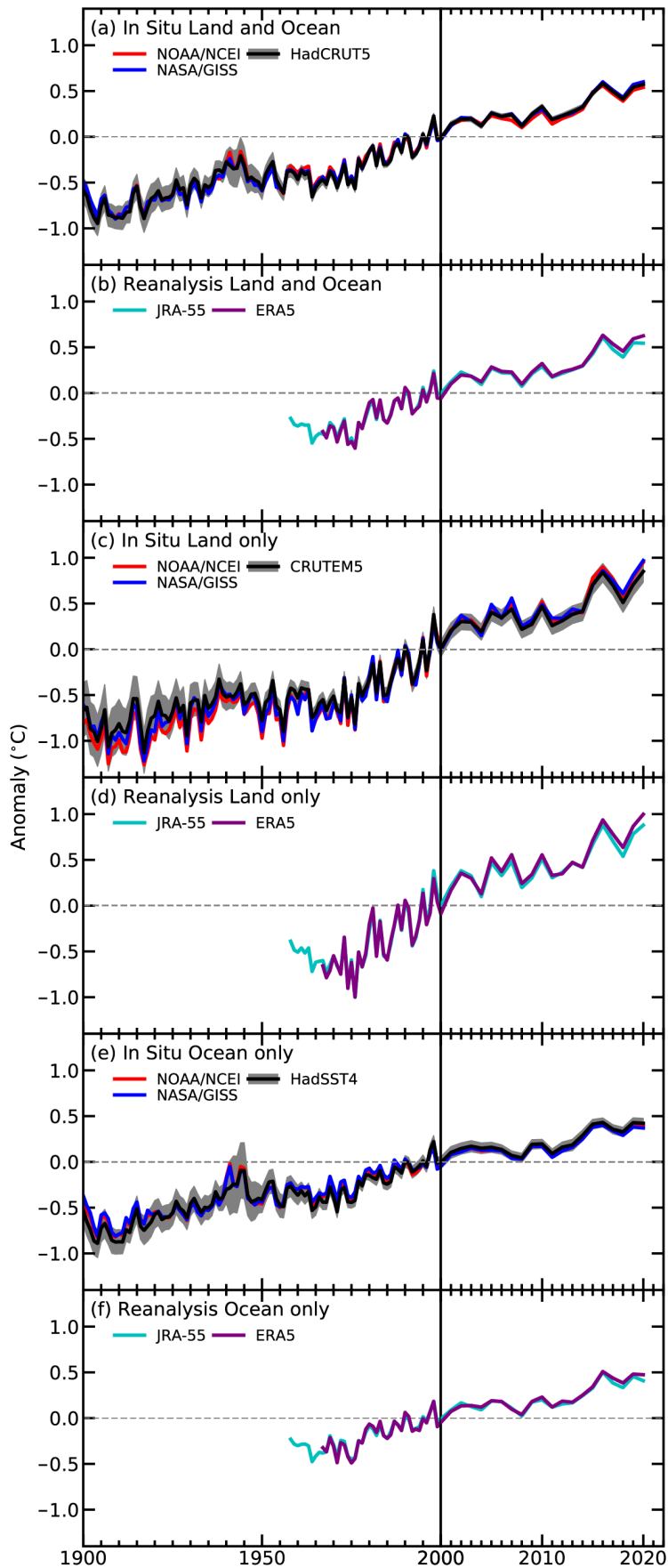


Fig. 2.1. Global average surface air temperature anomalies ($^{\circ}\text{C}$; 1981–2010 base period). In situ estimates are shown from NOAA/NCEI (Zhang et al. 2019), NASA-GISS (Lenssen et al. 2019), HadCRUT5 (Morice et al. 2021), CRUTEM5 (Osborn et al. 2021), and HadSST4 (Kennedy et al. 2019). Reanalyses estimates are shown from ERA5 (Hersbach et al. 2020) and JRA-55 (Kobayashi et al. 2015). Please note change in x-axis scale pre/post 2000.

over the Great Lakes are adjusted as described in Simmons et al. (2021) to correct for a production error. This correction has a negligible impact on the global average temperature. The other reanalysis, JRA-55, provides data from 1958 onward. The JRA-55 global average temperature is computed as in Simmons et al. (2017, 2021), that is by using JRA-55 analysis temperature over land and its background temperature over ocean and other water bodies. For both reanalyses, the 2-m air temperature is used over both land and ocean whereas the global in situ analyses use SST over ocean. This difference is expected to have only a very small impact on the global averages assessed here (see Fig. 1 of Simmons et al. 2017).

While annual temperature rankings provide an intuitive measure of the state of global temperatures, a recently introduced global annual temperature score (Arguez et al. 2020) complements the annual temperature ranking by providing a basic characterization of the impacts of interannual variability on global temperature relative to the sustained upward trend since the mid-1970s. Scores range from 1 to 10, with a score of 1 (10) indicating the coldest (warmest) 10% of anomalies relative to the trend. In an era of seemingly perpetual near-record warm rankings, the annual temperature scores can help characterize whether the annual temperature ranking attained in a given year was due primarily to the secular trend, interannual variability, or both. For example, 2016 was not only the warmest year on record, but it also exhibited a temperature score of 10, whereas 2014 previously attained a ranking of warmest yet exhibited a temperature score of 4 (on the colder half of the scale). This indicates that, on top of the secular trend, interannual variability had a prominent contribution to the record temperature in 2016, whereas interannual variability did not synergistically contribute to 2014's previous record temperature. Using global annual time series from 1975 through 2020, the year 2020 registers a global annual temperature score of 9 (corresponding to the 80th–90th percentile) in the NASA-GISS and NOAA GlobalTemp datasets and a score of 8 (70th–80th percentile) in the HadCRUT5 dataset. This indicates that 2020, much like 2019, was moderately-to-considerably warmer than would be expected due to the secular trend alone, suggesting that its ranking of warmest or second warmest for the three in situ datasets was enhanced by the effects of the interannual variability.

Separately, the global land surface temperature for 2020 was the highest in four of the five datasets, surpassing the previous record set in 2016 by 0.05°–0.11°C. The fifth dataset (JRA-55) has the global land surface temperature tying with 2016 as the highest. The globally averaged SST was either third or fourth highest on record, depending on the dataset.

The year was characterized by higher-than-average temperatures across much of the globe (Plate 2.1a; Appendix Figs. A2.1–A2.4). The most notable feature of 2020 is the very large positive temperature anomalies (+4.0°C or higher above the 1981–2019 base period) over Arctic Siberia and the adjacent sector of the Arctic Ocean (Appendix Fig. A2.2). Large positive anomalies (+2.0°C or higher) are also found across northern Europe, northern Asia, and the North Pacific Ocean. In contrast, average to below-average conditions were limited to the central and eastern tropical Pacific Ocean and across parts of northern North America, subpolar North Atlantic, and the southern Indian Ocean.

2) *Lake surface water temperature*—L. Carrea, C. Merchant, B. Calmettes, and J.-F. Cretaux

In 2020, the worldwide averaged satellite-derived lake surface water temperature (LSWT) warm-season anomaly was +0.11°C with respect to the 1996–2016 baseline. The mean warming trend during 1996–2020 was $0.22 \pm 0.01^\circ\text{C decade}^{-1}$, broadly consistent with previous analyses (Woolway et al. 2017; Woolway et al. 2018; Carrea et al. 2019, 2020). On average, anomalies in 2020 were only 0.01°C higher than in 2019. The warm-season anomalies for each lake are shown in Plate 2.1b. Lake mean temperature anomalies were positive for 55% of lakes and negative for 45%. Some lakes in eastern Africa recorded notable positive anomalies for both LSWT and lake water level (LWL; section 2d6). The LWL is defined as the height, in meters above the geoid (the shape that the surface would take under the influence of the gravity and rotation of Earth), of

the reflecting surface. Changes in lake water levels can be critical, as they affect water quantity and quality, food stocks, recreational opportunities, and transportation.

Globally, distinct regions of coherent warm and cool LSWT anomalies can be identified in 2020. Lakes in subtropical eastern China were markedly warm, with the three largest warm anomalies (+2.54°C, +2.39°C, +2.38°C) in this region. In northern Europe, Canada, the southeastern United States, and southeastern Australia, negative anomalies were observed for 70% or more of the water bodies, while southern Europe, Alaska, the Middle East, northern Russia, and eastern Africa had positive anomalies.

Four regions are considered here in more detail: Canada (number of lakes, $n = 246$, Fig. 2.2); Europe ($n = 127$, Fig. 2.2); Tibet ($n = 104$, Fig. 2.2); and Africa ($n = 70$). The boreal warm season (July–September) LSWT calculated from the satellite data shows a warming tendency of $+0.39 \pm 0.01^\circ\text{C decade}^{-1}$ in Europe (Fig. 2.2a) and $+0.18 \pm 0.01^\circ\text{C decade}^{-1}$ in Canada (Fig. 2.2d). In Africa and Tibet, the tendency is closer to neutral (Figs. 2.2b,c). In Canada, 166 lakes had negative anomalies and 80 had positive in 2020, with an overall average of -0.22°C . In Tibet, 72% of the lakes had moderate-positive anomalies and 28% had negative anomalies, with an average of $+0.20^\circ\text{C}$. In Europe, cool anomalies in northern Europe (67 lakes) balanced warmer anomalies in the south (60 lakes), producing $+0.03^\circ\text{C}$ on average. In Africa, positive anomalies were recorded for 80% of the 70 lakes over the considered period. Several of the warmest anomalies occurred in eastern Africa, where the LWL was also consistently higher than the 1996–2016 average. Therefore, for some of the eastern African lakes, LSWT was compared with their LWL anomalies, calculated using a time series of LWL changes obtained from satellite altimetry.

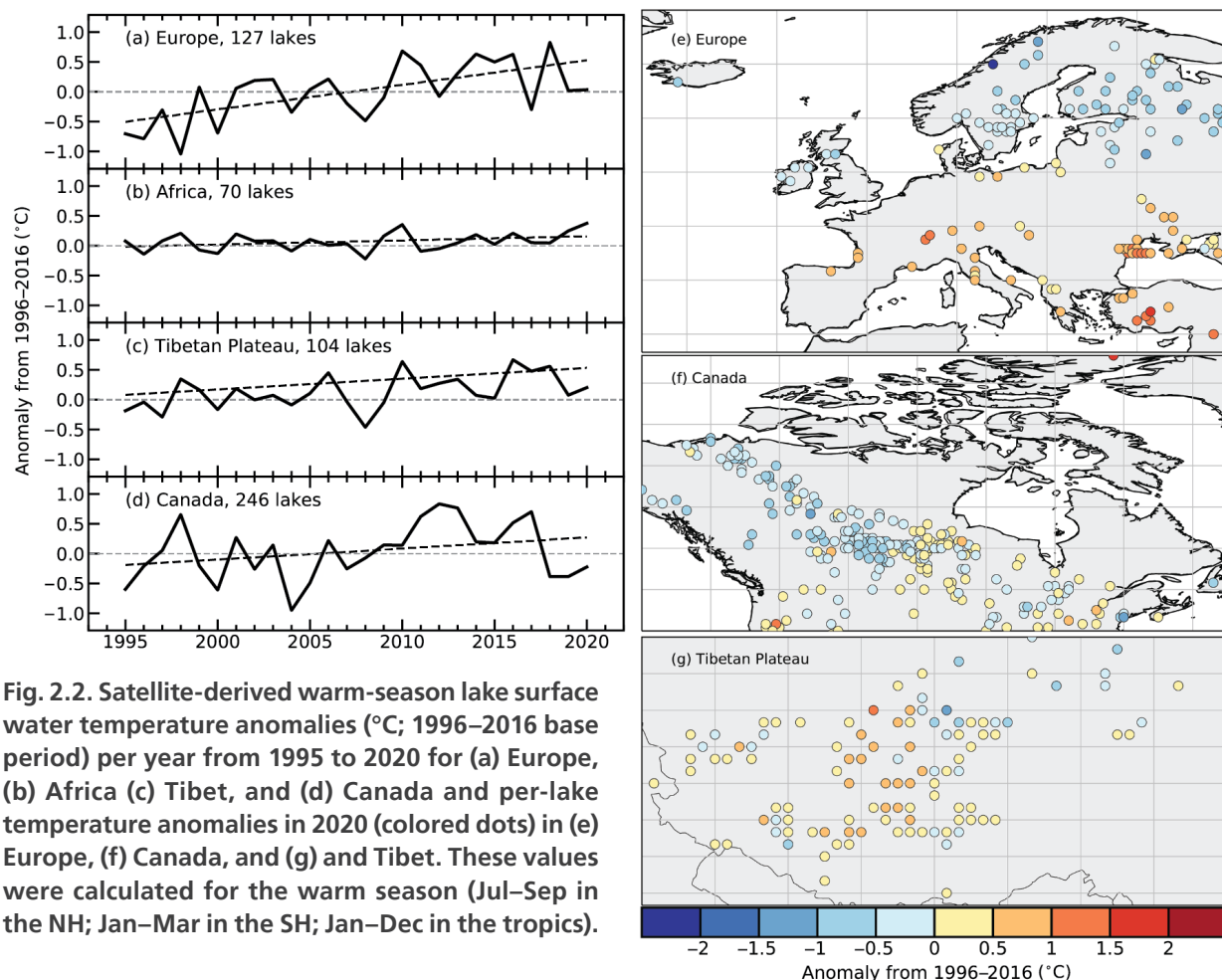


Fig. 2.2. Satellite-derived warm-season lake surface water temperature anomalies ($^\circ\text{C}$; 1996–2016 base period) per year from 1995 to 2020 for (a) Europe, (b) Africa (c) Tibet, and (d) Canada and per-lake temperature anomalies in 2020 (colored dots) in (e) Europe, (f) Canada, and (g) and Tibet. These values were calculated for the warm season (Jul–Sep in the NH; Jan–Mar in the SH; Jan–Dec in the tropics).

Figure 2.3 presents a selection of African lakes (Victoria, Tanganyika, Malawi, Turkana, Rukwa, Albert, Kyoga, Edward, Mweru, Tana, and Bangweulu) for which the LSWT and the LWL normalized anomalies from 1996 to 2020 are reported for each of the lakes, together with the spatial distribution of the 2020 LSWT anomalies. All the lakes exhibit positive LWL anomalies in 2020, while Lakes Turkana, Edward, and Rukwa have notably high LSWT positive anomalies. For these lakes, the LSWT 2020 anomalies were consistently positive across their full spatial extent, while there was a mix of positive and negative anomalies spatially across other lakes. Most of the lakes exhibited an upward long-term trend for both the LSWT and LWL.

The LSWT warm-season averages for midlatitude lakes are computed for summers (July–September in the Northern Hemisphere [NH] and January–March in the Southern Hemisphere [SH]), and whole-year averages (January–December) are presented for tropical lakes (within 23.5° of the equator).

The LSWT time series were derived from satellite observations from the series of Along Track Scanning Radiometers (ATSRs), the Advanced Very High Resolution Radiometers (AVHRRs) on MetOp A and B, and the Sea and Land Surface Temperature Radiometers (SLSTRs) on Sentinel3A and 3B. The retrieval method of MacCallum and Merchant (2012) was applied on image pixels filled with water according to both the inland water dataset of Carrea et al. (2015) and a reflectance-based water detection scheme. The LWL observations for 11 African lakes were analyzed where long time series are available from radar altimetry (Cretaux et al. 2011). The LWL were validated using a set of in situ data over lakes in South America, North America, Russia, and Europe (Ričko et al. 2012). For lakes with sizes comparable to those in East Africa, the accuracy is generally within 0.1 m (Cretaux et al. 2018; Quartly et al. 2020).

The satellite-derived LSWT data are spatial averages for each of 947 lakes, for which high-quality temperature records were available in 2020. The satellite-derived LSWT data were validated with in situ measurements with an average satellite minus in situ temperature difference less than

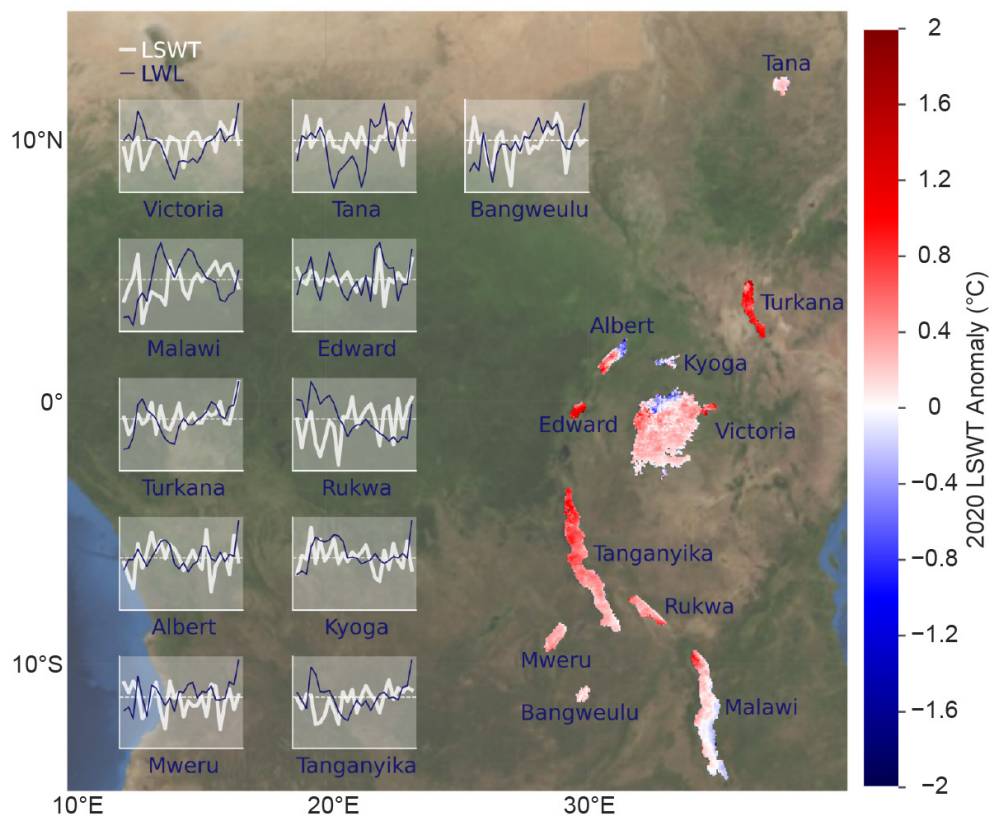


Fig. 2.3. Satellite-derived lake surface water temperature (LSWT) and lake water level (LWL) normalized anomalies relative to the 1996–2016 period from 1995 to 2020 for 11 lakes in East Africa, together with the spatial distribution of the 2020 LSWT anomalies (in °C) for the same lakes.

0.5°C and, consequently, a good agreement was found. Lake-wide average surface temperatures have been shown to provide a more representative picture of LSWT responses to climate change than single-point measurements (Woolway and Merchant 2018).

3) *Land and marine temperature extremes*—S. E. Perkins-Kirkpatrick, R. J. H. Dunn, R. W. Schlegel, M. G. Donat, and Michael G. Bosilovich.

Averaged over global land regions using the Global Historical Climatology Network-Daily dataset (GHCNDEX; Donat et al. 2013), 2020 recorded the highest number of days where the maximum temperature was above the climatological 90th percentile (TX90p, “warm days”; Fig. 2.4). There were over 70 days, which is almost double the average of 36.5 days during 1961–90, and 10 days more than 2019. The number of cool nights (TN10p, where the minimum temperature was below the 10th percentile) was lower than the 1961–90 average, at just over 20 nights throughout the year. This was below average compared to the last 70 years but comparable to the recent decade.

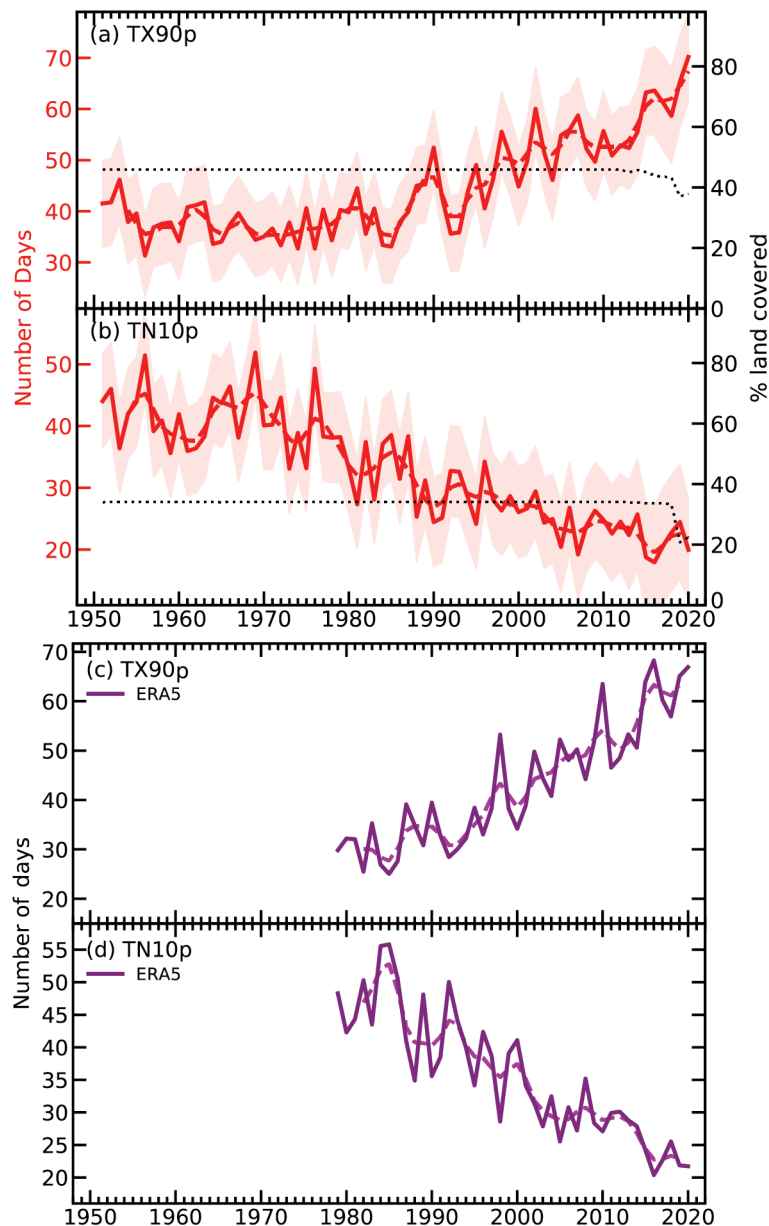


Fig. 2.4. Time series of (a) TX90p (warm days) and (b) TN10p (cool nights) from GHCNDEX relative to 1961–90. The red dashed line shows a binomial smoothed variation and red shading the coverage uncertainties estimated using ERA5 following Brohan et al. (2006). The dotted black line shows the percentage of land grid boxes with valid data in each year. Time series of (c) TX90p (warm days) and (d) TN10p (cool nights) from ERA5 relative to 1981–2010.

The behavior of the GHCNDX time series is comparable to the more spatially complete ERA5 dataset (Fig. 2.4; Hersbach et al. 2019) for the last 40 years.

More detail on regional extreme temperature events is available in Chapter 7. There was a high number of warm days during 2020 in Europe, China, and northeast Australia compared to average (Plate 2.1c), and the number of warm days was larger than the number of cool nights almost everywhere (Plate 2.1d). Many extreme maximum temperatures were recorded (Table 2.2), several of which are described in the following text, and others discussed in Chapter 7 and the World Meteorological Organization (WMO) *State of the Global Climate* (2021).

Table 2.2. Examples of extreme maximum temperatures in 2020 described in this section.				
Country	Location	Date	Value (°C)	Notes
UK	Heathrow	31 Jul	37.8	Third-hottest UK day
Spain	Around Seville	5 Mar	36	—
Russia	Verkhoyansk (Siberia)	20 Jun	38	Hottest regional day (Provisional Arctic Circle record)
United States	Furnace Creek, Death Valley, California	16 Aug	54.4	Globally third-hottest day on record
United States	Woodland Hills, Los Angeles	6 Sep	49.4	—
Canada	Montreal	27 May	36.6	Hottest May
Canada	Miramichi	19 Jun	37.2	New annual record
Iraq	Basra	27 and 28 Jul	53	—
Iraq	Baghdad	28 Jul	51.8	New record
Lebanon	Houch al-Oumara?	28 Jul	45.6	New record
Syria	Damascus	29 Jul	46	New record
Japan	Hamamatsu	18 Aug	41.4	Equal record
Australia	Sydney	29 Nov	25.4	Hottest November night
Antarctica	Casey	24 Jan	9.2	New record
Antarctica	Esperanza Base	6 Feb	18.3	New Antarctic record

In the United States, Furnace Creek in Death Valley (California) recorded a yet-to-be certified temperature of 54.4°C—the hottest temperature measured on Earth since 1931—on 16 August during a heat wave that affected the western and midwestern states. Another heat wave hit the southwest in early September where the extreme heat fueled wildfires (see sections 2h3, 7b2) and set new records. In Canada, Montreal and Burlington experienced six consecutive days at 32°C during a June heat wave. This heat wave lasted into July, enhancing conditions for wildfires in the Quebec province and seeing numerous daily maximum temperature records broken. Many locations in South America experienced extreme temperatures during September and October, with multiple records broken. Concepción, Paraguay, reached 42.6°C on 2 October; Sao José de Chiquitos, Bolivia, reached 43.4°C on 8 October, and Sao Paulo, Brazil, recorded four of its five highest daily maximum temperatures on record during this time (see sections 7d2, 7d3). Extreme heat also occurred over the Caribbean and Mexico during April. Daily maximum temperatures reached 39.7°C and 48.8°C at Veguitas, Cuba, and Gallinas, Mexico, respectively, on 12 April.

A protracted extreme temperature event occurred over Siberia during the first half of 2020. Heat wave frequency (HWF) and magnitude (HWM) indices for April–June over Siberia were the largest in the MERRA2 record (Collow et al. 2020; Fig. 2.5). The long-term and widespread heat helped

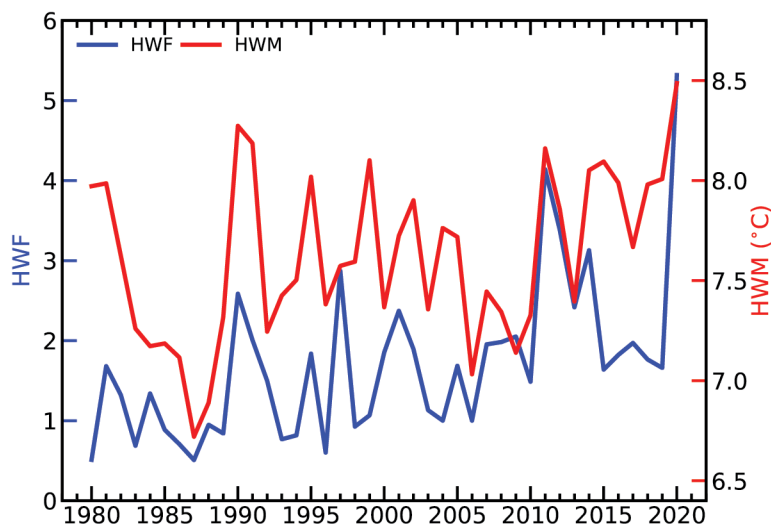


Fig. 2.5. MERRA-2 Apr–Jun seasonal heatwave frequency (HWF; count) and heatwave magnitude (HWM; °C; Callow et al. 2020) area averaged for the Siberian region affected by anomalous heat wave conditions (60°–160°E, 50°–80°N, land only).

fuel large wildfires in the region (see sections 2h3, 7g2, Sidebar 5.1). Verkhoyansk recorded 38.2°C on 22 June, provisionally the highest temperature ever measured within the Arctic Circle.

Antarctica experienced a period of record-breaking temperatures during 23–26 January 2020 at Casey, where minimum temperatures did not fall below 0°C and the highest ever daily maximum and minimum temperatures were recorded (9.2°C and 2.5°C, respectively). On 6 February, the highest Antarctic temperature on record was measured at Esperanza Base (18.3°C; see section 6b, Sidebar 6.1). This was part of a warm spell lasting from 5–13 February, causing widespread glacial melting.

During early August, record warm nights were widespread across the United Kingdom, with parts of the southeast experiencing five consecutive tropical nights (temperatures greater than 20°C) and 6 days with peak temperatures over 34°C (see section 7f2). A heat wave (defined as a period of three or more consecutive TX90p days [Perkins and Alexander 2013]) affected Spain and Portugal in May (see section 7f5).

An intense heat wave occurred over the Middle East during July, with daily maximum temperatures reaching over 53°C in Basra (Iraq) on both the 27th and 28th and widespread maximum temperatures over 45°C. During a heat wave in August, Tokyo experienced three consecutive days of maximum temperature above 35°C and multiple locations in central southwest Japan recorded temperatures above 39°C on 17 August. Numerous large-scale heat waves occurred over Vietnam, with maximum daily temperatures greater than 35°C over large parts of the country during June.

Australia had a warm start to 2020, with its second-warmest summer (December 2019–February 2020) on record for maximum and minimum temperature (2.11°C and 1.64°C above the 1961–90 average, respectively). On 4 January the Sydney suburb of Penrith recorded 48.9°C, the hottest temperature ever recorded across all Australian metropolitan areas. The country also experienced an anomalously warm spring, with records for nationally averaged minimum spring (September–November) and November temperatures (1.91°C and 2.9°C above average, respectively). Numerous local maximum temperature records across the southeast were also broken during November (see section 7h4 for details).

Marine heatwaves (MHW) are defined as SST above the climatological 90th percentile for five or more days (Hobday et al. 2016). Categories of MHW are defined in Hobday et al. (2018). Using NOAA OISST v2 (Banzon et al. 2020), 84% of the surface of the ocean experienced at least one MHW in 2020 (Fig. 2.6). Category 2 – Strong events were the most common (45%), vastly exceeding Category 1 – Moderate events (28%), marking the seventh consecutive year that Category 2 – Strong MHWs have been the dominant category. The ocean experienced a global average of 77 MHW days, exceeding the 2019 average of 74 days, but fewer than the 2016 record of 83 days (Fig. 2.6). On average, 21% of the surface of the ocean in 2020 was experiencing a MHW on any given day (Fig. 2.6). This is slightly higher than the 2019 average of 20%, but lower than the 2016 record of 23%. Roughly the entire surface of the ocean experienced at least one MHW in 2020, with the exception of the equatorial Pacific Ocean. This is likely because heat anomalies in the equatorial Pacific Ocean are tightly linked with the ENSO, which was in a neutral or moderately

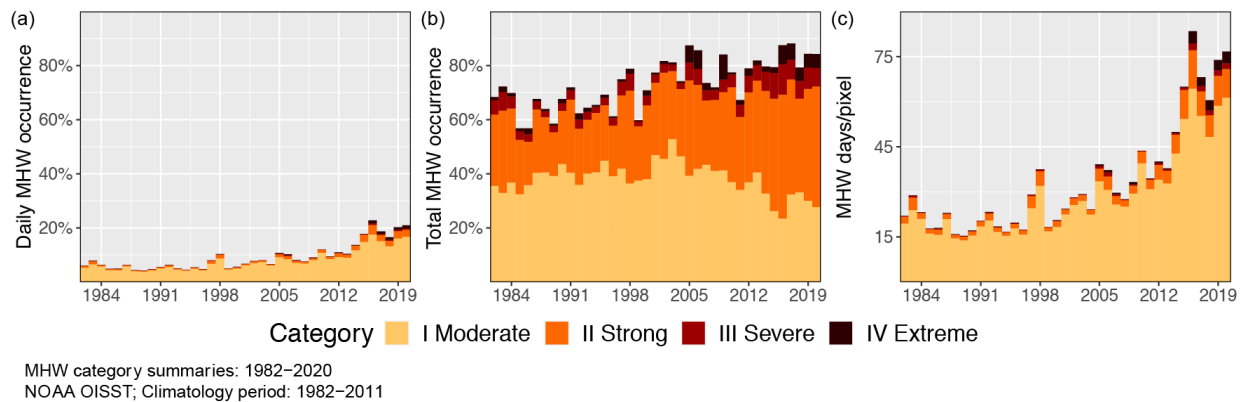


Fig. 2.6. Annual global marine heatwave (MHW) occurrence from NOAA OISST using a climatology base period of 1982–2011. (a) Daily average percent of the ocean that experienced an MHW. (b) Total percent of the ocean that experienced an MHW at some point during the year. The values shown are for the highest category of MHW experienced by each ocean grid cell during 2020. (c) Total average of daily MHW occurrence throughout the entire ocean.

negative phase in 2020 (see section 4b). The subpolar North Atlantic, southeast of Greenland, was another area that did not experience MHWs in 2020, a pattern persistent from 2014–18.

To show temperature extremes over land, we use a subset of the moderate extremes indices developed by the WMO Expert Team in Climate Change Detection and Indices (ETCCDI; Zhang et al. 2011). In the GHCNDEX dataset (Donat et al. 2013), daily temperature values from the GHCND (Menne et al. 2012) are interpolated onto a regular 2.5° grid. As in previous years, the spatial coverage is sparse (Plates 2.1c,d) and restricted to North America, parts of Eurasia, and Australia. To fill the gaps, we use the ERA5 reanalysis (Hersbach et al. 2019), though we have not included the preliminary release of the extension from 1950 to 1978. With the shorter temporal coverage, the reference period for the extremes indices is 1981–2010 (compared to 1961–90 for GHCNDEX), which can lead to differences when comparing recent trends (Dunn et al. 2020a; Yosef et al. 2021). Siberian heat waves were calculated from the MERRA-2 dataset (Gelaro et al. 2017; Collow et al. 2020). HWF frequency is the count of days satisfying heat wave conditions, where heat waves are defined as the MERRA-2 daily mean 2-m temperature exceeding the calendar day 90th percentile for at least three consecutive days. HWM magnitude is the average daily mean 2-m temperature anomaly over all heat wave days.

4) Tropospheric temperature—S. Po-Chedley, J. R. Christy, L. Haimberger, and C. A. Mears

The 2020 annual global lower tropospheric temperature (LTT) tied with 2016 as the highest on record. The annual average LTT was 0.49°–0.72°C above the 1981–2010 average, depending on dataset, and 10%–16% of Earth’s surface experienced record high temperatures (Plate 2.1e). Such expansive and record warmth is notable because it occurred even though the ENSO exhibited neutral or La Niña conditions throughout the year (Fig. 2.7a) and is thus consistent with the background upward trend since 1958. In the past, record warm and cold tropospheric temperatures have typically followed El Niño and La Niña events, respectively (Figs. 2.7a,b). A La Niña pattern was established in August, which will likely depress the LTT in 2021 because tropospheric temperature lags ENSO by several months.

More than 90% of Earth’s lower troposphere experienced above-average temperatures (Plate 2.1e). Regions experiencing record warmth included much of Europe and Russia, the Indian Ocean, the northeast and South Pacific, and a region off the coast of East Antarctica. Limited areas of below-average LTT included Canada, Greenland, and parts of Antarctica and the Southern Ocean.

Above-average lower tropospheric temperatures are consistent with long-term greenhouse gas warming and less-pronounced volcanic cooling over the past 3 decades (relative to significant cooling from the eruptions of Agung, El Chichón, and Pinatubo in 1963, 1982, and 1991, respectively;

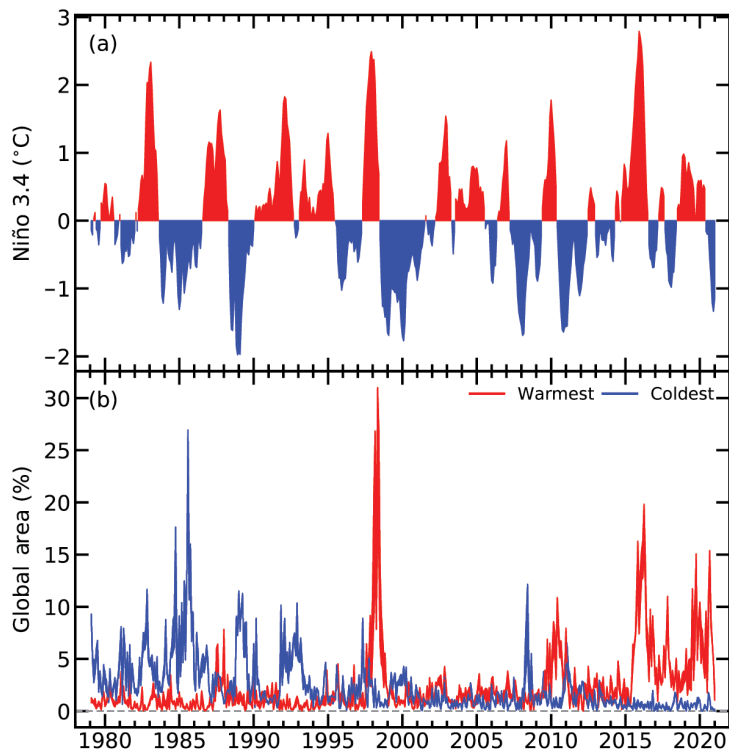


Fig. 2.7. (a) Sea surface temperature anomaly (°C) in the Niño 3.4 region in the central equatorial Pacific. (b) Fraction of Earth (%) with record warm (red) and cold (blue) monthly LTT values. The width of the line represents the difference between the UAH and RSS datasets.

e.g., Santer et al. 2014; Christy and McNider 2017). Recent warmth is recorded by in-situ radiosonde (balloon-borne), microwave (satellite), and reanalysis datasets (Fig. 2.8). Global and tropical tropospheric temperature (TTT) trends since 1958 and 1979 are approximately $+0.18^{\circ}\text{C decade}^{-1}$ (Table 2.3). While the individual tropospheric temperature datasets are broadly consistent, the temperature time series and trends vary across datasets, by altitude (TTT samples temperature at higher altitudes than LTT), and by region. As noted above, 2016 and 2020 are statistically tied for the warmest year on record; the average annual near-global LTT across all eight datasets was 0.68°C and 0.65°C above the climatological normal, respectively. In individual datasets, 2016 was the warmest year in the RATPACvA2, RICHv1.7, and RAOBCORE v1.7 radiosonde datasets (Free et al. 2004; Haimberger et al. 2012), the UAH v6.0 satellite product (Spencer et al. 2017), and JRA-55 reanalysis (Kobayashi et al. 2015). 2020 was the warmest year in the RSS v4.0 satellite product (Mears and Wentz 2016) and the ERA5 and MERRA-2 reanalyses (Hersbach et al. 2020; Gelaro et al. 2017). Structural uncertainty in satellite dataset construction can also affect the spatial pattern of record warm temperatures. RSS has a larger global surface area of record warm LTT values in 2020 compared to the UAH dataset (16% versus 10%, respectively; Plate 2.1e).

The tropical troposphere is expected to experience substantial warming in response to the increasing concentration of atmospheric carbon dioxide (CO_2 ; Flato et al. 2013). Simulations of satellite era tropical and global tropospheric warming in the most recent generation of climate models generally exhibit substantially greater warming than observations (McKittrick and Christy 2018, 2020). Over 1979–2014, the multimodel average TTT trend is $+0.30^{\circ}\text{C decade}^{-1}$, while satellite-derived trends range from 0.09° to $0.20^{\circ}\text{C decade}^{-1}$ (Po-Chedley et al. 2021). The difference in the rate of warming is partially attributable to Pacific decadal climate variability, which has reduced warming in the observed record (Po-Chedley et al. 2021). Such internal climate variability is random and is only captured by chance in climate model simulations. A number of individual model realizations simulate similar Pacific decadal climate variability and approximately 13% (24%) have tropical (global) tropospheric temperature trends that are within the range of satellite observations (Po-Chedley et al. 2021). Other possible drivers of this model-observational

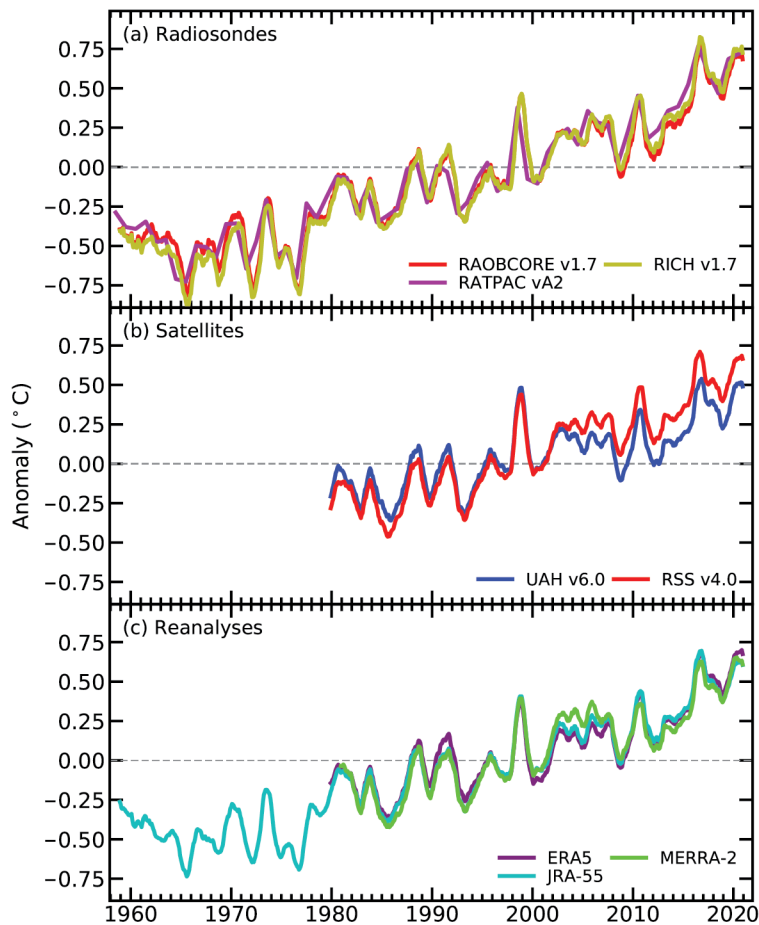


Fig. 2.8. Monthly average lower tropospheric temperature (LTT) anomalies ($^{\circ}\text{C}$) for (a) radiosonde, (b) satellite, and (c) reanalysis datasets. Time series are smoothed using a 12-month running average. Annual averages are displayed for the RATPAC dataset.

Table 2.3. Temperature trends ($^{\circ}\text{C decade}^{-1}$) for near-global lower tropospheric temperature (LTT) and tropical tropospheric temperature (TTT) over 1958–2020 and 1979–2020.

Start Year		LTT (90°S – 90°N)		TTT (20°S – 20°N)	
		1958	1979	1958	1979
Radiosonde	NOAA/RATPACvA2	0.19	0.21	0.16	0.17
	RAOBCOREv1.7	0.18	0.19	0.15	0.15
	RICHv1.7	0.20	0.21	0.17	0.19
Satellite	UAHv6.0	—	0.14*	—	0.13
	RSS v4.0	—	0.22	—	0.18
	UWv1.0	—	—	—	0.18
	NOAA STAR v4.1	—	—	—	0.23
Reanalyses	ERA5	—	0.18	—	0.16
	JRA-55	0.17	0.19	0.16	0.15
	NASA/MERRA-2	—	0.19	—	0.19
Median		0.19	0.19	0.16	0.18

*The vertical sampling in UAH LTT is slightly different from other datasets and results in temperature trends that are approximately $0.01^{\circ}\text{C decade}^{-1}$ smaller than other datasets.

discrepancy include model biases in their response to greenhouse gas forcing, deficiencies in the external forcing applied to models, and observational biases.

The 2σ trend error estimate for individual satellite datasets is approximately $0.04^{\circ}\text{C decade}^{-1}$ (Mears et al. 2011; Po-Chedley et al. 2015; Spencer et al. 2017). Uncertainty in satellite datasets arise from instrument calibration and the removal of non-climatic artifacts, particularly between 2000 and 2005 (Christy et al. 2018). The conversion of level temperatures in radiosonde and reanalysis data to synthetic satellite brightness temperatures and incomplete spatial sampling in radiosonde data contribute to the trend error (Mears et al. 2011). The 2σ tropospheric trend error associated with these effects is approximately $0.01^{\circ}\text{C decade}^{-1}$ and $0.02^{\circ}\text{C decade}^{-1}$, respectively, in both the tropical and global domain.

5) *Stratospheric temperature and winds*—W. J. Randel, C. Covey, and L. Polvani

Temperatures in the middle and upper stratosphere continued to exhibit strong decadal-scale cooling as a result of anthropogenic CO_2 increases. Lower stratospheric temperatures have been relatively constant since ~1998 as the Montreal Protocol stabilized ozone levels, but a transient temperature increase occurred in early 2020, likely related to enhanced stratospheric aerosols from extreme Australian bushfires. The Arctic and Antarctic stratospheric polar vortices were remarkably strong and undisturbed in 2020, with accompanying large polar ozone depletion in both hemispheres. Additionally, a new anomalous disruption of the stratospheric quasi-biennial oscillation (QBO) occurred in 2020, following a similar event in 2016.

Time series of global monthly temperature anomalies from the lower to upper stratosphere based on satellite measurements are shown in Fig. 2.9. The middle and upper stratosphere data (Stratospheric Sounding Unit [SSU] 1, 2, 3) represent ~20-km thick layers from infrared (SSU) data merged with more recent measurements (Zou and Qian 2016; Randel et al. 2016), while the lower stratospheric temperatures (TLS) represent the layer over ~13–22 km from microwave data. As shown in previous reports (Randel et al. 2020), the satellite TLS measurements agree well with radiosonde and reanalysis datasets. Middle- and upper-stratosphere temperatures show strong cooling since 1979 with larger negative trends at higher altitudes, a long-predicted response to increases in atmospheric CO_2 (Manabe and Wetherald 1967). The upper stratospheric cooling is modulated by stratospheric ozone changes, with weaker cooling after 1998 tied to observed increases in upper-stratospheric ozone (Maycock et al. 2018). The ozone is evolving as a response to changes in ozone-depleting substances linked to the Montreal Protocol (WMO 2018). In addition to long-term cooling, the upper-stratosphere time series show modulation by the 11-year solar cycle and transient warming from large volcanic eruptions in 1982 and 1991.

TLS have been relatively constant since the later 1990s with small year-to-year variability. Over most of the globe, the TLS layer spans the cross-over between tropospheric warming and stratospheric cooling associated with CO_2 increases; hence ozone variations strongly influence temperatures in this layer. TLS cooling prior to ~1998 is tied to ozone decreases in the lower stratosphere, while there are small ozone changes thereafter (WMO 2018). The TLS in Fig. 2.9 show an unusually large short-term warm anomaly in early 2020 that is probably related to enhanced stratospheric aerosols in the SH caused by extreme Australian bushfires and resulting smoke injection into the stratosphere (Kablick et al. 2020; Khaykin et al. 2020; Schwartz et al. 2020; Hirsch and Koren 2021; Yu et al. 2021).

The stratospheric winter polar vortices were uniquely strong and undisturbed in both hemispheres in 2020. The Arctic polar vortex was the strongest since the beginning of the satellite era and coincided with record-low stratospheric ozone levels in the Arctic that lasted into spring, together with a record-breaking positive Arctic Oscillation index in the troposphere during January–March (Lawrence et al. 2020). The Antarctic polar vortex in 2020 was also anomalously strong and persistent, with polar temperatures at record cold levels throughout spring (November–December). This strong vortex was linked to a large and persistent ozone hole over the Antarctic,

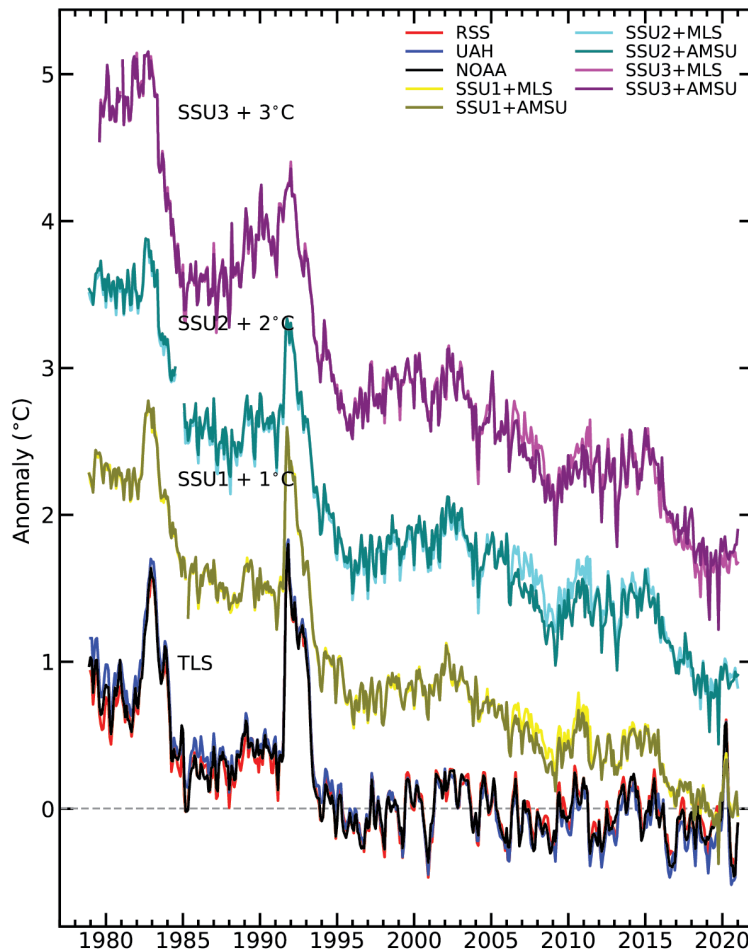


Fig. 2.9. Monthly global stratospheric temperature anomalies from the lower to upper stratosphere (bottom to top). Middle and upper stratosphere data are from the stratospheric sounding unit (SSU), representing thick-layer averages centered near 30, 38, and 45 km (SSU1, SSU2, and SSU3, respectively). Lower stratosphere temperatures (TLS) are ~13–22 km layer averages from satellite microwave measurements. Each time series has been normalized to zero for the period 1995–2005, and curves are offset for clarity.

which lasted to the end of December. While the polar vortices were anomalously cold, they have minimal influence on global average temperatures.

Another notable feature of stratospheric circulation in 2020 was a new disruption of the QBO, which is a repeating reversal of equatorial zonal winds, characterized by downward-propagating easterly and westerly wind regimes with a mean periodicity of ~28 months. While regular downward propagation from the upper to lower stratosphere had been observed continuously since its discovery in the early 1960s, a disruption occurred in 2016, when anomalous easterlies appeared in the lower stratosphere disconnected from upper levels, and a similar disruption occurred in 2020 (see Fig. 2.46). This behavior has been attributed to strong wave forcing from extratropical latitudes (e.g., Osprey et al. 2016; Coy et al. 2017; Anstey et al. 2021). With two disruptions over the last 5 years, there is now substantial uncertainty regarding QBO predictability and future evolution.

Sidebar 2.1: **Night marine air temperature**—R. C. CORNES, D. I. BERRY, R. JUNOD, E. C. KENT, AND N. A. RAYNER

Sea surface temperature (SST) is the principal variable for monitoring surface temperature change across ocean regions. Ship-based SST measurements provide the mainstay of the record, which extends back to the mid-nineteenth century, and these data have been supplemented with observations from moored and drifting buoys since the 1990s. In addition to recording SST, many ships also take measurements of air temperature but in general these marine air temperature (MAT) data are sparser than SST and the values are prone to daytime heating biases (Berry et al. 2004). To mitigate these biases and improve the accuracy of gridded anomaly datasets, only the nighttime values are selected. These night marine air temperature (NMAT) datasets provide a useful independent comparison against SST datasets.

NMAT readings require adjustment to account for variations in ship observation height, including an increase over time in the mean height of the bridge where the observations are typically taken (Kent et al. 2013). If this adjustment is not applied, a reduced trend would be apparent in the data series since temperature generally decreases with height. The temperature values are typically adjusted to the standard reference height of 10-m although the CLASSnmat dataset (Cornes et al. 2020) also provides values adjusted to 2 m and 20 m for comparison against other air temperature datasets.

Over long time periods and over sufficiently large spatial regions it has been assumed that anomalies of SST and NMAT anomalies show similar variability and trends (Kennedy et al. 2019). Climate model simulations indeed depict this relationship. Huang et al. (2015) demonstrate using the GFDL-coupled model that NMAT and SST display a consistent trend over the 1875–2000 period, and this evidence was used to justify the use of NMAT to bias-correct the SST data in the ERSST dataset. However, in situ NMAT and SST datasets indicate a divergent trend at the global scale, with NMAT anomalies increasing at a slower rate than SST (Cornes et al. 2020; Folland and Karl 2001; Kennedy et al. 2019). Initial analyses into this subject concluded that while it is difficult to ascertain the cause, the magnitude of the difference is small relative to the global warming trend (Folland and Karl 2001). However, the more up-to-date CLASSnmat and UAHNMAT (Junod and Christy 2020) datasets indicate an increase in this differential (Fig. SB2.1)—particularly in recent years—when compared against modern SST datasets, in this case HadSST4 (Kennedy et al. 2019).

The NMAT-SST discontinuity may appear as a step-like change in the early 1990s (Kennedy et al. 2019), although this may be a manifestation of a long-term divergence between SST and NMAT coupled with the use of a common 1961–90 base period for the calculation of the anomalies. In the evaluation of the long-term trends in NMAT and SST, differences in spatial coverage may have a large influence on the results (Jones 2020). In general, SST is more spatially complete than NMAT. This results from both the increase in drifting buoy observations and the considerable decline in voluntary observing ships (VOS; https://www.vos.noaa.gov/vos_scheme.shtml) from >7000 in the 1980s to ~1000 at present. Hence, only co-located grid-cell values across the three datasets are averaged in Fig. SB2.1. Note that differences in actual temperatures cannot be inferred from this figure because the time series are expressed as anomalies from climatological averages.

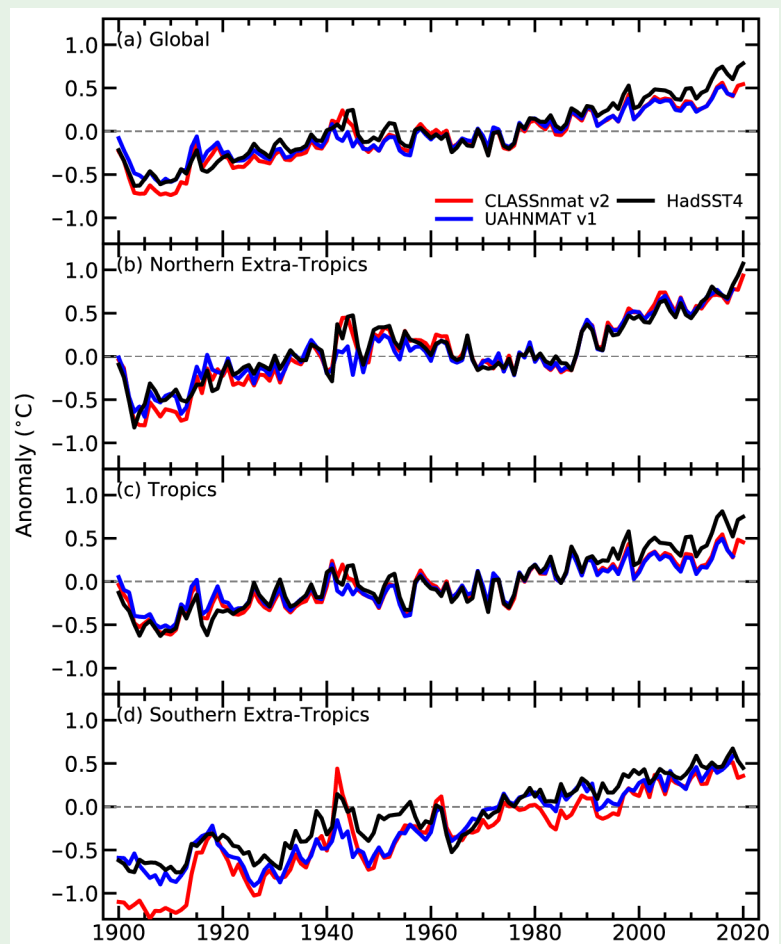


Fig. SB2.1. Large-scale average annual anomalies in the CLASSnmat (Cornes et al. 2020), UAHNMAT (Junod and Christy 2020), and HadSST4 (Kennedy et al. 2019) datasets relative to a 1961–90 base period over the period 1900–2020 (UAHNMAT to 2018).

The trend difference in NMAT and SST is strongest in the tropics (Fig. SB2.1), which may be attributable to changes in the atmospheric circulation across the region (Christy et al. 2001). Recent analyses by Rubino et al. (2020) examined the difference in MAT (day and night) and SST data recorded by moored tropical ocean atmosphere buoys in the tropical Pacific Ocean. The buoy data series are generally short in length (covering at most the period 1985–2010) relative to the century-long ship data, which inhibits definitive conclusions regarding long-term trends in MAT data relative to SST. However, the authors observed marked differences in these variables, particularly on sub-decadal timescales, which highlight the difficulty in assuming that MAT and SST are interchangeable.

Table SB2.1. Decadal trends ($^{\circ}\text{C decade}^{-1}$) in large-scale average anomalies from 1979 to 2020 in the sea surface temperature (SST) and marine air temperature (MAT) data from ERA5 and in CLASSmat and HadSST4. Note that ERA5 has complete coverage over ocean regions whereas CLASSmat and HadSST4 are not complete. CLASSmat and HadSST4 are masked to have the same spatial coverage.

Region	ERA5		CLASSmat	HadSST4
	SST	Air Temperature		
Global	0.120	0.127	0.093	0.125
Northern extratropics	0.171	0.183	0.114	0.151
Tropics	0.116	0.123	0.039	0.101
Southern extratropics	0.081	0.084	0.069	0.098

Reanalysis datasets provide additional information about the (N)MAT-SST trend difference. Figure SB2.2 shows global and hemispheric annual average 2-m air temperature and SST anomalies (relative to 1981–2010) calculated from ERA5 over the period 1950–2020. This figure indicates a comparable trend in SST and co-located air temperature across all regions including the tropics (see also Table SB2.1), which is in contrast to the results in Figure SB2.1 using the gridded NMAT and SST datasets. Note that ERA5 is spatially complete (apart from the masking of sea ice regions) in Fig. SB2.2 whereas the in situ datasets have missing grid cells. Conversely, ERA5 data across the Arctic region, which are excluded in the Figure SB2.2 averages, show a much greater warming trend in air temperature relative to SST (Fig. SB2.3); however, SST is derived indirectly in these regions using sea ice concentration data (Hirahara et al. 2016).

It remains unclear if the trend difference seen in SST and NMAT datasets is due to physical processes or if it results from biases in either the SST or NMAT data or both. Understanding this feature is particularly important because global mean surface temperature (GMST) data products (Lenssen et al. 2019; Morice et al. 2021; Vose et al. 2012) combine anomalies of near-surface temperature over land with anomalies of SST rather than MAT. Resolving this question would also inform the debate about the suitability of comparing these merged GMST datasets against global climate model simulations of air temperature (Cowtan et al. 2015; Jones 2020), especially since simulated values using MAT for the marine component of global air temperature have been shown to warm at a slightly faster rate than a comparable dataset that used SST as the marine component (Richardson et al. 2018)

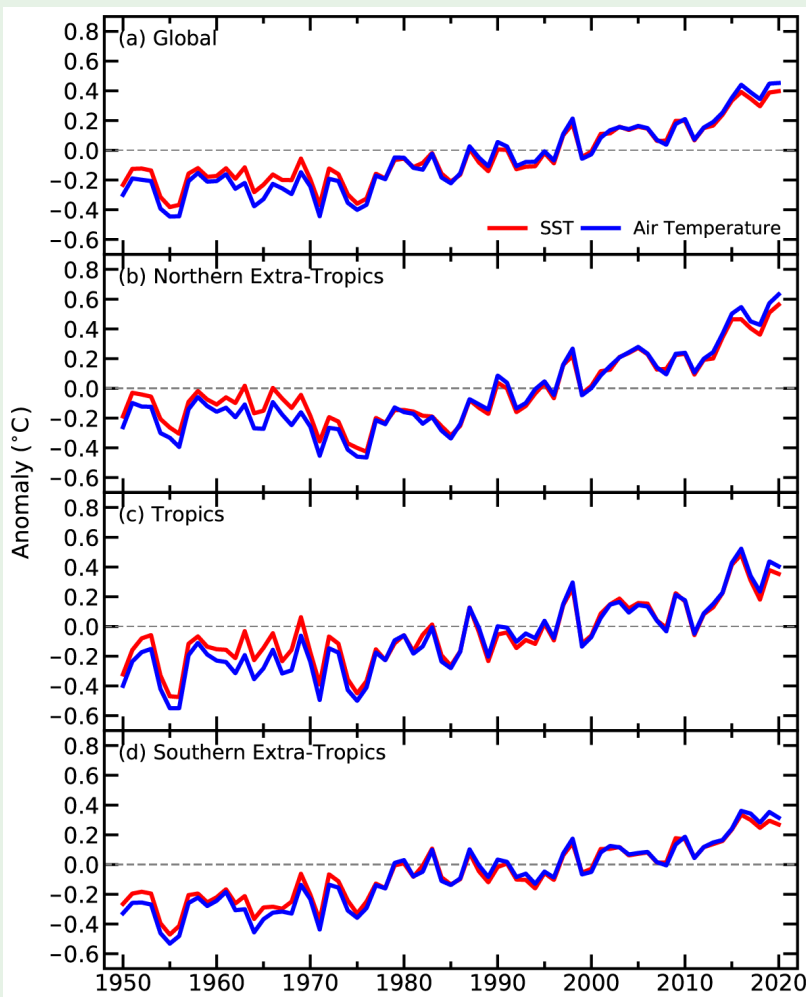


Fig. SB2.2. Large-scale average anomalies in 2-m air temperature across ocean regions and sea surface temperature from the ERA5 reanalysis dataset (Hersbach et al. 2020) from 1950 to 2020. Note that in contrast to Fig. SB2.1, the anomalies in this figure are expressed relative to 1981–2010 averages. The data prior to 1978 are currently considered experimental. Areas with sea ice are masked from the averaging.

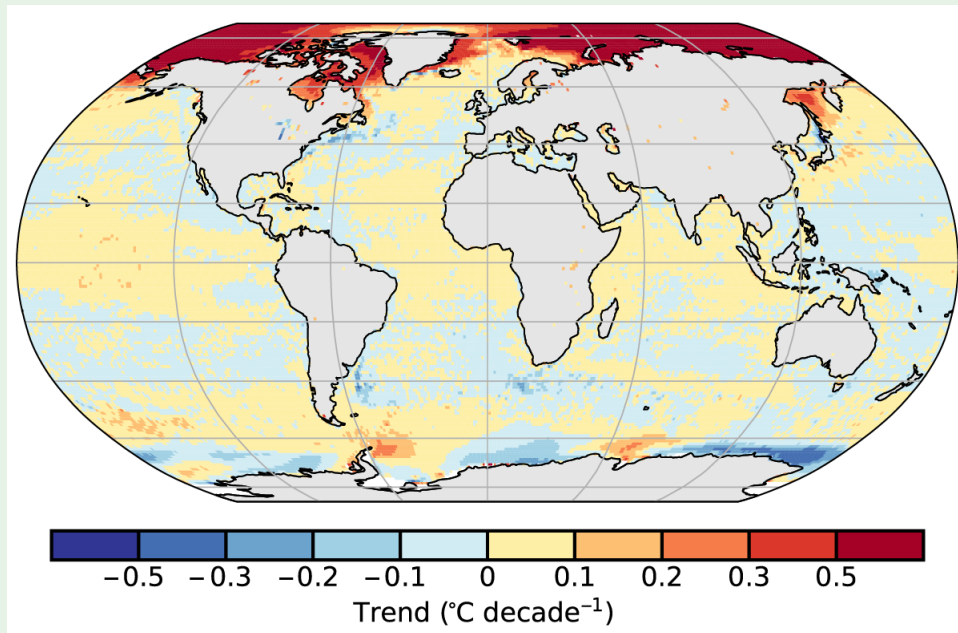


Fig. SB2.3. Linear trends in the difference between 2-m air temperature and sea surface temperature (SST) anomalies ($^{\circ}\text{C decade}^{-1}$; relative to 1981–2010 averages) in the ERA5 dataset over the period 1980–2020. Red colors indicate where air temperature is warming faster than SST and blue colors where the reverse is true.

These analyses of NMAT and MAT illustrate the importance of exploring many different variables, using as many different methods as possible, and that some questions are yet unanswered. Despite the various issues discussed and differences in long-term trend, NMAT and MAT show similar year-to-year variability to spatially-matched SST in terms of the global

average time series (Figs. SB2.1, SB2.2) and spatially for the annual average anomalies (Plate 2.1f). However, while 2020 was marginally the warmest year in globally average SST and reanalysis-derived MAT data (see section 2.b.1), this is not the case with CLASSnmat, which was cooler than 2016 and thus ranked 2020 as the second-warmest year in the record.

c. Cryosphere

1) *Permafrost thermal state*—J. Noetzli, H. H. Christiansen, F. Hrbacek, K. Isaksen, S. L. Smith, L. Zhao, and D. A. Streletskiy

Ongoing increases in global permafrost temperatures have occurred over the past several decades, with regional variability in magnitude. There have been short breaks in the warming trend due to shorter-term meteorological fluctuations, such as summer heat waves or snow-poor winters (e.g., Biskaborn et al. 2019; Romanovsky et al. 2007; Harris et al. 2009; Wu and Zhang 2008; PERMOS 2019; Etzelmüller et al. 2020). The largest increases were observed for sites with low permafrost temperatures, i.e., several degrees below 0°C, and low ground ice contents. Warmer and ice-rich permafrost warms up at a lower rate due to latent heat uptake during ice melt. This global picture continued in 2020. Record values were observed at many sites in polar and mountain regions. However, data could not be collected from all permafrost observation sites in 2020 (particularly in North America) due to pandemic-related travel restrictions.

Permafrost temperatures reported in 2020 for the Arctic regions were the highest on record at a majority of the observation sites. Warming rates for colder permafrost were as high as 0.8°C decade⁻¹, compared to less than 0.3°C decade⁻¹ for permafrost at temperatures close to 0°C.

Details on Arctic permafrost are given in section 5h. Increasing permafrost temperatures were reported from the Antarctic Peninsula and Victoria Land for the past decade up to 2018 (cf. Noetzli et al. 2019); however, deep boreholes and complete time series were scarce and the trend lacks statistical significance.

Mountain permafrost accounts for approximately 30% of the global area underlain by permafrost (Hock et al. 2019). Data are primarily available from the European Alps, the Nordic countries, and central Asia (Qinghai-Tibetan Plateau; QTP), but they are sparse for other mountain regions. A mean permafrost temperature increase of 0.19°C decade⁻¹ was observed for 2007–16 (Biskaborn et al. 2019). Warming rates are heterogeneous due to the high spatial variability in thermal conditions resulting from complex topography, snow regime, and ground ice content. Highest rates are observed for bedrock with a low ice content and permafrost temperatures several degrees below 0°C and without a thicker winter snow cover. Permafrost temperatures recorded in 2020 in the European Alps were higher than in 2019 and close to or above the previous maximum observed in 2015 at the majority of sites (Fig. 2.10; Noetzli et al. 2020; updated from Pogliotti et al. 2015; PERMOS 2019) due to an early onset of the snow cover in autumn 2019 and the warmest year

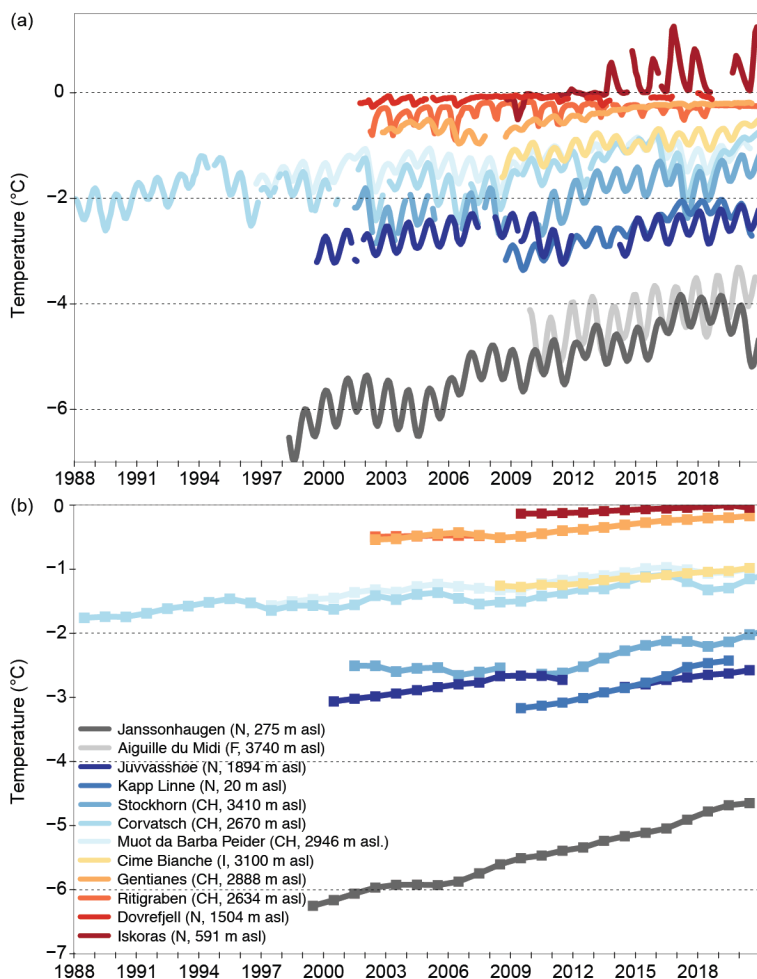


Fig. 2.10. Permafrost temperature measured in boreholes in the European Alps and the Nordic countries at a depth of approximately 10 m (monthly means, upper panel) and 20 m (annual means, lower panel). (Sources: Switzerland: Swiss Permafrost Monitoring Network PERMOS; Norway: Norwegian Meteorological Institute and the Norwegian Permafrost Database NORPERM; France: updated from Magnin et al. 2015; Italy: updated from Pogliotti et al. 2015.)

recorded in Europe (Copernicus Climate Change Service 2021). Permafrost temperatures are thus higher or similar as before the temporary cooling in 2016 and 2017, which persisted in 2018 and only started to reverse in 2019. Temperatures at Murtèl-Corvatsch in the Engadin (Switzerland) increased by $\sim 0.6^{\circ}\text{C}$ at 20-m depth and by more than 1°C at 10-m depth over the past 3 decades. On Stockhorn above Zermatt (Switzerland), temperatures at 23-m depth increased by $\sim 0.4^{\circ}\text{C}$ over the past 2 decades. Surface velocities of rock glaciers generally follow the evolution of the permafrost temperatures. In the European Alps, rock glacier surface velocities for the year 2020 are at or above the previous maximum observed in 2015 (see Sidebar 2.1).

In the Nordic countries, permafrost temperatures measured in 2020 were the highest or second highest on record, continuing the reported warming trend (Fig. 2.10; Noetzli et al. 2020; Etzelmüller et al. 2020). In the cold mountain permafrost at Juvvasshøe in southern Norway, permafrost temperatures at 20-m depth increased by 0.5°C from 1999 to 2020. Permafrost temperatures decreased in Svalbard at 10-m depth compared to the previous extremely warm years due to the relatively cold winters in 2019 and 2020 (Christiansen et al. 2021). However, they are still above the long-term average; for example, at Kapp Linne they were 0.7°C higher in 2020 than at the start of the record in 2009.

Permafrost temperatures measured in the hinterland of the QTP in Central Asia continued to increase at all sites, with remarkable warming trends but variable rates: at 10-m depth they range between $0.45^{\circ}\text{C decade}^{-1}$ (QTB15, Fig. 2.11) and $0.04^{\circ}\text{C decade}^{-1}$ (QTB06), and at 20-m depth between 0.24 and $0.02^{\circ}\text{C decade}^{-1}$ (Zhao et al. 2020, 2021).

The active layer thickness (ALT) is the ground layer that freezes and thaws annually and lies above the permafrost. Changes in ALT are a key indicator for changing permafrost conditions. ALT was not or only partly reported for some sites in Canada and Alaska due to COVID-19 travel restrictions. The ALT in northern Alaska was 6 cm thinner in 2020 than the decadal average (2008–17) and 8 cm thinner than in 2019. In the Alaska Interior, ALT was thicker than average, but 5 cm thinner than in 2019. ALT at the majority of sites in the Nordic region was similar to the previous year, at or close to record values. In Russia, ALT was thicker than average and thicker than in 2019 in all regions, except for Chukotka, where ALT was thinner than in 2019. The Siberian heat wave (see section 7g2, Sidebar 5.1) caused particularly thick ALT, with more than 10 cm larger values than in 2019 in West Siberia and neighboring sites in northwestern Russia. ALT in the regions of central and eastern Siberia was only 3 cm above previous regional averages. More details on ALT in Arctic regions are given in section 5h.

In the Scandinavian and European Alps, ALT values for 2020 were at or close to the previous maximum at most of the sites. In the Swiss Alps, record values were observed in 2020 for most sites, with values up to 10 m in extreme cases. Along the Qinghai-Tibet Highway (Kunlun mountain pass to Liangdaohe), an ALT increase was observed with a mean of $19.5\text{ cm decade}^{-1}$ from 1981 to 2019 (Fig. 2.12). In Antarctica, the February 2020 heat wave in the northwest Weddell Sea sector (section 2b3) accelerated active layer thickening. Thaw depth on James Ross Island reached 80 cm. This is comparable to observations in 2016/17 (Hrbáček et al. 2021), one of the warmest years so far measured in this sector (J. Turner et al. 2020).

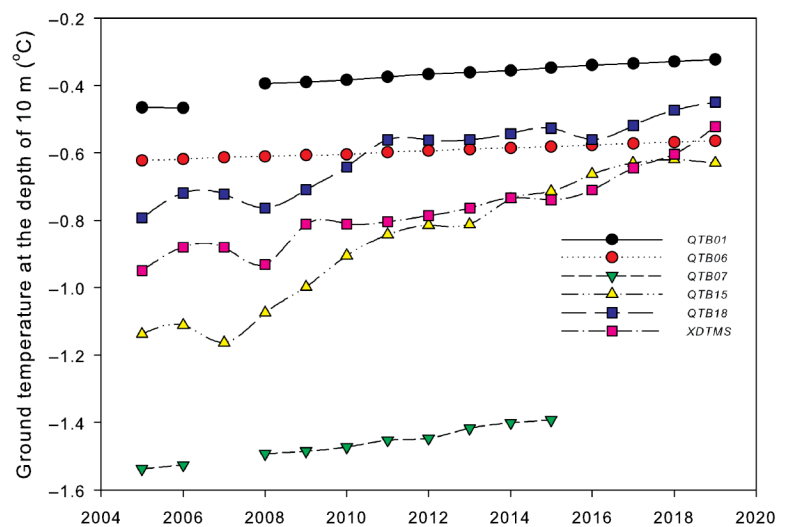


Fig. 2.11. Temperature measured in permafrost boreholes along the Qinghai-Xizang Highway on the Tibetan Plateau at 10-m depth from 2005 to 2019. (Source: Cryosphere Research Station on Qinghai-Xizang Plateau, CAS.)

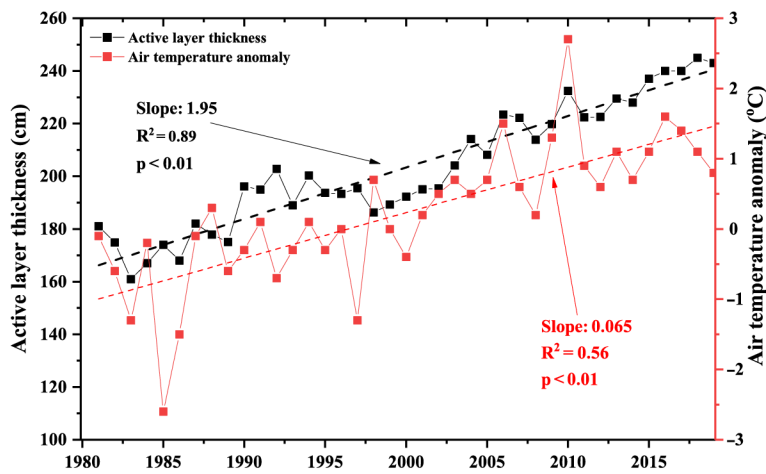


Fig. 2.12. The active layer thickness (cm) and air temperature anomaly (°C) in the permafrost zone along the Qinghai-Tibet Highway during the period 1981–2019. The air temperature anomaly is estimated relative to the climate baseline 1981–2010.

cal probing where possible and has an accuracy of ~1 cm. Probing is not possible in bedrock or debris material, particularly in mountain regions. Here, ALT is interpolated from temperature sensors in boreholes. The current global coverage of permafrost monitoring sites is sparse; it is particularly limited in regions such as Siberia, central Canada, Antarctica, and the Himalayan and Andes Mountains.

Sidebar 2.2: Rock glacier kinematics—C. PELLET, X. BODIN, R. DELALOYE, V. KAUFMANN, J. NOETZLI, E. THIBERT, AND A. KELLERER-PIRKLBAUER

Rock glaciers are geomorphological indicators of permafrost occurrence in mountain areas and develop in most mountain ranges worldwide. Their kinematics derived from surface displacement measurements typically range from several centimeters up to several meters per year (Kääb and Vollmer 2000). Long-term studies from the European Alps have shown that the velocity of rock glaciers in a specific region responds sensitively and synchronously to interannual and decennial changes in ground temperature (e.g. Bodin et al. 2009; Delaloye et al. 2008, 2010; Kääb et al. 2007; Kellerer-Pirklbauer and Kaufmann 2012, 2018; Staub et al. 2016; Thibert et al. 2018; PERMOS 2019). Measurements of the surface velocity of rock glaciers based on aerial images and geodetic surveys first started in the 1960s in the European Alps (Haeberli 1985). Today, the majority of monitored rock glaciers are in the European Alps, and surface velocity measurements based on repeated terrestrial geodetic surveys have become part of operational permafrost monitoring in several European countries (Austria, France, Switzerland; see PERMOS 2019). In addition to their importance as climate indicators, rock glaciers are highly relevant for natural hazards risk management in mountain regions as well as for land use planning. Active rock glaciers are sediment conveyers and their

Long-term observation of permafrost relies on field observations of ALT and permafrost temperatures measured in boreholes. International data are collected by the Global Terrestrial Network for Permafrost (GTN-P) as part of the Global Climate Observing System (GCOS). Permafrost temperatures are logged manually or continuously using multi-sensor cables in boreholes reaching at least the depth of the zero annual amplitude. An assessment of the measurement accuracy of permafrost temperatures worldwide varied from 0.01° to 0.25°C, with an assumed overall accuracy of about 0.1°C (Biskaborn et al. 2019; Romanovsky et al. 2010). ALT is determined by mechanical

increasing velocity can lead to a higher frequency of rock fall or debris flows from their frontal parts (e.g., Kummert et al. 2018).

The surface velocity of the majority of the observed rock glaciers in the European Alps behaved similarly during the past decades, despite variable size, morphology, and velocity range (Fig. SB2.4). The surface velocity increased by a factor of 2 to 10 from 1980s to 2015, and a maximum was reached in 2015. The acceleration was temporarily interrupted (i.e., velocity decrease was observed) for most of the landforms between 2004 and 2006, as well as between 2016 and 2018, coinciding with a decrease in ground temperatures (Noetzli et al. 2018; PERMOS 2019). The acceleration resumed in 2018. In 2020, the surface velocity of rock glaciers was close to or even higher than the maximum observed in 2015, which corresponds to the high ground temperatures observed (see section 2c1). Compared to the values of 2019, the surface velocity increase spans from +17% (Dösen [Austria] and Gemmi/Furggentälti [Switzerland]) to +45% (Grosses Gufer [Switzerland] and Hinteres Langtalkar [Austria]), which is in the same range as the acceleration observed between 2014 and 2015.

Long-term in situ measurements of rock glacier kinematics are scarcely available from other regions of the world. However,

the increasing emergence of open-access and high-resolution satellite data (e.g., optical and Synthetic Aperture Radar [SAR]) facilitates the setup of regional surveys worldwide (e.g., Strozzi et al. 2020). Recent studies in northern Norway (Eriksen et al. 2018) and in the Tien Shan Mountains (Kääb et al. 2020) found an overall increase of the rock glaciers' surface velocity from the 1950s on. These observations are consistent with the results obtained in the European Alps.

According to in situ measurement (e.g., Arenson et al. 2002; Buchli et al. 2018) and modeling approaches (e.g., Kannan and Rajagopal 2013), the displacement at the surface of rock glaciers mainly results from shearing within a layer of several decimeters to a few meters thickness, which typically lies between 15- and 30-m depth. The changes in rock glacier kinematics are mostly

related to the evolution of ground temperature and liquid water content between the permafrost table and the main shearing horizon at depth: the closer to 0°C the temperature is, the faster the rock glacier is moving (Cicoira et al. 2019; Frauenfelder et al. 2003; Staub et al. 2016). A time lag of around 1 to 2 years has been observed between high air temperatures and the resulting acceleration (Kellerer-Pirklbauer and Kaufmann 2012; Staub et al. 2016).

The consistent regional evolution of rock glacier velocity and its sensitivity to changes in ground temperature, together with their global presence, make rock glaciers ideal climate indicators. An Action Group of the International Permafrost Association (IPA; see Delaloye et al. 2018) aims to internationally harmonize and coordinate measurements of rock glacier kinematics (RGK).

Based on their recommendation, the Global Terrestrial Network for Permafrost (GTN-P) is proposing to include RGK as a new product of the GCOS essential climate variable (ECV) permafrost, in addition to the thermal state of permafrost and active layer thickness. RGK measurements are based on repeated terrestrial geodetic surveys or determined photogrammetrically using aerial images. Geodetic surveys are performed annually at the same time of the season (usually at the end of the summer). The coordinates and elevation are measured for a number of selected boulders (10–100 per landform) with an average accuracy in the range of millimeters to centimeters (Delaloye et al. 2008; PERMOS 2019). Multi-temporal aerial images are compared with each other to obtain rock glacier-wide movement information. Typically, horizontal displacement metrics are computed based on 2D ortho-image matching algorithms or digital elevation model matching. The accuracy of the photogrammetrically derived displacements strongly depends on the spatial resolution of the aerial images and on the image quality (e.g., sharpness, contrast, and so forth).

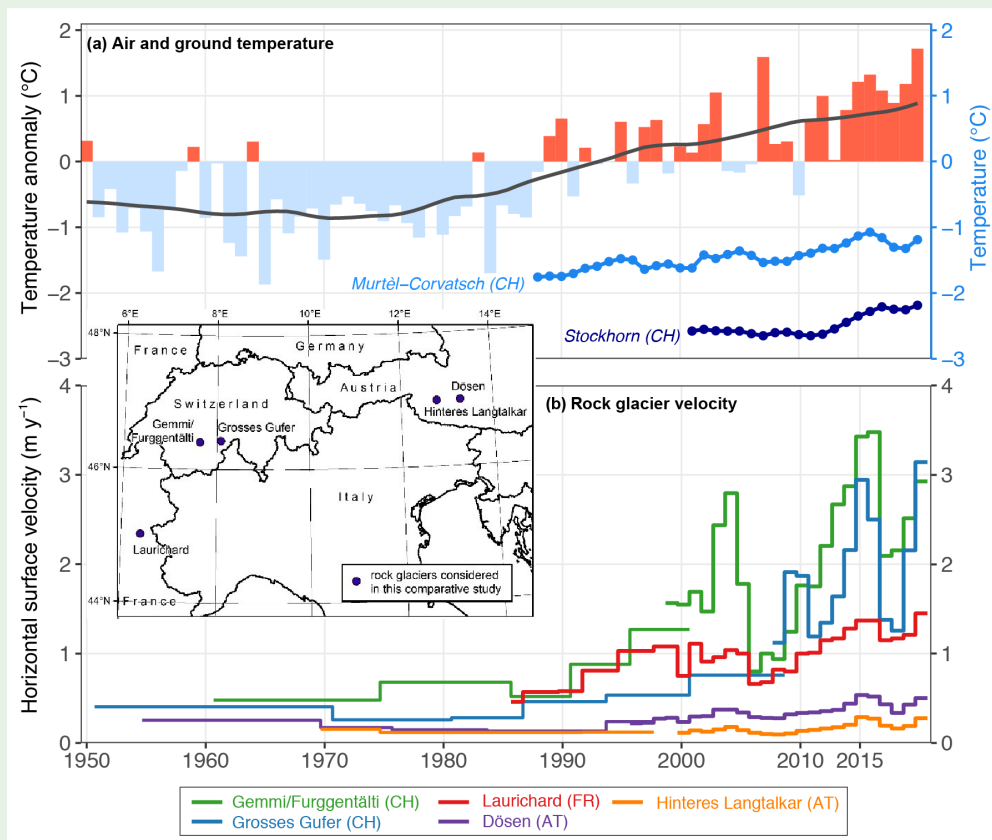


Fig. SB2.4. (a) Long-term in situ permafrost temperature measured at 20-m depth [blue lines] and air temperature measurements (composite anomaly to the 1981–2010 norm [red and blue bars]) and composite 20-year running mean (solid line) at five selected sites in the European Alps (Switzerland, France, Austria): Besse France, Grand Saint-Bernard Switzerland, Sonnblick Austria and Zugspitze Germany. (b) Rock glacier surface velocities (m yr⁻¹) measured using in situ geodetic surveys and photogrammetrics. (Sources: Météo France, Deutscher Wetterdienst DWD, MeteoSwiss, Zentralanstalt für Meteorologie und Geodynamik ZAMG, Swiss Permafrost Monitoring Network, University of Fribourg, University of Graz, Graz University of Technology, Université Grenoble Alpes [INRAE].)

2) Northern Hemisphere continental snow cover extent—D. A. Robinson

Snow cover extent (SCE) displays considerable intra- and interannual variability. As such, variations in SCE impact surface albedo and thus, the overall surface energy balance. SCE also plays a role in atmospheric circulation and surface hydrology. Annual SCE over Northern Hemisphere (NH) lands averaged 24.1 million km² in 2020. This is 1.0 million km² less than the 51-year average (mapping extends back to late 1966, although three early years in the record are incomplete) and ranks 2020 as having the fourth-least extensive cover on record (Fig. 2.13; Table 2.4) and 0.7 million km² less than the 2019 mean extent. SCE over both NH continents, including the Greenland ice sheet, was considered in this analysis. Monthly SCE in 2020 ranged from 46.4 million km² in January to 2.3 million km² in August. The only years in the satellite record with less NH SCE than in 2020 were, from lowest upward, 1990, 1988, and 2007.

During the first half of 2020, SCE was well below average across the NH. Monthly rankings ranged from below average for the 54-year record in January to third-least extensive in February. NH spring (March–May) SCE ranked fourth lowest on record, consistent with a generally persistent earlier snow melt in recent decades. Rankings of second- to fourth-least extensive cover occurred across Eurasia from February to June. North American snow cover was below average in five of the first six months of 2020, the exception being April, where a delayed melt resulted in above-average cover.

The NH SCE was above average in October and November, ranking 10th- and 12th-most extensive, respectively. The past nine autumns (September–November) have had average SCE exceeding 20 million km², while only eight of the prior 41 years exceeded that mark. December SCE was close to average. The excessive cover was primarily driven by conditions in North America, where October cover was the largest on record and November cover was 13th largest. December SCE was close to average in Eurasia, while a major turnaround occurred across North

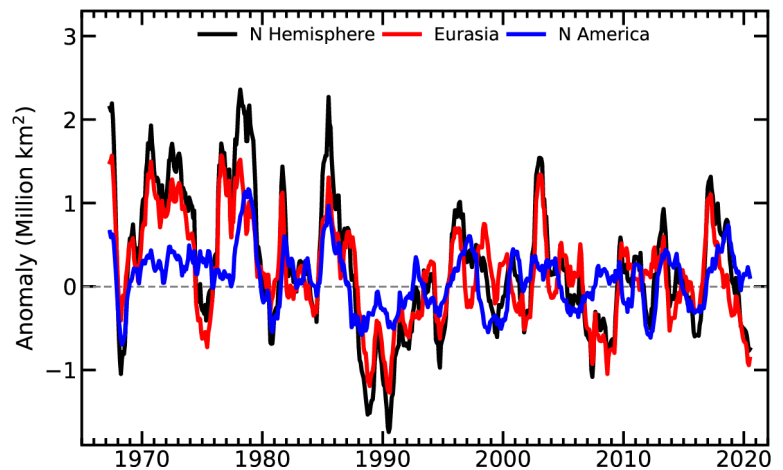


Fig. 2.13. Twelve-month running anomalies of monthly snow cover extent (million km² over NH lands as a whole, and Eurasia and North America separately, plotted on the seventh month using values from Nov 1966 to Dec 2020. Anomalies are calculated from NOAA snow maps. Mean hemispheric snow extent is 25.1 million km² for the full period of record. Monthly means for the period of record are used for nine missing months during 1968, 1969, and 1971 to create a continuous series of running means. Missing months fall between Jun and Oct, no winter months are missing.

Table 2.4. Monthly and annual climatological information on NH and continental snow extent between Nov 1966 and Dec 2020. Included are the numbers of years with data used in the calculations, NH means, standard deviations, 2020 values, and rankings. Areas are in million km². The years 1968, 1969, and 1971 have 1, 5, and 3 missing months, respectively, thus are not included in the annual calculations. N. Am. includes Greenland. Ranks are from most extensive (1) to least (ranges from 51 to 55 depending on the month).

	Years of data	Mean	Std. Dev.	2020	2020 NH rank	2020 Eurasia rank	2020 N Am. rank
Jan	54	47.2	1.5	46.4	37	39	33
Feb	54	46.0	1.8	43.5	52	52	39
Mar	54	40.4	1.9	37.7	50	51	32
Apr	54	30.5	1.7	29.1	42	52	14
May	54	19.2	2.0	16.7	49	52	28
Jun	53	9.4	2.5	6.0	49	52	43
Jul	51	3.9	1.2	2.4	50	51	50
Aug	52	3.0	0.7	2.3	50	52	42
Sep	52	5.4	0.9	4.5	42	50	22
Oct	53	18.6	2.7	21.2	10	19	1
Nov	55	34.3	2.1	36.0	12	17	13
Dec	55	43.7	1.8	43.7	32	26	37
Ann	51	25.1	0.8	24.1	48	49	26

America, with SCE below average. Research by Allchin and Dery (2020) supports the autumn increases, attributing this to atmospheric circulation patterns that have increased moisture fluxes into areas that are cold enough to sustain an autumn snow cover but previously were somewhat moisture deficient.

SCE over the contiguous United States during the first half of 2020 saw monthly rankings of third- to 20th-least extensive, with the exception of April which had above-average cover for the 54-year record. October 2020 was its most extensive SCE on record, with November above average and December below average.

SCE is calculated at the Rutgers Global Snow Lab from daily SCE maps produced by meteorologists at the National Ice Center (a United States joint NOAA, Navy, and Coast Guard facility), who rely primarily on visible satellite imagery to construct the maps (Estilow et al. 2015). Maps depicting daily, weekly, and monthly conditions, daily and monthly anomalies, and monthly climatologies for the entire period of record may be viewed at the Rutgers Global Snow Lab website (<https://snowcover.org>). Monthly SCE for the NH, Eurasia, North America, contiguous United States, Alaska, and Canada are also posted, along with information on how to acquire weekly areas and the weekly and monthly gridded products.

3) *Alpine glaciers*—M. Pelto

For 2019/20, the overall mean annual mass balance of 33 reporting reference glaciers, from 12 nations on four continents, was -621 mm and was -590 mm for all 79 reporting glaciers to date (World Glacier Monitoring Service [WGMS] 2020). This makes 2020 the 33rd consecutive year with a global alpine mass balance loss and the 12th consecutive year with a mean global mass balance below -500 mm, but it was less negative than the previous 2 years, which were the most negative of the entire 1950–2020 record. In the hydrological year 2017/18, reference glaciers experienced a mass balance loss of -1184 mm and in 2018/19 of -1177 mm.

Figure 2.14 illustrates glacier mass balance for the WGMS global reference glaciers with more than 30 continued observation years for the period 1950–2019. Global values were calculated using a single value (averaged) for each of 19 mountain regions in order to avoid a bias to well-observed regions. Zemp et al. (2019) indicated that the collective loss of alpine glaciers from 2006 to 2016 provided a global sea level contribution of 0.92 ± 0.39 mm yr^{-1} (see section 3f).

The decadal averaged annual mass balance was -214 mm in the 1980s, -499 mm in the 1990s, -527 mm in the 2000s, and -896 mm for the 2010s. The average mass loss reported by Slater et al (2021) identified a similar rise with a loss of 62 Gt yr^{-1} in the 1980s, 206 Gt yr^{-1} in the 1990s, 252 Gt yr^{-1} in the 2000s, and 327 Gt yr^{-1} in the 2010s. The increasing rate of glacier mass loss, with eight out of the 10 most negative mass balance years recorded after 2010 during a period of retreat, indicates that alpine glaciers are not approaching equilibrium and retreat will continue to be the dominant terminus response (WGMS 2020).

All 19 reporting glaciers in the Alps had a negative mass balance averaging -873 mm in 2020. In Austria in 2019, of the 92 glaciers with annual terminus observations, 86 (93.4%) withdrew, five remained stationary, and one advanced (Lieb and Kellerer-Pirklbauer 2020). This retreat trend continued in 2020.

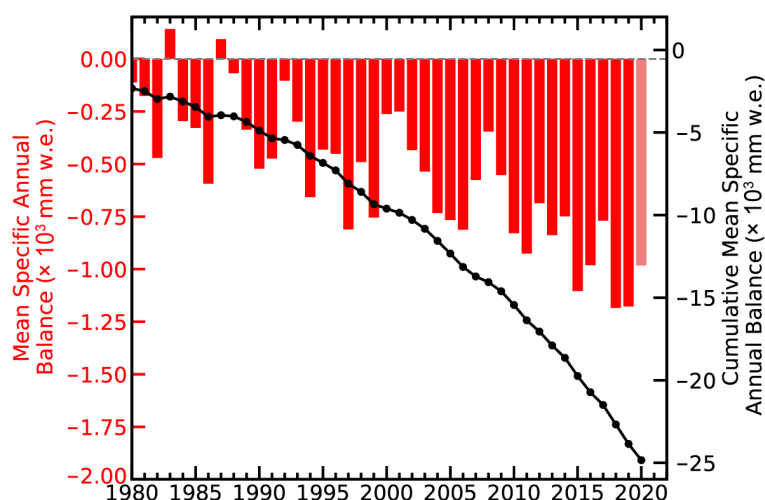


Fig. 2.14. Mass balance of alpine glaciers reporting to the World Glacier Monitoring Service in mm of water equivalent (mm w.e.). The values from 1980 to 2020 are based on average annual value determined for 19 different Alpine regions.

In Sweden, all three glaciers reporting had a negative balance averaging -320 mm. In Norway, the eight reporting glaciers had a positive average mass balance of $+365$ mm in 2020. All 36 Norway glaciers surveyed in 2019 were retreating (Andreasson 2020). On Svalbard, the mean loss of three glaciers in 2020 was -1485 mm. Iceland completed surveys of nine glaciers, of which eight had negative balances with a mean mass balance of -442 mm.

In Alaska and Washington, all 14 glaciers observed in 2020 had a negative mass balance averaging -722 mm. This was significantly larger than the long-term average of four United States Geological Survey benchmark glaciers, which had a cumulative mass loss since the mid-twentieth century that averaged from -580 to -300 mm yr⁻¹ (O’Neel et. al. 2019).

In South America, 2020 mass balance data were reported from two glaciers in Chile, one in Ecuador, and one in Argentina; all were negative with a mean of -1056 mm. This was greater than the 2000–18 average loss observed in the Andes of -720 ± 220 mm yr⁻¹ (Dussailant et. al. 2019).

In Kyrgyzstan and Kazakhstan, nine glaciers in the Tien Shan Range had near equilibrium balances. In the Himalayas, the two reporting reference glaciers had negative balances averaging -487 mm. King et al. (2019) identified that in the Mount Everest region mass loss has increased each of the last 6 decades. In 2020, the post-monsoon season and early winter were warm and dry in the Himalayas, leading to the ablation season extending into January with the snow line retreating over 100 m from October into January (Fig. 2.15; Patel 2021). This raises the question, when does the ablation season end in the region in our warmer climate?

The WGMS record of mass balance and terminus behavior (WGMS 2017, 2018) provides a global index for alpine glacier behavior. Glacier mass balance is the difference between accumulation and ablation, reported here in mm of water equivalent (mm w.e.).

4) Lake ice—S. Sharma and R. I. Woolway

In the 2019/20 winter, lake ice phenology (the timing of ice-on and ice-off) across the NH (calculated from Copernicus Climate Change Service [C3S] ERA5 [Hersbach et al. 2020]) continued to experience later ice-on dates, earlier ice-off dates, and shorter seasonal ice continuing the pattern seen over 1980–2020 (Magnuson et al. 2000; Benson et al. 2012; Woolway et al. 2020). The hemispheric average for ice-on was 1.5 days later decade⁻¹ and ice-off was 1.5 days earlier per decade⁻¹. In line with these calculated changes in ice phenology, the data suggest that the duration of lake ice cover was shortening at an average rate of 3 days decade⁻¹, albeit with considerable inter-annual variability ($R^2 = 0.44$). Relative to the 1981–2010 base period, NH lakes froze,

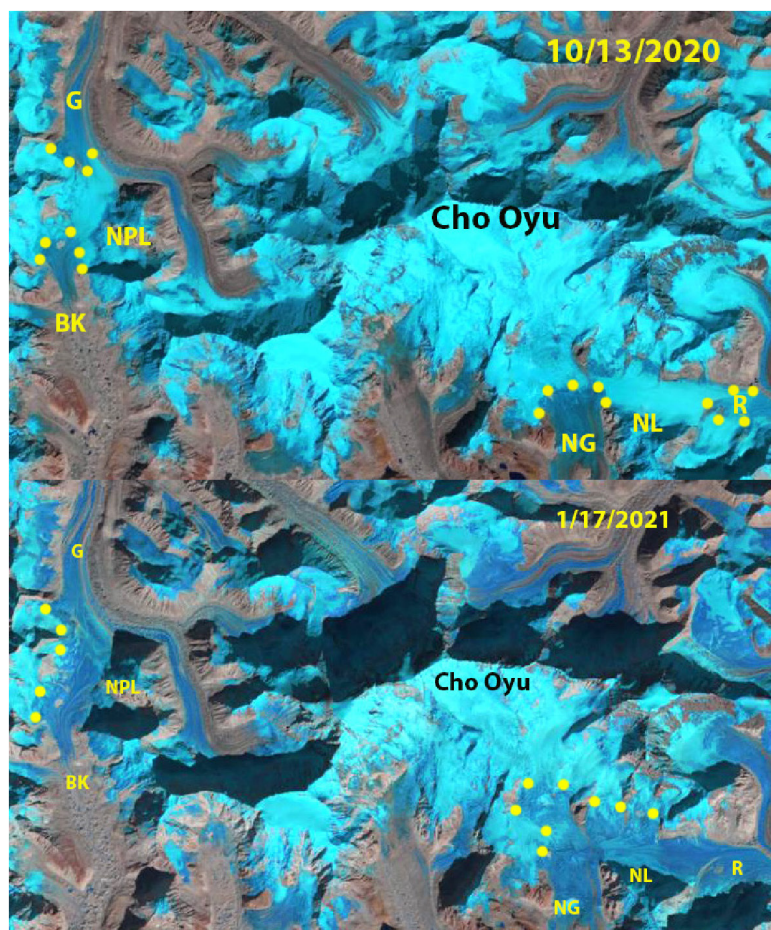


Fig. 2.15. LandSat imagery of Nangpa La (NPL-5806 m) and Nup La (NL-5850 m) 25–50 km west of Mount Everest, indicating the rise of the snow line from 13 Oct 2020 to 17 Jan 2021, leaving Nangpa La at the crest of the Gyabarg (G) and Bhote Koshi Glacier (BK) snow free. Nup La at the crest of Rongbuk (R) and Ngozumpa Glacier (NG) is also snow free on 17 Jan 2021.

on average, 3 days later and thawed 5.5 days earlier during the 2019/20 winter season (Fig. 2.16). By ranking these ice phenology metrics according to the earliest and latest days in which they occurred since 1979/80 (the years in which these records began) we calculated that, in 2019/20, the hemispheric average ice-on was the eighth latest on record and ice-off was the third earliest. Relative to the 1981–2010 average, lake ice duration in 2019/20 was 8.5 days shorter across the NH. This was the third-shortest ice cover season since 1979/80. The regional variations in ice duration were consistent with the NH cold season (November–April) average surface air temperature anomalies (relative to 1981–2010) in 2019/20, similar to previous studies (Sharma and Woolway 2020). Most notably, some regions in North America, such as Canada, experienced below-average air temperatures, which resulted in longer-than-average ice duration. Conversely, many regions in Eurasia experienced warmer-than-average conditions that resulted in shorter-than-average ice duration (Figs. 2.16c,d).

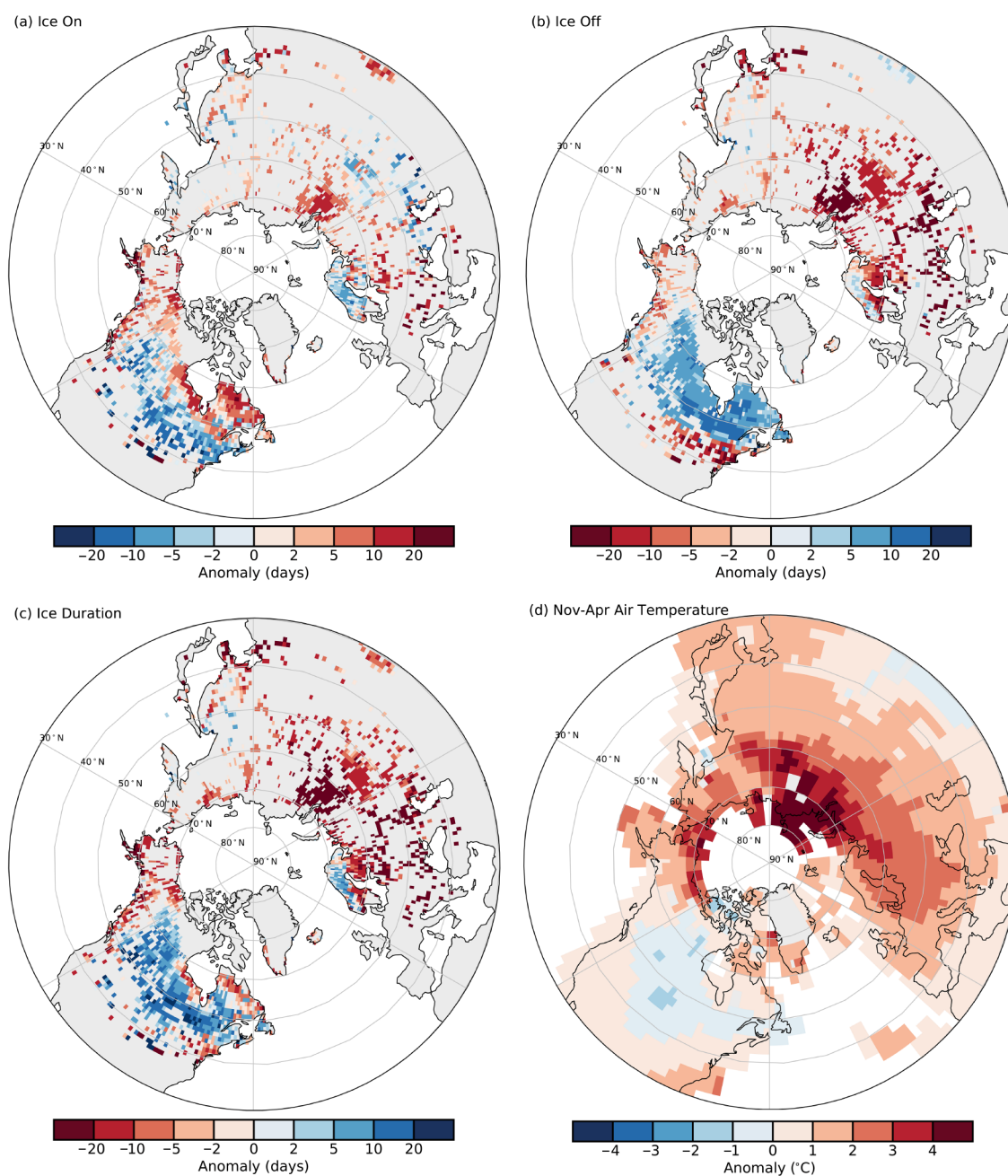


Fig. 2.16. Anomalies (days) in 2020 in (a) ice on, (b) ice off, and (c) ice duration for lakes across the NH, and (d) surface air temperature anomalies (°C) for the NH cold-season (Nov–Apr average), the time of year in which lakes typically freeze. The base period is 1981–2010. (Sources: ERA5, GISTEMP.)

In situ ice phenological records from 20 monitored lakes, situated mostly in Finland, the United States, Russia, and Canada, reveal that ice-on was 15 days later, ice-off was 11 days earlier, and there were 27 fewer days of ice cover over the winter season in 2020, on average, relative to 1981–2010 (Fig. 2.17). Lakes in Finland experienced remarkably warm conditions such that ice-on was 29 days later, ice-off was 13 days earlier, and ice duration was 42 days shorter. Typically, these Finnish lakes freeze in early December. However, during the 2020 winter, some of these same lakes froze as late as February (e.g., Lakes Nasijarvi and Visuvesi). Lakes in North America also experienced a warmer winter in 2020, with 16 fewer days of ice cover on average. Ice cover was especially anomalously low in the Finger Lakes region of New York state. For example, ice-on was 26 days later, ice-off was 16 days earlier, and ice duration was 43 days shorter for Cazenovia Lake. The winter of 2020 generally followed the long-term warming trend of 11 fewer days of ice cover for the 20 in situ lakes, on average.

In 2020, the Laurentian Great Lakes had substantially less ice cover, consistent with a warmer winter in the region. On average, the Laurentian Great Lakes had 33.9% less maximal ice coverage relative to 1981–2010. The smallest and most southern lake, Lake Erie, had the highest anomaly with a 65.4% reduction in ice coverage. Maximal ice coverage decreased by 38.1% in Lake Superior and 30.8% in Lake Huron, the two largest and most northern Great Lakes (Fig. 2.18).

To estimate the timing of ice-on and ice-off and, ultimately, the duration of winter ice cover across NH lakes, ice simulations from the ECMWFs ERA5 reanalysis product (Hersbach et al. 2020) were analyzed. Here, ice cover metrics were only calculated for pixels where lakes occupied greater than 1% of the land surface area. Lake ice conditions in 2020 were given as anomalies, calculated relative to the 1981–2010 average.

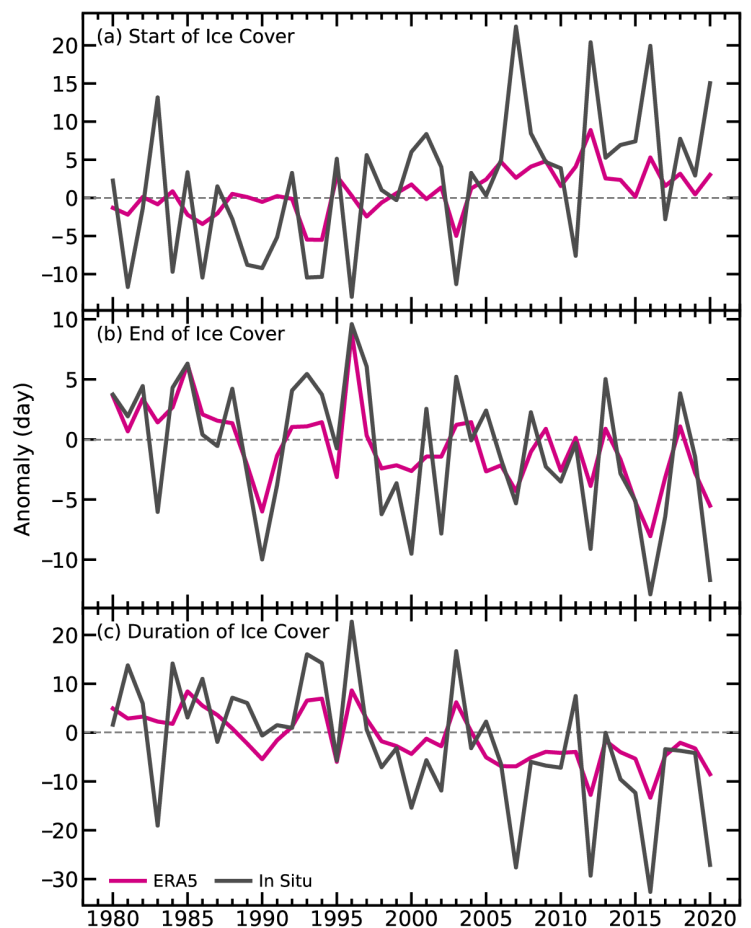


Fig. 2.17. (a) Lake ice on, (b) ice off, and (c) ice duration anomalies from 1980 to 2020 derived from in situ observations and ERA5. Base period is 1981–2010. In situ observations of ice on, ice off, and ice duration are derived from nine lakes monitored in Finland, one lake in Russia, nine lakes in the United States, and one lake in Canada.

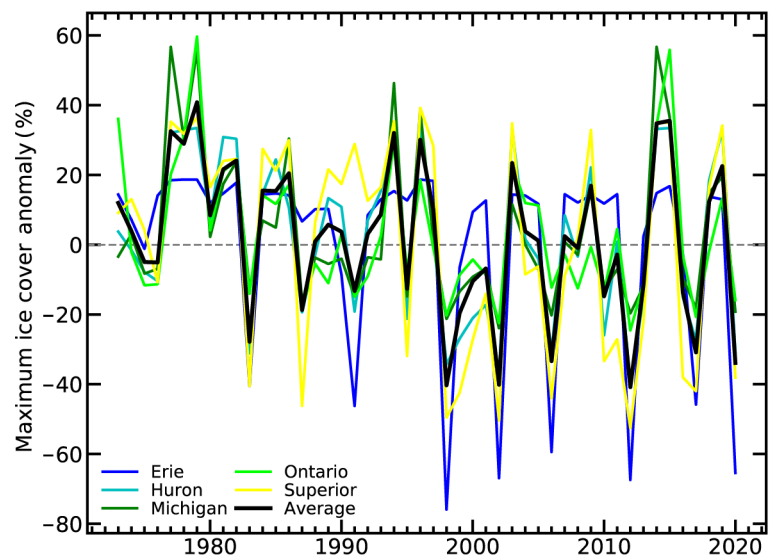


Fig. 2.18. Anomalies in Great Lakes maximum ice cover extent (%) for 1973–2020 (base period is 1981–2010). The black line shows the average anomaly for all of the Great Lakes, whereas the other lines show individual lakes (Erie, Michigan, Superior, Ontario, Huron).

Long-term in situ observations of ice-on, ice-off, and ice duration data were obtained for nine lakes in Finland, one lake in Russia, nine lakes in the United States, and one lake in Canada (Benson et al. 2000). Further, annual maximum ice cover (%) data for each of the Laurentian Great Lakes from 1973–2020 was obtained from the Great Lakes Environmental Research Laboratory. A combination of composite ice charts and observations from satellites, ships, and aircraft were used to quantify the maximum amount of ice coverage observed over the winter season in the Great Lakes (<https://www.glerl.noaa.gov/data/ice/>).

Surface air temperature data for the NH cold season (November–April average) were downloaded from the NASA GISS surface temperature analysis (Lenssen et al. 2019).

d. Hydrological cycle

1) Surface humidity—K. M. Willett, A. Vance, A. Simmons, M. Bosilovich, D. I. Berry, and D. Lavers

During 2020, the land surface specific humidity (q_{land})—a measure of atmospheric water vapor—remained well above average (0.14 to 0.36 g kg⁻¹), while relative humidity (RH_{land})—a measure of saturation—remained well below average (–1.28 to –0.68 %rh). Over oceans, q_{ocean} was a record high (0.23 to 0.41 g kg⁻¹) but RH_{ocean} was close to the 1981–2010 average (–0.14 to 0.13 %rh). Although the various estimates broadly agree there are differences in magnitudes and rankings (Fig. 2.19). In situ-based HadISDH and reanalyses MERRA-2 and JRA-55 show 2020 q_{land} as moister than 2019, ranking third, first, and fourth, respectively, within their records. ERA5 reanalysis shows 2020 tied with 2019, as sixth moistest on record. JRA-55 and HadISDH RH_{land} were also more saturated in 2020 but still low (third and fifth, respectively). ERA5 RH_{land} was slightly more arid than 2019, making it a record low for the second consecutive year. Over ocean, q_{ocean} was a record moist year by a large margin for HadISDH and ERA5. MERRA-2 and JRA-55 ranked q_{ocean} second and close to 2019. RH_{ocean} was more saturated in HadISDH and JRA-55 while marginally more arid in ERA5.

Taking HadISDH uncertainty into account, these rankings are less clear, but the 2020 q_{ocean} record lies outside the uncertainty range for all other years. HadISDH and ERA5 differ in input data, coverage, and processing, especially over ocean where no ship humidity data are assimilated (Simmons et al. 2021). The 2-sigma uncertainty for HadISDH broadly encompasses the ERA5 ocean values but not ERA5 land.

Surface humidity is driven by temperature and circulation patterns. The high q_{land} and record high q_{ocean} concur with the record/near-record high temperatures (section 2b1). Despite relatively neutral El Niño–Southern Oscillation (ENSO) conditions evolving to moderate La Niña conditions (section 4b), the q_{ocean} peak surpasses those of strong El Niño events (e.g., 1998, 2010, 2015–16); and the q_{land} peak is comparable for all datasets apart from ERA5.

Despite 2020 rankings differences, there is good agreement across estimates in long-term trends of increased q and decreased RH (Table 2.5). On average, the warmer air contains more water vapor, but not as much as it could, given its temperature. So, the air has become less saturated, even over oceans; ERA5, JRA-55, and HadISDH show small RH_{ocean} decreases. This is surprising given that several climate model studies show negligible or small increases in future RH_{ocean} (Held and Soden 2006; Schneider et al. 2010; Byrne and O’Gorman 2013, 2016, 2018).

HadISDH is affected by instrument and recording errors and biases along with changes in observation density, frequency, and precision (Willett et al. 2013, 2014, 2020). Reanalyses contain model and data biases and temporally changing data assimilation streams (Gelaro et al. 2017; Hersbach et al. 2020; Simmons et al. 2021). Unlike reanalyses, HadISDH is spatially incomplete, especially over the Southern Hemisphere oceans and many dry regions (where fewer people live and hence fewer weather stations). Spatially matching ERA5 to HadISDH slightly improves agreement (Fig. 2.19; Table 2.5). Over land, HadISDH reflects the well-observed regions and, hence, regions that are generally well constrained by observations in the reanalyses. Over oceans, ERA5 does not assimilate ship humidity or air temperature observations and thus poorer observational coverage has no effect, but various changes in satellite contributions do. Comparing trends over just the

Table 2.5. Global average decadal trends for specific humidity (q , g kg^{-1}) and relative humidity (RH; %rh) over 1979–2020 fitted using ordinary least squares regression. The 90th-percentile confidence intervals are shown in parentheses, fitted using AR(1) correction following Santer et al. (2008). Trends shown in bold are considered significantly different from a zero trend in that the confidence intervals do not cross the zero line.

Variable	HadISDH	ERA5	MERRA-2 (1980–2020)	JRA-55	HadISDH (continuous gridboxes)	ERA5 (continuous HadISDH gridboxes)	ERA5 (no HadISDH gridboxes)
Land q	0.09 (0.02)	0.06 (0.01)	0.09 (0.02)	0.07 (0.01)	0.10 (0.02)	0.10 (0.02)	0.05 (0.01)
Land RH	-0.22 (0.07)	-0.44 (0.06)	NA	-0.32 (0.04)	-0.33 (0.07)	-0.46 (0.07)	-0.24 (0.03)
Ocean q	0.08 (0.01)	0.05 (0.02)	0.10 (0.02)	0.04 (0.01)	0.10 (0.02)	0.14 (0.03)	0.05 (0.02)
Ocean RH	-0.05 (0.05)	-0.18 (0.09)	NA	-0.05 (0.01)	-0.08 (0.05)	-0.17 (0.04)	-0.18 (0.02)

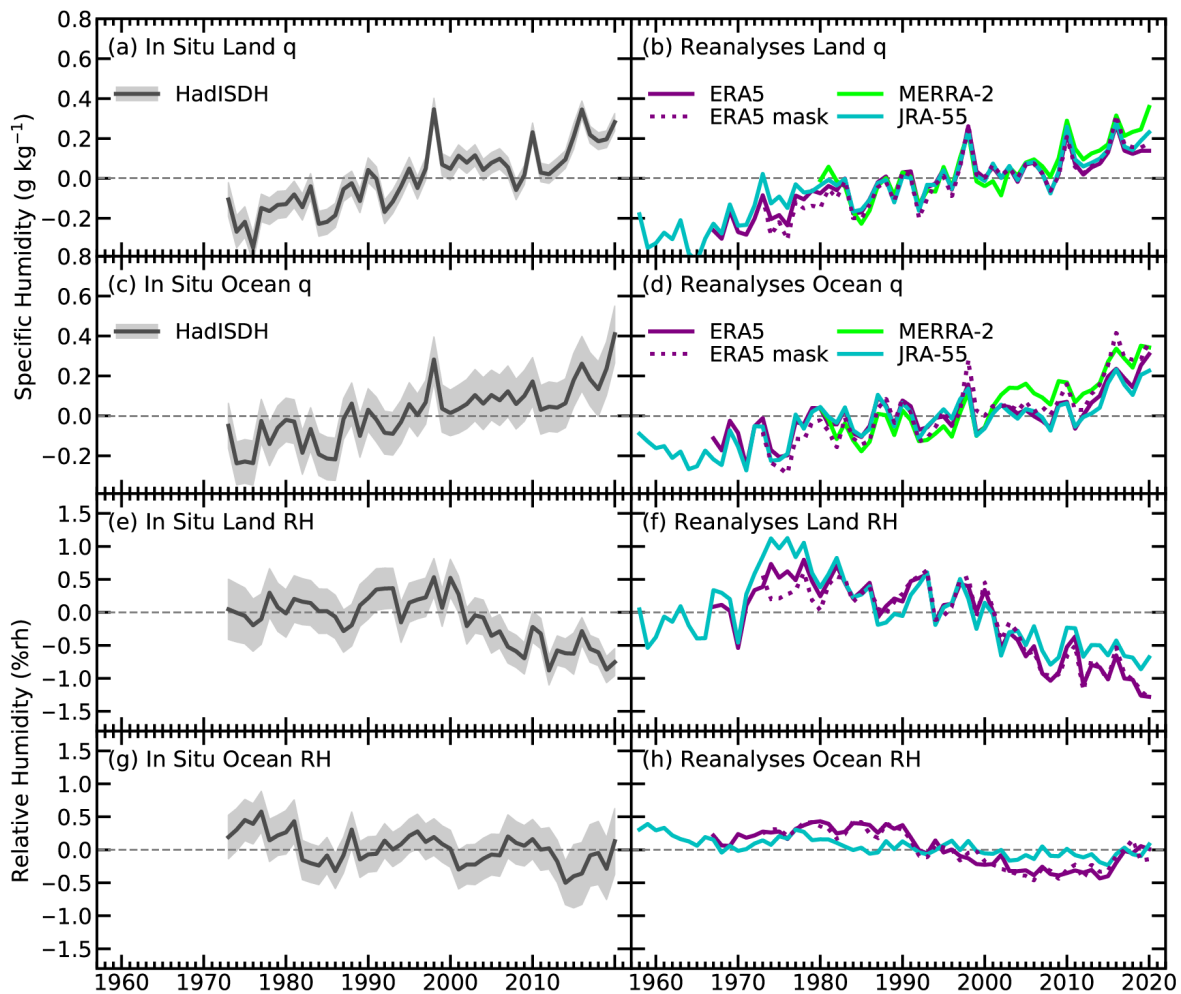


Fig. 2.19. (a)–(d) Global average land and ocean surface humidity annual anomalies of specific humidity (q ; g kg^{-1}) and (e)–(h) relative humidity (RH; %rh) from in situ and reanalyses datasets relative to the 1981–2010 base period. For the in situ datasets 2-m surface humidity is used over land and ~ 10 m over the oceans. For the reanalysis, 2-m humidity is used over the whole globe. For ERA5, ocean series-only points over open sea are selected. 2-sigma uncertainty is shown for HadISDH capturing the observation, gridbox sampling, and spatial coverage uncertainty. (Sources: HadISDH [Willett et al. 2013, 2014, 2020]; ERA5 [C3S 2017, Hersbach et al. 2020]; JRA-55 [Kobayashi et al. 2015]; MERRA-2 [Gelaro et al. 2017].)

temporally complete HadISDH grid boxes with matched ERA5 grid boxes (Table 2.5) shows closer agreement. Compared to full coverage ERA5, HadISDH matched ERA5 shows stronger increasing q but near-identical decreasing RH, and HadISDH shows marginally stronger increasing q and slightly stronger decreasing RH. Trends over ERA5 where there are no HadISDH data are generally

weaker apart from RH_{ocean} . This suggests that HadISDH is biased towards regions with stronger moistening (q), especially over oceans. Possibly, ERA5 q is showing weaker moistening/stronger drying where it is unconstrained by surface observations. Further investigation is needed. Regardless, compared to the 1960–70s, when humidity monitoring records begin, in 2020, Earth contained more water vapor at the surface, while being less saturated.

2) Total column water vapor—C. A. Mears, S. P. Ho, O. Bock, X. Zhou, and J. P. Nicolas

In 2020, global land and ocean averages of total column water vapor (TCWV), the total amount of water vapor in the atmosphere, were well above the 1981–2010 climatology, ranging from 0.75 to 1.06 mm over ocean and 0.58 to 0.94 mm over land, yet did not approach the record levels observed in 2016 (Fig. 2.20). This is surprising at first because global temperatures in 2020 were essentially tied with those from 2016 in most surface and lower-tropospheric datasets (sections 2b1, 2b4). This discrepancy is likely explained by the highest temperature anomalies having occurred well away from the tropics (Plates 2.1a,e) where the sensitivity of TCWV to temperature changes is largest because of the Clausius-Clapeyron relationship.

Water vapor is an important part of the transport of energy in the atmosphere, and influences patterns of precipitation and evaporation, and thus drought and floods. Large-scale averages of TCWV are strongly correlated with atmospheric and surface temperature. Thus, as the planet warms, TCWV will also increase. TCWV estimates are derived from satellite-borne microwave radiometers over the ocean (RSS Satellite; Mears et al. 2018), from Global Positioning System–Radio Occultation (GPS-RO) observations from the COSMIC, Metop-A, -B, and -C and COSMIC-2 satellite missions over land and ocean (satellite RO; Ho et al. 2020a,b, 2010a,b; Teng et al. 2013; Huang et al. 2013), and from ground-based Global Navigation Satellite System (GNSS) stations over land (Bock 2020). In addition, three reanalysis products are also used here: ERA5 (Hersbach et al. 2020), MERRA-2 (Gelaro et al. 2017), and JRA-55 (Kobayashi et al. 2015). All three reanalyses assimilate satellite microwave radiometer and GPS-RO data and are therefore not independent from these two datasets. Ground-based GNSS measurements are not assimilated and are thus independent.

The most prominent TCWV anomaly features for 2020 (Plate 2.1i) were the strong north–south asymmetry over the tropical Pacific Ocean and the excess vapor anomaly over most of the tropical and subtropical Indian Ocean. Other regions showed a mix of smaller anomalies, with more regions showing positive anomalies than negative. The ocean patterns in TCWV from ERA5 (Plate 2.1i) are confirmed by the RSS satellite data (Appendix 2, Fig. A2.8), satellite RO ocean

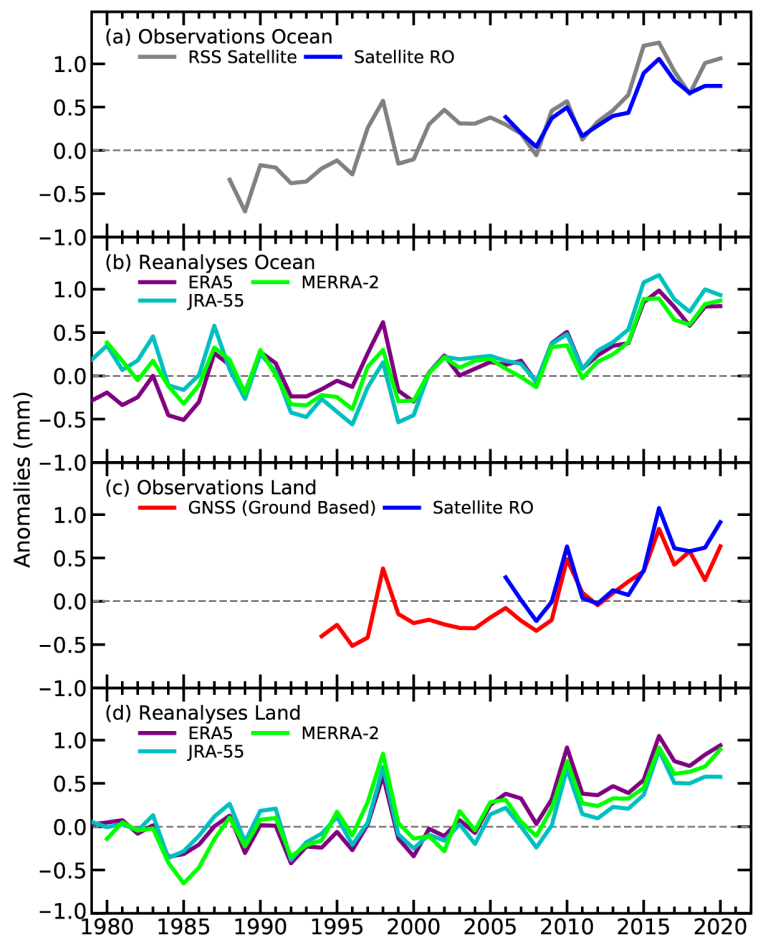


Fig. 2.20. Global mean total column water vapor annual anomalies (mm) over the oceans from (a) observations and (b) reanalyses, and over land from (c) observations and (d) reanalyses averaged over 60°S – 60°N . The shorter time series from the observations have been adjusted so that there is zero mean difference relative to the ERA5 results during their respective periods of record.

measurements, and by the other two reanalyses. Over land, the patterns agree less well. There is good agreement in the dry anomalies over central South America and central Africa and in the wet anomalies over the Gulf of Mexico, Caribbean, North Africa, East Africa, and India. However, over the United States, satellite RO shows dry anomalies to the west and wet anomalies to the east, which is the opposite of ERA5 and ground-based GNSS. There are also opposing anomalies in western Europe, the southwest tip of Africa, eastern Asia, and central Australia. In ERA5, the Pacific Ocean wet–dry dipole and wetter-than-average Indian Ocean, in addition to many of the more regional features (e.g., dry western United States, wet East Africa), are consistent with those shown for surface specific humidity (section 2d1). Specific humidity should be broadly similar to TCWV in that the vast majority of water vapor lies close to the surface. The poorer agreement between ERA5 and RO over land may be partly due to different and incomplete temporal and spatial sampling from the satellite RO data. In 2020, only COSMIC-2, Metop-A, -B, and -C are used because COSMIC data are only available from January to April. COSMIC-2 mainly covers from 45°S to 45°N with about 4000 daily occultations and a relatively uniform local time coverage. The other RO missions (i.e., Metop-A, -B, and -C) cover both tropical and midlatitudes (60°S to 60°N) but with only about 1000 daily occultations and non-uniform local time coverage.

Ocean TCWV global average anomaly time series (Figs. 2.20a,b) from reanalyses and RSS satellite data show maxima in 1983–84, 1987–88, 1997–98, 2009–10, and 2015–16 associated with El Niño events. Both 2019 and 2020 approach, but do not exceed, the 2015–16 record levels due to the overall increasing trend. The RSS satellite data show a discernible increasing trend. On the other hand, the reanalysis products show different long-term trends up until the 1990s but agree well with each other and with the radiometer data after 2000. The satellite RO data are in good agreement with both the radiometer and reanalysis data but show a lower overall trend. TCWV is strongly driven by surface temperature and thus El Niño–Southern Oscillation conditions. After the 2015–16 El Niño peak, all datasets show a return to lower TCWV due to a generally neutral/weak La Niña in 2017–18, followed by larger TCWV anomalies associated with the weak El Niño in boreal winter-spring 2018–19. The positive anomaly continued into 2020. Although 2020 began with weak El Niño conditions, there was a shift by August, ending in moderate La Niña conditions in December (sections 2e1 and 4b).

Over land, the reanalyses, satellite RO missions, and ground-based GNSS agree well in terms of the global average anomaly time series (Figs. 2.20c,d). The small differences between ground-based GNSS and the other datasets are due to asymmetry in the spatial sampling, with more stations located in the Northern Hemisphere, but the general trend and interannual variability are consistent among all datasets. An ERA5 latitude–time Hövmuller plot of TCWV anomalies over land and ocean (Fig. 2.21) indicates that the long-term increase in TCWV occurs at all latitudes, with less variability outside the tropics. Following the most recent strong El Niño in 2015–16, elevated moisture has persisted in the tropics, mainly north of the equator.

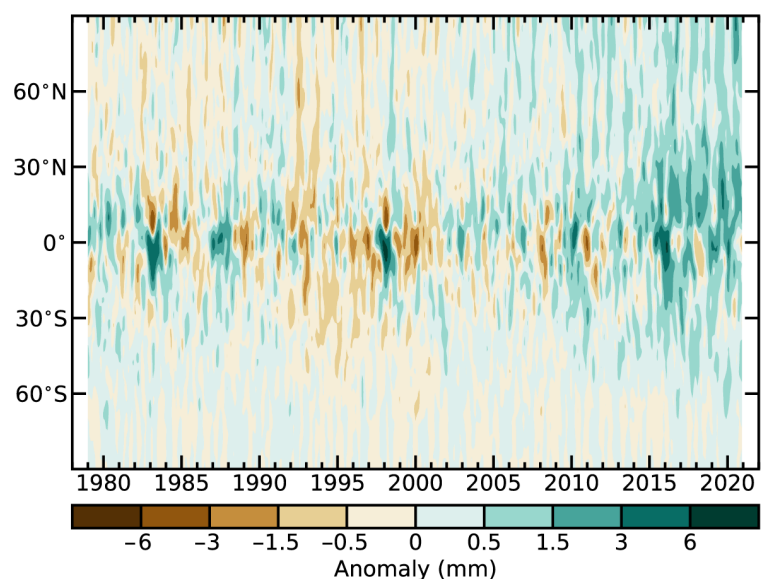


Fig. 2.21. Hövmuller plot of total column water vapor anomalies (mm; base period 1981–2010) derived from the ERA5 reanalysis.

3) Upper tropospheric humidity—V. O. John, L. Shi, E.-S. Chung, R. P. Allan, S. A. Buehler, and B. J. Soden

The 2020 near-global-average (60°S–60°N) upper tropospheric (relative) humidity (UTH) remained close to the 2001–10 average (0.04, –0.16, and –0.35 %rh for the three datasets shown in Fig. 2.22a). This implies a continued moistening of the upper troposphere with warming. A near-zero decadal trend (less than 0.01 %rh per decade for all datasets in Fig. 2.22) in the UTH indicates an increase in absolute (specific) humidity in line with the warming mid- and upper troposphere (about 0.2 K per decade as shown, for example, in Santer et al. 2017 and Christy et al. 2020), and hence is consistent with a positive (amplifying) water vapor feedback (Chung et al. 2016).

This moistening of the free troposphere is demonstrated in Fig. 2.22b, which shows the difference between the Microwave Sounding Unit/Advanced Microwave Sounding Unit (MSU/AMSU) channel 2 brightness temperature (T₂; sensitive to upper-tropospheric temperature emissions from oxygen molecules) and High Resolution Infra Red Radiation Sounder (HIRS) upper tropospheric channel brightness temperature (T₁₂). As shown in Chung et al. (2014), the difference, T₂ minus T₁₂, measures the divergence in emission levels between upper-tropospheric water vapor and oxygen. This divergence provides a direct measure of the extent of upper-tropospheric moistening as the emission level of T₁₂ elevates with increasing concentrations of water vapor, while the T₂ emission level remains the same because the oxygen concentration does not change over time. The positive trend in the T₂ minus T₁₂ time series thus indicates the moistening of the upper troposphere. The water vapor feedback is determined mainly by the mid- to upper troposphere though the concentration of water vapor is small there. This is because the radiative effect of absorption by water vapor is roughly proportional to the logarithm of its concentration, so it is the fractional change in water vapor concentration, not the absolute change, that governs its strength as a feedback mechanism (Allan et al. 1999; Held and Soden 2000; John and Soden 2007).

The microwave satellite data (Chung et al. 2013) and the ERA5 reanalysis (Hersbach et al. 2020) data show below-average UTH values throughout the year. However, the HIRS infrared satellite data (Shi and Bates 2011) show above-normal UTH values since summer 2020; the reason for this discrepancy is not yet understood. Despite this, there is broad agreement among the three datasets in interannual variability. During their common period, there is a correlation of 0.6 between the two satellite datasets and 0.5 between ERA5 and either of the satellite datasets. The mean and standard deviation of the anomaly time series are -0.01 ± 0.54 , 0.08 ± 0.65 , and -0.01 ± 0.33 %rh for the ERA5, HIRS, and microwave datasets, respectively, during their common period. HIRS and ERA5 show larger interannual variability compared to the microwave data, which can be

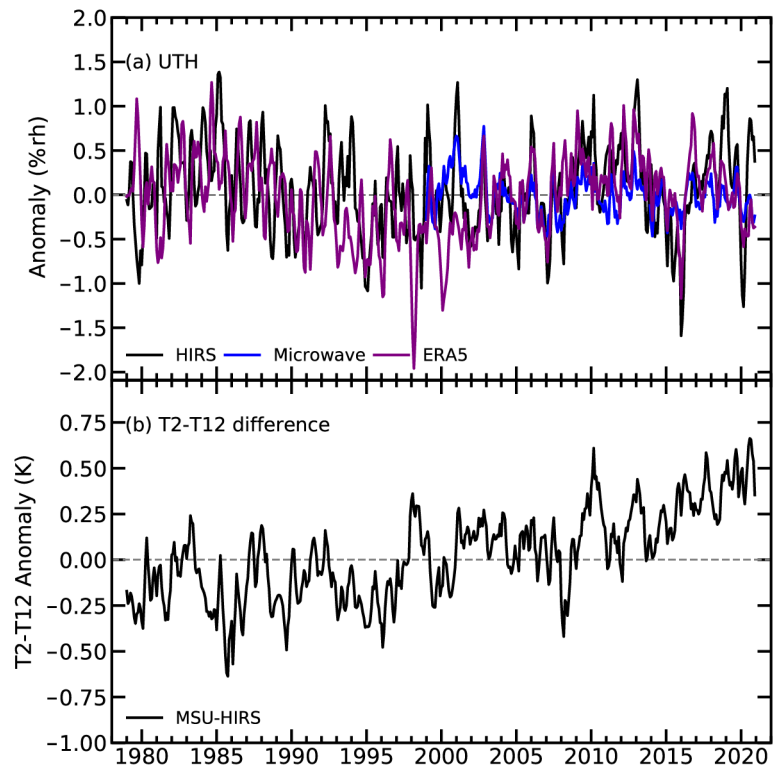


Fig. 2.22. (a) Global (60°S–60°N) average time series of upper tropospheric humidity anomalies (%rh) using HIRS (black), microwave (blue), and ERA5 (purple) datasets. (b) Anomalies of MSU/AMSU channel 2 brightness temperature (T₂) minus HIRS channel 12 brightness temperature (T₁₂) with increasing values indicative of higher absolute or specific humidity. The anomalies are computed with respect to the 2001–10 average, and the time series are smoothed to remove variability on time scales shorter than 3 months.

attributed in part to the clear-sky sampling of the infrared HIRS observations (e.g., Fig. 10 of John et al. 2011) and to the use of a single level (400 hPa) RH for the ERA5. Negative (dry) anomalies in all datasets can be observed during strong El Niño events (e.g., 2015–16).

Annual anomalies of UTH for 2020 are shown in Plate 2.1j and Appendix Fig. A2.9 for the microwave and HIRS datasets, respectively. Preconditioned in 2018–19 by a strong positive Indian Ocean dipole (IOD), the neutral to slightly positive phase of the IOD during 2020 led to widespread flooding in eastern Africa (Wainwright et al. 2020) and droughts in southeast Asia (Wang and Cai 2020). This is clearly reflected in the UTH data by positive anomalies over eastern Africa and surrounding oceans and negative anomalies over southeast Asia and eastern Australia. During the positive phase of IOD, sea surface temperature (SST) in the Indian Ocean near Africa's east coast is warmer than usual, while SST in the waters northwest of Australia is comparatively cooler. These conditions lead to above-average precipitation in the western equatorial Indian Ocean and surrounding areas and the opposite in southeast Asia (section 2d4). Severe drought conditions in Madagascar, South America, and the western United States are also reflected in the anomalies. Above-normal monsoon rainfall in central and southern India is indicated by the positive anomalies in UTH over those regions. Dry anomalies over Europe are associated with the high geopotential height associated with a blocking pattern that led to dry, sunny conditions, especially in spring 2020 (van Heerwaarden et al. 2021; section 7f). This close connection of UTH to convection makes it suitable for monitoring large-scale dynamics of the troposphere.

The inter-satellite calibrated and bias-corrected infrared and microwave satellite measurements sample a broad upper tropospheric region (roughly between 500 and 200 hPa, but this layer varies slightly depending upon the atmospheric humidity profile) twice per day, and infrared observations only sample clear-sky scenes (John et al. 2011). The ERA5 reanalysis is based on model runs constrained with in situ and satellite data including the HIRS and microwave radiances. ERA5 samples all regions every hour but here are only displayed at 400 hPa.

4) *Precipitation*—R. S. Vose, R. Adler, A. Becker, and X. Yin

Precipitation over global land areas in 2020, as estimated from three different monitoring products, was near to or above the 1981–2000 long-term average (Fig. 2.23a). All three products indicate that global average precipitation in 2020 was higher than 2019. The observational datasets with the most complete global coverage, that is, the gauge-based product from the Global Precipitation Climatology Centre (GPCC; Becker et al. 2013) and the blended gauge–satellite product from the Global Precipitation Climatology Project (GPCP; Adler et al. 2018), had near-normal precipitation for 2020 (area-average anomalies of +0.46 mm and +0.63 mm, respectively). In contrast, the gauge-based Global Historical Climatology Network (GHCN; Peterson and Vose 1997) dataset was well above the long-term normal, with an area-average anomaly of +49.38 mm. GHCN has had consistently higher precipitation estimates than the other products for the past 4 years. According to the GPCP dataset, the precipitation anomaly over the global ocean (Fig. 2.23b) was +3.93 mm, and the global (land and ocean) anomaly (Figure 2.23c) was +3.22 mm, the latter being a slight increase from the previous year.

Examining the geographic distribution of precipitation anomalies, there was substantial variability across the planet in 2020 (Plate 2.1k). Over global land areas, the largest positive anomalies were over eastern China, with much of central Asia and sub-Saharan Africa also well above average. The strongest positive anomaly over land was in eastern China, the scene of devastating and long-lasting floods primarily during the summer months (see Sidebar 7.3). The largest negative anomalies were over the continent of South America, with much of temperate North America also below average (see sections 7d and 7b, respectively). Over the global oceans, the largest positive anomalies were over the Maritime Continent and the Indian Ocean, as well as along the Intertropical Convergence Zone (ITCZ) and the South Pacific Convergence Zone (SPCZ) in the Pacific Ocean. Much of the rest of the Pacific Ocean, however, had negative anomalies, as did much of the North

Atlantic and part of the southern Indian Ocean. Rainfall excesses associated with tropical cyclones were evident in several areas, including the southeastern United States and in the Caribbean and South China Seas.

Precipitation patterns in 2020 reflect the transition from weak El Niño-like conditions early in the year to a moderate La Niña late in the year (see sections 2e1, 4b). During the first 3 months of 2020, there was excess rainfall in the central Pacific along the equator and generally below-average precipitation over the Maritime Continent associated with the El Niño-like conditions. During the last 3 months of the year, influenced by La Niña, the central Pacific reversed from a positive anomaly to an intense negative anomaly, and the Maritime Continent became positive. Outside the ENSO-affected regions, the large-scale patterns, e.g., over the subtropics of the Pacific and the Atlantic, stayed roughly the same during the year.

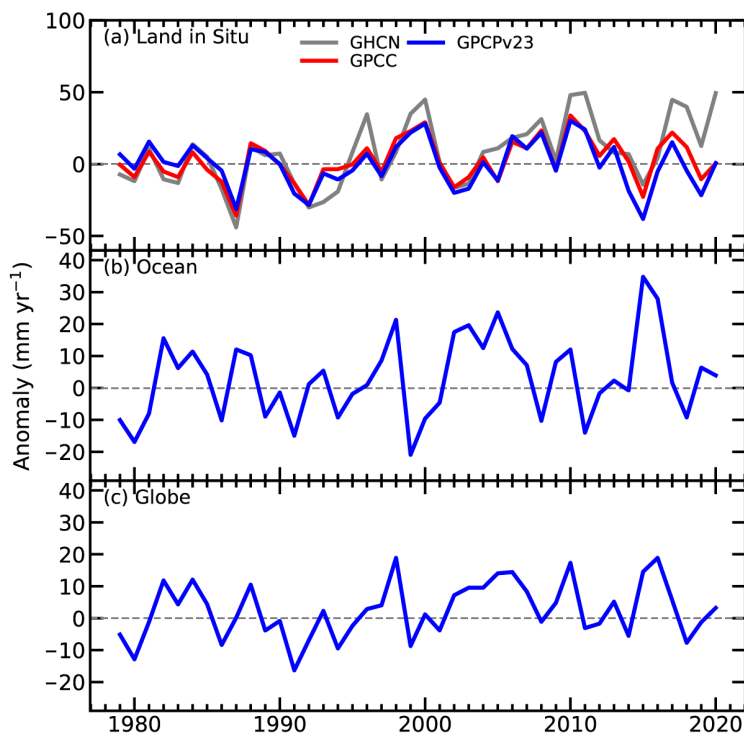


Fig. 2.23. Globally averaged precipitation anomalies (mm yr^{-1}) relative to the 1981–2000 base period over (a) land, (b) ocean, and (c) the globe. Land and ocean time series were created using a proportional land/sea mask at the $1^\circ \times 1^\circ$ scale.

5) Land-based precipitation extremes—M. R. Tye, S. Blenkinsop, M. G. Bosilovich, M. G. Donat, I. Durre, A. J. Simmons, and M. Ziese

Overall, extreme events during 2020 were less intense than normal across most of Eurasia and North America and more intense than normal over the tropics. The patterns of global mean and extreme anomalies illustrate the uneven spatial and temporal distribution of precipitation, whereby the heaviest events contribute disproportionately to the annual total volumes (PRCPTOT [see Table 2.6 for extremes index descriptions]; Pendergrass and Knutti 2018; see section 2d4, Plate 2.1k). Parts of Central America, Europe, and Asia reported very high PRCPTOT; and as illustrated by Plate 2.1l, Fig. 2.24 and Appendix Fig. A2.10, eastern China was influenced by very intense extremes (R95p, Rx1day, Rx5day) rather than frequent heavy rain days (R10mm, R20mm). Conversely, dryness in South America for instance, arose from the combined absence of heavy rain days and anomalous low intensity of extremes. In contrast with 2019, there was a far clearer pattern of exceptionally wet or dry regions (Blenkinsop et al. 2020), with global insured losses

Table 2.6. Precipitation indices used in this section and their definitions, as developed by the WMO ETCCDI (Zhang et al. 2011).

Index	Definition	Figure/Plate
Rx1day	Highest 1-day precipitation amount (mm)	Plate 2.1l; Figs. 2.24c,d; 2.25
Rx5day	Highest 5-day precipitation amount (mm)	Appendix Figs. A2.10c,d
R10mm	Heavy precipitation days >10 mm (days)	Appendix Figs. A2.10c,d
R20mm	Very heavy precipitation days >20 mm (days)	Fig. 2.24
R95pTOT	Total precipitation on days exceeding the 95th percentile of wet days (mm)	Not shown
PRCPTOT	Annual total precipitation falling on wet (>1 mm) days (mm)	Not shown

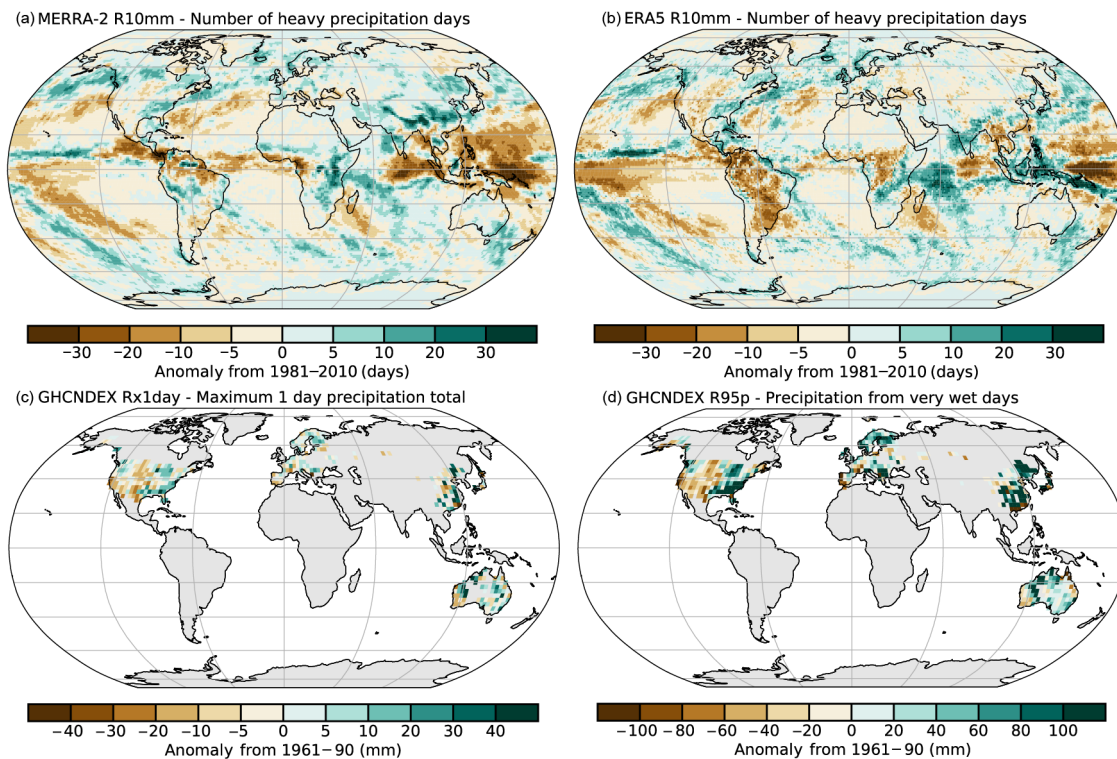


Fig. 2.24. Anomalies of 2020 indices relative to a 1981–2010 baseline for: R20mm (days) derived from (a) MERRA-2 (Gelaro et al. 2017) and (b) ERA5 (Hersbach et al. 2020) reanalyses, (c) Rx1day (mm), and (d) R95p (mm) derived from the in situ-based GHCNDEX relative to a 1961–90 baseline (Donat et al. 2013).

of \$76 billion U.S. from natural hazards largely driven by floods from severe convective storms and drought-influenced fires (Swiss Re 2020).

Several notable events stand out in relation to the long-term mean of extreme precipitation indices (Table 2.6). Reanalysis products (MERRA-2, Gelaro et al. 2017; ERA5, Hersbach et al. 2020) and gridded observations (GPCC, Schamm et al. 2013; GHCNDEX, Donat et al. 2013) generally show similar patterns, with the exception of the tropics, parts of central and southern Africa, and South America for extreme indices (e.g., R10mm, Rx1day) as noted in recent publications (Alexander et al. 2020; Hersbach et al. 2020). Rx1day and Rx5day highlight storm tracks and anomalous events over the Middle East, southeast Asia, southeastern United States, and northern and eastern Australia (Fig. 2.24, Appendix Fig. A2.10b, Table 2.7).

The “Dragon Storm” over the Middle East/North Africa on 12 March was an unusually powerful midlatitude cyclone for early boreal spring, bringing ~70 mm of precipitation in 24 hours to the north coast and Nile Delta in Egypt (NESDIS 2020; The Watchers 2020). Above-average SSTs in the Indian Ocean (see section 3b), coupled with favorable atmospheric conditions over East Africa, resulted in a particularly wet long-rains season (March–June), with several prolonged duration events contributing to floods (see section 7e4). These events follow a pattern of increased duration and total volume in persistent extremes (Du et al. 2019). Exceptionally wet monsoon conditions led to the highest Rx1day on record in Karachi-Faisal, Pakistan (see section 7g4; WMO 2021; Table 2.7), compounding the effects of Super Cyclonic Storm Amphan over India and Bangladesh (Floodlist 2020a). The Indian Ocean conditions also contributed to the first known landfalling tropical cyclone in Somalia, with accompanying precipitation extremes (Floodlist 2020b).

Few records were broken over Australia during 2020, the exception being the Northern Territory during January where the highest Rx1day totals on record accompanied Cyclone Claudia (see section 4g7; BoM 2020; Table 2.7). Eastern Australia was wetter than average, reversing drought conditions in the southeast. New Zealand experienced a drier-than-normal year over the northern and eastern North Island, and near-normal conditions in most other locations.

Table 2.7. Notable events and new precipitation maxima.				
Location	Duration	Amount	Comment	Reference
Wagait Beach and Dum in Mirrie, Australia	24 hours	515.2 mm 562 mm	10 Jan pre-cyclone Claudia (Wagait Beach—new January record, Dum in Mirrie—new record for Northern Territory)	BoM 2021
Belo Horizonte, Brazil	24 hours	172 mm	24 Jan (new record)	WMO 2021
Kolkata, India Ishwardi, Bangladesh	24 hours	250 mm 155 mm	20 May Super Cyclonic Storm Amphan	Floodlist 2020a
Karachi-Faisal, Pakistan	24 hours	231 mm	28 Aug (new record for Karachi area)	WMO 2021
Khombole, Senegal	24 hours	225.8 mm	5 Sep (new record)	WMO 2021
Jeju Island, South Korea	48 hours	963.5 mm	7 Sep Tropical Cyclone Julian (Mayask)	WMO 2021
Hué, Vietnam	7 days	1500 mm	7–13 Oct	WMO 2021
Napier, New Zealand	1 hour 24 hours	54 mm 242.4 mm	9 Nov (new hourly record)	Floodlist 2020d
Ciro Marina, Calabria Italy	48 hours	456.8 mm	20–22 Nov	Floodlist 2020c
Bosaso Somalia	24 hours	128 mm	22 Nov Tropical Cyclone Gati	Floodlist 2020b

A longer-term perspective using near-complete series of extreme indices (≥ 50 years) from ~ 6000 gauges over Europe (Klein Tank et al. 2002) indicates new Rx1day (Rx5day) records at 70 (40) gauges. These are fewer than normally expected and suggestive of an inactive year for European rainfall extremes. Many record-breakers were in Germany (Fig. 2.25), which accounted for 43 Rx1day records, but also included a total of 200.2 mm in Dimitrovgrad, Serbia, exceeding the previous record of 123.3 mm. In total, 11.6% (7.5%) of the Rx1day (Rx5day) values ranked in the top 10% of annual values for an individual gauge in 2020. Comparing these data on upper decile events for each year in the period 1980–2020 shows that 2020 ranked 15th (34th) out of the 41 years for which at least ~ 4500 gauges contribute. The R10mm (R20mm) indices for 2020 were around average with 8.8% (10.6%) of gauges in the top decile for the location, ranking 24th (19th) with new records at 82 (84) gauges, particularly across Scandinavia.

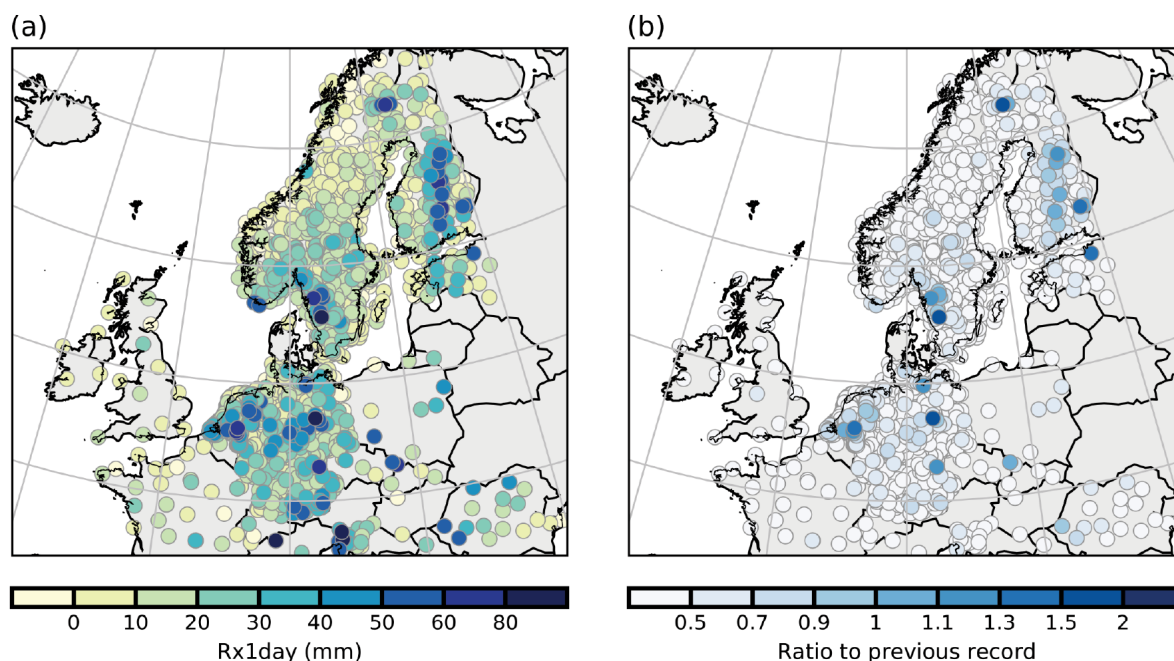


Fig. 2.25. Comparison of absolute Rx1day values (mm) and their ratio to the previous record from GHCN-Daily (Menne et al. 2012) over Germany.

Component 4 of the U.S. NOAA Climate Extremes Index (CEI4, area of the United States that experienced 1-day precipitation totals exceeding the 90th percentile; Gleason et al. 2008; NOAA 2021) was low for 2020, ranking 75th in the 111-year record. Of the seasonal indices, only autumn ranked in the top tercile at 34th. From a regional perspective, the western United States registered CEI4 = 0% in all seasons, or no areas of heavy precipitation. CEI4 registered in the top decile during spring and summer in the upper midwest and autumn in the southeast, also illustrated by the location of Rx1day events (Plate 2.11; Fig. 2.24c). Despite the very active Atlantic hurricane season (see section 4g2), CEI4 values along the eastern seaboard were at or below average.

6) Lake water levels—B. M. Kraemer

In 2020, the average water level anomaly across 249 of Earth’s largest lakes was +1.05 m (range: -9.16 m to +44.45 m) compared to their mean lake water levels from 1993–2001 (Fig. 2.26). Water level anomalies were positive in 73% of the lakes (183 out of the 249) compared to 68% in the previous year. Measurements of lake water level variation provide an important indicator of global hydrological change, water availability, drought, and human hydrological influence. Publicly available satellite altimetry data are used to assess changes in surface water storage. This year there are an additional 51 monitored lakes compared to 2019.

The 2020 water level anomalies differed widely both between and within regions. Lakes in southern Brazil and the Caucasus region had consistent negative water level anomalies while

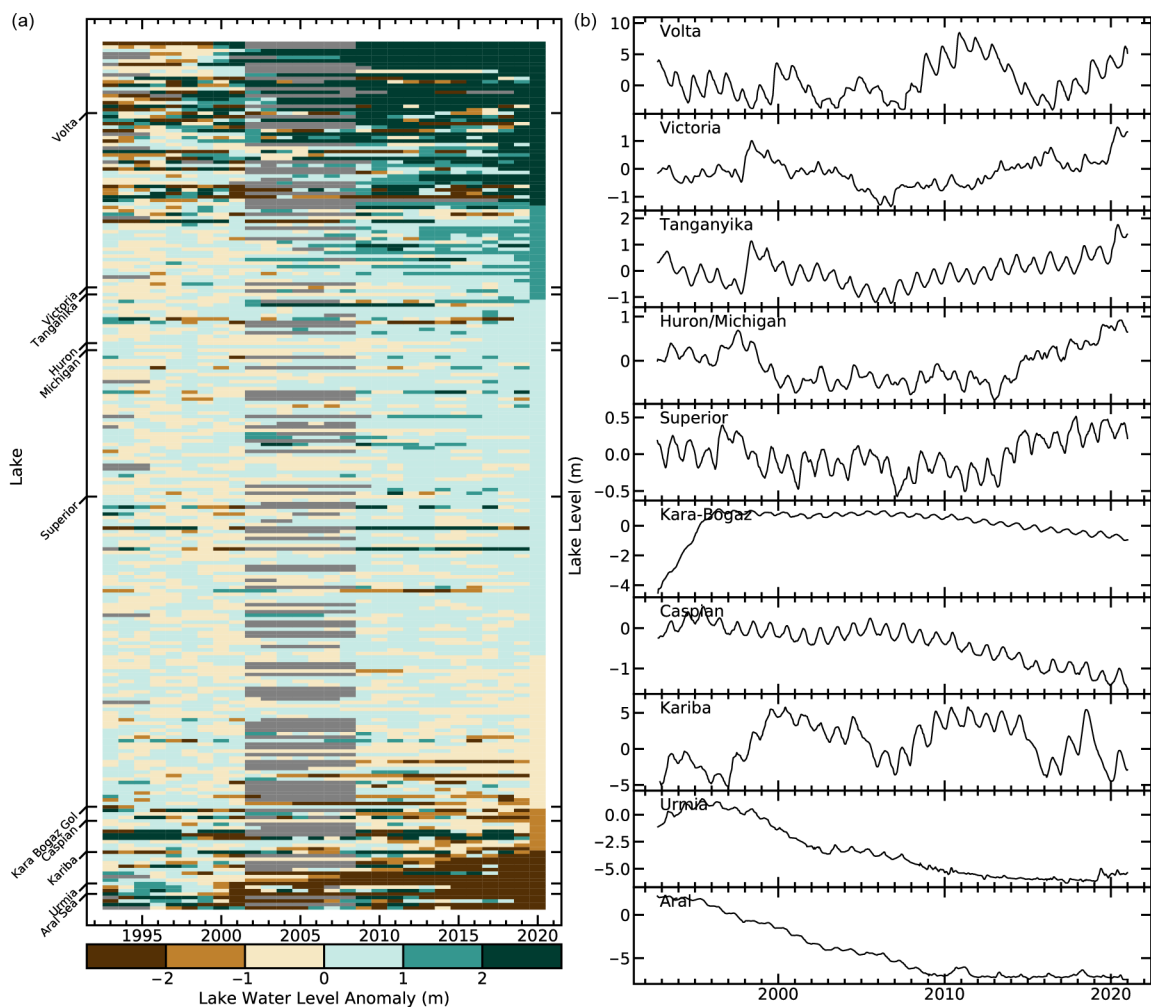


Fig. 2.26. (a) Lake water level time series for 249 globally distributed lakes ranked by their 2020 anomaly (m) relative to the 1993–2001 mean. Ninety-five of the 249 water level time series had substantial data gaps from 2002 to 2008. The subset of lakes that are named on the y-axis of (a) and plotted in (b) are those with the five largest positive anomalies and five largest negative anomalies when water levels anomalies were weighted by the surface area of each lake.

Canada, equatorial Africa, and western China had consistent positive water level anomalies (Plate 2.1m). The Tibetan-Qinghai Plateau experienced positive water level anomalies in most lakes (Plate 2.1m), consistent with the expected effects of climate change on regional rainfall and glacier melt (Woolway et al. 2020). Aside from broadscale and consistent regional variability, lake water level anomalies in nearby lakes within regions also varied. For example, Cahora Bassa and Kariba, two large, nearby reservoirs on the Zambezi River in southern Africa (within 185 km), had strongly diverging water levels (+4.38 m and -2.28 m, respectively), potentially due to differences in their water level management as reservoirs. The Middle East, Australia, and northern Asia all included lakes with both strong positive water level anomalies and strong negative anomalies, often in close proximity.

When lake level anomalies were multiplied by the lake surface area, the resulting approximate volumetric anomalies were most negative for the Caspian Sea (-433 km³), Aral Sea (-47 km³), Kara-Bogaz-Gol (-32 km³), Urmia (-22 km³), and Kariba (-19 km³). The largest positive volumetric anomalies were found in Tanganyika (+26 km³), Volta (+28 km³), Superior (+45 km³), Victoria (+76 km³), and Huron/Michigan (+105 km³). These lakes are highlighted in the time series shown in Fig. 2.26. The largest volumetric water level anomalies matched global patterns in terrestrial water storage assessed using data from the Gravity Recovery and Climate Experiment (GRACE) satellite mission (see Fig. 2.31).

Water level data were acquired from the NASA/CNES Topex/Poseidon and Jason satellite missions via the Global Reservoir and Lake Monitoring (G-REALM) project version 2.4 and via Theia's Hydroweb database. The 2020 water level anomalies in 80 lakes that had data from both sources were averaged across the two sources. One hundred and sixty lakes were unique to the G-REALM dataset and nine lakes were unique to the Hydroweb dataset. Satellite altimeters were originally developed to map ocean surface height. A small subset of the world's lakes are monitored in this way because the space-borne sensors must pass directly over the lake with sufficient regularity to produce accurate and complete time series. The lakes in this study comprise the 249 lakes with the longest (>29 years) and highest temporal resolution time series which are updated in near real time. Comparing the satellite altimeter measurements to in situ measurements, the root mean squared error of elevation variations is ~5 cm for large lakes such as those analyzed here. Water levels are typically measured every 10 days, but the exact dates on which water levels are measured vary from lake to lake. To make water level data temporally consistent, we have linearly interpolated each lake's time series to the daily scale so that all lakes had time series of the same interval. Of the 249 water level time series, 95 had substantial data gaps from 2002 to 2008, so we used a period prior to these gaps (1993–2001) as the baseline for calculating 2020 water level anomalies.

In situ monitoring of lake water levels is vital for cross-validating and calibrating altimeter-based estimates of long-term water level variation in lakes. However, our capacity to monitor changes in a global population of lakes with in situ data alone is currently limited due to the scarcity of publicly available near-real time data from key regions. Impediments to data sharing need to be overcome, and data delivery needs to be more timely in order to monitor water cycle variation with in situ data. Landsat-based surface water extent datasets, such as those produced by the Copernicus Programme (Pekel et al. 2016), could be used for near real-time monitoring of water storage in many thousands of lakes but to date, no near real-time data products exist to support such efforts.

7) *Cloudiness*—M. J. Foster, L. Di Girolamo, C. Phillips, M. Stengel, S. Sun-Mack, and G. Zhao

Global cloudiness in 2020 increased by 0.31% ($\pm 0.14\%$) relative to 2019, based on several satellite records (Fig. 2.27). Mean global cloudiness tends to stay reasonably stable, but regional distribution of cloud changes year-to-year. Some of this is due to normal variation in synoptic-scale weather events, but cloudiness can also be driven by modes of variability, the best-known being the El Niño–Southern Oscillation (ENSO). ENSO is characterized by a shifting gradient of SST and

low-level winds between the eastern and central equatorial Pacific and Indonesia. This gradient can in turn enhance or suppress convection, which drives the formation of clouds. This means that different phases of ENSO (and other modes) are frequently accompanied by characteristic patterns of cloudiness, which typically have a seasonal dependence. These large-scale patterns are important for several reasons. Clouds cool Earth by reflecting incoming solar radiation and warm it by trapping outgoing terrestrial radiation. Whether the overall effect is one of cooling or warming depends on many factors including the geographic distribution, height, and opacity of clouds (Bony et al. 2015). Clouds are also a gauge for moisture, and their presence may increase or decrease the risk of hydrological hazards like droughts, flooding, and wildfires.

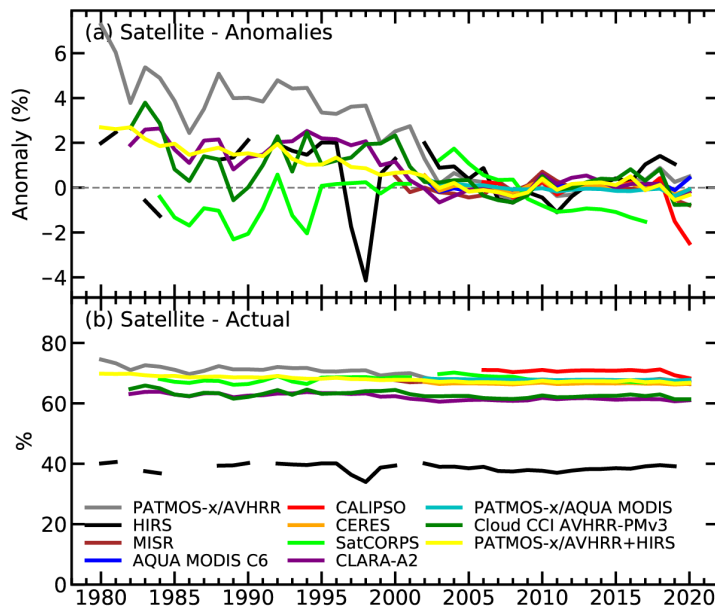


Fig. 2.27. Annual global cloudiness (a) anomalies and (b) actual (%) for 1980–2020. The anomaly is defined as the annual value minus the mean, derived between 2003 and 2015, a period common to the satellite records excluding CALIPSO, where the entire record was used instead. The datasets include (1) PATMOS-x/AVHRR (Pathfinder Atmospheres Extended; Heidinger et al. 2013), (2) HIRS High Cloud (Wylie et al. 2005, Menzel et al. 2016), (3) MISR (Multi-angle Imaging SpectroRadiometer; Di Girolamo et al. 2010), (4) Aqua + Terra MODIS C6 (Moderate Resolution Imaging Spectroradiometer Collection 6; Platnick et al. 2015), (5) CALIPSO (Cloud-Aerosol Lidar and Infrared Pathfinder Satellite Observation; Winker et al. 2007), (6) CERES Aqua MODIS (Clouds and the Earth’s Radiant Energy System; Trepte et al. 2010; Minnis et al. 2008), (7) SatCORPS (satellite cloud and radiative property retrieval system; Minnis et al. 2016), (8) CLARA-A2 (cloud, albedo, and radiation dataset; Karlsson et al. 2017), (9) PATMOS-x/AQUA MODIS (created specifically for this report), (10) CLOUD_CCI (Cloud Climate Change Initiative AVHRR-PM v3.0; Stengel et al. 2017), and (11) PATMOS-x/AVHRR+HIRS (Foster et al. 2018).

The Indian Ocean dipole (IOD) can also be characterized by a shifting gradient in SST but affects the Indian Ocean, and a positive phase typically means fewer clouds and drier-than-normal conditions over much of Australia (BoM 2021). After being strongly positive and the most notable mode of variability present in 2019, the IOD returned to neutral conditions in 2020 (see section 4f). Meanwhile, ENSO shifted from neutral conditions to a moderate La Niña phase, which began in the boreal summer and persisted through the rest of the year (see section 4b). These features are apparent in the cloudiness anomalies across the four typical seasons of 2020 (Fig. 2.28). Positive cloudiness anomalies and wet conditions in the tropical central and eastern Pacific are indicative of weak El Niño-like conditions during December 2019–February 2020, while negative anomalies over the western tropical Pacific paired with positive anomalies over Indonesia are characteristic of La Niña during June–August 2020.

Plate 2.1n shows global cloudiness anomalies for 2020. Large and/or persistent changes over a specific region can result in a statistically significant cloudiness anomaly. This is an anomaly that, when averaged over the entire year, falls more than 2 standard deviations outside the mean as determined from the PATMOS-x/AVHRR climatology base period (1981–2010). In 2020 there were several such anomalies, and, in particular, there were large numbers of negative continental anomalies. Significant maritime anomalies include increased cloudiness in the eastern tropical Pacific and northern Indian ocean, particularly the Arabian Sea and Gulf of Aden, and decreased cloudiness in the northern Pacific. The increased cloudiness in the tropical Pacific is on either side of the ITCZ, the equatorial belt where northern and southern trade winds converge to produce precipitating convective clouds, and suggests a poleward shift of convective activity. Continental

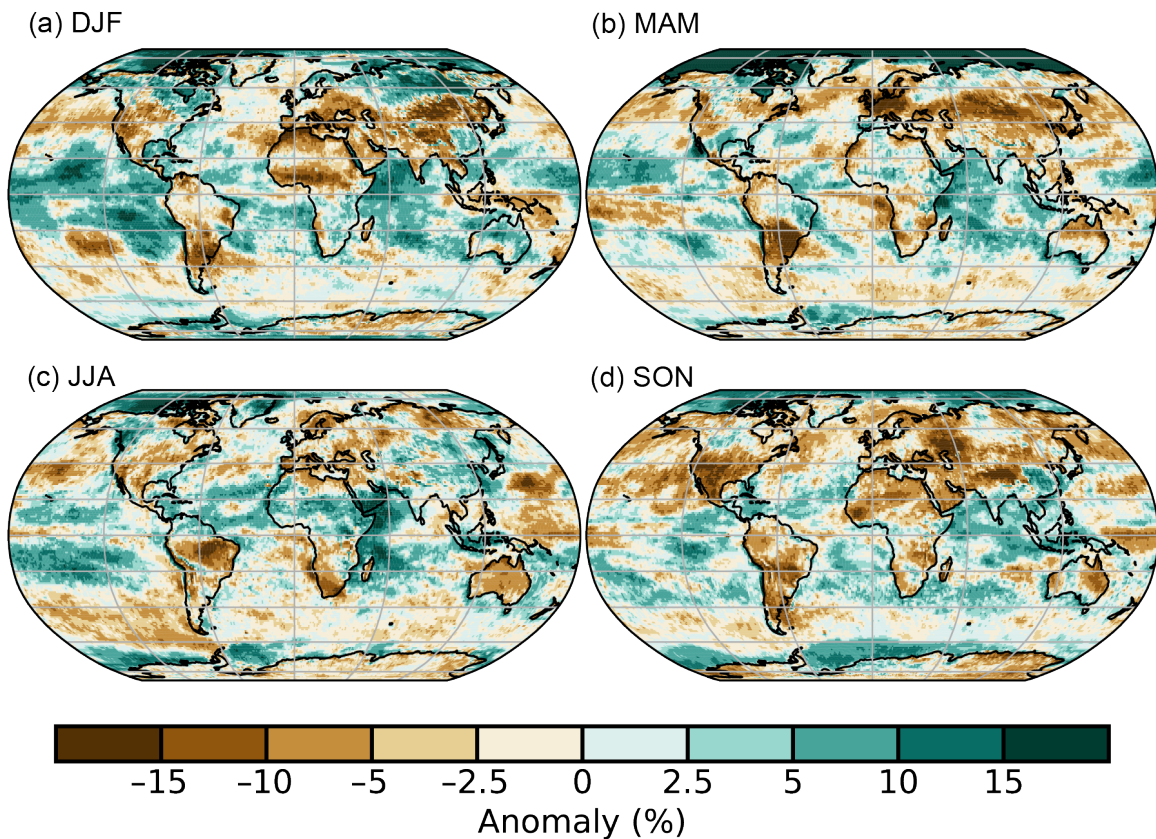


Fig. 2.28. Global seasonal cloudiness anomaly (%; 1981–2010 base period) for (a) Dec–Feb (DJF), (b) Mar–May (MAM), (c) Jun–Aug (JJA), and Sep–Nov (SON) generated from the 30-year PATMOS-x/AVHRR+HIRS cloud climatology.

anomalies include decreased cloudiness in the Americas over the western United States and portions of Brazil, Paraguay, Uruguay, and Argentina. Africa experienced decreased cloudiness in the south over Namibia and South Africa and in the north over Libya, Tunisia, and Algeria. Europe experienced negative anomalies driven by decreased cloudiness during March–May (Fig. 2.28). Decreased cloudiness also occurred in Asia over Turkey, southern Russia, Kazakhstan, Mongolia, and parts of western China. The continental anomalies frequently coincided with regions that experienced below-average precipitation and/or severe wildfires (Plates 2.1k,x,z,ag).

8) River discharge and runoff—H. Kim and D. Tokuda

Since 2017, global land has been overall slightly wetter than average, and the anomalies of runoff (Plate 2.1o) and discharge (Plate 2.1p) make clear that the distribution of wet and dry regions were similar to those of 2019. In many regions, the deviations intensified during 2020. A wet state of runoff prevailed in a large area of the United States (except the west), Canada (except the southeast), and the Eurasian continent. In particular, a strong wet signal has been discerned in East Asia (i.e., China, Japan, and Korea) in contrast to the strong dry spell of the previous year. During summer, anomalous runoff was generated by a disastrous amount of rainfall fostered by the enhanced Changma (also known as Meiyu in China and Baiu in Japan; see Sidebar 7.3 for details). According to recent studies, the East Asia Summer Monsoon lifecycle has intensified (Park et al. 2020; Wang et al. 2019). The United Kingdom also observed an anomalous wet year due to an exceptionally wet 2019/20 winter, and all the seasons of 2020 except for the record-breaking sunny spring (see section 7f2; Met Office 2020). Most regions of the European continent suffered anomalous dry spells, while the climate state of Scandinavian countries shifted to become wetter. Also, a large area of South America experienced a drier hydroclimate. Such anomalous states of climate were reflected in the global distributions of runoff and river discharge.

It has been well-known that ENSO and Pacific Decadal Oscillation (PDO; Zhang et al. 1997) are key drivers modulating global freshwater discharge (e.g., Kim 2020). The long-term variability of total runoff and those climate modes are shown in Fig. 2.29. This indicates that a positive (negative) phase inherent to ENSO and PDO tends to be associated with a drier (wetter) state of the global freshwater discharge by which about 46% of total variance is explained by the combined contribution of ENSO and PDO. Globally, a continuous wet state since 2017 was prolonged and then further intensified during 2020 due to the emergence of La Niña in the second half of the year. 2020 saw the third-highest (~95th percentile) runoff of the 63-year period (1958–2020).

Figure 2.30 displays the inter-annual variability and climatology of freshwater discharge into the Atlantic, Pacific, Indian, and Arctic basins, which comprise approximately 75% and 85% of the entire terrestrial land area and river discharge, respectively. For the Atlantic Ocean, it was nearly neutral during 2020, while river runoff was above normal for much of the past decade. The seasonality was relatively weaker due to the excess and deficit of discharge during the dry and wet season, respectively. The Pacific Ocean received significantly greater volumes of water from rivers during the wet season (May–July) and over the rest of the year. In terms of long-term variability, there is a strong upward trend since the 1990s. Therefore, it was significantly wet during 2020. A similar upward trend is seen in the Indian Ocean as well, following a long-term decline since the mid-twentieth century. During the entire analysis period, the freshwater discharge into the Arctic Ocean has been increasing, and the wet season of 2020 was significantly anomalous (see section 5g for details).

The 63-year series of runoff and freshwater discharge were provided from off-line hydrologic simulations of the Ensemble Land State Estimator (ELSE; Kim et al. 2009) and a global-scale river routing model, Catchment-based Macro-scale Floodplain (CaMa-Flood; Yamazaki et al. 2011) over 1° and 0.5° global grids, respectively. To keep uniformity with the other estimates, river networks information was prepared in a regular grid system, 30-min drainage direction map (DDM30; Döll and Lehner 2002), and sub-grid-scale parameters (e.g., river length and floodplain shape) were derived accordingly. To distinguish the freshwater discharge to each oceanic basin, the World Ocean Atlas 2018 (Garcia et al. 2019) was referenced. The Japanese global atmospheric reanalysis (JRA-55; Kobayashi et al. 2015) and the GPCP Monitoring Product version 2020 (Schneider et al. 2020) were combined to produce the atmospheric boundary conditions.

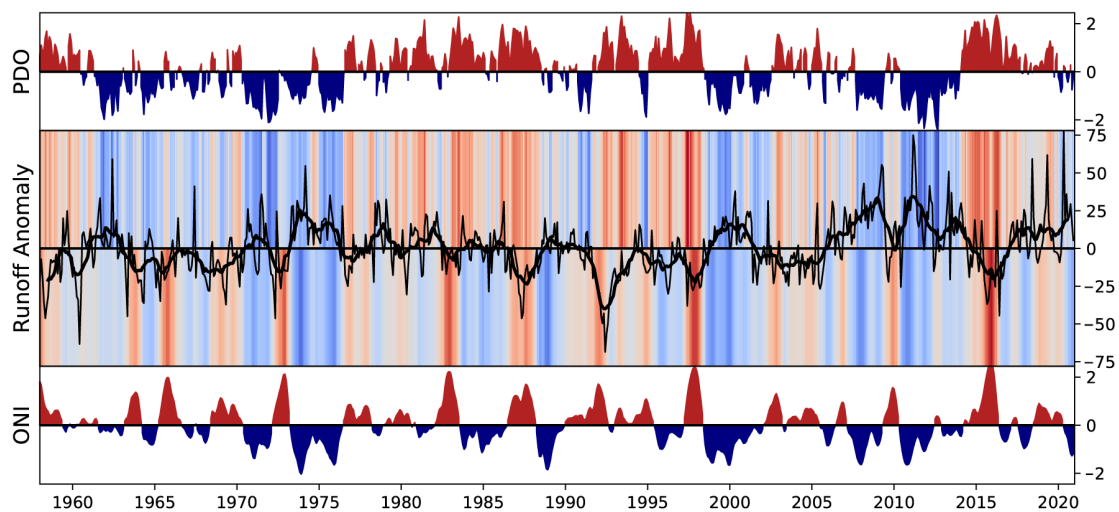


Fig. 2.29. Interannual variability of Ocean Niño Index (ONI; lower), Pacific Decadal Oscillation (PDO) index (upper), and global runoff (middle; mm; thick black line is 12-month moving average). ONI and PDO index are shaded red (positive phase) or blue (negative phase). Shading above and below the zero-line of global runoff is proportional to PDO and ONI, respectively.

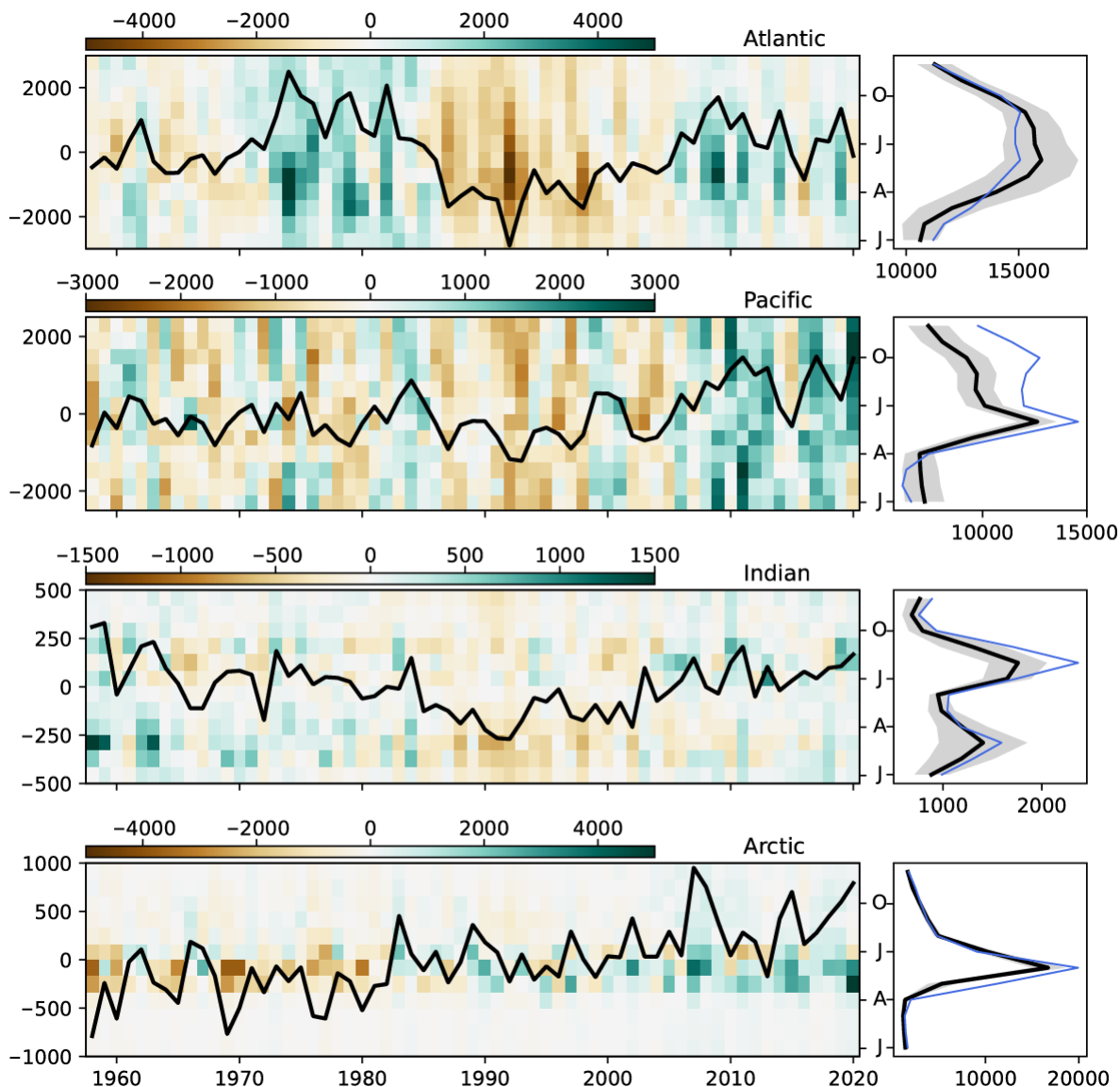


Fig. 2.30. Interannual variability of freshwater discharge to global ocean basins ($\text{km}^3 \text{yr}^{-1}$). Line and shades indicate annual mean and monthly anomaly, respectively. (Left) Seasonality of freshwater discharge to global ocean basins ($\text{km}^3 \text{yr}^{-1}$). Thick black line, thin blue line, and gray shade indicate long-term climatology, seasonal variation during 2020, and 1σ of long-term variability. J, A, J, O for the tick labels of the shared-ordinate between left and right panels indicate Jan, Apr, Jul, and Oct, respectively (right).

9) Groundwater and terrestrial water storage—M. Rodell and D. Wiese

Terrestrial water storage (TWS) comprises all the water on and below the land surface: groundwater, soil moisture, surface water, snow, and ice. In general, snow and ice dominate interannual TWS variability at high latitudes and in alpine regions, surface water dominates in the wet tropics, and groundwater dominates elsewhere (Getirana et al. 2017).

Changes in mean annual TWS between 2019 and 2020 as measured by the GRACE (Tapley et al. 2004) and GRACE-FO (Landerer et al. 2020) satellite missions, shown in Plate 2.1q as equivalent heights of water in centimeters (cm), integrate the effects of multiple hydroclimatic variables (see Plates 2.1k,p,t). Of note in 2020, heavy rains raised TWS in a large region of south-central and eastern Africa by 12–25 cm equivalent height of water. Exacerbated by increased runoff due to environmental degradation and urbanization (Mafaranga 2020), Lake Victoria consequently gained more than a meter of water (see sections 2d6, 7e4), with flooding in the surrounding region. Groundwater and TWS remained depressed over most of Europe, excluding Scandinavia, following losses in 2019. Much of India experienced large TWS gains, but, directly to the east, drought worsened in the Indochina Peninsula. Above-normal precipitation increased TWS in

much of the rest of far eastern Asia as well as north-central Asia. TWS changes in Australia were of mixed sign and generally mild. In North America, the most notable changes were considerable increases in TWS in central Canada and the southeastern United States and drying that stretched from the coast of California to eastern Texas, all of which were driven by precipitation anomalies (see section 7b2). Consistent with past years (Tapley et al. 2004), some of the most massive TWS changes occurred in South America, including large increases in eastern Brazil and a north–south swath of large decreases down the center of the continent (see section 7d).

Figures 2.31 and 2.32 depict time series of zonal mean and global mean monthly TWS anomalies after removing the seasonal cycle. Ice sheet and glacier ablation continued to produce large TWS declines in Antarctica, Greenland, the Gulf Coast of Alaska, and polar islands, hence we excluded these regions from the data used in Figs. 2.31 and 2.32, but additional ice mass loss is still apparent at high latitudes in Fig. 2.31. The large TWS increase in south-central and eastern Africa was apparent near the equator in Fig. 2.31. TWS decreases near 40°N can be attributed to four factors (Plate 2.1q): droughts in California, the central United States, and the land adjacent to the Aegean Sea and Black Seas; glacier ablation in the Alay Mountains of Tajikistan; persistent water level decline in the Caspian Sea; and groundwater depletion to support irrigated agriculture in the North China Plain. At the global scale (Fig. 2.32), mean TWS decreased by about 7 mm equivalent height of water from the start of 2020 through June and then quickly gained nearly 12 mm, much of that in central Africa, causing a temporary 4 mm decline in sea level (see section 3f).

In situ measurement records of the TWS components are rarely available outside of the United States and parts of Europe and Australia; however, GRACE and GRACE-FO have provided monthly, global maps of TWS anomalies based on precise measurements of Earth’s time-varying gravity field. The GRACE and GRACE-FO data were the basis for this analysis. Uncertainty in the derived TWS anomalies varies depending on the latitude (higher near the equator), size of the region of interest (higher at small scales), TWS anomaly averaging period (higher for short periods), and orientation (higher for north–south oriented regions near substantially different gravity change signals). At scales greater than about 500,000 km², uncertainty in monthly TWS anomalies is typically around 1–2 cm equivalent height of water (Wiese et al. 2016).

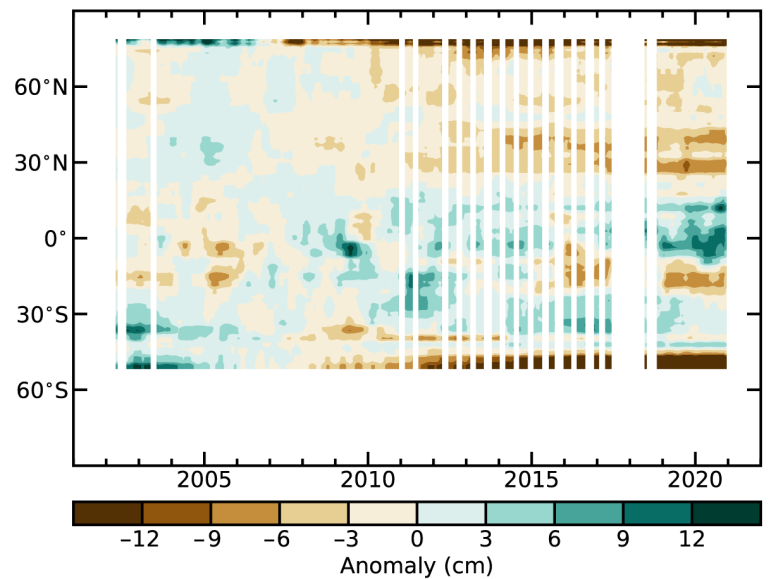


Fig. 2.31. Zonal means of terrestrial water storage anomalies, excluding those in Antarctica, Greenland, the Gulf Coast of Alaska, and polar islands, in cm equivalent height of water, based on gravity observations from GRACE and GRACE-FO. The anomalies are relative to a base period of 2004–09.

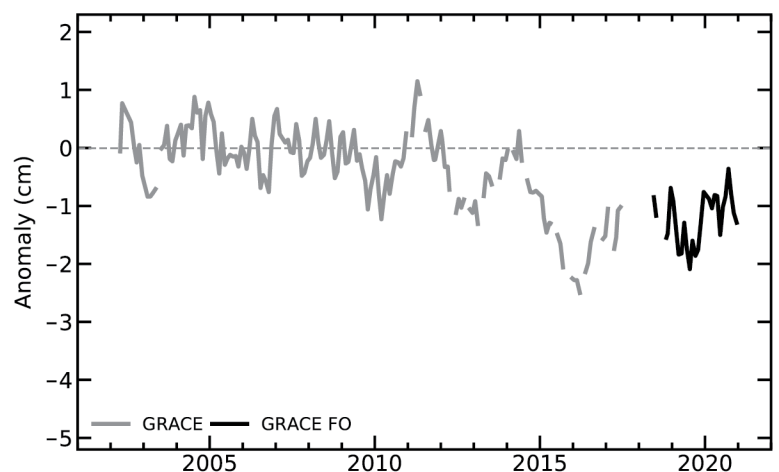


Fig. 2.32. Global average terrestrial water storage anomalies from GRACE (gray) and GRACE-FO (black), in cm equivalent height of water, relative to a 2004–09 mean baseline.

10) Soil moisture—R. van der Schalie, T. Scanlon, W. Preimesberger, A. J. Pasik, M. van der Vliet, L. Möisinger, N. J. Rodríguez-Fernández, R. Madelon, S. Hahn, M. Hirschi, R. Kidd, R. A. M. de Jeu, and W. A. Dorigo

Monitoring global soil moisture conditions is key for our understanding of the climate system, as soil moisture has a defining role in the energy and water fluxes at the land–atmosphere boundary. The global surface soil moisture conditions in 2020, as measured by satellite, were on average close to the climatology derived from historical data of the 1991–2010 period (Fig. 2.33), being slightly wetter than normal at the start of the year. Although still present, the large discrepancy between the Northern Hemisphere (NH) and Southern Hemisphere (SH) observed at the end of 2019 became slightly less pronounced in 2020 (Fig. 2.34). Drier-than-usual conditions persisted in the SH throughout 2020, and while the record wet peak of the NH at the end of 2019 weakened, it remained historically high in 2020. Plate 2.1r and Appendix Fig. A2.11a show the yearly and monthly soil moisture anomalies for 2020, respectively. There are strong spatial anomalies, which are discussed per individual continent.

In North America the year started with mostly wet conditions, but from the spring onward a strong deviation started to develop between the eastern United States, northwest Canada, and Alaska, with wet anomalies, and the Great Plains, southwestern United States, and Mexico, with strong dry anomalies. In the United States, this was linked to the precipitation anomalies (NOAA 2021), which show a similar pattern, with Nevada and Utah posting record lows. The peak in dry anomalies occurred in autumn and coincided with the record-breaking 2020 western United States wildfire season (see section 7b2 for details about the U.S. drought and wildfires). Consistent with the La Niña forming in the second half of the year (see section 4b), these dry conditions remained in place until the end of 2020.

For Europe an overall wet anomaly was recorded, with the only exception being the region around the Black Sea, which experienced drier-than-normal conditions. April diverted from this, with high-pressure systems dominating the weather in Europe, causing extraordinary warm, sunny, and dry conditions, and consequently led to a sharp decline in soil moisture conditions. The eastern part

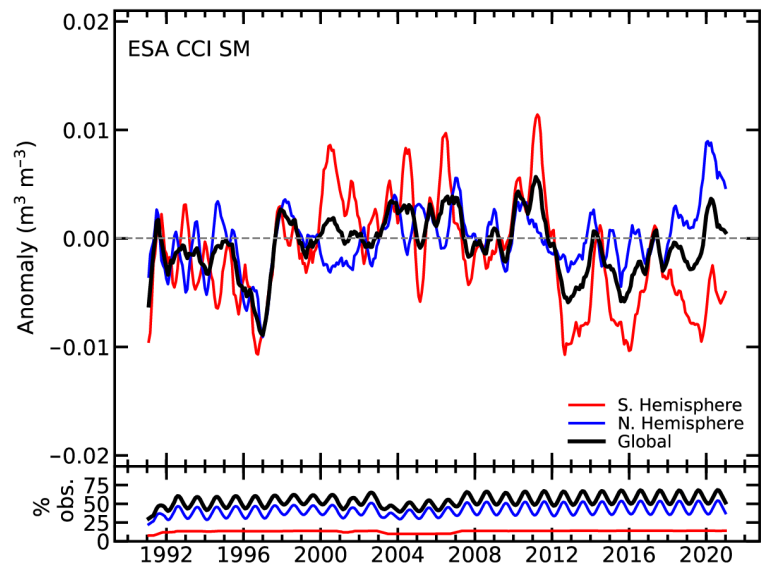


Fig. 2.33. Time series of global, NH, and SH surface soil moisture anomalies for 1991–2020 (upper, $\text{m}^3 \text{m}^{-3}$; 1991–2010 base period) and the percentage of valid retrievals over land (lower, %). Data are masked where no retrieval is possible or where the quality is not assured and flagged due to dense vegetation, frozen soil, radio frequency, interference, and so forth. (Source: ESA CCI Soil Moisture.)

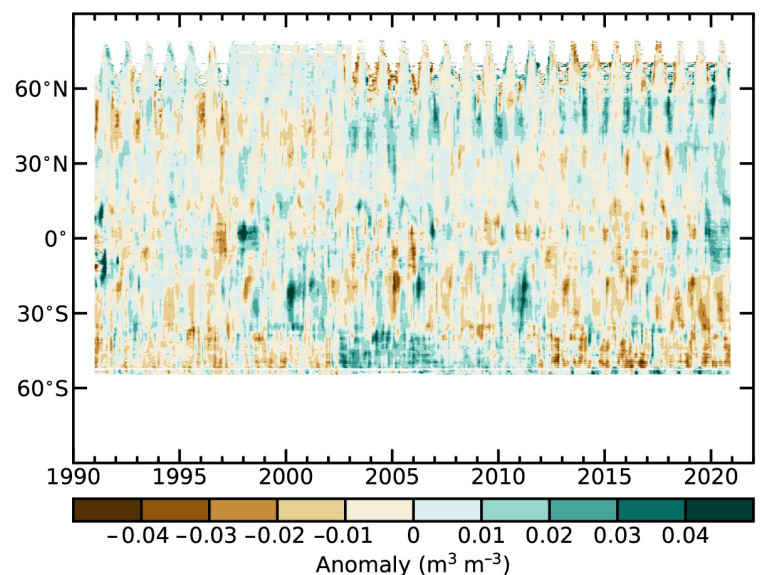


Fig. 2.34. Time–latitude diagram of surface soil moisture anomalies ($\text{m}^3 \text{m}^{-3}$; 1991–2010 base period). Data are masked where no retrieval is possible or where the quality is not assured and flagged due to dense vegetation, frozen soil, radio frequency, interference, and so forth. (Source: ESA CCI Soil Moisture.)

of Europe was the most affected, and related early season wildfires were recorded in multiple countries, including Germany, Poland, and Ukraine. From the second half of May onward, the moisture deficiencies returned to wetter-than-usual conditions for most of Europe (see section 7f).

South America experienced a widespread drought (see section 7d), which is clearly visible in the strong dry anomalies found over central Brazil, Bolivia, Paraguay, Uruguay, and Argentina. This situation was amplified by the emergence of La Niña (section 4b) in the second half of the year (Penalba and Rivera 2016). One region that clearly stands out with a severe dry anomaly is Brazil's Pantanal, known as the world's largest wetland, which endured its worst drought in almost 50 years and saw more than a quarter of its area burned. Eastern Brazil is the only major exception to this, with an opposite strong wet anomaly caused by heavy rains early on in the year. Wetter-than-usual conditions in this region generally coincide with La Niña events (see section 7d for details).

In eastern Africa an intensification of the already above-average wet conditions was observed. In the second half of 2019 above-average rainfall was recorded in this region, caused by a strong positive Indian Ocean dipole (Preimesberger et al. 2020), leading to above-average conditions in early 2020. This wet anomaly remained intact due to exceptionally heavy seasonal rains. The dry conditions in southern Africa alleviated in 2020, while southern Madagascar became much drier. The Sahel saw strong wet anomalies developing from August onwards, caused by heavy rainfall (see section 7e for details).

Asia mainly experienced wetter-than-normal soil moisture conditions throughout 2020, especially in India, China, Mongolia, North Korea, and South Korea, where unusually long and strong monsoon rains were reported (see section 7g). The countries in the Lower Mekong Basin continued to experience dry conditions, according to the Mekong River Commission, with below-average annual rainfall in 2019 and a shorter-than-normal monsoon season in 2020. In eastern Siberia, a widespread dry anomaly was observed in the region that experienced massive wildfires and a record heat wave (Overland and Wang 2020; see section 7g2).

While most of Australia still recorded below-average soil moisture conditions in 2020, it shifted considerably toward the long-term mean following the extraordinary low values seen in 2019 (Preimesberger et al. 2020). The only exception to this was southeastern Australia, where soil moisture increased to above-average conditions, providing some much needed relief from the multi-year drought (see section 7h4 for details).

The soil moisture anomalies used in this analysis were derived from the COMBINED product of ESA's Climate Change Initiative for Soil Moisture v05.3 (ESA CCI SM; Dorigo et al., 2017), which is a product that merges satellite soil moisture retrievals from multiple active (Wagner et al. 2013) and passive microwave (Van der Schalie et al. 2017) sensors to achieve the most accurate and consistent climate data record of soil moisture (representing the top ~5 cm of the soil). Merging is done based on both the quality and the temporal and spatial availability of observations, in order to achieve both an improved coverage and quality as compared to any single sensor dataset (Gruber et al. 2017, 2019).

11) Monitoring global drought using the self-calibrating Palmer Drought Severity Index—

J. Barichivich, T. J. Osborn, I. Harris, G. van der Schrier, and P. D. Jones

The sharp increase in global drought area based on different severities of the self-calibrating Palmer Drought Severity Index (scPDSI) that began in mid-2019 (Barichivich et al. 2020), continued in 2020, and reached a historical peak in October, with a small decrease afterward (Fig. 2.35). Around 6.8% of the global land area experienced extreme drought conditions in October, marking the third historical peak since 1950 after earlier peaks in October 1984 (7.7%) and October 1983 (7.3%). The extent of severe plus extreme drought conditions peaked at 15% of the global land area in October and November, matching the largest historical peaks of this drought severity in September 1983. Moderate or worse drought conditions peaked in August at 27.8% of the global

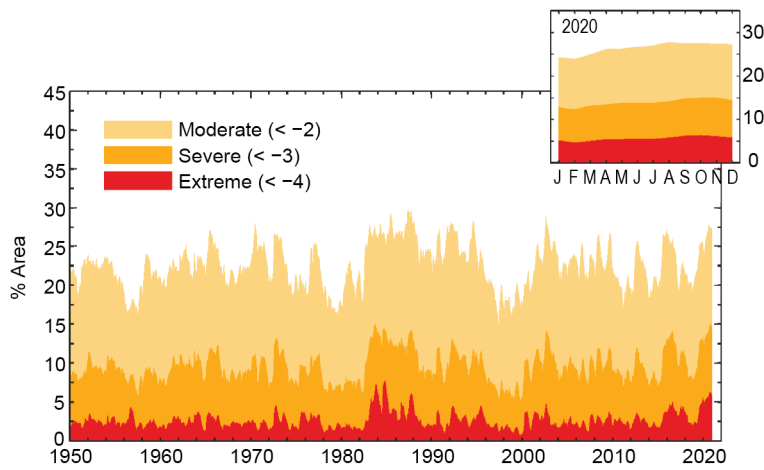


Fig. 2.35. Percentage of global land area (excluding ice sheets and deserts) with scPDSI indicating moderate (< -2), severe (< -3) and extreme (< -4) drought for each month of 1950–2020. Inset: Each month of 2020, denoted by first letter.

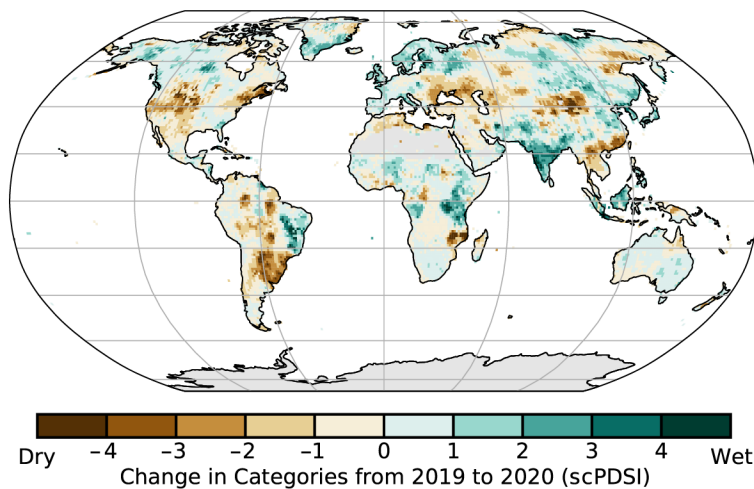


Fig. 2.36. Change in drought from 2019 to 2020 (mean scPDSI for 2020 minus mean scPDSI for 2019). Increases in drought severity are indicated by negative values (brown), decreases by positive values (green). No calculation is made where a drought index is meaningless (gray areas: ice sheets or deserts with approximately zero mean precipitation).

of disaster as many parts of the country had remained under extreme drought since 2018. Wet conditions from 2019 in most of Central and East Africa persisted in 2020 (Plate 2.1s), though moisture anomalies in these regions were uncertain due to sparse coverage of station data. Previous drought conditions also eased in Australia (Fig. 2.36) but most of the country remained under drought during 2020 (Plate 2.1s).

In Southeast Asia, extreme drought because of a weak monsoon season affected Malaysia, Myanmar, Thailand, Cambodia, Vietnam, and particularly Laos (Plate 2.1s), contributing to record low levels of the Mekong River. Extreme drought affected a vast region of northeastern Siberia. Dry conditions through the Sakha Republic, Russia, were associated with anomalously extensive wildfires that burned around 6 million ha. Most of the midlatitude belt from Mongolia in central Asia to western Europe and the Mediterranean saw moderate to extreme drought severity during 2020 (Plate 2.1s). Extreme drought in Europe was once again exacerbated by increasingly recurrent spring and summer heat waves combined with below-average spring precipitation and

land area, marking the fifth historical peak after June 1987 (29.6%) and the largest peak since August 2002 (29%).

Extensive severe-to-extreme drought conditions during 2020 affected most of the SH, southern and central Europe, the Middle East, and Southeast Asia (Plate 2.1s). Compared to 2019 (Barichivich et al. 2020), drought severity worsened to extreme in central South America (Fig. 2.36). Worsening drought during the dry season (austral winter and spring) contributed to ravaging fires across the Chaco floodplains and Pantanal wetland in northern Argentina and southern Brazil (Rodríguez 2020; see section 7d). The decadal drought in north-central Chile (Garreaud et al. 2017; Alvarez-Garretón et al. 2021) continued through its 11th year in 2020, with extreme conditions in the central and most populated region of the country (Plate 2.1s). In North America, the east–west moisture contrast observed across the United States since 2017 (Osborn et al. 2018; Barichivich et al. 2020) also persisted during 2020 (Plate 2.1s). Extensive wet conditions extended over the whole eastern half of the country and moderate but protracted drought prevailed in the west. Under these persistent drought conditions, California saw another extreme season of wildfires (Goss et al. 2020).

Previous drought conditions in southern Africa eased slightly in general, but worsened in northern Mozambique (Fig. 2.36). South Africa declared a state

antecedent soil moisture deficit. In the midst of two heat waves, France experienced its driest July on record. As in 2019, the most intense annual drought persisted across northern Germany and Poland, where a strong soil moisture deficit has developed since 2018 (Fig. 2.36). In contrast to central and southern Europe, wet conditions occurred across northern Europe from the British Isles to Fennoscandia and the Ural Mountains.

Hydrological drought results from a period of abnormally low precipitation, sometimes exacerbated by a concurrent increase in evapotranspiration (ET). Its occurrence can be apparent in reduced river discharge, soil moisture, and/or groundwater storage, depending on season and duration of the event. Here, a simple estimate of drought as measured by the scPDSI (Wells et al. 2004; van der Schrier et al. 2013) is presented, using global precipitation and Penman-Monteith Potential ET from an early update of the Climatic Research Unit gridded Time Series (CRU TS 4.05 dataset; Harris et al. 2020). Moisture categories are calibrated over the complete 1901–2020 period to ensure that “extreme” droughts and pluvials (wet periods) relate to events that do not occur more frequently than in approximately 2% of the months. This calibration affects direct comparison with other hydrological cycle variables in Plate 2.1 that use a different baseline period.

12) Land evaporation—D. G. Miralles, A. Koppa, D. Rains, H. E. Beck, and M. F. McCabe

The geographical patterns of land evaporation anomalies for the year 2020 are illustrated in Plate 2.1t. Several regions experienced anomalously low evaporation, including most of the west and central United States and parts of Russia and central Africa. Moreover, a strong negative anomaly was recorded in central South America, comprising Bolivia, Paraguay, and large parts of Brazil and Argentina. This anomaly reflected severe meteorological drought conditions in autumn, which propagated as agricultural and hydrological drought as the year progressed, leading to the unprecedented dry-out of the Parana River (see sections 2d11, 7d3). Likewise, the drought conditions in the west and central United States led to lower-than-usual evaporation across vast areas of the country. On the other side of the spectrum, regions of positive anomalies included the eastern half of the United States, western Europe, the Amazon basin, the Greater Horn of Africa, and India. In the first three instances, these anomalies related to higher-than-usual surface net radiation and air temperature (see sections 2b1, 2b3). In the case of Amazonia, they occurred despite the widespread meteorological drought conditions in South America, highlighting the positive influence that mild droughts can have on rainforest productivity and transpiration due to associated anomalies of incoming solar radiation (see e.g., Liu et al. 2017). In India, the seasonal monsoon was exceptionally wet in 2020 (see sections 4e, 7g4), which explains the large positive anomaly in evaporation over the region.

The global mean land evaporation in 2020 was the highest on record, exceeding the values of the 2010 La Niña year (Fig. 2.37). The trend of approximately 0.3 mm year^{-1} , according to the Global Land Evaporation Amsterdam Model (GLEAM) v3.5, falls within the range reported in recent literature (Zhang et al. 2016a; Brutsaert et al. 2017; Anabalón and Sharma 2017). This multi-decadal tendency to higher evaporation has been attributed to increasing global temperatures (Miralles et al. 2014) and greening (Cheng et al. 2017). The overall positive

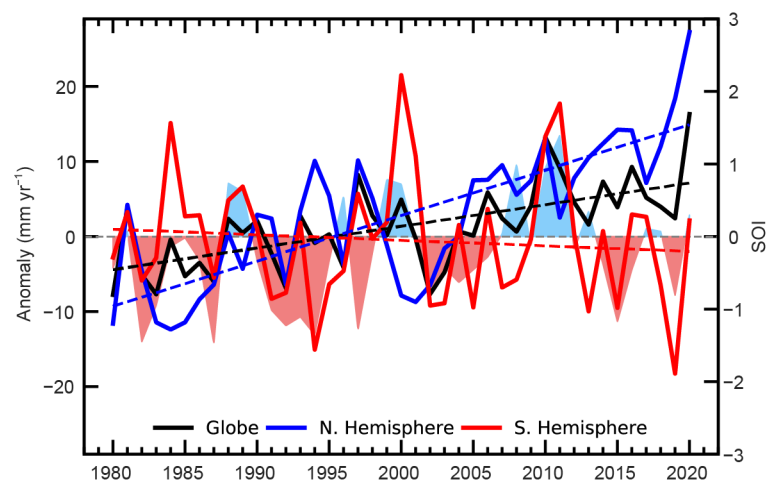


Fig. 2.37. Land evaporation anomaly (mm yr^{-1} ; 1981–2010 base period) for the NH, SH, and the entire globe (blue, red, and black solid lines, respectively). Linear trends in evaporation (dashed lines) and the Southern Oscillation Index (SOI) from CRU (right axis, shaded area) are also shown. (Source: GLEAM.)

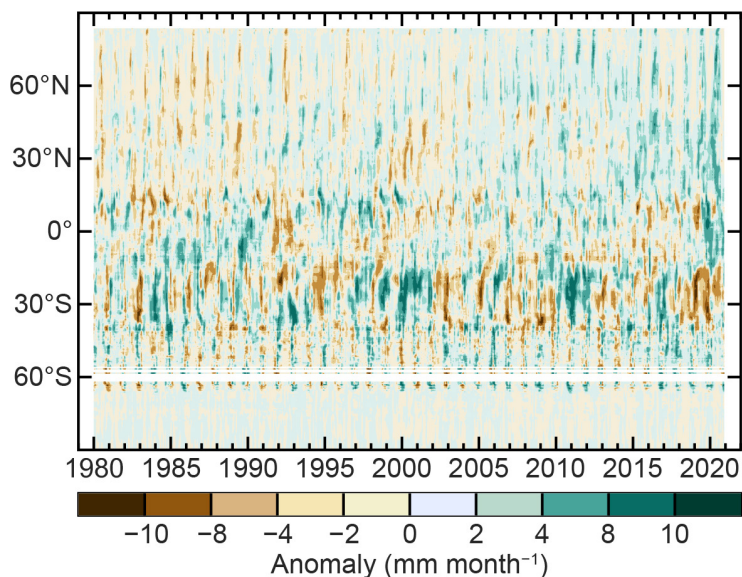


Fig. 2.38. Zonal mean terrestrial evaporation anomalies (mm month⁻¹; 1981–2010 base period). (Source: GLEAM.)

Evaporation is the phase change of liquid water into vapor. On average, two-thirds of the precipitation over land is evaporated (Dorigo et al. 2021). The ability to monitor its spatial and temporal dynamics is critical for agriculture and water management, as well as to diagnose climate changes. Its crucial climatic role, combined with an increased monitoring ability, has led to the recent consideration of land evaporation as an essential climate variable (ECV) by the World Meteorological Organization (WMO). This consideration was enabled by the proliferation, over the past 2 decades, of approaches dedicated to quantifying this flux at regional to continental scales based on satellite data (McCabe et al. 2016; Miralles et al. 2016). A handful of such approaches regularly update their simulations, including the Land Surface Analysis Satellite Applications Facility (LSA-SAF; Ghilain et al. 2011), the Atmosphere–Land Exchange Inverse (ALEXI; Anderson et al. 2011), and GLEAM (Miralles et al. 2011). The latter provides global-scale estimates and serves as the basis for the results presented in this section.

The accuracy of GLEAM v3 has been reported to be on the order of 0.7 mm day⁻¹ (unbiased root mean square error), and its correlation against in situ eddy covariance measurements is around 0.8 on average (Martens et al. 2017). Some climate zones are known to be challenging for models of terrestrial evaporation such as GLEAM (McCabe et al. 2017a; Fisher et al. 2017; Talsma et al. 2018): in semiarid regions, difficulties in capturing the response of evaporation to drought stress affect the accuracy, while for tropical forests, interception loss remains a key source of uncertainty. Moreover, reported global trends are affected by the poor representation of the effects of carbon dioxide (CO₂) and atmospheric aridity on stomatal conductance in current evaporation models (Zhang et al. 2016a). Further advances in the field of global terrestrial evaporation monitoring need to be realized in order to reduce these uncertainties. These may include developments in high-resolution optical platforms (McCabe et al. 2017b) and thermal missions such as ECOSTRESS (Fisher et al. 2020) or TRISHNA (Lagouarde et al. 2018).

e. Atmospheric Circulation

1) Mean sea level pressure and related modes of variability—R. Allan and B. Noll

Global atmospheric circulation patterns are dominated by the El Niño–Southern Oscillation (ENSO), measured in the atmosphere by the Southern Oscillation Index (SOI), and in the Northern Hemisphere (NH) by the Arctic Oscillation (AO) and the North Atlantic Oscillation (NAO); ENSO is measured in the Southern Hemisphere (SH) by the Antarctic Oscillation (AAO), also known as

global evaporation anomaly in 2020 resulted from the mean positive anomaly in the NH (Figs. 2.37, 2.38), likely associated to the unusually high temperatures across Eurasia (see sections 2b1, 2b3, 7f). The characteristic negative anomalies in land evaporation in the SH during El Niño years (Miralles et al. 2014; Martens et al. 2018) dissipated as the atmosphere returned to a neutral ENSO state during early 2020 and then shifted toward La Niña later in the year (see Southern Oscillation Index; SOI in Fig. 2.37). Nonetheless, evaporation in the SH remained below average, particularly during the first half of the year, and especially over the latitudes where the South American drought occurred (Fig. 2.38).

the Southern Annular Mode (SAM; see Fig. 2.39). A detailed summary of all the above modes, their definitions, and so forth, are given in Kaplan (2011).

In section 4b, 2019 to mid-2020 conditions are denoted as being ENSO-neutral, with evidence for the development of a La Niña by August–September 2020. However, from March–April 2018 until July–August 2020, monthly Niño-4 sea surface temperature (SST) anomalies (<https://www.cpc.ncep.noaa.gov/data/indices/sstoi.indices>) remained positive and thus passed one criterion for this period being indicative of a protracted El Niño episode (Allan et al. 2019). Different “flavors” of ENSO have been addressed in the literature (Capotondi et al. 2015; L’Heureux et al. 2017; Wang et al. 2017; Timmermann et al. 2018; Santoso et al. 2019), including protracted El Niño and La Niña episodes (Allan and D’Arrigo 1999; Allan et al. 2019). The latter are distinguished by periods of both sustained above-average SST anomalies in the Niño-4 region in the western equatorial Pacific (5°S–5°N, 160°E–150°W) and a persistent negative SOI. This pattern is similar to El Niño and La Niña episodes known as Modoki (Ashok et al. 2007; Weng et al. 2007; Ashok and Yamagata 2009) and they could be argued to be the same phenomenon (Allan et al. 2019; see also section 4b).

The second criteria, for the SOI to have acted similarly by being consistently negative (allowing for at most two consecutive months to have gone positive), occurred from June 2018 to August 2020 (Fig. 2.39). This period of continuously warm Niño-4 SST anomalies led to enhanced atmospheric convection over that region and the generation of a teleconnection that caused large-scale subsidence across eastern Australia in the early 2018 to mid-to-late 2020 period (Allan et al. 2021). Together with the continued impact of a positive Indian Ocean dipole (IOD) from late 2019, the warm Niño-4 SST teleconnection suppressed rainfall across southern and eastern Australia and New Zealand (Zhang et al. 2021; see also sections 2d5, 7h).

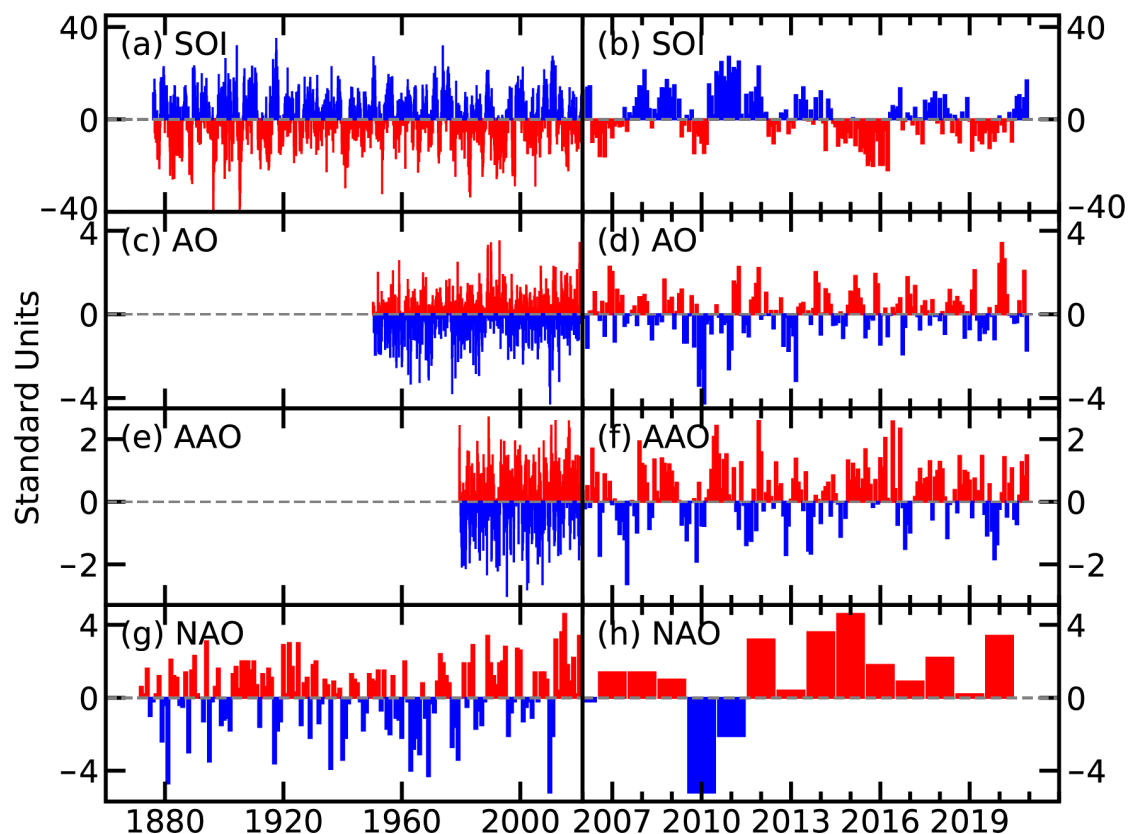


Fig. 2.39. Time series for modes of variability described using sea level pressure for the (left) complete period of record and (right) 2006–20. (a),(b) Southern Oscillation Index (SOI; provided by the Australian Bureau of Meteorology); (c),(d) Arctic Oscillation (AO; NOAA NCEP Climate Prediction Center); (e),(f) Antarctic Oscillation (AAO; NOAA NCEP Climate Prediction Center); (g),(h) winter (Dec–Feb) North Atlantic Oscillation (NAO) average (NCAR; presented for winter at the beginning of each year so winter 2020/21 is not shown).

In the NH, the last several boreal winters have displayed a variety of AO and NAO conditions (Figs. 2.39, 2.40). The 2019/20 boreal winter (Figs. 2.40b,e) was characterized by a persistent, mainly positive NAO, which led to mild conditions across the entire European region (see section 7f). This NAO phase contributed to heavy rainfall leading to flooding and a series of deep Atlantic cyclones, culminating in large storms in February 2020 (e.g., Storms Ciara and Dennis that impacted the United Kingdom; see section 7f2 for details). A strong stratospheric polar vortex dominated the winter, extending down through the troposphere and leading to abnormally cold air temperatures extending eastward from Alaska to Greenland and Svalbard (see section 5b).

During the 2020/21 boreal winter (Figs. 2.40c,f), the NAO was near average in December but shifted to negative throughout January, becoming the most negative observed in 11 years, and this extended through the first half of February 2021. In December 2020, Europe experienced its fourth-warmest December on record, with such conditions most pronounced over Scandinavia. Above-average precipitation occurred over most of western, northern, and southern Europe, with localized damage and flooding. This extended into January and February for western and central Europe, while temperatures were generally close to average across the continent, though colder in the west and north.

In the SH, the AAO was positive over 60% of the time during 2020, associated with a wide swath of higher-than-normal air pressure in the southwest Pacific (Figs. 2.40b,e), both early and again late in the year. This, along with the continued impact of a positive IOD event from late 2019, was associated with one of the worst droughts on record for northern New Zealand (NIWA 2020; see section 7h5). Slightly higher-than-normal air pressure in the Great Australian Bight also occurred as Australia recorded its fourth-warmest year on record (BoM 2020a; see section 7h4). Pressures were also above normal across South America, leading to Argentina's second-warmest year on record (see section 7d3). Influenced by the aforementioned IOD and the Pacific Niño-4 teleconnection, tropical cyclone activity was near or slightly above normal in the South Indian Ocean and southwest Pacific but below normal in the Australian region (see section 4g).

The frequently positive AAO also meant that pressures were below normal across Antarctica, which in September 2020 experienced an above-average maximum sea ice extent of 19.06×10^6 km² (NOAA 2021; see section 6f). Frequent patterns of lower-than-normal pressure near South Africa caused a wetter-than-normal winter during 2020 (see section 7e5), leading to the full recharge of Cape Town's dams for the first time in about 6 years (City of Cape Town 2021), following the severe drought of 2015–18 (Otto et al. 2018; section 2d9; SOTC 2018)

The AAO remained mostly positive during the 2020/21 austral summer (Figs. 2.40c,f), contributing to a drier-than-normal summer across New Zealand for the second consecutive year (NIWA 2021; see section 7h5). During December, Severe Tropical Cyclone Yasa formed as a pulse of enhanced convection crossed the tropical Pacific, becoming the South Pacific's strongest tropical cyclone since Winston in 2016 and making landfall in Fiji. Above-average sea surface temperatures to the north of Australia, as is typical during La Niña, led to above-normal rainfall totals in the tropical north and southeast, a marked change compared to the previous year (BoM 2021).

2) *Land and ocean surface winds*—C. Azorin-Molina, R. J. H. Dunn, L. Ricciardulli, C. A. Mears, T. R. McVicar, and J. P. Nicolas

The strengthening in global average surface wind speed over land (i.e., ~10 m above the ground) persisted in 2020, consistent with the reversal in global terrestrial winds observed since around 2010 (e.g., Azorin-Molina et al. 2020; Zeng et al. 2019; Fig. 2.41a). Prior to ~2010, a slowdown of terrestrial surface winds (termed stilling; Roderick et al. 2007) had dominated globally and regionally since the 1960s (e.g., Kim and Paik 2015; Azorin-Molina 2018a; Zeng et al. 2019). The global land average wind speed anomaly in 2020 with respect to the 1981–2010 climatology (Table 2.8) showed a positive value ($+0.052$ m s⁻¹), which was the highest over the last 2 decades. Europe ($+0.082$ m s⁻¹), Central Asia ($+0.178$ m s⁻¹), and East Asia ($+0.051$ m s⁻¹) continued with the recovery of

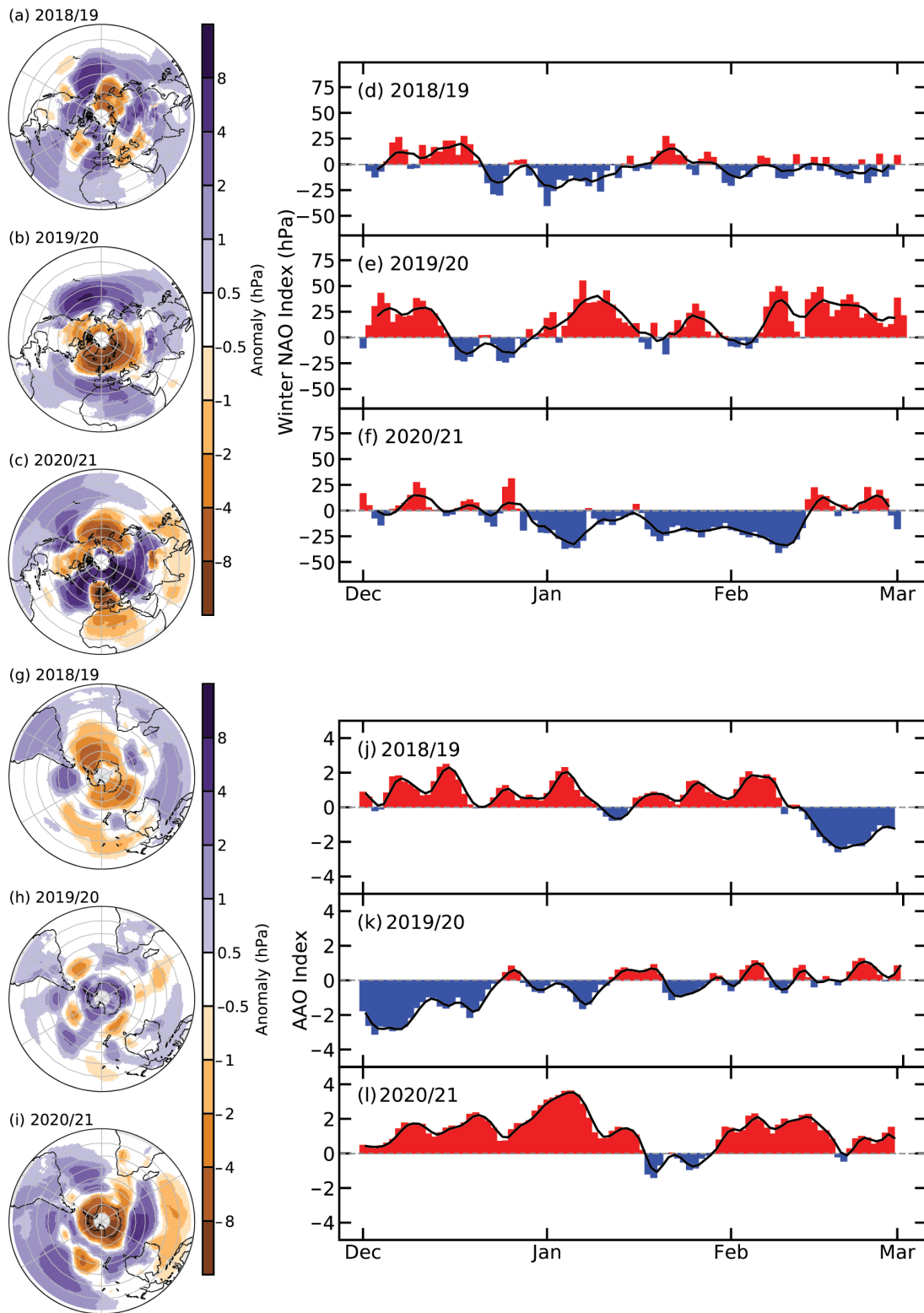


Fig. 2.40. Boreal winter sea level pressure anomalies (hPa; 1981–2010 base period) around the NH averaged over Dec–Feb for (a) 2018/19, (b) 2019/20, and (c) 2020/21 (constructed using ERA5, Hersbach et al. 2019). North Atlantic Oscillation (NAO) daily time series (hPa) for boreal winter (d) 2018/19, (e) 2019/20, and (f) 2020/21. The 5-day running mean is shown by the solid black line (constructed using Met Office MIDAS data). Austral summer sea level pressure anomalies (hPa; 1981–2010 base period) around the Southern Hemisphere (hPa; 1981–2010 base period) averaged over Dec–Feb for (g) 2018/19, (h) 2019/20, and (i) 2020/21 (constructed using ERA5). Antarctic Oscillation (AAO) daily time series (hPa) for austral summer (j) 2018/19, (k) 2019/20, and (l) 2020/21 (NOAA NCEP Climate Prediction Center).

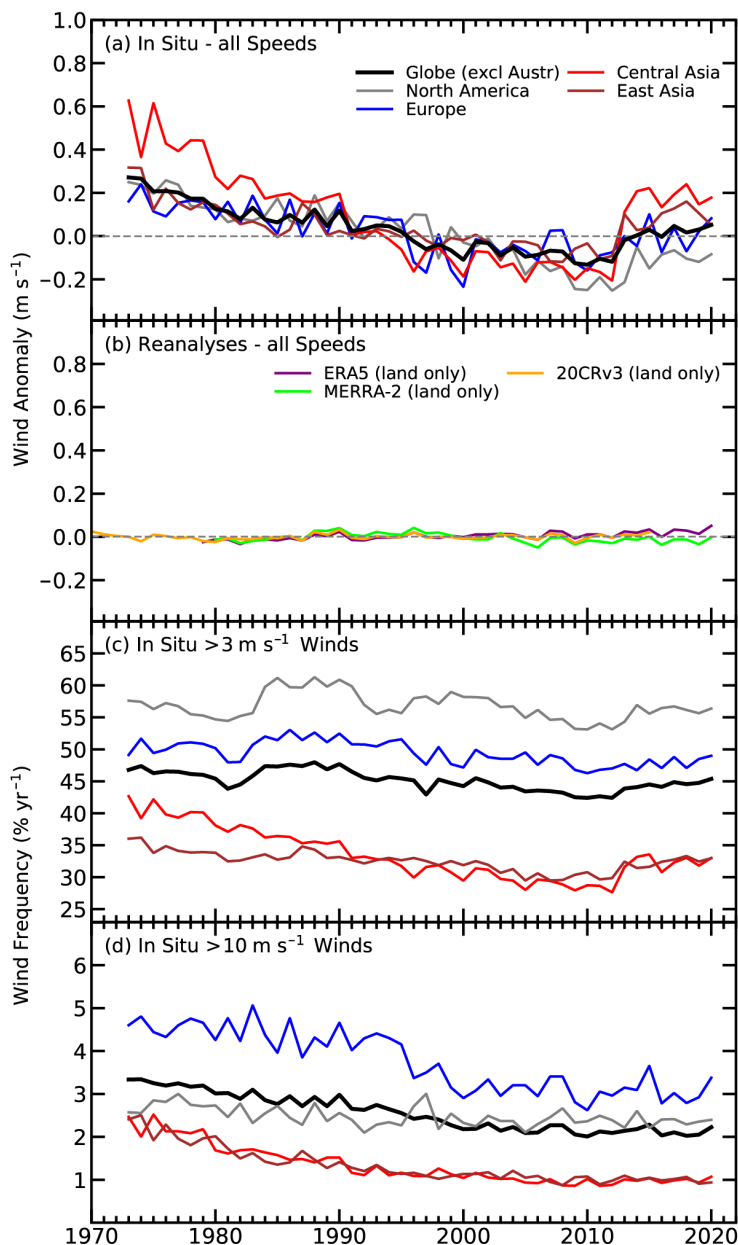


Fig. 2.41. Global (excluding Australia in panels [a], [c] and [d]) and regional annual time series of land surface wind speed anomaly (m s^{-1} ; 1981–2010 base period) using (a) HadISD3 (1973–2020) and (b) ERA5 (1979–2020), MERRA-2 (1980–2020), and 20CRv3 (1836–2015, only 1970–2015 shown here). HadISD3 occurrence frequencies (in %) for wind speeds (c) $> 3 \text{ m s}^{-1}$ and (d) $> 10 \text{ m s}^{-1}$.

compared to previous reports (Azorin-Molina et al. 2020) and especially when compared to the global average trend in observed terrestrial near-surface wind speeds of $-0.140 \text{ m s}^{-1} \text{ decade}^{-1}$ reviewed by McVicar et al. (2012). Regions also exhibited a weakening of negative trends and in the magnitudes of the 5th to 95th percentile confidence ranges because of the reversal of winds in the 2010s, with Central Asia and North America showing the strongest changes, and Europe and East Asia the weakest. As shown in Fig. 2.42, negative trends mostly occur across midlatitude regions of the NH, where most land-based observations exist. In the SH, ERA5 shows a greater dominance of weak positive trends over continents, particularly for Antarctica. In fact, the percentage of positive trends for stations and grid-points increased from 37% in 2019 to 42% because of the recovery of terrestrial winds, especially in Asia.

winds, while North America showed less negative anomalies (-0.084 m s^{-1}) compared to the lowest value (-0.253 m s^{-1}), which occurred in 2012. Wind speed frequencies above a moderate threshold ($> 3 \text{ m s}^{-1}$; Fig. 2.41c) exhibited a weak recovery in the last decade, with no trend for stronger wind speeds over land ($> 10 \text{ m s}^{-1}$; Fig. 2.41d).

The assessment of wind speed changes across land and ocean surfaces for the 1979–2020 period is based on two types of products. First, global in situ anemometer observations were obtained from the quality-controlled HadISD3 dataset (v3.1.1.2020f; 1973–2020; Dunn et al. 2012, 2016, 2019) for 2554 stations that had sufficient coverage during the 1981–2010 climatology period. Second, wind speed estimates from three gridded reanalysis products were used to cover Earth’s surface evenly: (i) ERA5 (1979–2020; Hersbach et al. 2020); (ii) MERRA-2 (1980–2020; Gelaro et al. 2017); and (iii) 20CRv3 (1836–2015; Slivinski et al. 2019). A major shortcoming of these products is their inability to capture the stilling and reversal phenomena shown by observations (Fig. 2.41b; Torralba et al. 2017; Ramon et al. 2019; Wohland et al. 2019); therefore, trends should be interpreted with caution.

Despite the rebound of surface winds observed since 2012, the sign of the long-term 1979–2020 trends of terrestrial wind speed remained negative. Globally, land surface winds weakened at a rate of $-0.056 \text{ m s}^{-1} \text{ decade}^{-1}$ (Table 2.8). This slowdown is of lesser magnitude compared to previous reports (Azorin-Molina et al. 2020) and especially when compared to the global average trend in observed terrestrial near-surface wind speeds of $-0.140 \text{ m s}^{-1} \text{ decade}^{-1}$ reviewed by McVicar et al. (2012).

Table 2.8. Global and regional statistics for land surface wind speed (m s^{-1}) using the observational HadISD3 dataset for 1979–2020.

Region	Mean 1981–2010 (m s^{-1})	Anomaly 2020 (m s^{-1})	Trend 1979–2020 ($\text{m s}^{-1} \text{ decade}^{-1}$) and 5th–95th percentile confidence range	Number of stations
Globe (excluding Australia)	3.324	+0.052	-0.056 (-0.065 → -0.040)	2554
North America	3.709	-0.084	-0.080 (-0.092 → -0.069)	578
Europe	3.677	+0.082	-0.042 (-0.053 → -0.032)	765
Central Asia	2.890	+0.178	-0.089 (-0.116 → -0.060)	258
East Asia	2.726	+0.051	-0.028 (-0.037 → -0.015)	459

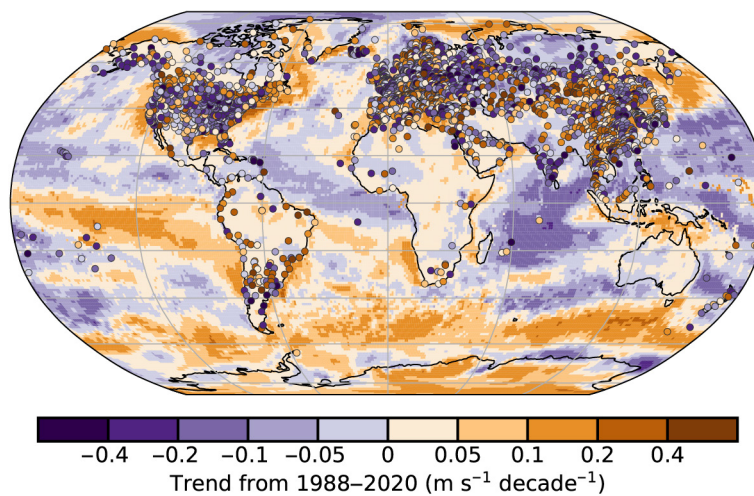


Fig. 2.42. Wind speed trends ($\text{m s}^{-1} \text{ decade}^{-1}$) for the observational HadISD3 dataset (circles) over land, and ERA5 reanalysis output over land/ice and RSS satellite radiometers (SSM/I, SSMIS, TMI, GMI, AMSR2, AMSR-E, and WindSat) over ocean for 1988–2020 (shaded areas).

Ocean surface winds for 1988–2020 were assessed using: (i) reanalyses (MERRA-2, ERA5, and 20CRv3) and (ii) satellite-based products including the Special Sensor Microwave/Imager (SSM/I), the Special Sensor Microwave Imager/Sounder (SSMIS), the Advanced Microwave Scanning Radiometer (AMSR-E and AMSR2), and microwave imagers TMI, GMI, WindSat, QuikSCAT, and ASCAT (Wentz 1997; Wentz et al. 2007, 2015; Ricciardulli and Wentz 2015; Ricciardulli 2016). For 2020, satellite radiometers showed a near-zero global mean wind speed anomaly over ocean (-0.013 m s^{-1} ; Fig. 2.43), consistent with the satellite scatterometers (ASCAT) and with MERRA-2; whereas ERA5 shows a positive anomaly and biases compared to the other products. In general, the magnitudes of any positive wind speed anomalies in 2020 were weak (Plate 2.1v), except in the Arctic Ocean, the North Atlantic Ocean, the southern fringe of both the South Pacific and South Atlantic Oceans, and the Bering Sea. In contrast, negative wind speed anomalies dominated tropical and subtropical ocean surfaces in 2020, particularly in the Atlantic and Indian Oceans. The ocean wind speed trend from satellite radiometers is nearly zero ($+0.002 \text{ m s}^{-1} \text{ decade}^{-1}$) for 1988–2020 (Fig. 2.42), with a dominance of negative regional trends (moderate ones in the Indian Ocean and western Pacific Ocean), except for the positive trends found in the Southern Ocean, and the Pacific and Atlantic trade winds south of the equator (Young and Ribal 2019)

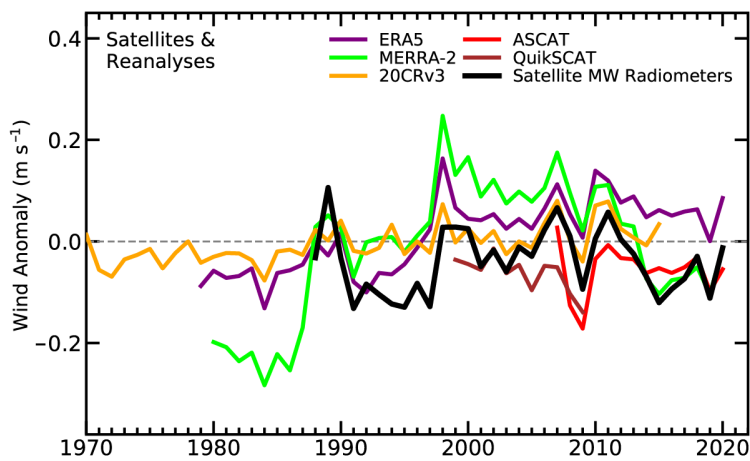


Fig. 2.43. Annual global mean wind speed anomalies (m s^{-1} ; 1981–2010 base period) over the ocean from satellite radiometers and scatterometers, and reanalysis outputs. The values for the first year of both ASCAT and QuikSCAT are based on 6 months of deseasonalized data (monthly anomaly compared to monthly climatology).

Decadal-scale variations and trends of land and ocean surface winds are likely driven by internal decadal ocean–atmosphere oscillations (Zeng et al. 2019) and anthropogenic greenhouse gas forcing (Deng et al. 2021), respectively, with vegetation growth (Vautard et al. 2010), urbanization (Chen et al. 2020), and instrumentation issues (Azorin-Molina et al. 2018b) having a lesser impact. After decades of a slowdown of winds over land, the recent reversal, which continued in 2020, is increasing potential wind energy across the world (Zeng et al. 2019). The most challenging research questions now are to predict how long the positive anomalies will last and to estimate future wind projections given a changing climate with a direct impact on the wind energy sector.

3) Upper air winds—L. Haimberger, M. Mayer, and V. Schenzinger

The 2020 global mean wind speed anomaly at 850 hPa has slightly recovered from a minimum in late 2019 to values close to the long term (1981–2010) average (Fig. 2.44). However, the clear positive trend over the past 40 years remains in all four included reanalyses. The wind time series start now in 1950, thanks to the backward extension of ERA5 (Bell et al. 2021). In the NH extratropics, there is no evidence of wind stilling at 850 hPa, in contrast to surface winds (section 2e2).

Plate 2.1w shows the meridional (positive northward) wind anomaly averaged over September–December 2020 at 850 hPa. That period showed a pronounced wave train with wavenumber 4 around 55°N , with particularly strong southerly winds of up to 4 m s^{-1} in the 4-month average over northeastern Europe and far eastern Newfoundland. This pattern, together with ongoing climate change, led to the highest autumn temperatures on record in this region (Copernicus 2021). The dynamics that led to this pattern need to be fully investigated but are likely an example of enhanced resonance of Rossby waves in a warming climate (Petoukhov et al. 2013; Mann et al. 2019; Wills et al. 2019).

Turning to higher altitudes, we first assess the impact of tropical climate anomalies on upper-tropospheric circulation through inspection of 200-hPa

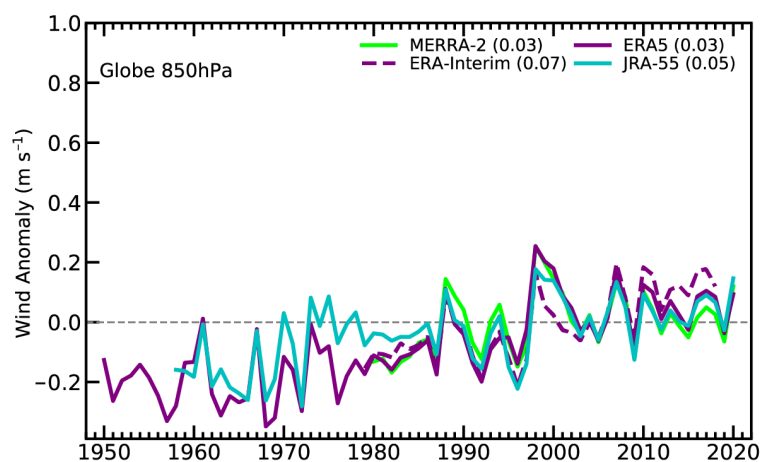


Fig. 2.44. Annual anomalies of global mean wind speed (m s^{-1} ; 1981–2010 base period) at 850 hPa from four reanalyses (ERA5, ERA-Interim, MERRA-2, JRA-55). The numbers in parentheses are linear trends in $\text{m s}^{-1} \text{ decade}^{-1}$ for the period 1980–2020. The y-axis range matches that for the land surface winds (Fig. 2.41).

velocity potential. After a strong positive IOD event in 2019, IOD conditions returned to neutral in 2020 (section 4f). In the Pacific, cold equatorial sea surface temperature (SST) anomalies appeared from early boreal summer 2020 and developed into a moderate La Niña event had formed by the end of the year (if defined by ONI index as > -1.0 value, see section 4b).

Figure 2.45 depicts the imprint of these major tropical climate anomalies on upper air circulation. In August–September (Fig. 2.45a), negative velocity potential anomalies were present over the tropical Indian Ocean, with local minima over the northwestern and southeastern parts of the basin, indicating widespread, positive upper-air divergence anomalies. This differs from 2019 when there was a clear east–west dipole in the Indian Ocean velocity potential anomalies. An explanation for this difference is that SSTs were above normal both in the western and eastern equatorial Indian Ocean in 2020 (suggestive of a positive state of the Indian Ocean Basin Mode; Yang et al. 2007) but with more pronounced anomalies in the east (see also section 4f). The generally positive SST anomalies were favorable for enhanced upper-air divergence. At the same time, positive velocity potential anomalies were present over the western Pacific, consistent with reduced atmospheric convection associated with the developing La Niña event.

Velocity potential anomalies shifted eastward in October–November (Fig. 2.45b). Negative anomalies were centered over the Indo-Pacific Warm Pool. This is consistent with enhanced atmospheric convection over the eastern Indian Ocean associated with positive SST anomalies in this region. Moreover, in October–November changes to the Pacific Walker Circulation related to the negative SST anomalies of the now more mature La Niña event were centered farther eastward in the Pacific. This is reflected in positive velocity potential anomalies centered east of the date line arising from suppressed convection and likely contributed to the negative anomaly over the Indo-Pacific Warm Pool.

La Niña years provide more favorable conditions for Atlantic hurricanes, and indeed the late 2020 hurricane season was exceptionally intense (see section 4g). The imprint of the strong

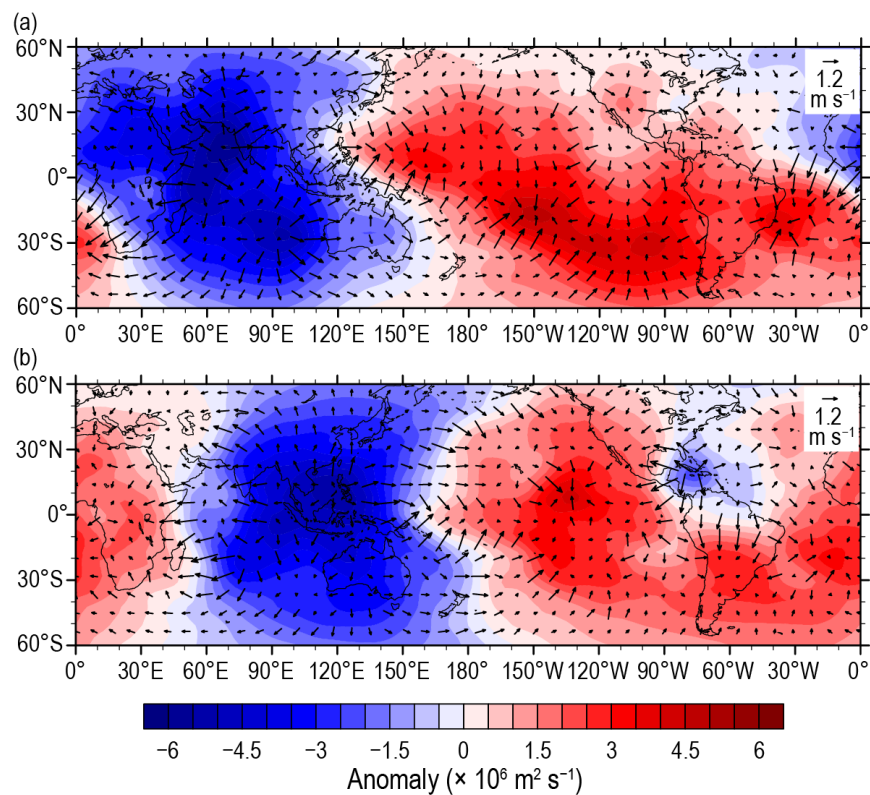


Fig. 2.45. Anomalous 200-hPa velocity potential ($\times 10^6 \text{ m}^2 \text{ s}^{-1}$) and divergent winds (m s^{-1}) averaged over (a) Aug–Sep and (b) Oct–Nov 2020 (1981–2010 base period) based on ERA5 data.

hurricane activity can also be seen in Fig. 2.45b, with a prominent negative anomaly over the Caribbean. Such a pattern favored hurricane activity, but likely was also enhanced by the strong upper-air divergence in the hurricanes once they had formed.

After the anomaly around the 2015/16 year transition (Osprey et al. 2016), the quasi-biennial oscillation (QBO) saw its second disruption in 2019/20. In both cases, a thin layer of westerlies appeared to be split off the descending westerly phase around 40 hPa and propagated upward through the stratosphere (Fig. 2.46). While these winds were overall weaker in the recent anomaly, the disruption, as measured by the explained variance of the first two empirical orthogonal functions (EOFs), was much stronger (Anstey et al. 2020). Typically, the first two EOFs explain around 90% of the vertical wind variance. In the 2015/16 disruption, this value dropped to around 60% and in 2019/20 down to 20%.

While the anomaly in 2015/16 was associated with unusually high wave-momentum fluxes from the NH (Osprey et al. 2016), the 2019/20 anomaly was probably caused by meridional momentum fluxes from the SH (Anstey et al. 2020). The QBO pattern stabilized again around May 2020. The combination of the QBO phase shifts following the disruptions results in the phase again aligning with the expectation from the historical record (Anstey et al. 2020). However, with long-term changes in the tropical circulation like increased upwelling, it remains to be seen whether the QBO returns to its regular cycle for a longer period of time.

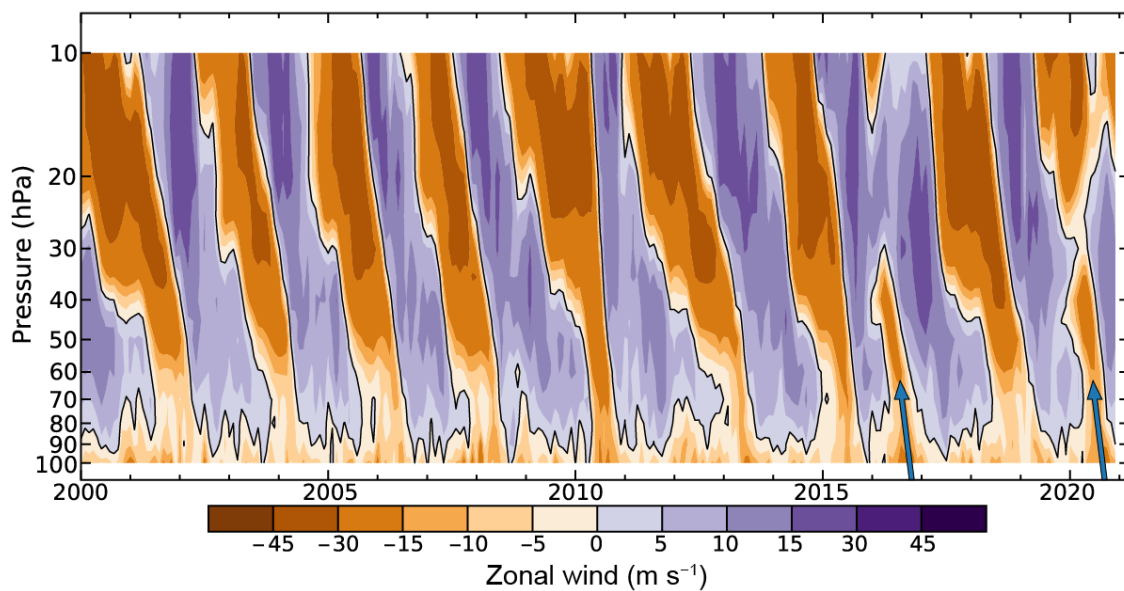


Fig. 2.46. Monthly mean stratospheric zonal winds (m s^{-1}) at Singapore with 2016 and 2020 highlighted by arrows (FU Berlin, 2021). Purple shades show westerly winds; orange colors show easterly winds.

f. Earth radiation budget

1) Earth radiation budget at top-of-atmosphere—P. W. Stackhouse Jr., T. Wong, P. Sawaengphokhai, A. C. Wilber, S. K. Gupta, D. P. Kratz, and N. G. Loeb

The energetic state of the Earth–atmosphere system is defined by the balance of the incoming total solar irradiance (TSI), the reflected shortwave (RSW), and the outgoing longwave radiation (OLR) from Earth. This balance defines Earth’s radiation budget (ERB) at the top of the atmosphere (TOA) and its regional distribution drives atmosphere and ocean circulations.

An analysis of all Clouds and the Earth’s Radiant Energy System (CERES) ERB measurements (Table 2.9) shows that 2020 global annual mean OLR increased by $\sim 0.20 \text{ W m}^{-2}$ and RSW increased by $\sim 0.40 \text{ W m}^{-2}$ relative to their corresponding values in 2019 (rounded to nearest 0.05 W m^{-2}).

Table 2.9. Global annual mean top of atmosphere (TOA) radiative flux changes (W m^{-2}) between 2019 and 2020, the 2020 global annual mean radiative flux anomalies relative to their corresponding 2001–19 mean climatological values (also shown), and the 2-sigma interannual variabilities of the 2001–19 global annual mean fluxes for the outgoing longwave radiation (OLR), total solar irradiance (TSI), reflected shortwave (RSW), absorbed shortwave (SW; TSI minus RSW), absorbed SW (TSI – RSW), and total net fluxes (TSI minus RSW minus OLR)). All flux values have been rounded to the nearest 0.05 W m^{-2} and only balance to that level of significance.

	One-Year Change (2020 minus 2019) (W m^{-2})	2020 Anomaly (Relative to Climatogy) (W m^{-2})	Climatological Mean (2001–19) (W m^{-2})	Interannual Variability (2001–19) (W m^{-2})
OLR	0.20	+0.65	240.20	± 0.65
TSI	0.05	-0.05	340.00	± 0.15
RSW	0.40	-0.70	99.00	± 1.00
TSI – RSW	-0.40	+0.65	241.00	± 0.95
Net	-0.60	0.00	0.80	± 0.80

Over the same timeframe, the global annual mean TSI increased by 0.05 W m^{-2} , showing a steady increase, possibly toward the next solar maximum. The sum of these components amounts to a decrease of $\sim 0.60 \text{ W m}^{-2}$ in the global annual mean total net radiation relative to 2019. Figure 2.47 shows the annual mean regional difference maps in the OLR and RSW between 2019 and 2020. The largest reductions in OLR and increases in RSW are observed over the tropical Indian Ocean extending over Indonesia and southeastward over and east of Australia (a recovery from a 2019 Indian Ocean dipole event; see sections 2a1, 2d7, 4f), as well as a feature in the tropical Atlantic. The largest increases in OLR and reductions in RSW were observed in the tropical western and south-central Pacific regions. These regional differences appear associated with the change from near-neutral ENSO conditions at the end of 2019 to La Niña conditions by August 2020 that persisted through the end of the year (see section 2e1, 4b). Also noted are broad areas of moderate OLR increase and RSW decrease over both North and South America corresponding to reduced cloudiness and increased surface warmth in these regions (see sections 2d4, 2d7, 2d11 and 2b1). Relative to the 2001–19 climatological average, the 2020 global annual mean flux anomalies are $+0.65$, -0.05 , -0.70 , and $+0.00 \text{ W m}^{-2}$

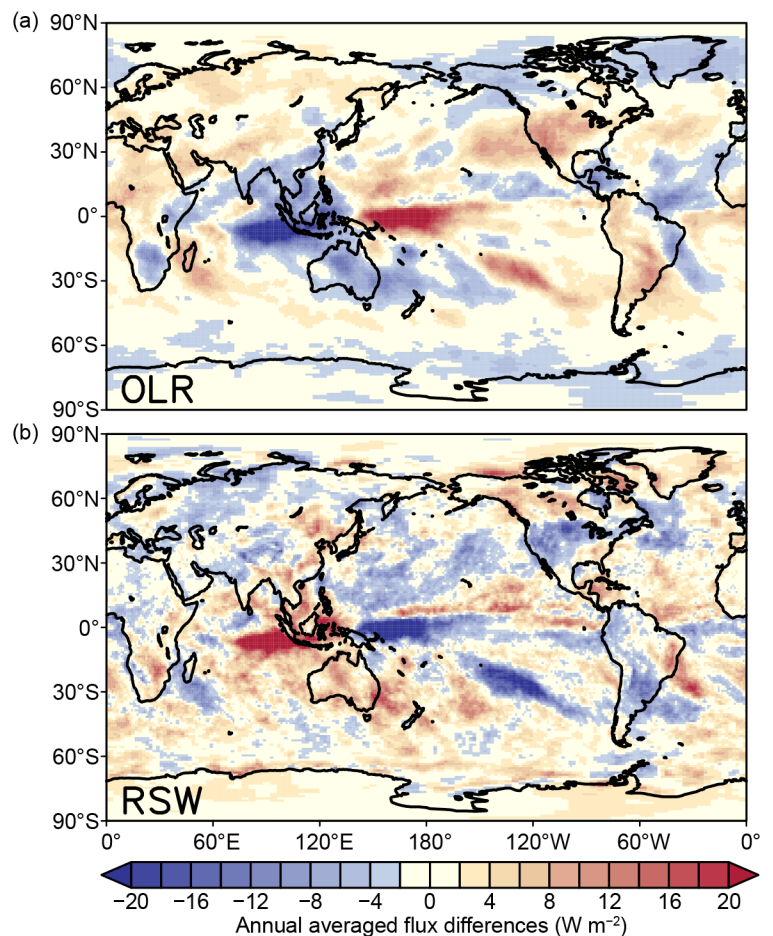


Fig. 2.47. Annual average top of atmosphere (TOA) flux differences between 2020 and 2019 (W m^{-2}) for the (top panel) OLR and (bottom panel) TOA reflected shortwave (RSW). The annual mean maps for 2020 were derived after adjusting December 2020 FLASHFlux v4A using the difference between EBAF and FF v4A in 2019. The pattern of differences shows several significant features including changes over the Indian and tropical western and south-central Pacific Oceans. The tropical Indian/Pacific Ocean pattern is dominated by an atmospheric shift from neutral ENSO conditions during the latter half of 2019 and early 2020 to La Niña conditions that persisted from Aug through Dec 2020 and also includes a transition from an IOD event in 2019 (see section 4f).

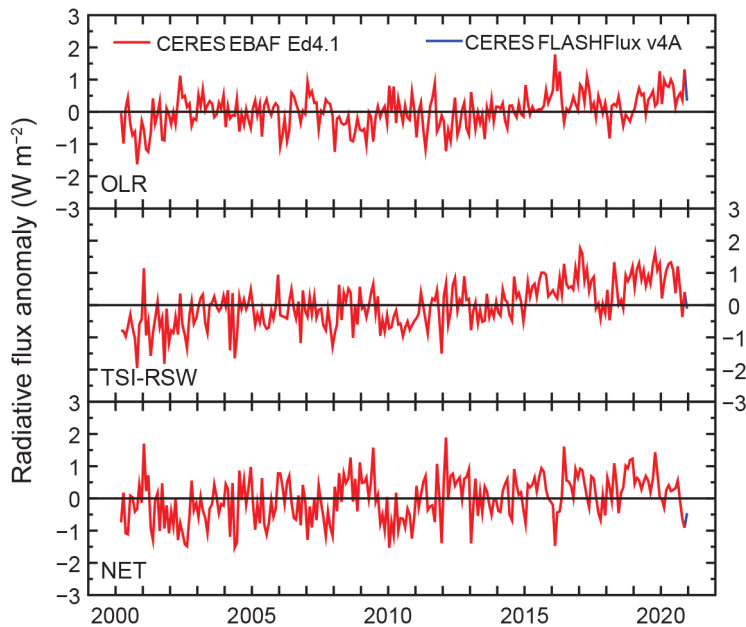


Fig. 2.48. Time series of global monthly mean deseasonalized anomalies (W m^{-2}) of top-of-atmosphere (TOA) Earth radiation budget for outgoing longwave radiation (OLR; upper); absorbed shortwave (total solar irradiance [TSI] minus reflected shortwave [RSW]; middle); and total net (TSI minus RSW minus OLR; lower) from Mar 2000 to Dec 2020. Anomalies are relative to their calendar month climatology (2001–19). Time series shows the CERES EBAF Ed4.1 1-Deg data (Mar 2000–Nov 2020) in red and the CERES FLASHFlux version 4A data (Dec 2020) in blue; see text for merging procedure. (Sources: <https://ceres-tool.larc.nasa.gov/ord-tool/jsp/EBAF41Selection.jsp> and https://ceres-tool.larc.nasa.gov/ord-tool/jsp/FLASH_TISASelection.jsp.)

anomaly, which is calculated from the absorbed SW anomaly minus the OLR anomaly, began 2020 with a value of -0.05 W m^{-2} , reached a maximum value of $+0.75 \text{ W m}^{-2}$ in August, then decreased rapidly to about -0.90 W m^{-2} in November, ending the year at -0.45 W m^{-2} . The positive OLR anomalies approximately balanced the positive absorbed SW anomalies in 2020, resulting in a global annual mean total net anomaly of 0.0 W m^{-2} . The total net anomaly decreased by $\sim 1.65 \text{ W m}^{-2}$ between August and November 2020. Although this corresponds to the onset of the 2020 La Niña, more analysis is required for definitive attribution. Long-term trend analyses that include the last month of the merged dataset are discouraged because of the natural fluctuation in ERB components, uncertainty from the data-merging process, and potential for drift in the FLASHFlux product.

The TSI data used in this study are provided by the Total Irradiance Monitor aboard the Solar Radiation and Climate Experiment (SORCE) mission (Kopp and Lean 2011) and the Royal Meteorological Institute of Belgium composite dataset (Dewitte et al. 2004), both renormalized to the SORCE Version 15. Starting in February 2020, data from the Total Solar and Spectral Irradiance Sensor-1 (TSIS-1, Coddington, 2017) mission on board the International Space Station is normalized to SORCE Version 15. The RSW and OLR data were obtained from the CERES instruments (Wielicki et al. 1996, 1998) aboard *Terra* and *Aqua* spacecraft. The time series (Fig. 2.48) were constructed from the CERES EBAF (Energy Balanced And Filled) Ed4.1 product (Loeb et al. 2009, 2012, 2018) for March 2000–November 2020 and from the CERES Fast Longwave and Shortwave Radiative Fluxes (FLASHFlux) version 4A product (Kratz et al. 2014) for December 2020. The normalization of the FLASHFlux data (Stackhouse et al. 2016) results in 2-sigma monthly uncertainties of ± 0.47 , ± 0.07 , ± 0.24 , and $\pm 0.58 \text{ W m}^{-2}$ for the OLR, TSI, RSW, and total net radiation, respectively.

for OLR, TSI, RSW, and total net flux, respectively (Table 2.9), all at or within their corresponding 2-sigma interannual variability (Table 2.9).

The global monthly mean anomaly time series of TOA fluxes (Fig. 2.48) reveal that the global monthly mean OLR anomaly remained positive throughout the first half of 2020 at a level of about $+1.00 \text{ W m}^{-2}$. During the second half of 2020, the OLR anomalies remained positive, but decreased to less than $+0.50 \text{ W m}^{-2}$ except for November, which spiked to $+1.30 \text{ W m}^{-2}$. This large November OLR anomaly is consistent with the values obtained from the NOAA HIRS OLR (Lee and NOAA CDR Program 2011) and NASA AIRS OLR (Susskind et al. 2012) datasets (not shown). The global monthly mean absorbed shortwave (SW; TSI minus RSW) anomaly began 2020 at $+0.20 \text{ W m}^{-2}$, peaked in May at around $+1.35 \text{ W m}^{-2}$, and then decreased sharply after August, ending the year with a value of -0.10 W m^{-2} . For the year as a whole, the 2020 global annual mean absorbed SW anomaly was $+0.65 \text{ W m}^{-2}$.

The global monthly mean total net

2) *Mauna Loa apparent transmission*—J. A. Augustine, K. O. Lantz, and J.-P. Vernier

Initiated in 1958 as part of the International Geophysical Year, one of the longest records of atmospheric transmission, i.e., the percent of top of atmosphere (TOA) solar radiation that reaches the surface, has been recorded on the island of Hawaii at 3397 m above mean sea level, just below the summit of the Mauna Loa volcano. Because of the clean nature of the atmosphere over Mauna Loa, its elevation and vertical separation from the marine boundary layer, atmospheric transmission there is considered a proxy of stratospheric aerosol loading. One exception is the effect from the annual transport of Asian dust over Hawaii at high-tropospheric levels in springtime (Bodhaine et al. 1981).

The updated time series of “apparent” transmission (see definition below) through 2020 is presented in Fig. 2.49. Plotted are monthly averages and a 6-month-smoothed fit that reveals intra-annual variability caused mainly by springtime Asian dust. The most pronounced features are deviations caused by three major volcanic eruptions: Agung, Indonesia, in 1963; El Chichon, Mexico, in 1982; and Pinatubo, Philippines, in 1991. Resultant deep reductions in transmission are followed by slow recoveries that last up to 8 years and reflect the long residence time of aerosols in the stratosphere. For reference, the horizontal dashed line in Fig. 2.49 represents the average transmission prior to Agung (0.934) when the stratosphere was exceptionally clean. That level of stratospheric purity has been achieved only briefly over the 62-year time series, most notably in the late 1970s and from the late 1990s into the early 2000s. A steady decrease from 2002 to 2010 is associated with a series of tropical and high-latitude volcanic eruptions (Andersson et al. 2015; Vernier et al. 2011), each of which affected the stratosphere for a year or less (Augustine et al. 2020). Apparent transmission over Mauna Loa increases after 2010 and remains relatively stable through 2018. A slow decline is apparent through 2019 from the eruptions of Mt. Raikoke on the Kuril Islands north of Japan in June 2019 and Mt. Ulawun in Papua New Guinea in June and August 2019.

The only major volcanic event in 2020 was the explosive eruption of Mt. Taal in the Philippines on 12 January, but there is no indication from the Cloud-Aerosol Lidar with Orthogonal Polarization (CALIOP) space-borne lidar that it significantly affected the stratosphere. The most notable aerosol events of 2020 were wildfires in Australia from December 2019 to early 2020 (Kablick et al. 2020) and the record-setting Saharan dust event in June (Francis et al. 2020). However, neither affected Mauna Loa. Stratospheric aerosols from Australian wildfire pyrocumulus had limited cross-equatorial transport, and Saharan dust reached just ~3–7 km in altitude and only affected the troposphere in the low-latitude North Atlantic Ocean, the Caribbean, and eastern North America (Francis et al. 2020). Aerosols from wildfire pyrocumulus in the western United States that began in August 2020, especially in central California, were observed in the lower stratosphere in September by CALIOP and in September and October by SAGE III aboard the International Space Station (see <https://appliedsciences.nasa.gov/our-impact/news/californias-creek-fire-blasts-smoke-stratosphere>). Satellite visualization shows a relatively small amount of that smoke reaching Hawaii in late August and September 2020 and is probably partially responsible for the transmission decrease in September

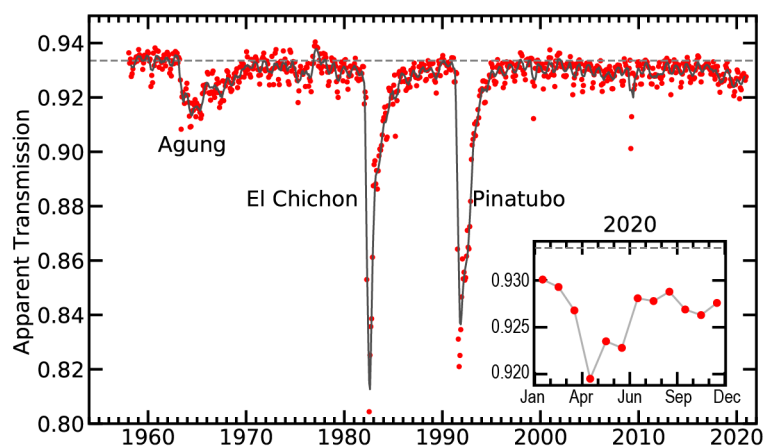


Fig. 2.49. Apparent transmission at Mauna Loa, Hawaii, from 1958 through 2020. Red dots are monthly average morning transmissions, the gray curve is a fit with a 6-month smoother applied, and the dashed horizontal line is the average transmission for the clean period before the eruption of Agung. Insert is an enlargement of the newest data for 2020.

apparent in the inset of Fig. 2.49. Residual effects from the 2019 eruptions of Raikoke and, to a lesser extent Ulawun, were likely responsible for maintaining a relatively low transmission of 0.9265 ± 0.0029 in 2020. CALIOP shows those stratospheric volcanic plumes much reduced from 2019 levels but still present at the latitude of Mauna Loa through October 2020, which is the extent of CALIOP data analyzed. Transmission reached the annual minimum of 0.919 in April, presumably from the addition of springtime Asian dust.

Atmospheric transmission is defined as the ratio of the solar beam intensity at the surface to that at the top of the atmosphere over a vertical path. Given the impracticality of that calculation, Ellis and Pueschel (1971) showed mathematical equivalency of vertical transmission to the ratio of surface solar beam measurements at two distinct integer path lengths. However, because broadband transmission is influenced by path length, that calculation is referred to as “apparent” transmission. Here, a representative daily apparent transmission is the mean of three successive ratios of pyrhelimeter measurements at 2, 3, 4, and 5 atmospheric path lengths. Only morning data are considered because upslope winds typically contaminate afternoon measurements with marine-layer aerosols. Individual points in Fig. 2.49 represent the average of all acceptable morning transmissions within a particular month. Neither the radiometer calibration factor nor the solar intensity at TOA are needed, resulting in a precise time series back to 1958.

g. Atmospheric composition

1) Long-lived greenhouse gases—X. Lan, P. Tans, B. D. Hall, G. Dutton, J. Mühle, J. W. Elkins, and I. Vimont

Increased atmospheric burdens of long-lived greenhouse gases (LLGHGs) are the dominant driver of warming climate (IPCC AR5 2013). Carbon dioxide (CO_2), methane (CH_4), and nitrous oxide (N_2O) are naturally present in the atmosphere but have been greatly increased by human activity in the industrial era.

Systematic measurements of atmospheric CO_2 began at Mauna Loa, Hawaii (MLO), in 1958, when CO_2 was approximately 315 ppm (parts per million by moles in dry air). In 2020, annually averaged CO_2 at MLO reached 414.2 ± 0.1 ppm (all uncertainties are reported as 1 sigma [σ] in this section), while globally averaged CO_2 derived from remote marine boundary layer (MBL) measurements from NOAA’s Global Greenhouse Gas Reference Network (GGGRN) was 412.5 ± 0.1 ppm (Fig. 2.50a; gml.noaa.gov/ccgg/trends). Both levels were the highest since the systematic measurements of CO_2 started. The globally averaged level represents an increase of 48% over pre-industrial values of 278 ppm (Etheridge et al. 1996). Annual growth in global mean CO_2 has accelerated from 0.8 ± 0.3 ppm yr⁻¹ ($\pm 1 \sigma$ for interannual variability) in the 1960s to an average of 2.4 ± 0.4 ppm yr⁻¹ during 2010–19 (Fig. 2.50a). The annual increase in global mean CO_2 in 2020 was 2.5 ± 0.1 ppm. In 2020, the radiative forcing due to anthropogenic CO_2 increased to 2.11 W m^{-2} relative to pre-industrial times (1750 CE; Table 2.10; gml.noaa.gov/gmd/aggi/; Hofmann et al. 2006).

The main driver of increasing atmospheric CO_2 is fossil fuel (FF) burning, with emissions (including a minor amount from cement production) between 2010 and 2019 averaging $9.4 \pm 0.5 \text{ Pg C yr}^{-1}$ (Friedlingstein et al. 2020). If all of this CO_2 remained in the atmosphere, the average 2010–19 increase would have been 4.4 ppm yr^{-1} instead of 2.4 ppm yr^{-1} . Thus, only about 55% of FF-emitted CO_2 in 2010–19 has remained in the atmosphere, while the rest has been stored by the ocean and the terrestrial biosphere. While emissions of CO_2 from FF combustion drive its increasing atmospheric burden, the large interannual variability in the CO_2 growth rate is mostly driven by terrestrial biospheric exchange of CO_2 , which is confirmed by stable carbon isotope (^{13}C) measurements (e.g., Keeling et al. 1985; Alden et al. 2010). Terrestrial biosphere flux variability is influenced by both temperature and moisture anomalies (Cox et al. 2013; Hu et al. 2019; Humphrey et al. 2018). For example, the terrestrial impacts of the strong El Niño that peaked in late-2015 contributed to a strong global CO_2 increase of 3.0 ppm yr^{-1} (Betts et al. 2016). Because El Niño–Southern Oscillation (ENSO) changed from neutral to La Niña during 2020, it is not surprising that the observed CO_2 increase was near the 2010–19 mean.

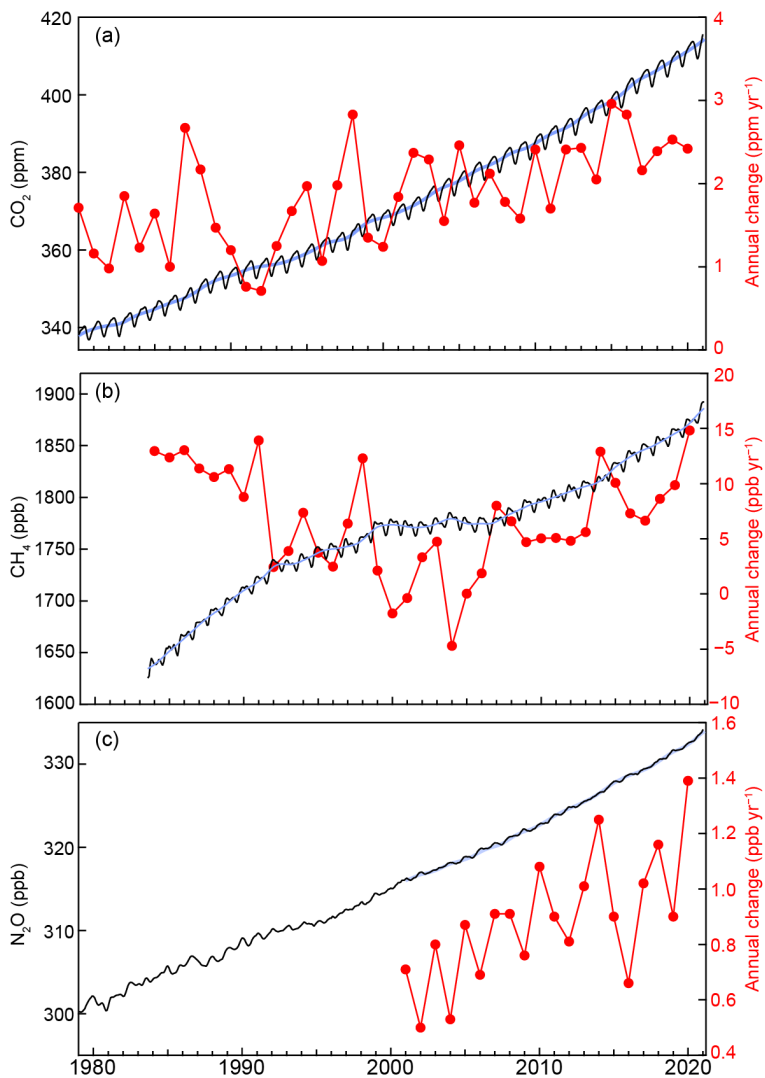


Fig. 2.50. Global monthly mean dry-air surface mole fractions (black, left axis) and annual increases (red, right axis) of (a) carbon dioxide (CO_2), (b) methane (CH_4), and nitrous oxide (N_2O) derived from NOAA Global Greenhouse Gases Reference Network marine boundary layer measurement sites. Deseasonalized trend curves (see Dlugokencky et al. 1994 for methods) are shown in blue; annual increases are defined as 1 Jan minus 1 Jan of consecutive years from the trend line. N_2O data prior to 1995 are insufficient and noisy, thus hindering the calculation of a growth rate.

changing balance between emissions and chemical destruction. The CH_4 annual increase averaged $11.4 \pm 1.4 \text{ ppb yr}^{-1}$ from 1983 to 1992, followed by a strong decrease to $4.4 \pm 1.8 \text{ ppb yr}^{-1}$ between 1992 and 1998, and further reduced to near zero ($0.5 \pm 3.0 \text{ ppb yr}^{-1}$) during 1999–2006. The rise and then flattening of the global methane abundance is consistent with an approach to steady state if there was no trend in its lifetime (Dlugokencky et al. 2003). Atmospheric CH_4 growth restarted again in 2007 and the average growth rate after 2014 was higher than 2007–14 (red line in Fig. 2.50b). The annual increase in 2020 was $14.8 \pm 0.5 \text{ ppb}$, which is by far the largest annual increase since systematic atmospheric CH_4 measurements began. There is no obvious explanation at this time for this large anomaly. CH_4 now contributes 0.52 W m^{-2} in direct radiative forcing (Table 2.10) relative to pre-industrial times, while the CH_4 -related production of tropospheric ozone (O_3) and stratospheric water vapor (H_2O) contributes $\sim 0.3 \text{ W m}^{-2}$ in indirect radiative forcing (Myhre et al. 2013).

Anthropogenic CO_2 emissions are estimated to have decreased by about 6%–7% due to reduced human activities during the COVID-19 pandemic (Friedlingstein et al. 2020; Le Quere et al. 2020; BP Statistical Review of the World Energy 2021). However, this reduction is not obvious in observed global atmospheric CO_2 signals, because it is a relatively small signal compared with natural variability that is driven by the large fluxes from photosynthesis and respiration of ecosystems on land. The estimated $\sim 6\%$ – 7% reduction in global CO_2 emissions of $\sim 10 \text{ Pg C yr}^{-1}$ would result in a $\sim 0.3 \text{ ppm}$ decrease in global CO_2 (given a conversion factor of $2.12 \text{ Pg C ppm}^{-1}$; Ballantyne et al. 2012), which is within the $1\text{-}\sigma$ interannual variability of CO_2 annual growth in 2010–19 ($0.4 \pm 0.1 \text{ ppm yr}^{-1}$). The impact of emission changes during COVID-19 may be more discernible in urban atmospheric CO_2 measurements because most of the emission reductions come from urban areas (A. J. Turner et al. 2020).

Methane is the second-most important anthropogenic greenhouse gas after CO_2 . Its abundance in the atmosphere increased to $1879.2 \pm 1.0 \text{ ppb}$ (parts per billion by moles in dry air) in 2020, a 160% increase compared to its pre-industrial level of $722 \pm 15 \text{ ppb}$. Since the beginning of NOAA's systematic CH_4 measurements in 1983, the global CH_4 annual increase has varied between -4.9 and 14.8 ppb yr^{-1} (red line in Fig. 2.50b) as a result of the

Table 2.10. Summary table of long-lived greenhouse gases for 2020 (Carbon dioxide [CO₂] abundances [mole fractions] are in ppm, nitrous oxide [N₂O] and methane [CH₄] in ppb, and all others in ppt).

Industrial Designation or Common Name	Chemical Formula	Included in the AGGI ^a ? (Yes/No)	Radiative Efficiency (W m ⁻² ppb ⁻¹) ^b	Rad. Forcing (W m ⁻²)	Mean surface mole fraction, 2020 (change from 2019) ^c	Lifetime (years)
Carbon Dioxide	CO ₂	Y	1.37 × 10 ⁻⁵	2.11	412.5 (2.5)	—
Methane	CH ₄	Y	3.63 × 10 ⁻⁴	0.52	1879.2 (12.7)	9.1
Nitrous Oxide	N ₂ O	Y	3.00 × 10 ⁻³	0.21	333.0 (1.2) ^d	123
Chlorofluorocarbons						
CFC-11	CCl ₃ F	Y	0.26	0.058	224.5 (−1.8) ^c	52
CFC-12	CCl ₂ F ₂	Y	0.32	0.159	497.3 (−3.9) ^c	102
CFC-113	CCl ₂ FCCl	Y	0.30	0.021	69.0 (−0.7) ^c	93
Hydrochlorofluorocarbons						
HCFC-22	CHClF ₂	Y	0.21	0.052	246.4 (1.4)	11.9
HCFC-141b	CH ₃ CCl ₂	Y	0.16	0.004	24.2 (0.03)	9.4
HCFC-142b	CH ₃ CClF	Y	0.19	0.004	21.6 (−0.2)	18
Hydrofluorocarbons						
HFC-134a	CH ₂ FCF ₃	Y	0.16	0.018	111.5 (5.1)	14
HFC-152a	CH ₃ CHF ₂	Y	0.10	<0.001	6.2 (−0.03)	1.6
HFC-143a	CH ₃ CF ₃	Y	0.16	0.004	24.9 (1.5)	51
HFC-125	CHF ₂ CF ₃	Y	0.23	0.007	33.0 (3.0)	30
HFC-32	CH ₂ F ₂	N	0.11	0.002	21.1 (2.9)	5.4
HFC-23	CHF ₃	Y	0.18	0.006	33.7 (1.3)	228
HFC-365mfc	CH ₃ CF ₂ C	N	0.22	< 0.001	1.0 (0.02)	8.9
HFC-227ea	CF ₃ CHFC	N	—	< 0.001	1.70 (0.15)	36
Chlorocarbons						
Methyl Chloroform	CH ₃ CCl ₃	Y	0.07	< 0.001	1.4 (−0.2)	5.0
Carbon Tetrachloride	CCl ₄	Y	0.17	0.013	86.8 (−0.9) ^c	32
Methyl Chloride	CH ₃ Cl	N	0.01	< 0.001	546.6 (8.7)	0.9
Bromocarbons						
Methyl Bromide	CH ₃ Br	N	0.004	< 0.001	6.70 (0.15)	0.8
Halon 1211	CBrClF ₂	Y	0.29	0.001	3.11 (−0.10)	16
Halon 1301	CBrF ₃	Y	0.30	0.001	3.31 (0.0)	72
Halon 2402	CBrF ₂ CB	Y	0.31	< 0.001	0.40 (0.0)	28
Fully fluorinated species						
Sulfur Hexafluoride	SF ₆	Y	0.57	0.006	10.3 (0.3)	> 600
PFC-14	CF ₄	N	0.09	0.005	86.4 (0.9)	~ 50 000
PFC-116	C ₂ F ₆	N	0.25	0.001	4.94 (0.09)	~ 10 000
PFC-218	C ₃ F ₈	N	0.28	< 0.001	0.70 (0.02)	~ 2600
PFC-318	c-C ₄ F ₈	N	0.32	< 0.001	1.82 (0.06)	~ 3200

^a Annual Greenhouse Gas Index (AGGI). See <https://gml.noaa.gov/aggi/> for more information

^b Radiative efficiencies and lifetimes were taken from Appendix A in WMO (2018), except for SF₆ lifetime from Ray et al. (2017) and CH₄ lifetime from Prather et al. (2012). For CO₂, numerous removal processes complicate the derivation of a global lifetime. For more on radiative forcing, see <https://www.esrl.noaa.gov/gmd/aggi/>

^c Mole fractions are global, annual surface means for the 2020 determined from the NOAA Global Greenhouse Gas Reference Network, except for PFC-14, PFC-116, PFC-218, PFC-318, and HFC-23, which were measured by AGAGE (Mühle et al. 2010; Miller et al. 2010). Changes indicated in brackets are the differences between the 2020 and 2019 means, the relevant quantities for calculating radiative forcing. These changes are somewhat different from the 2020 annual increases reported in 2.g.1, which are determined as the difference between Jan. 1, 2021 and Jan. 1, 2020. All values are preliminary and subject to minor updates.

^d Global mean estimates derived from multiple NOAA measurement programs (“Combined Dataset”).

Given the complexity of the CH₄ budget and the uncertainty in CH₄ source partitioning, the magnitudes and long-term trends of many CH₄ sources are still uncertain. FF exploitation is estimated to account for ~19% of total global CH₄ emissions since 2000 based on top-down approaches that use atmospheric CH₄ measurements and inverse models (Saunio et al. 2020). However, studies including the radiocarbon (¹⁴C) or stable carbon (¹³C) isotopes of CH₄ suggest a much larger fraction of FF emissions (~30%; Lassey et al. 2007; Schwietzke et al. 2016). Measurements of δ¹³C-CH₄ also suggest that increased emissions from biogenic sources, from natural and/or anthropogenic origins, are the dominant drivers for the post-2006 growth (Chang et al. 2019; Nisbet et al. 2019; Schaefer et al. 2016; Schwietzke et al. 2016). Global atmospheric δ¹³C-CH₄ has become more depleted since 2008, which is consistent with an increased contribution from biogenic sources with more negative δ¹³C-CH₄ signatures. Increased wetland emissions may play a role in the post-2006 renewed increase (Yin et al. 2020), but further investigation is required to better quantify wetland emissions given the large uncertainties associated with wetland emission areas and processes controlling wetland CH₄ emissions (Bloom et al. 2017). A decrease in biomass burning and a small increase in FF emissions (Worden et al. 2017) may also play a smaller role in post-2006 global CH₄ change (Lan et al. 2021).

Methane is removed from the atmosphere mainly by reaction with hydroxyl radical (OH); OH has a very short lifetime (~1 s), which makes it difficult to constrain by direct observations. While recent studies suggest that a decreasing OH sink may not be the dominant driver for the post-2006 renewed increase in global atmospheric CH₄ (Fujita et al. 2020), uncertainties remain in the temporal variations of the OH sink and other CH₄ sinks such as oxidation by tropospheric chlorine (Cl; Hossaini et al. 2016; Gromov et al. 2018) and soils. The global soil CH₄ sink is estimated to be ~30 Tg yr⁻¹; however, up to a 77% decrease was reported for 1988–2015 based on long-term measurements and data reviews (Ni and Groffman 2018). A decrease in the soil CH₄ sink is consistent with an observed global decrease in δ¹³C-CH₄ (Lan et al. 2021).

Nitrous oxide (N₂O) is an important LLGHG that also depletes stratospheric ozone (Ravishankara et al. 2009). Atmospheric N₂O has been increasing steadily throughout the industrial era except for a brief period in the 1940s (MacFarling Meure et al. 2006; Thompson et al. 2019). The mean global atmospheric N₂O abundance in 2020 was 333.0 ± 0.1 ppb, while the annual increase in 2020 was 1.4 ± 0.1 ppb (Fig. 2.50c), and a 23% increase over pre-industrial levels of 270 ppb. The 1.4 ppb increase in the annual mean is similar to average rate of increase of 1.0 ± 0.2 ppb yr⁻¹ over the past decade (2010–19), but slightly larger than the average rate in previous decade (2000–09) of 0.7 ± 0.2 ppb yr⁻¹. The observed increase in atmospheric N₂O over preindustrial levels is mostly caused by nitrogen-containing fertilizers and manure used for agriculture (Davidson 2009). A recent study found that anthropogenic N₂O emissions have increased by 30% since 1980, with significant contributions from developing countries such as Brazil, China, and India (Tian et al. 2020). Radiative forcing from N₂O in 2020 is now 0.21 W m⁻² relative to pre-industrial times (Table 2.10).

The combined radiative forcing in 2020 from major and minor LLGHGs was 3.2 W m⁻² (Fig. 2.51). Annual increases in radiative forcing correspond roughly with variability in CO₂, since CO₂ is responsible for about 65% of radiative forcing by LLGHGs and its increase during 2015–20 accounts for 82% of total increase in radiative forcing.

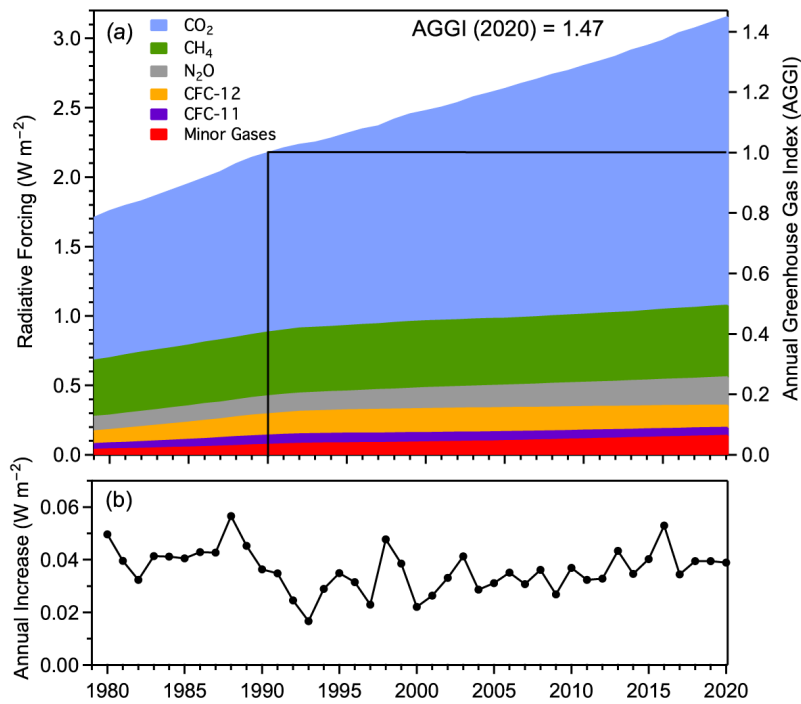


Fig. 2.51. (a) Direct radiative forcing (W m^{-2}) due to five major long-lived greenhouse gases (LLGHG) and 15 minor gases (left axis) and the associated values of the NOAA AGGI (right axis). The Annual Greenhouse Gas Index (AGGI) is defined to have a value of one in 1990. (b) Annual increase in direct radiative forcing (W m^{-2}).

2) *Ozone-depleting substances*—I. J. Vimont, B. D. Hall, S. A. Montzka, G. Dutton, C. Siso, M. Crotnell, and M. Gentry

Our climate is affected by the presence of halogenated trace gases in the atmosphere. This group of compounds includes, but is not limited to, chlorofluorocarbons (CFCs), hydrochlorofluorocarbons (HCFCs), hydrofluorocarbons (HFCs), chlorinated hydrocarbons, and halons. These compounds both directly (via radiative forcing) and indirectly (via ozone depletion in the stratosphere) influence the radiative balance of the atmosphere (Karpechko and Maycock 2018).

The Montreal Protocol (1987) and its subsequent amendments regulate the production and consumption of these ozone-depleting substances (ODS) and other compounds. These controls started in the late 1980s by phasing out production of CFCs and were followed by the reduction and phaseout of halons in the 1990s and early 2000s. The year 2020 marks the near-complete phaseout of HCFCs in developed countries. These controls have resulted in declines in atmospheric abundance for many of these gases (Engel and Rigby, 2018). CFC-11 and CFC-12 declined $16\% \pm 1\%$ and $8\% \pm 0.3\%$, respectively, from their maximum values by 2020 (Fig. 2.52). Additionally, while the reduction of CFC-11 in the atmosphere slowed after 2012 owing to an unexpected increase in emissions that were likely linked to unreported production of CFC-11 (Montzka et al. 2018; Rigby et al.

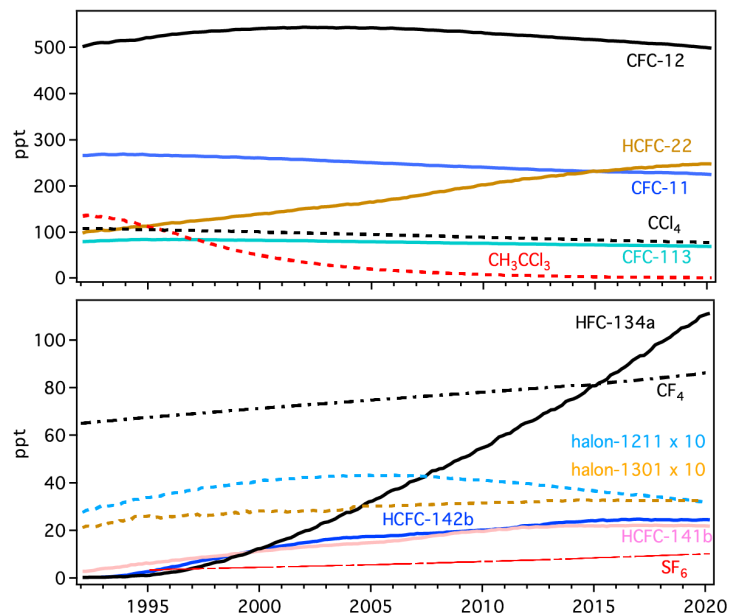


Fig. 2.52. Global mean abundances (mole fractions) at Earth's surface ($\text{ppt} = \text{nmol mol}^{-1}$ in dry air) for several halogenated gases, many of which also deplete stratospheric ozone. See Table 2.10 for the 2020 global mean mole fractions of these and other gases.

2019), continued monitoring has shown an accelerated decline from 2018 to 2019, signaling a decline in these emissions (Montzka et al. 2021; Park et al. 2021).

As HCFCs replaced CFCs, their abundances increased in the atmosphere. More recently, however, as the phaseout of HCFC production nears completion, growth rates of atmospheric HCFC-22, HCFC-141b, and HCFC-142b have slowed (Fig. 2.52). Notably, atmospheric abundances of both HCFC-141b and HCFC-142b have remained nearly constant since 2018 (Table 2.10; Fig. 2.52). With the near-complete phaseout of HCFCs in developed nations scheduled for 2020, and significant reductions in production and consumption occurring in developing countries, the atmospheric abundances of these compounds may soon begin to decline. The Kigali Amendment to the Montreal Protocol has mandated the phase-down of HFCs, which are substitutes for ODS. While these compounds do not contribute to ozone destruction, they contribute to radiative forcing, and atmospheric abundances for most have been increasing in the atmosphere (Table 2.10, Fig. 2.52). HFC-134a is the largest contributor to radiative forcing among the HFCs, and its global abundance increased by 5.3 ppt (4.7%) from 2019 to 2020, similar to the mean yearly increase over the last decade (~ 5.5 ppt yr^{-1} ; Fig. 2.52).

In order to quantify the overall efficacy of ozone-destroying halogen in the stratosphere, equivalent effective stratospheric chlorine (EESC) is calculated from the weighted global average surface abundance of ozone-depleting gases (Daniel et al. 1995). The weights represent the ozone-destruction efficiency of the halogens contained in each ODS, the destruction rates of each ODS in the stratosphere, and transport and mixing processes within the stratosphere (Montzka et al. 1996; Newman et al. 2007). EESC is calculated for the Antarctic (EESC-A) and the midlatitude (EESC-M) stratosphere. The abundance of reactive halogen in the Antarctic stratosphere is higher than in midlatitudes because air reaching the Antarctic stratosphere has been in the stratosphere longer and has been transported to higher altitudes, factors that lead to both ODS destruction and release of reactive halogen (Montzka and Reimann et al. 2011). CFCs, despite their decreasing global abundance, contribute strongly to EESC (Fig. 2.53), because they account for most of the reactive halogen present in the atmosphere today.

At the beginning of 2020, EESC-A was 3685 ppt, and EESC-M was 1562 ppt, decreases of 25 ppt and 12 ppt, respectively, relative to 2019. To put these values into context of stratospheric reactive halogen reduction, the Ozone Depleting Gas Index (Hoffmann and Montzka, 2009, gml.noaa.gov/odgi/) is defined for both the Antarctic and midlatitude stratosphere (ODGI-A and ODGI-M). This index is defined as 100 for the peak EESC and 0 at the 1980 level of EESC, for both the Antarctic and midlatitude stratosphere. Even though ozone destruction was occurring

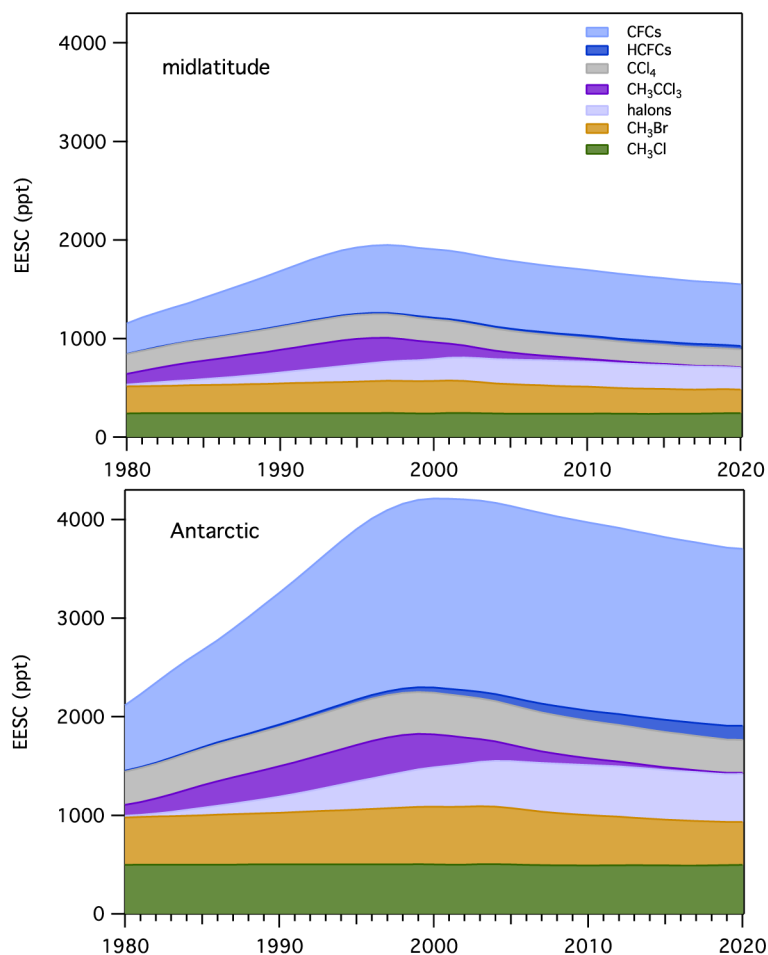


Fig. 2.53. Equivalent effective stratospheric chlorine (EESC, ppt) for the midlatitude and Antarctic stratosphere derived from surface measurements. The EESC values represent EESC on 1 Jan of each year.

in 1980, returning the stratosphere to 1980 levels of reactive halogen would represent a major accomplishment for the Montreal Protocol and the global community. At the beginning of 2020, the ODGI-A was 77, and the ODGI-M was 52, representing progress of 23% and 48% toward the 1980 benchmarks, respectively. Carpenter et al. (2018) estimate that ODGI-A will reach zero around 2070, and ODGI-M will reach zero around 2045, assuming all other factors remain constant.

3) Aerosols—S. Rémy, N. Bellouin, Z. Kipling, M. Ades, A. Benedetti, and O. Boucher

Atmospheric aerosols play an important role in the climate system by scattering and absorbing radiation, and by affecting the life cycle, optical properties, and precipitation activity of clouds (Boucher et al. 2013). Aerosols also represent a serious public health issue in many countries, and hence are subject to monitoring and forecasting as part of air quality policies. There is also growing evidence that aerosols influence ecosystems through changes in the quality and quantity of light (over land) and deposition flux of nutrients (over land and ocean) such as iron (e.g., Hamilton et al. 2019).

The Copernicus Atmosphere Monitoring Service (CAMS; <http://atmosphere.copernicus.eu>) runs a near-real time global analysis of aerosols and trace gases. The CAMS project also produced a reanalysis of global aerosols and trace gases that covers the years 2003–20, named the CAMS reanalysis (CAMSRA; Inness et al. 2019) by combining state-of-the-art numerical modeling and aerosol remote-sensing retrievals from MODIS (Levy et al. 2013) and the Advanced Along Track Scanning Radiometer (AATSR) (Popp et al. 2016). Verification of aerosol optical depth (AOD) at 550 nm against independent AERONET observations shows that the CAMS reanalysis has a smaller bias and error than its predecessors, the CAMS interim reanalysis (Flemming et al. 2017)

and the Monitoring Atmospheric Composition and Climate (MACC) reanalysis (Inness et al. 2013). This section uses data exclusively from the CAMS reanalysis. Here, we assess aerosols in terms of the AOD at 550 nm because this wavelength corresponds to the middle of the visible part of the spectrum, and because many remote-sensing products provide retrievals at this wavelength.

The time series of monthly and yearly globally-averaged total AOD during 2003–20 are depicted in Fig. 2.54b, showing strong seasonality, driven mainly by dust episodes between March and July in the Sahara, Middle East, and the Taklimakan/Gobi Desert and seasonal biomass burning in Africa, South America, and Indonesia. There is no significant trend over the period, but extreme events such as the July–October 2015 fires over Indonesia associated with El Niño can have an impact on the global mean. Globally averaged AOD in 2020 was on average lower than in 2019, with a less pronounced summer maximum, mostly because of less intense biomass burning in the Northern Hemisphere summer and autumn over Indonesia and parts of equatorial Africa as well as Canada. Figure 2.54a shows the geographical distribution of AOD in

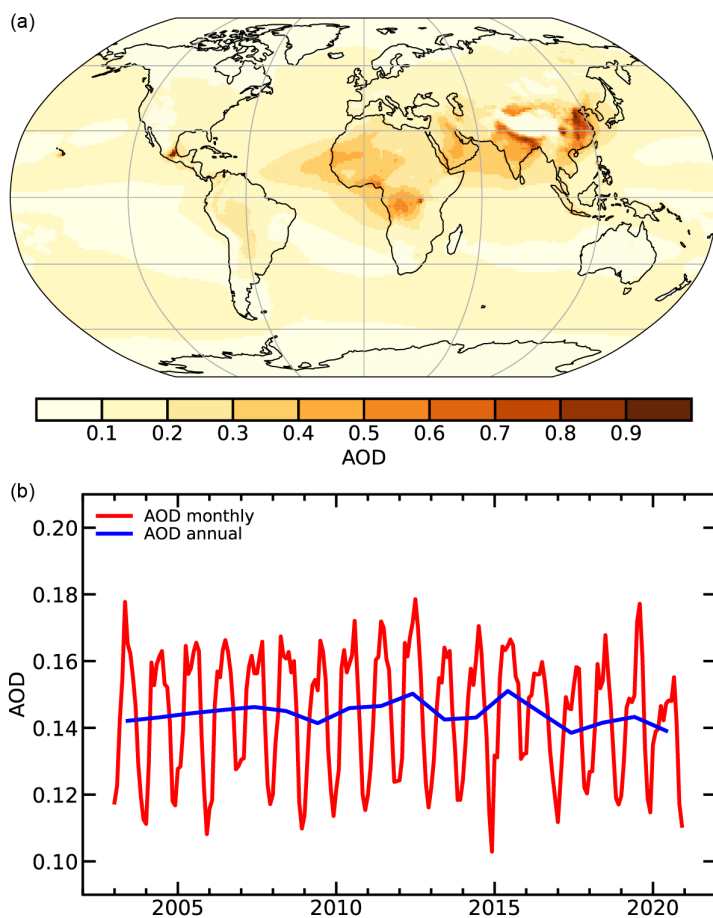


Fig. 2.54. (a) Global aerosol optical depth (AOD) at 550 nm in 2020 from CAMSRA. (b) Global average of total AOD at 550 nm for monthly (red) and annual (blue) periods for 2003–20.

2020, with maxima from anthropogenic aerosols over India and China, as well as less pronounced maxima over the Arabian Peninsula and parts of the Sahara from dust, and over equatorial Africa from biomass burning aerosols.

Average AOD between 2003 and 2020 (Fig. 2.55a) is marked by high values over the highly populated regions of India and China, mainly caused by anthropogenic emissions. High AOD values over the Sahara and Middle East are from dust, while the maxima over central Africa, Indonesia, the Amazon Basin, and parts of Siberia are caused by biomass burning. The high values over Hawaii and close to Mexico City are a known artifact of the CAMS reanalysis related to volcanic outgassing.

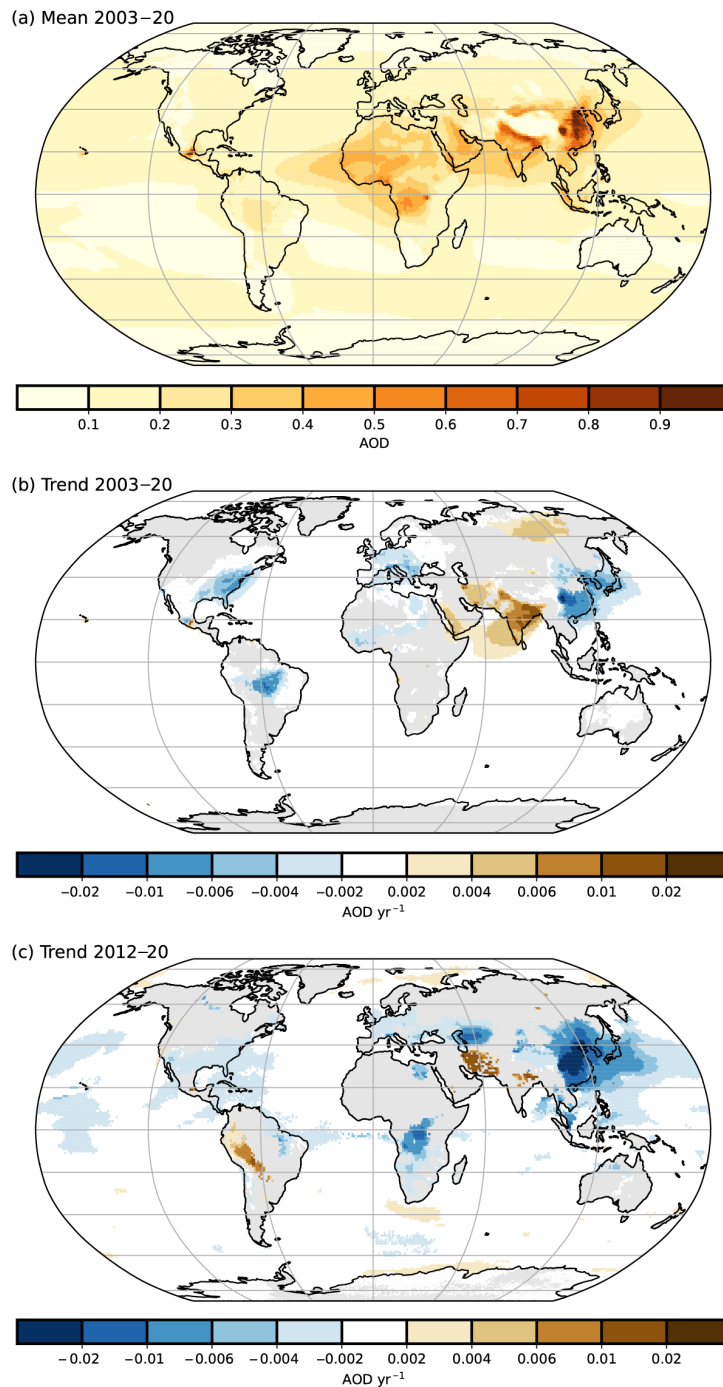


Fig. 2.55. (a) Total aerosol optical depth (AOD) at 550 nm averaged over the period 2003–20 from CAMSRA. Note the regional differences, with much greater total AOD values over parts of northern Africa, the Arabian Peninsula, southern Asia, and eastern China. (b) Linear trends of total AOD (AOD unit yr^{-1}) for 2003–20 and 2012–20. (c) Only trends that are statistically significant (95% confidence level) are shown. Regions with decreasing trends include the eastern United States, most of Europe, parts of Brazil and China, as well as the Korean peninsula and Japan.

As compared to the 2003–19 average from the CAMS reanalysis, total AOD in 2020 shows negative anomalies over most of Europe, Africa, and East Asia, as well as parts of the Amazon basin, United States, and Canada (Plate 2.1x). The negative anomalies over the eastern United States, Europe, and China/Japan are part of a longer trend over these regions (Fig. 2.55b). As shown by Fig. 2.55c, the trend is more negative over China for 2012–20 than for 2003–20, which is consistent with the observed decrease of anthropogenic aerosol emissions there since around 2012 (Li et al. 2017). The 2012–20 trends are positive or not significant over much of the Amazon basin, while the 2003–20 trends are mostly negative over the same area, showing that most of the decrease in AOD occurred before 2012. Reduced anthropogenic emissions because of COVID-19 lockdowns may have contributed to local AOD anomalies, although the impact was probably more important for surface particulate matter ($PM_{2.5}$).

Positive anomalies of total AOD in 2020 (Plate 2.1x) were found over parts of Brazil and Bolivia, Siberia, and the western United States. These positive anomalies are associated with large fire events. The positive anomaly over southeast Australia and large parts of the southern Pacific Ocean were caused by the extreme fires over New South Wales in late 2019 and early 2020. The positive anomalies over parts of western Africa and the Atlantic Ocean were caused by an extreme dust event in June 2020, while the positive anomaly over Iran was caused by meteorological conditions that favored severe pollution events (Broomandi et al. 2020). The positive anomaly over the Indian subcontinent corresponds to a long-term trend of increasing anthropogenic aerosol emissions (Satheesh et al. 2017), as shown in Figs. 2.55b,c. Plate 2.1y shows the ratio of AOD at 550 nm in 2020 to the 2003–19 average, which gives a measure of the relative importance of the anomalies as compared to climatological values. The highest relative anomalies in 2020 are almost all associated with fire events (Siberia, southeastern Australia, western United States, southwestern Brazil), except over Iran. The exceptional severity of the Australian fires of early 2020 and of the associated plume over the southern Pacific is highlighted in Plate 2.1z, which shows the number of days in 2020 with daily AOD at 550 nm above the 99.9th percentile of the 2003–19 daily values. The same plot also shows the exceptional nature of the fires that affected the western United States in August and September 2020, as well as the dust plume that crossed the Atlantic from western Africa to the Caribbean Sea in June 2020.

Anthropogenic AOD and radiative forcing resulting from aerosol–radiation (RFari) and aerosol–cloud interactions (RFaci) are shown in Fig. 2.56 for the period 2003–20. They are estimated using the methods described in Bellouin et al. (2020). 2020 was characterized by a small anthropogenic AOD and a weak RFari and RFaci in the context of the past 18 years. This may be partly due to regional decreases in aerosol primary and precursor emissions caused by the response to the COVID-19 pandemic. Such decreases have, for example, reduced aerosol radiative effects off the coast of China, at least in cloud-free conditions (Ming et al. 2020), which would weaken RFari. The data suggest a weakening trend in aerosol radiative forcing starting around 2015, but the trend would need to be sustained over a longer period to become statistically significant.

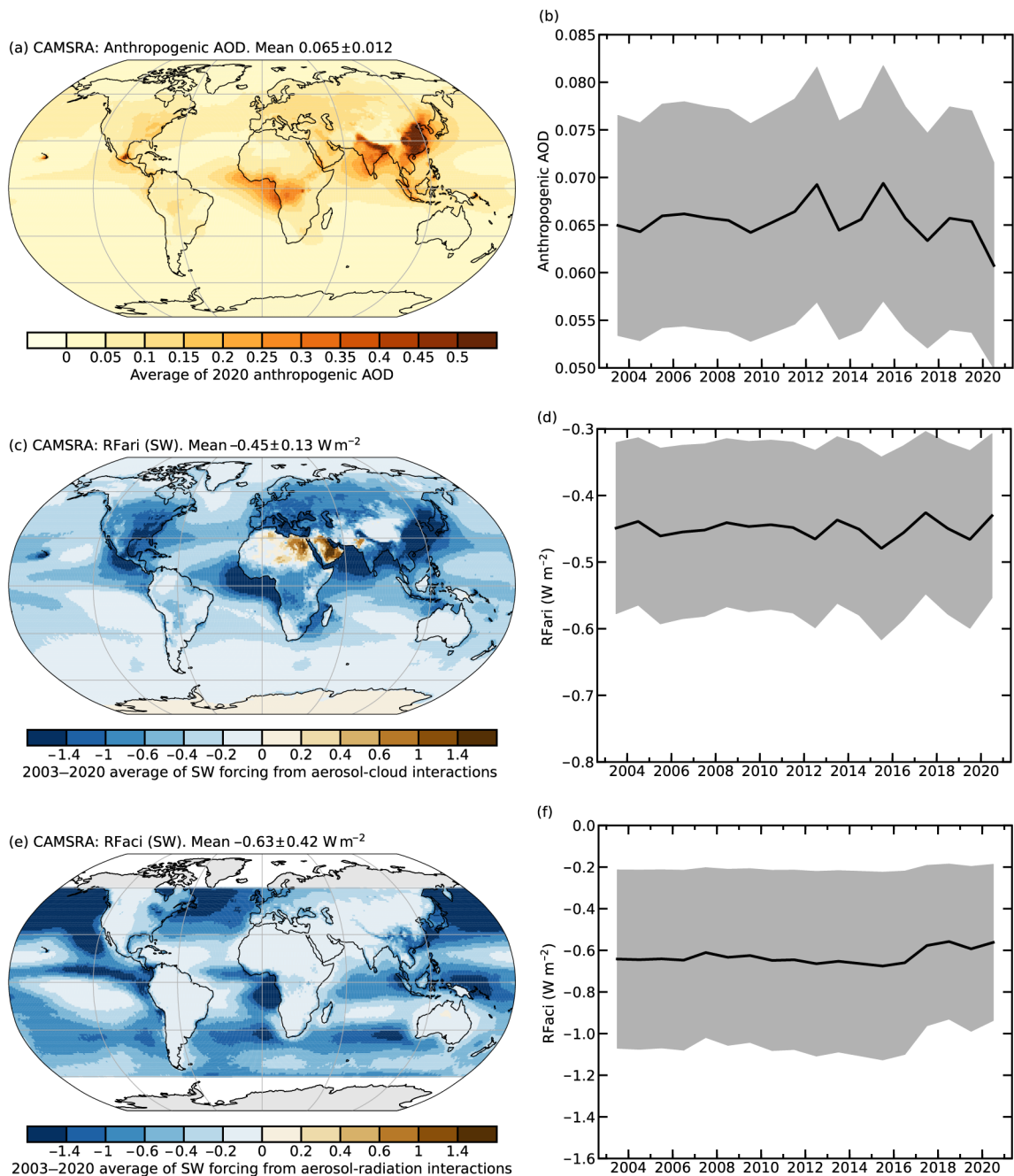


Fig. 2.56. CAMSRA (a) 2020 average of anthropogenic aerosol optical depth (AOD); (b) global annual average of anthropogenic AOD from 2003 to 2020. Radiative forcing in the shortwave (SW) spectrum due to (c),(d) aerosol-radiation (RFari) and (e),(f) aerosol-cloud interactions (RFaci). The left column shows the average distribution for the period 2003–20. The right column shows time series of global averages for the same period, with the 1- σ uncertainties of these estimates shown in gray.

4) Stratospheric ozone—M. Weber, W. Steinbrecht, C. Arosio, R. van der A, S. M. Frith, J. Anderson, L. Castia, M. Coldey-Egbers, S. Davis, D. Degenstein, V. E. Fioletov, L. Froidevaux, D. Hubert, D. Loyola, C. Roth, A. Rozanov, V. Sofieva, K. Tourpali, R. Wang, and J. D. Wild

Stratospheric ozone protects Earth’s biosphere from harmful ultraviolet (UV) solar radiation. The total ozone column determines how much UV reaches the surface. Most of the ozone resides in the lower stratosphere (“ozone layer”), where it is recovering slowly from anthropogenic Ocean Depleting Substances (ODS). Clearer signs of ozone recovery, due to the phase-out of ODSs mandated by the Montreal Protocol in the late 1980s (section 2g2), are seen in the upper stratosphere (WMO 2018).

The year 2020 was remarkable because the annual mean anomaly of total column ozone was negative for most of the globe (Plate 2.1aa). This negative anomaly was due to the combination of

very low polar ozone during Arctic winter/spring (Manney et al. 2020; Inness et al. 2020; Dameris et al. 2021) and a large and unusually long-lasting Antarctic ozone hole (see sections 5j and 6h, respectively). Low winter/spring polar ozone is a consequence of stable and cold stratospheric winter vortices with very low temperatures that permit wide-spread formation of polar stratospheric clouds (PSC), chlorine activation, and large polar ozone depletion (Solomon et al. 1999, 2015).

Figure 2.57 shows time series of Arctic and Antarctic daily minimum total column ozone. Generally, Arctic minimum total ozone increases from early winter (November) to spring (April). However, in cold Arctic winters, with stratospheric temperatures sufficiently low for persistent PSC formation (~195 K), minimum total ozone decreases over the winter, due to both chemical loss and reduced poleward ozone transport related to a weak Brewer-Dobson circulation (BDC; Lawrence et al. 2020). In March 2020 record low column values slightly below 220 Dobson unit (DU) were reached (Inness et al. 2020, Dameris et al. 2021), less than in previous cold winters (e.g., 2010/11). Even these record minimum values are, however, higher than values observed in the Southern Hemisphere (SH) ozone hole. Chemical ozone losses of up to 2.8 ppm near 18 km altitude and 88 DU (vortex average) by the end of March 2020 were similar to losses observed in March 2011, but due to the larger polar vortex area, the ozone mass loss was higher in 2020 and reached a new record after the previous record in 2011 (Manney et al. 2020; Weber et al. 2021). Without the Montreal Protocol phaseout of ODS, this chemical ozone loss would have been even higher (Feng et al. 2021). Above Antarctica, minimum total column ozone remained extremely low in 2020 and only rose rapidly at the end of November about 2 months later than in 2016, which had a winter with an average size ozone hole.

The low total ozone levels during winter/spring in both hemispheres contributed significantly to the annual mean low ozone anomaly (Plate 2.1aa). Zonally averaged annual mean total column ozone was as much as 20 and 60 DU below the long-term mean of 1998–2008 at northern middle and Arctic latitudes, respectively. The band of positive anomalies in the outer tropics along with

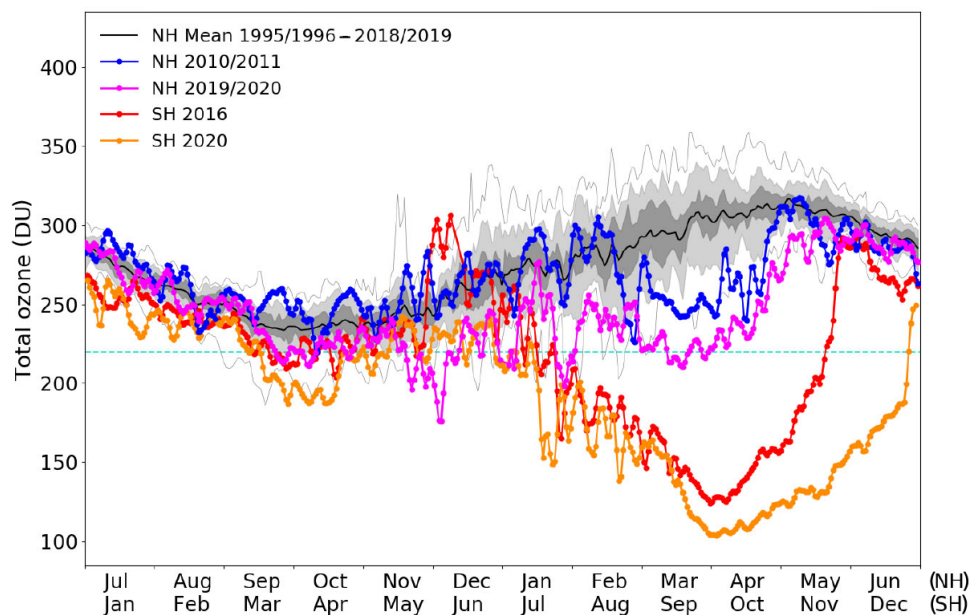


Fig. 2.57. Annual cycle of daily minimum total column ozone values (Dobson Units [DU]) in the polar regions between 50° and 90° in both hemispheres derived from the European GOME-type Total Ozone Essential Climate Variable (GTO) satellite record from Jul 1995 to Jun 2019 and TROPOMI data thereafter. The black line shows the GTO mean annual cycle in the north polar region. The thin gray lines indicate the maximum and minimum values of the observed daily minima from Jul 1995 to Jun 2019. The light gray shading denotes the 10th percentile and 90th percentile, the dark gray shading the 30th percentile and 70th percentile, respectively. The cyan dashed line shows the upper limit of 220 DU that defines the edge of the Antarctic ozone hole. Total ozone minimum time series are shown for winter/spring 2010/11 (blue) and 2019/20 (magenta) in the Northern Hemisphere (Jul–Jun) and in Antarctic winter/spring 2016 (red) and 2020 (orange) in the Southern Hemisphere (Jan–Dec). Updated from Dameris et al. (2021).

the negative anomalies at high latitudes are a typical pattern during quasi-biennial oscillation (QBO) westerly phases, as explained in previous reports. The Arctic Oscillation (AO) index was at a record high during Northern Hemisphere (NH) winter/spring and contributed to the very low ozone observed in the NH extratropics resulting from a very weak meridional circulation (Lawrence et al. 2020).

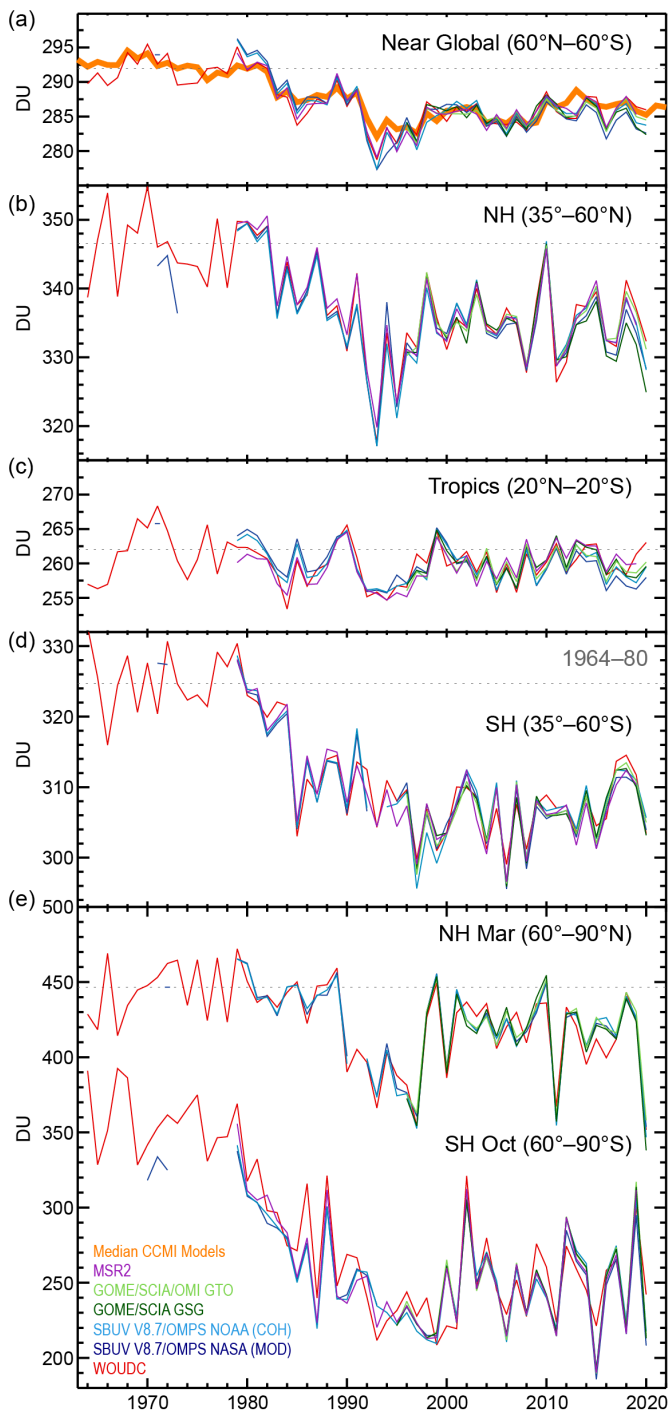


Figure 2.58 shows the long-term evolution of total column ozone for different zonal bands. Except for the polar region (NH: March mean; SH: October mean) annual mean total column ozone is shown. Following the decline until the middle 1990s due to ODS increases, total column ozone has remained at a steady level with substantial year-to-year variability during the last 2 decades, but still well below the 1964–80 mean (indicated by the dashed line). Near-global mean total column ozone (Fig. 2.58a) is on average still about 2% below the 1964–80 mean. The median ozone from the Chemistry Climate Model Initiative (CCMI) model simulations (SPARC/IO3C/GAW 2019), accounting for ODS and greenhouse gas changes, is in good agreement with observations. This shows that ozone observations are consistent with the expected slow ozone recovery due to the phasing out of certain ODSs (section 2g2).

In 2020, the annual means in all latitude bands, as well as the Arctic March and Antarctic October mean (Fig. 2.58), were all below the decadal average of 1998–2008, but were within the variability observed in recent years (except March 2020).

Figure 2.59 shows the ozone evolution at different altitudes in the stratosphere. Ozone in the upper stratosphere showed a large decline in the 1980s caused by ODS increases, which was stopped in the late 1990s, thanks to the ODS phase-out mandated by the Montreal Protocol. Since about 2000, upper stratospheric ozone has been in a phase of slow recovery. In

Fig. 2.58. Time series of annual mean total column ozone (Dobson Units [DU]) in (a)–(d) four zonal bands, and (e) polar (60°–90°) total column ozone in Mar (Northern Hemisphere) and Oct (Southern Hemisphere), the months when polar ozone losses usually are largest. Red: WOUDC ground-based measurements combining Brewer, Dobson, SAOZ, and filter spectrometer data (Fioletov et al. 2002, 2008). Dark blue and light blue: BUV/SBUV/SBUV2 V8.6/OMPS merged products from NASA (MOD V8.6, Frith et al. 2014, 2017) and NOAA (Wild and Long, personal communication, 2019), respectively. Dark green and light green: GOME/SCIAMACHY/GOME-2 products GSG from University of Bremen (Weber et al. 2018) and GTO (additionally includes OMI and TROPOMI) from ESA/DLR (Coldewey-Egbers et al. 2015; Garane et al. 2018). Purple: MSR-2, which assimilates nearly all available ozone datasets after corrections based on the ground-based data (van der A et al. 2015). All datasets have been bias-corrected by subtracting averages for the reference period 1998–2008 and adding back the mean of these averages. The dashed gray lines in each panel show the average ozone level for 1964–1980 calculated from the WOUDC data. The thick orange line shows the median from CCMI model runs (SPARC/IO3C/GAW, 2019). Most of the observational data for 2020 are preliminary.

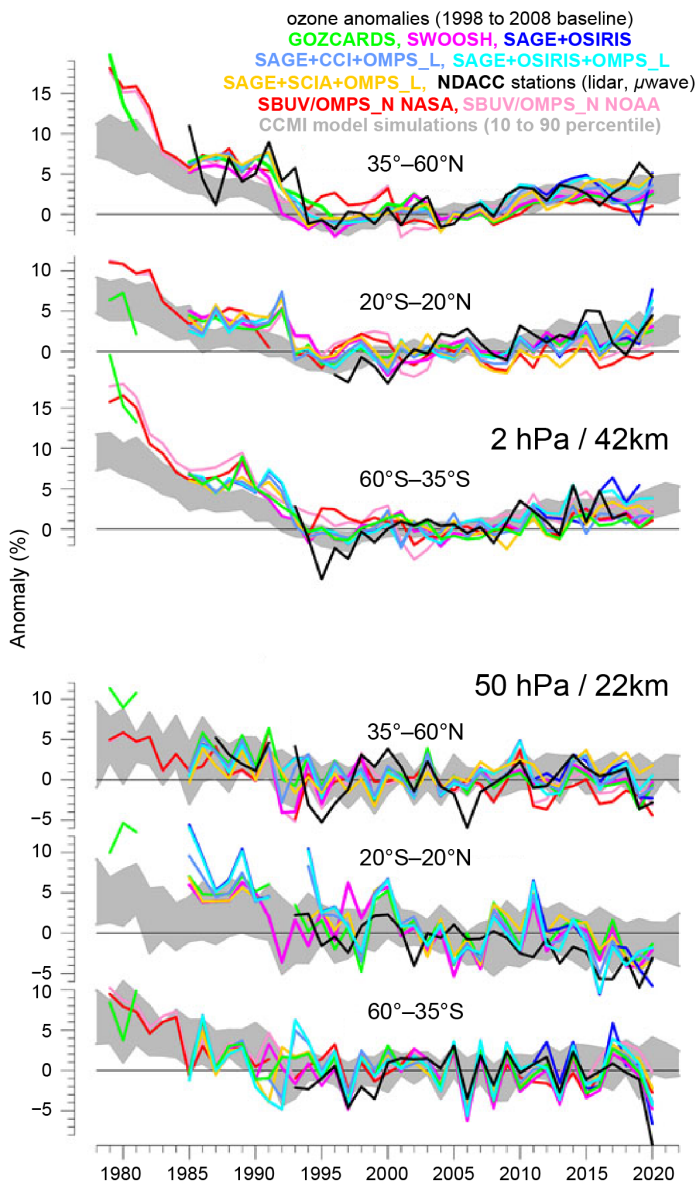


Fig. 2.59. Annual mean anomalies of ozone in the upper stratosphere (top three panels) near 42-km altitude or 2-hPa pressure, and in the lower stratosphere (bottom three panels, near 22 km or 50 hPa for three zonal bands: 35°–60°N, 20°S–20°N (tropics), 35°–60°S respectively). Anomalies are referenced to the 1998–2008 baseline. Colored lines are long-term records obtained by merging different limb (GOZCARDS, SWOOSH, SAGE+OSIRIS, SAGE+CCI+OMPS-L, SAGE+SCIAMACHY+OMPS-L, SAGE+OSIRIS+OMPS-L) or nadir-viewing (SBUV, OMPS-N) satellite instruments. The nadir-viewing instruments have much coarser altitude resolution than the limb-instruments. This can cause differences in some years, especially at 50 hPa. The black line is from merging ground-based ozone records at seven NDACC stations employing differential absorption lidars and microwave radiometers. See Steinbrecht et al. (2017), WMO (2018), and Arosio et al. (2018) for details on the various datasets. Gray-shaded area shows the range of simulations from CCM1 (SPARC/IO3C/GAW 2019). At the time of publication, ozone data for 2020 were not yet complete for all instruments and were still preliminary.

all recent years, including 2020, ozone values in the upper stratosphere from most datasets were above the 1998–2008 average, consistent with expectations from the CCM1 simulations (gray shaded range in Fig. 2.59; SPARC/IO3C/GAW 2019). In the lower stratosphere, however, long-term ozone variations are dominated by meteorological and transport variations (e.g., Chipperfield et al. 2018), and Fig. 2.59 shows no clear sign of ozone increases in this region over the last 20 or so years. This is consistent with total column ozone in Fig. 2.58. In 2020, lower

stratospheric values were at the low end of recent years, and also at the low end of the model predictions. The tropical (20°S–20°N) long-term ozone decline is linked to the acceleration of the meridional Brewer-Dobson circulation (Ball et al. 2018; Chipperfield et al. 2018; WMO 2018). The low annual mean 2020 values of lower stratospheric ozone in the northern and southern extratropical 35°–60° latitude bands, however, similar to the generally low total column ozone (Plate 2.1aa; Fig. 2.58), are the result of the weak meridional Brewer-Dobson circulation in winter in both hemispheres.

5) Stratospheric water vapor—S. M. Davis, K. H. Rosenlof, D. F. Hurst, and H. Vömel

Variations in stratospheric water vapor (WV) occur over a wide range of timescales and can impact stratospheric ozone (Dvortsov and Solomon 2001) and surface climate (Solomon et al. 2010). Such variations are forced by prominent modes of seasonal and interannual dynamical variability that influence temperatures in the tropical tropopause layer (TTL; ~14–19 km). In general, the amount of WV entering the stratosphere is controlled by the lowest temperature encountered by an ascending air mass (i.e., through the Clausius-Clapeyron relationship), with more WV entering the stratosphere when TTL temperatures are warmer. As a result, processes that cause temporal variability in TTL temperatures also lead to global-scale variability in stratospheric WV.

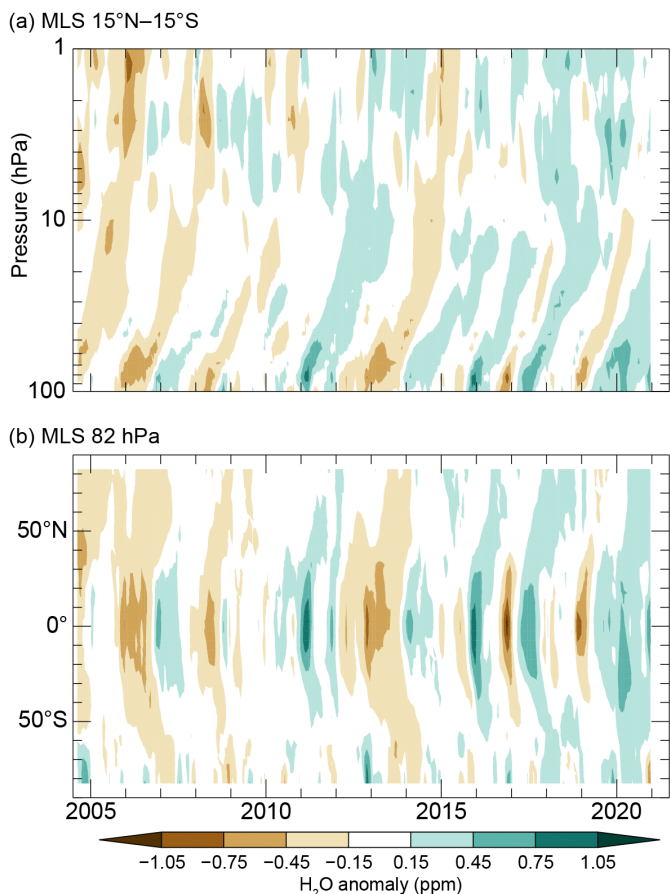


Fig. 2.60. (a) Time series of vertical profiles of tropical (15°S–15°N) lower stratospheric water vapor (WV) anomalies and (b) latitudinal distributions of WV anomalies at 82 hPa. Both are based on version 4.2 *Aura* MLS data from the SWOOSH v2.6 5° zonal mean product (Davis et al. 2016). Anomalies are differences from the mean 2004–20 water vapor mixing ratios (ppm) for each month. (b) shows the propagation of tropical lower stratospheric WV anomalies to higher latitudes in both hemispheres as well as the influences of dehydrated air masses from the Antarctic polar vortex as they are transported toward the SH midlatitudes at the end of each year. Tick marks denote the beginning of each year.

In general, interannual variations in CPTs are correlated with interannual variability in modes of climate variability such as the ENSO and QBO in equatorial stratospheric winds. These phenomena partly impact CPTs through their modulation of upwelling of air in the tropical lower stratosphere and the associated temperature response. Although we do not attempt formal attribution of the CPT and lower stratospheric WV variability to QBO and ENSO, below we discuss the changes in the phases of QBO and ENSO during 2020 as they pertain to WV variability.

The QBO westerly shear phase is associated with a negative upwelling anomaly and cold temperatures, whereas the reverse is true for easterly shear. Equatorial winds from the Singapore radiosonde wind data, which are a commonly used proxy for the QBO phase, were westerly at 70 hPa at the beginning of 2020, but transitioned to easterly from May through September, before returning back to westerly for the final 3 months of 2020 (sections 2b5, 2e3; see Fig. 2.46). The wind shear between 70 hPa and 100 hPa was positive (westerly over easterly) for all of 2020, with the exception of July and August. It is possible that these anomalies impacted tropical CPTs, as the most negative CPT anomaly of the year (−0.4 K) occurred in August (Fig. 2.61d).

In 2020, WV anomalies in the tropical lower stratosphere were positive (wet). Figure 2.60 shows the vertical–time cross section of tropical-averaged WV anomalies from the *Aura* satellite Microwave Limb Sounder (MLS; Fig. 2.60a), as well as the latitudinal distribution of WV anomalies as a function of time in the base of the stratosphere at 82 hPa (~17 km; Fig. 2.60b). The vertical–time plot shows a substantial region (in time and space) of positive water vapor anomalies ascending into the stratosphere starting in mid-2019 and continuing throughout 2020.

The 2020 *Aura* MLS (version 4.2) annual tropical average (15°S–15°N) WV anomaly at 82 hPa was 0.4 ppm (parts per million, i.e., $\mu\text{mol mol}^{-1}$), or 11% above the annual average since 2005. Monthly WV anomalies ranged from +0.1 ppm (+2%) in October to +0.8 ppm (+22%) in December, which was the fifth-wettest anomaly in the *Aura* MLS record dating back to August 2004. The tropical WV anomaly time series in 2020 is U-shaped, with strong positive anomalies at the beginning and end of the year and weak positive anomalies in the middle (Fig. 2.60b). The qualitative behavior of lowermost stratospheric WV observed by *Aura* MLS is consistent with balloon-borne frost-point hygrometer soundings at five locations, as shown in Fig. 2.61.

In 2020, tropical cold-point tropopause (CPT) temperature anomalies were positive (warm) from January through April, negative from May through August, and positive from September through the end of the year (blue line, Figs. 2.61c,d). The annual mean tropical cold-point anomaly was +0.48 K.

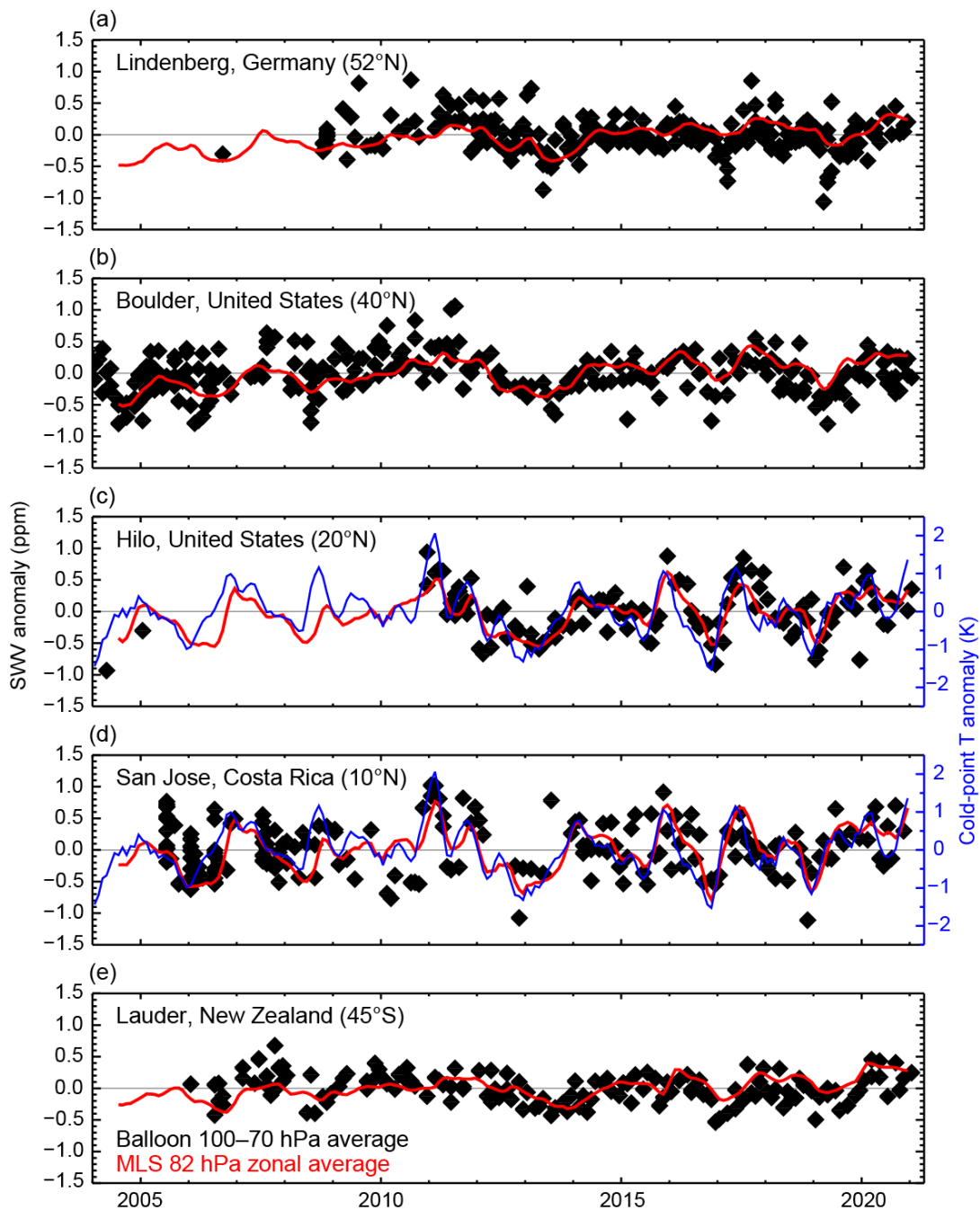


Fig. 2.61. Lower stratospheric water vapor (SWV) anomalies over five balloon-borne frost point (FP) hygrometer stations. Each panel shows the lower stratospheric anomalies of individual FP soundings (black) and of monthly zonal averages of Microwave Limb Sounder (MLS) retrievals at 82 hPa in the 5° latitude band containing the FP station (red). High-resolution FP vertical profile data were averaged between 70 hPa and 100 hPa to emulate the MLS averaging kernel for 82 hPa. Each MLS monthly zonal mean was determined from 2000–3000 profiles. Anomalies for MLS and FP data are calculated relative to the 2004–20 period for sites except for Lindenberg (2009–20) and Hilo (2011–20). Tropical CPT anomalies based on the MERRA-2 reanalysis (d, blue curve), which are generally well correlated with the tropical lower stratospheric WV anomalies, are the driving force behind the variations in tropical WV during 2020.

ENSO was in a neutral phase in the first half of 2020 before transitioning to La Niña in August and remaining in that phase through the end of the year (see sections 2e1, 4b). In boreal winter, La Niña is known to result in weaker tropical lower stratospheric upwelling, anomalously higher cold-point temperatures, and enhanced water vapor in the tropical lower stratosphere (Calvo et al. 2010; Garfinkel et al. 2018; Simpson et al. 2011). The large positive tropical anomalies in the lower stratospheric WV observed at the end of 2020 are consistent with the known behavior associated with a La Niña. This narrow band of positive anomalies in December 2020 is shown in contrast

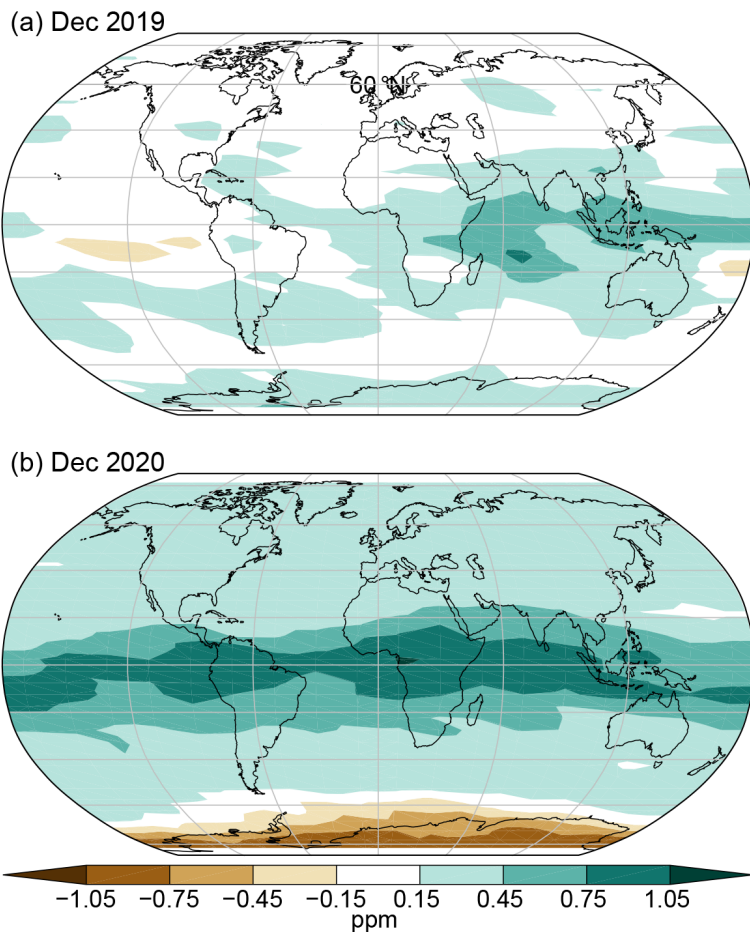


Fig. 2.62. Deseasonalized monthly lower stratospheric Microwave Limb Sounder (MLS) anomalies (ppm; 2004–20 base period) centered on 82 hPa in (a) Dec 2019 and (b) Dec 2020 from the *Aura* MLS.

to the same month of the previous year in Fig. 2.62.

In addition to the tropical stratospheric WV features in 2020, there are several notable higher latitude features. First, strong negative WV anomalies at high southern latitudes at 82 hPa in the last several months of 2020 (Figs. 2.60b, 2.62b) are likely the signal of anomalously strong dehydration associated with the very strong and persistent Antarctic vortex (see sections 2b5, 6h). The remarkably long-lived and stable Antarctic vortex likely explains why the dry anomaly is most noticeable at the very end of the year rather than earlier in austral spring.

Additionally, the positive tropical lower stratospheric WV anomaly discussed previously appears to be somewhat shifted toward the SH in the early part of the year (Fig. 2.60b). This anomaly may be related to the rapid injection of wet tropospheric air into the stratosphere by Australian bushfires of record-breaking intensity at the beginning of 2020 (Kablick et al. 2020; Khaykin et al. 2020). Of course, this anomaly occurs in concert with widespread positive WV anomalies in the tropics, so it is not possible

to quantitatively determine the contribution of the fires to stratospheric WV with the analysis presented here. Further modeling and analysis should be able to shed light on the contribution of the Australian bushfires to stratospheric WV levels in 2020 in the context of other sources of variability such as QBO and ENSO.

6) Tropospheric ozone—J. R. Ziemke and O. R. Cooper

Tropospheric ozone is the third-most effective climate-forcing greenhouse gas following CO₂ and CH₄ (IPCC 2013). Average global radiative forcing due to tropospheric ozone is $+0.4 \pm 0.2 \text{ W m}^{-2}$ and thus contributes to net warming of the atmosphere. In addition, tropospheric ozone is a surface pollutant damaging to vegetation and human health (Fleming et al. 2018; Mills et al. 2018), and it is the primary producer of OH radical (OH), which is the main oxidant of tropospheric pollutants. The sources for tropospheric ozone include transport from the stratosphere, non-combustive, non-biogenic volatile organic compound (VOC) sources such as solvents or fuel evaporation, photochemical production from precursors that include non-methane biogenic hydrocarbons, CH₄, lightning NO_x, and also emissions generated from the combustion of fossil fuels and biomass burning (Young et al. 2013, 2018; Monks et al. 2015; McDonald et al. 2018; Archibald et al. 2020). The main drivers of planetary-scale variability of tropospheric ozone include dynamical forcing from the ENSO and Walker circulation in the tropics, and “weather system” baroclinic waves in midlatitudes (Chandra et al. 1998, 2009; Sun et al. 2014; Ziemke et al. 2015). The main drivers of small-scale patterns in tropospheric ozone are local emissions of ozone precursors, both anthropogenic and natural, and ozone surface deposition driven mainly by vegetation

(Archibald et al. 2020). The large temporal variability of tropospheric ozone from diurnal to inter-annual timescales makes it difficult to determine decadal trends from regional to global scales (Neu et al. 2014; Cooper et al. 2014; Lin et al. 2014; Barnes et al. 2016; Strode et al. 2019; Tarasick et al. 2019).

Since 2012, all *State of the Climate* reports have provided updates on global tropospheric ozone based on independent measurements from ground- and satellite-based instruments (Ziemke and

Cooper 2019, and references therein). Due to limited annual updates of ground-based observations, these reports have relied primarily on combined *Aura* Ozone Monitoring Instrument (OMI) and MLS satellite ozone measurements (Ziemke et al. 2019). Vertical resolution of OMI/MLS monthly tropospheric column ozone is 2–3 km about the tropopause with ~2 DU (7%) precision in regional measurements; uncertainties in calculated trends are about 0.5 DU decade⁻¹ (1.5% decade⁻¹). OMI/MLS data show broad regions of positive 2020 tropospheric ozone column anomalies (relative to the 2005–19 average) of ~1.2 DU (4%) in the NH midlatitudes, with smaller anomalies of ~1 DU or less elsewhere (Plate 2.1ab). Hemispheric and global average tropospheric ozone burdens and their 95% confidence levels for 2020 were 160 ± 7 Tg (0°–60°N), 145 ± 8 Tg (0°–60°S), and 304 ± 8 Tg (60°S–60°N; Fig. 2.63). Trends and their 95% confidence levels (in units Tg yr⁻¹) in hemispheric and 60°S–60°N burdens from October 2004 through December 2020 are shown in Fig. 2.63; these trends correspond to increases of about 0.50 ± 0.15% yr⁻¹ for all three curves. Spatially, the trends are overwhelmingly positive, the strongest of which are ~+3.2 DU decade⁻¹ (~+1% yr⁻¹) above India and East/Southeast Asia, extending eastward over the North Pacific Ocean (Fig. 2.64). These trends are consistent with model estimates based on strengthening emissions of ozone precursors from Southeast, East, and South Asia, primarily due to fossil fuel combustion (Zhang et al. 2016b; Lin et al. 2014; Ziemke et al. 2019) and with NH ozone trends (1994–2016) as observed by instrumented commercial aircraft (Gaudel et al. 2020).

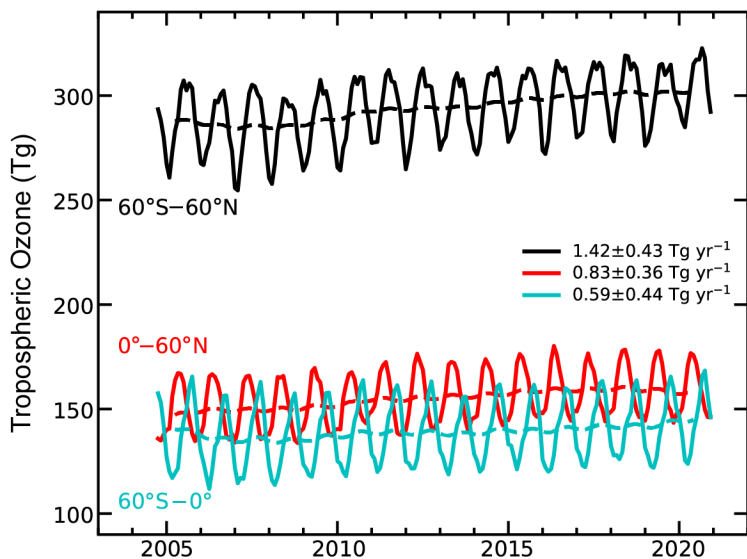


Fig. 2.63. Monthly averages of Ozone Monitoring Instrument / Microwave Limb Sounder (OMI/MLS) tropospheric ozone burdens (Tg) from Oct 2004 through Dec 2020. The top curve (black) shows 60°S–60°N monthly averages (solid) with 12-month running mean (dashed). The bottom two curves show monthly averages (solid) and running means (dashed) for the Northern Hemisphere (red) and Southern Hemisphere (blue). Slopes of linear fits to the data are presented with their 95% confidence-level uncertainties.

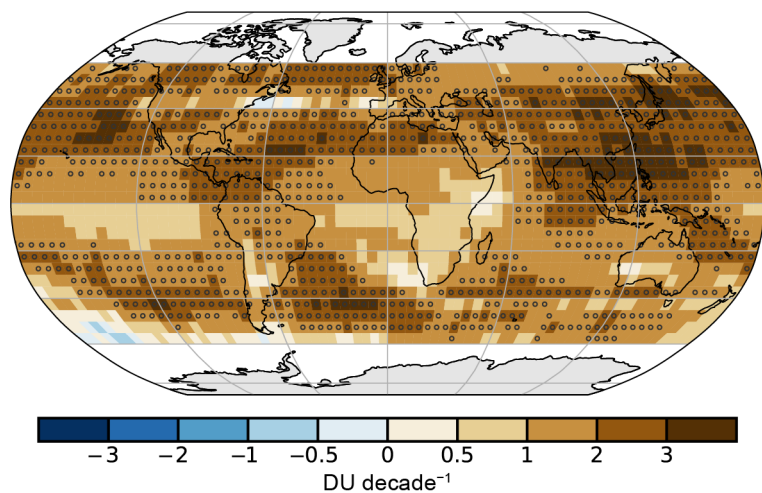


Fig. 2.64. Linear trends in Ozone Monitoring Instrument / Microwave Limb Sounder (OMI/MLS) tropospheric column ozone (DU decade⁻¹) on a 5° × 5° grid from Oct 2004 through Dec 2020. Asterisks denote trends with *p*-values less than 0.05. Trends were calculated using a multivariate linear regression model (e.g., Randel and Cobb 1994, and references therein) that included a seasonal cycle fit and the Niño-3.4 index as an ENSO proxy; trend uncertainties included autoregressive adjustment via Weatherhead et al. (1998).

Models indicate that ozone produced in these areas is transported northward and eastward in the free troposphere over the North Pacific Ocean (Zhang et al. 2020), as supported by the trend patterns in Fig. 2.64. Positive trends in the SH extra-tropics have been linked to a broadening of the Hadley circulation (Lu et al. 2018a).

Three long-term baseline monitoring sites with quality assured data are available for updating surface ozone trends through 2020: 1) Mauna Loa Observatory (MLO), Hawaii (19.5°N, 155.6°W, 3397 m a.s.l.); 2) South Pole Observatory (SPO), Antarctica (90°S, 59°E, 2840 m a.s.l.); and 3) Barrow Atmospheric Baseline Observatory (BRW), near Utqiagvik, Alaska (71.3°N, 156.6°W, 11 m a.s.l.). Continuous ozone measurements began at MLO in September 1973, at SPO in January 1975, and at BRW in March 1973, with reliable observations available at SPO for the years 1961–63 and at MLO for the years 1957–59 (Tarasick et al. 2019). Observations at remote baseline sites are important for understanding long-term ozone trends in the boundary layer, but they do not necessarily match the trends in the free troposphere, which have been overwhelmingly positive since the mid-1990s, as measured by ozonesondes, lidars, and commercial aircraft (Cooper et al. 2020).

Ozone levels at BRW in the Arctic increased by 3 ppbv (11%) since 1973. The limited data at MLO and SPO from the 1950s and 1960s indicate that ozone levels at these remote high-elevation sites were similar in the mid-twentieth century despite being located in different hemispheres. Ozone levels at SPO have changed little since the 1960s, with only a slight increase of ~2 ppbv (6%) from 1975 to 2020 (Fig. 2.65). In contrast, ozone levels at MLO increased at the rate of 0.14 ± 0.05 ppbv yr⁻¹, resulting in a 17% increase since 1973. MLO experiences high inter-annual ozone level variability due to its location in the transition region between tropical and extratropical air masses. The ozone level trend in the extratropical air masses can be isolated by focusing on the dry air masses, which tend to originate at higher altitudes and latitudes to the west and northwest of MLO (Gaudel et al. 2018). The trend in the dry air masses is 50% greater compared to the trend using all air masses (10.1 ppbv total increase since 1974, or 24%), which implies that the site is influenced by ozone level increases in upwind regions to the west and northwest, most likely Asia where surface and free tropospheric ozone levels have generally increased over the past 2 decades due to increased anthropogenic emissions of ozone precursor gases (Zhang et al. 2016b; Cohen et al. 2018; Lu et al. 2018b; Gaudel et al. 2018, 2020).

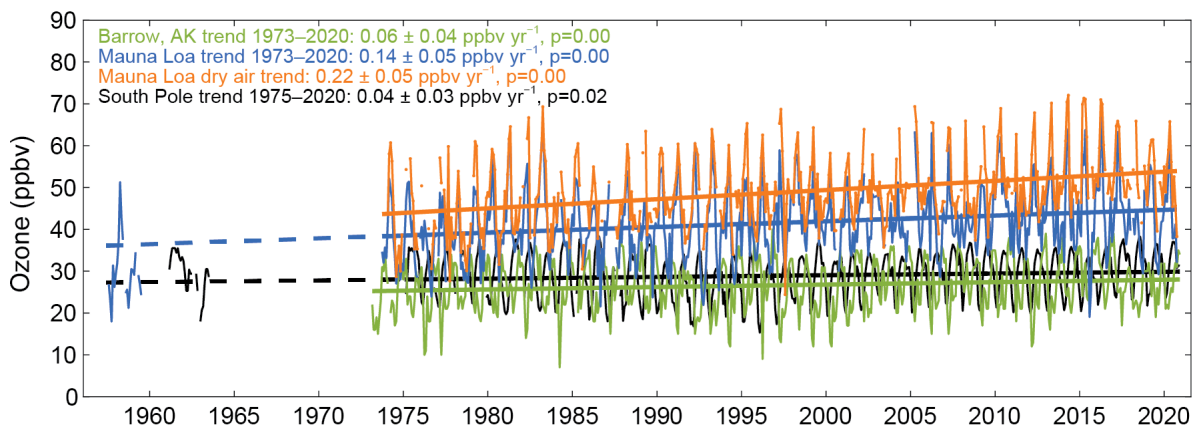


Fig. 2.65. Monthly median ozone (ppbv) at Barrow Observatory (Mar 1973–Dec 2020, green) and South Pole (Jan 1975–Dec 2020, black) using data from all hours of the day. Additional data from South Pole are shown for the early 1960s. Also shown are nighttime monthly median ozone values at Mauna Loa (MLO) calculated with all available data for months with at least 50% data availability, Oct 1973–Oct 2020 (blue), with early observations from the late 1950s. In addition, the monthly median values associated with dry air masses (orange) at MLO are included (dewpoint < the climatological monthly 40th percentile, and a sample size of at least 24 individual hourly nighttime observations). Trends (solid straight lines) are based on least-squares linear regression fit through the monthly values (1970s–2020), and reported with 95% confidence intervals and p -values. The MLO and South Pole trend lines are extrapolated back in time to the late 1950s (dashed lines).

7) Carbon monoxide—J. Flemming and A. Inness

Carbon monoxide (CO) plays a significant role in determining the abundance of climate-forcing gases like CH₄ and tropospheric ozone through OH chemistry (Hartmann et al. 2013). CO is therefore regarded as an indirect climate-forcing agent. Sources of CO include incomplete fossil fuel and biomass combustion and in situ production via the oxidation of CH₄, isoprene, and other organic trace gases. Combustion and atmospheric chemical sources typically produce similar amounts of CO on the global scale but vary in space and time because of the varying distribution of anthropogenic and biomass burning CO emissions as well as biogenic isoprene emissions.

CAMS (<https://atmosphere.copernicus.eu>) produced a retrospective analysis of CO, aerosols, and ozone for the period 2003–20 by assimilating satellite retrievals of atmospheric composition with the ECMWF model (Inness et al. 2019). This CAMS reanalysis assimilated thermal infrared (TIR) column CO retrievals of the Measurement of Pollution in the Troposphere (MOPITT) instrument (Deeter et al. 2014) globally, only excluding observations polewards of 65°N/S using the ECMWF 4D-VAR data assimilation system. The anthropogenic CO emissions used in the ECMWF model were taken from the MACC/CityZEN EU projects (MACCity) inventory (Granier et al. 2011), which estimates emission trends according to the IPCC RCP 8.5 scenario. No COVID-19 pandemic-related emissions modifications for 2020 were applied in the assimilation. Anthropogenic biomass burning emissions were taken from the Global Fire Assimilation System (GFAS) v1.2 (Kaiser et al. 2012; see section 2h3).

Figure 2.66 shows the time series of the monthly mean global burden of CO from the CAMS reanalysis for the period 2003–20. The total burden in 2020 was similar to the burden in the previous years, with the exception of the year 2015 when the global CO burden was dominated by emissions from fires in Indonesia (Huijnen et al. 2016). Approximated with a linear trend over the whole period, the total global CO burden has declined by $-1.5 \text{ Tg CO yr}^{-1}$, and as piecewise trends by -3.1 , -14.0 , and $+0.1 \text{ Tg CO yr}^{-1}$ for 2003–07, 2008, and 2009–20, respectively, following Flemming and Inness (2019). Figure 2.67 shows clean marine boundary layer (MBL) mean surface CO for five zonal bands based on measurements of weekly air samples collected at MBL sites in the NOAA Global Greenhouse Gas Reference Network (Novelli et al. 2003; Pétron et al. 2020). The global negative trend seen in both surface and satellite records is dominated by the decrease of the CO burden in the mid- and high-latitudes of the NH, likely as a result of reductions in vehicle emissions (Wang et al. 2012). The tropics and the SH exhibit no trends or a small positive trend.

The spatial patterns of the 2020 annual CO total column anomalies (Plate 2.1ac) agree with the multi-year trends and show about 0%–5% higher values throughout the SH and most of the tropics and negative values for most of the NH mid- and high-latitudes. The most noticeable negative

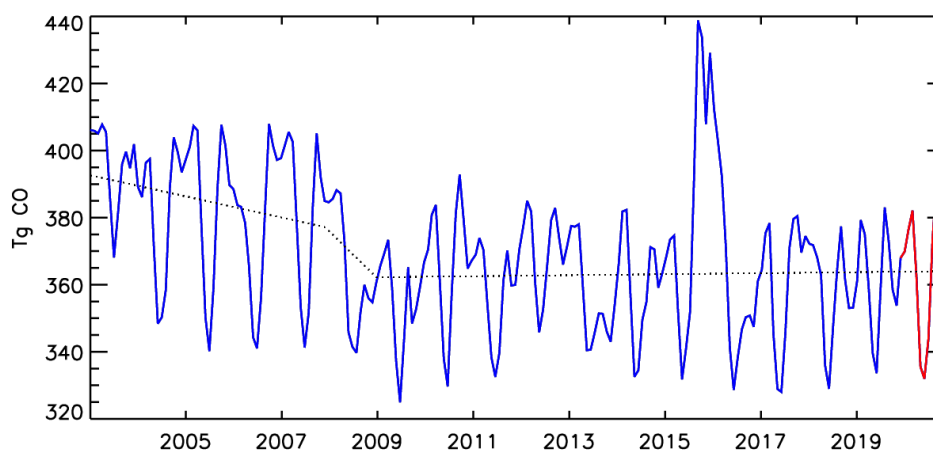


Fig. 2.66. Time series of monthly global carbon monoxide (CO) burdens (Tg CO) from the total column CO output from the CAMSRA (TCCO CAMSRA) and a piecewise linear trend for the periods 2003–07, 2008, and 2009–20. The red line indicates the year 2020.

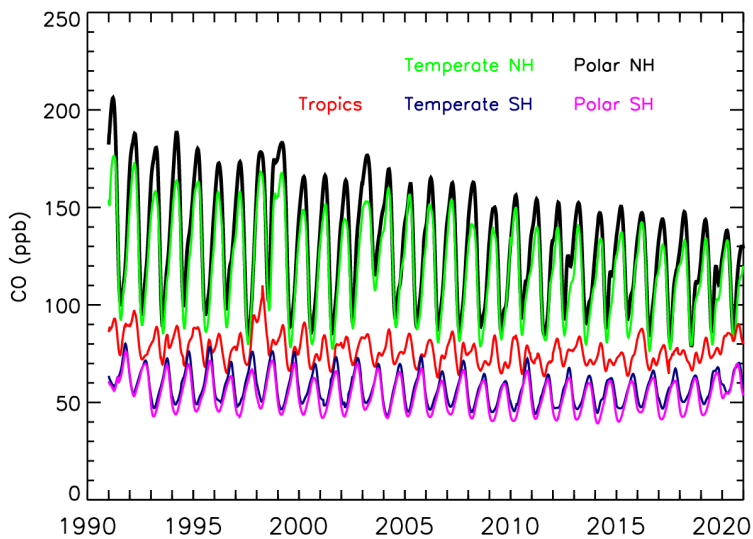


Fig. 2.67. Time series of carbon monoxide (CO) over the clean marine boundary layer for the polar NH (53.1°–90°N, black), temperate NH (17.5°–53.1°N, green), tropics (17.5°S–17.5°N, red), temperate SH (17.5°–53.1°S, dark blue), and SH (53.1°–90°S, magenta) for the period 1991–2020.

anomaly in 2020 appeared over maritime Southeast Asia (Indonesia) and was caused by low fire activity in the region, because La Niña conditions were starting to evolve in (austral) spring 2020. Positive anomalies occurred over the western United States and over northeast Siberia (Yakutia), caused by intense biomass burning in boreal summer and early autumn 2020 (see also sections 2g3, 2h3). The widespread positive anomaly over the southern South Pacific Ocean was the result of long-range transport of CO plumes originating from intense fires in southwestern Australia between December 2019 and January 2020. The observed increase in tropical and SH MBL CO in 2020 was also most likely caused by the Australian fires.

The reduction in anthropogenic CO emission during the COVID-19 pandemic has been estimated to be up to 30% in North America and Europe and 10%–20% over China during the height of the lockdown measures (Foster et al. 2020; Doumbia et al. 2021). The CAMSRA CO total columns over Europe and North America were the lowest since 2003 for the period February–April (Fig. 2.68). However, the attribution of these anomalies to COVID-19-related emission reduction is complicated by the multi-year negative CO trends in the regions and the unquantified influence of other factors such as meteorological conditions.

The reduction in anthropogenic CO emission during the COVID-19 pandemic has been estimated to be up to 30% in North America and Europe and 10%–20% over China during the height of the lockdown measures (Foster et al. 2020; Doumbia et al. 2021). The CAMSRA CO total columns over Europe and North America were the lowest since 2003 for the period February–April (Fig. 2.68). However, the attribution of these anomalies to COVID-19-related emission reduction is complicated by the multi-year negative CO trends in the regions and the unquantified influence of other factors such as meteorological conditions.

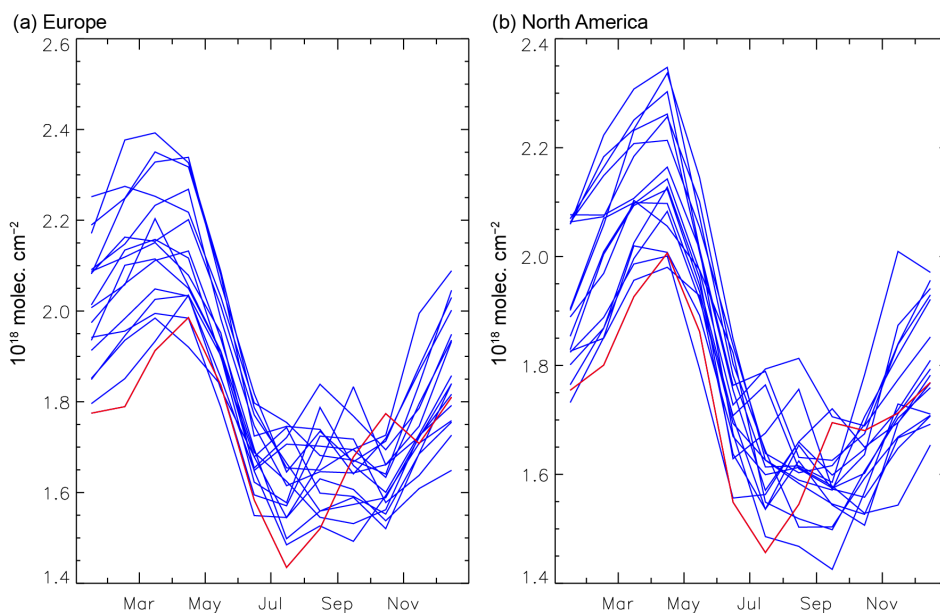


Fig. 2.68. Seasonal cycle of monthly global carbon monoxide (CO; ppb) total column (10^{18} molec. cm^{-2}) over (a) Europe and (b) North America for all years in the 2003–19 period (blue) and for 2020 (red) from the CO total column output from the CAMSRA (TCCOscf CAMSRA).

h. Land surface properties

1) Land surface albedo dynamics—G. Duveiller and N. Gobron

The presence and absence of snow cover dominates the large-scale spatial patterns of the land surface albedo for 2020 (Plates 2.1ad, ae). The most prominent feature was a strong reduction in albedo in Europe from western Germany to Moscow, and from southern Scandinavia to the Balkans, corresponding to a large deficit in snow cover over this area, particularly during the January–March 2020 period (see sections 2c2, 7f), when temperatures were particularly high (see section 2b1). This same effect occurred to a lesser extent in the eastern half of the United States. Reductions in the snow cover extent during spring over large parts of Siberia also contributed to reducing the overall albedo of the Northern Hemisphere (NH). Conversely, an anomalously high duration of snow cover resulted in a rise in albedo in several parts of the world. For northeastern China, the Tibetan plateau, and central parts of North America, excess snow cover duration occurred in boreal winter (January–March), for Canada and northern Scandinavia in boreal spring (April–June), and for Patagonia in austral winter (July–September). All left a clear mark in the annual maps of albedo, both in the visible and near infrared parts of the spectrum (Plates 2.1ad, ae).

Beyond the strong effect of snow, the land surface albedo dynamics were affected by vegetation growth, which darkens the surface, and by dry climatic conditions, which typically lighten the surface due to either the hastening of leaf senescence or the drying up of bare soil. In 2020,

warm conditions across most of the globe and during considerable portions of the year contributed to the development of greener surfaces (see section. 2h2), which translated to lower visible albedo. This was particularly evident over India, northern East Africa, and southeastern Australia, all of which had higher-than-average soil moisture during large parts of the year (see section 2d10). On the other hand, drought conditions increased visible albedo in southern Africa (mostly in Mozambique) and in central South America (around the Gran Chaco but also extending eastward and northward, see section 2d11). Rain deficits attributable to the development of La Niña in late 2020 further exacerbated the dry conditions in these regions of South America (see section 7d). However, drier conditions in the later part of the year over various parts of the NH did not considerably alter the albedo patterns that were mostly dominated by spring snow cover.

Overall, 2020 contributed to the general darkening trend of the land surface with respect to visible albedo (Figs. 2.69, 2.70). There was, however, a clear separation between NH and Southern Hemisphere (SH), with the SH seeing its second consecutive brighter year than the 2003–10 baseline, and following a steady

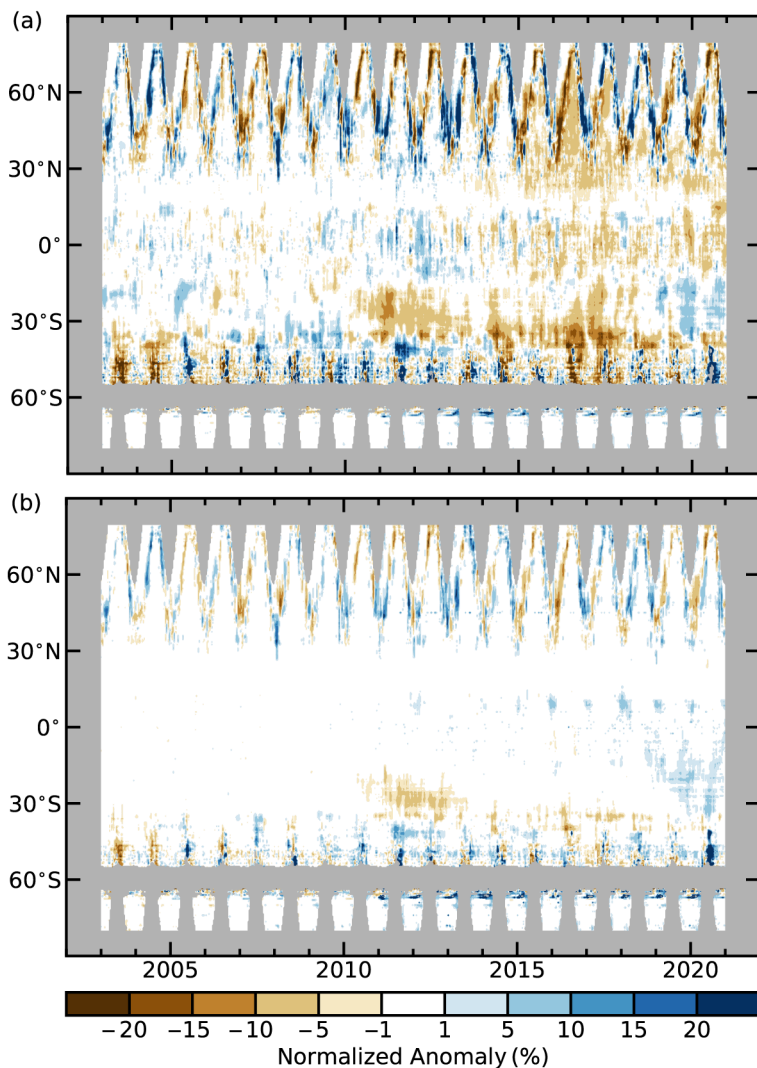


Fig. 2.69. Zonally averaged (a) white sky visible and (b) near infrared albedo anomalies (%) for the period 2003–20 using a 2003–10 baseline period.

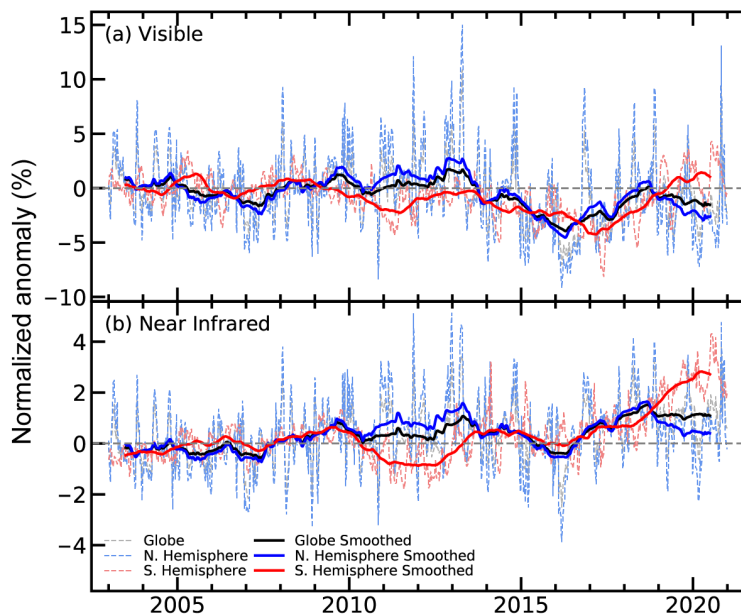


Fig. 2.70. Global (black/gray lines), NH (blue), and SH (red) land surface (a) visible and (b) near infrared albedo anomalies for the period 2003–20 using a 2003–10 baseline period. Dotted lines denote each monthly period; solid lines indicate the 6-month running averaged mean.

of vegetation (Cescatti et al. 2012). The MODIS albedo products provide separate estimations for different parts of the shortwave electromagnetic spectrum, allowing this analysis to focus separately on the visible and the near infrared parts of the spectrum. Furthermore, the analysis was based on estimation of white-sky albedo (bi-hemispherical reflectance), which is defined as albedo in the absence of a direct radiation component and when the diffuse radiation component is isotropic.

2) Terrestrial vegetation dynamics—N. Gobron

The Fraction of Absorbed Photosynthetically Active Radiation (FAPAR) plays a critical role in assessing the primary productivity of canopies, the associated fixation of atmospheric CO₂, and the energy balance of the surface. FAPAR anomalies from the 1998–2010 average show significant regional variations in the vegetation productivity conditions worldwide in 2020 (Plate 2.1af). The SH appeared similar to typical La Niña conditions, with largest negative anomalies (brown) occurring over Argentina, Paraguay, and Chile and largest positive (dark blue) in eastern Brazil, Malaysia, and Indonesia (see section 2e1). However, there were negative anomalies in regions such as Mozambique, southern Madagascar, and most of Australia, except the southeast. To a lesser extent, negative regional anomalies were observed near the northwest coast of the South American continent.

In the NH, the largest negative anomalies were observed over herbaceous vegetation in Norway, northern Sweden, and Canada. Local negative occurrences were notable in the north-central United States (Colorado, Iowa, North Dakota, and Wisconsin), but also in California, as well as in the Russian Far East, including Kamchatka. The biggest positive anomalies occurred in eastern China and India and north Pakistan, South Sudan, and Kenya, followed by southern and central Europe. Similar to 2016, some arctic regions in Russia and Canada also showed strong positive anomalies.

La Niña had an impact on vegetation health by contributing heavy rains over Indonesia, India, and western Brazil. In contrast, Argentina, Paraguay, and Chile recorded a strong negative anomaly that increased from June to December due to the dry conditions caused by La Niña coupled with above-normal temperatures (see section 2d4). At the start of the dry season in April,

brightening trend since its lowest point on the satellite record in 2017. With respect to the albedo in the near infrared part of the spectrum, the overall trend was toward a slight brightening, which was more pronounced in the SH than in the NH.

This analysis of the land surface albedo relied exclusively on satellite information. Surface albedo was retrieved from multi-spectral surface reflectance measured by the Moderate Resolution Imaging Spectroradiometer (MODIS) instrument on-board the *Aqua* and *Terra* satellite platforms (Schaaf et al. 2002). Satellite retrievals are probably the most accurate way to assess surface albedo at the global level as they rely on a limited set of assumptions. They have been shown to provide sufficiently accurate estimates when compared to ground measurements both on ice sheets (Stroeve et al. 2013) and over different types

northern Mozambique and western Madagascar suffered from rainfall deficits that induced the negative annual anomalies. Strong negative anomalies were also observed over some regions of Australia that suffered from the devastating 2019/20 summer bushfires, although vegetation partially recovered locally with adequate rains.

The European summer heat wave (see sections 2b3, 7f) significantly impacted the vegetation productivity, as can be seen in the annual anomaly of herbaceous vegetation in Sweden and Norway. The rest of Europe was also strongly affected during spring and summer, but this was not apparent per se in the annual analysis. During spring, Canadian vegetation suffered from very cold temperatures that affected the annual value. The western and central United States experienced both high temperatures and dry conditions in much of the year, and the impacts on central states were perceived in the annual study. Terrestrial photosynthesis was enhanced over eastern China, with vegetation growth noticeable since 2015 due to important changes in

the main land use, with a net increase in leaf area mainly from croplands (Gobron 2019; Chen et al. 2019). The strong positive anomalies over some northern latitudes were largely due to the warm spring that was ideal for vegetation growth. Furthermore, heavy rains enhanced the positive anomalies in China and East Africa.

Figure 2.71 shows the latitudinal anomalies average from 1998 to 2020 compared to the base period 1998–2010. The strong seasonal deviations mainly include positive anomalies north of 20°N after 2014. In 2020, this positive behavior extended south of the equator. Negative anomalies from 2002 to 2014 affected the SH, except in 2010–12. Around 30°S, 2019/20 anomalies again became again negative.

Figure 2.72 draws the global and bi-hemispherical anomalies, revealing more seasonal oscillations in the SH than in the NH. Analysis of SH data reveals two positive extreme peaks in 2000 and 2017, while extreme minima events occurred in 2008–09. Afterwards, SH anomalies increased with interannual variations and were positive since 2014. The NH experienced fewer extreme negative events compared to the SH, and its photosynthetic activity increased from 2010 to 2017 and, after a brief decline in late 2017/early 2018, increased again to a high value in 2020. The global average has been positive since 2010 with a positive trend.

Earth observations measurements are fundamental for monitoring the activity of vegetation worldwide. These observations are used to infer FAPAR,

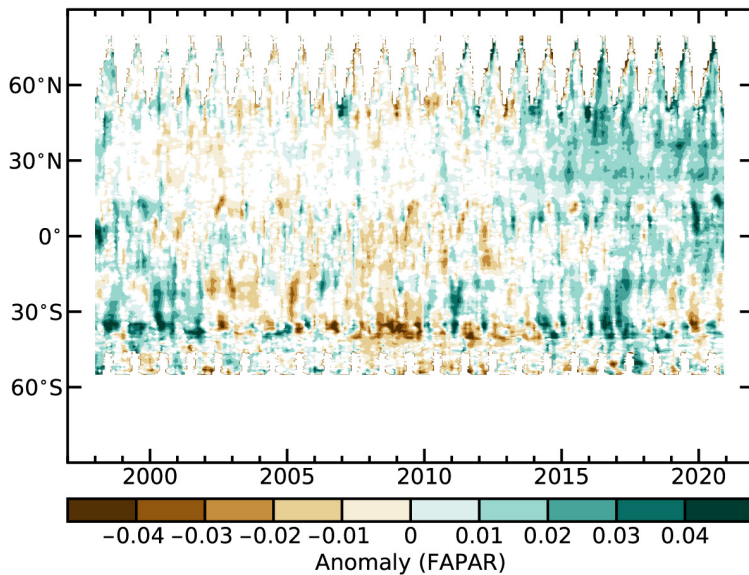


Fig. 2.71. Zonally averaged Fraction of Absorbed Photosynthetically Active Radiation (FAPAR) anomalies for 1998–2020 (1998–2010 base period).

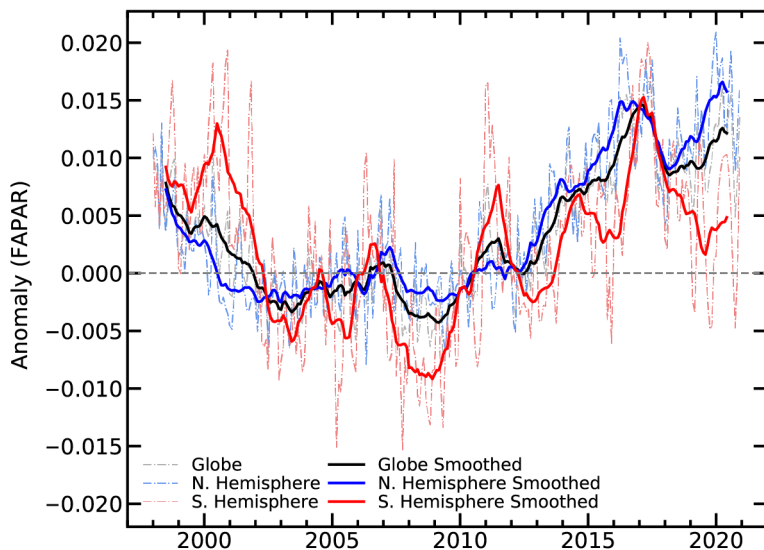


Fig. 2.72. Global (black/gray lines), Northern Hemisphere (blue), and Southern Hemisphere (red) Fraction of Absorbed Photosynthetically Active Radiation (FAPAR) anomalies for 1998–2020 (1998–2010 base period). Dotted lines denote each monthly period; solid lines indicate the 6-month running averaged mean.

an essential climate variable (as defined by GCOS [2016]). The 2020 analysis merged 23 years of global FAPAR monthly products based on three optical sensors from 1998 to 2020 (Gobron et al. 2010; Pinty et al. 2011; Gobron and Robustelli 2013; the base period is 1998–2010). Comparisons between each dataset and with multiple proxies using ground measurements provide an estimate of the uncertainties and biases. This long-term global FAPAR dataset presents an estimated average uncertainty close to 5%–10%.

3) Biomass burning—J. W. Kaiser and G. R. van der Werf

The year 2020 illustrates how two distinct trends that have emerged in global biomass burning over the last decade shape current pyrogeography: a declining trend in many savanna regions related to agricultural expansion and an increasing trend in many forested regions where climate change increases the flammability of the landscape. It was one of the lowest fire years in the Global Fire Assimilation System (GFAS) record (13% below the 2003–10 average), but there was also extreme regional fire activity (Table 2.11). This activity included the continuation of fires in southeastern Australia early in the year that had started in late 2019, fires above the Arctic circle in Russia, and in the western United States.

Global fire emissions are generally dominated by savanna burning (Fig. 2.73). For example, African fire emissions comprise roughly half of total global fire carbon emissions; but fires here and in many other savanna regions have decreased over the past decade (Andela et al. 2017). This trend continued in 2020 with Africa north (south) of the equator seeing emissions

11% (12%) below the 2003–10 average. Given the dominance of these regions, this reduction was reflected in the global total of 1741 Tg C emissions from biomass burning in 2020, which was the fourth lowest of the past 18 years. The lowest fire year in this period was 2018 with 1661 Tg C, followed by 2017 and 2013 with 1683 Tg C and 1690 Tg C, respectively. While the long-term trend is partly driven by agricultural expansion into savanna ecosystems and associated fragmentation of the landscape, anomalous rainfall years also influence interannual variability on top of the declining trend.

Tropical forests in the Amazon saw the highest fire activity since 2012, surpassing the year 2019, which attracted more media attention at that time. The emerging upward trend is also supported by independent VIIRS observations (<https://globalfiredata.org/pages/2020/09/22/amazon-fire-activity-in-2020-surpasses-2019>; Schroeder et al. 2014). In contrast, fire activity in tropical

Table 2.11. Annual continental-scale biomass burning budgets in terms of carbon emission (Tg C yr⁻¹) from Global Fire Assimilation System (GFASv1.4).

Time period		2003–10	2020	
Quantity in Tg C yr ⁻¹	Latitude/longitude	Mean value (range)	Value	Anomaly (percent)
Global		2010 (1828–2272)	1741	–269 (–13%)
North America	30°–75°N 190°–330°E	79 (63–109)	65	–14 (–18%)
Central America	13°–30°N 190°–330°E	42 (31–58)	42	0 (0%)
South America	13°–60°S 190°–330°E	427 (255–524)	418	–9 (–2%)
Europe and Mediterranean	30°–75°N 330°–60°E	37 (29–62)	30	–7 (–17%)
N. Hem. Africa	0°–30°N 330°–60°E	419 (353–453)	374	–45 (–11%)
S. Hem. Africa	0°–35°S 330°–60°E	484 (444–528)	426	–58 (–12%)
Northern Asia	30°–75°N 60°–190°E	176 (99–418)	193	+17 (+10%)
South-East Asia	10°–30°N 60°–190°E	128 (107–150)	104	–24 (–18%)
Tropical Asia	10°S–10°N 60°–190°E	118 (38–228)	23	–95 (–80%)
Australia	10°–50°S 60°–190°E	99 (47–137)	64	–34 (–35%)
Arctic	67°–90°N 0°–60°E	4 (0–11)	37	+32 (+724%)
Western United States	30°–49°N 230°–260°E	15 (7–25)	42	+27 (+183%)

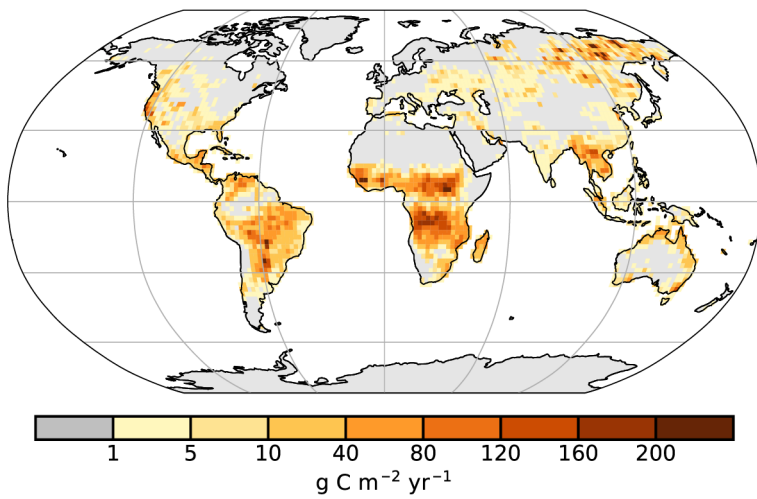


Fig. 2.73. Global map of fire activity in 2020 in terms of carbon consumption ($\text{g C m}^{-2} \text{yr}^{-1}$). (Source: Global Fire Assimilation System GFASv1.4.)

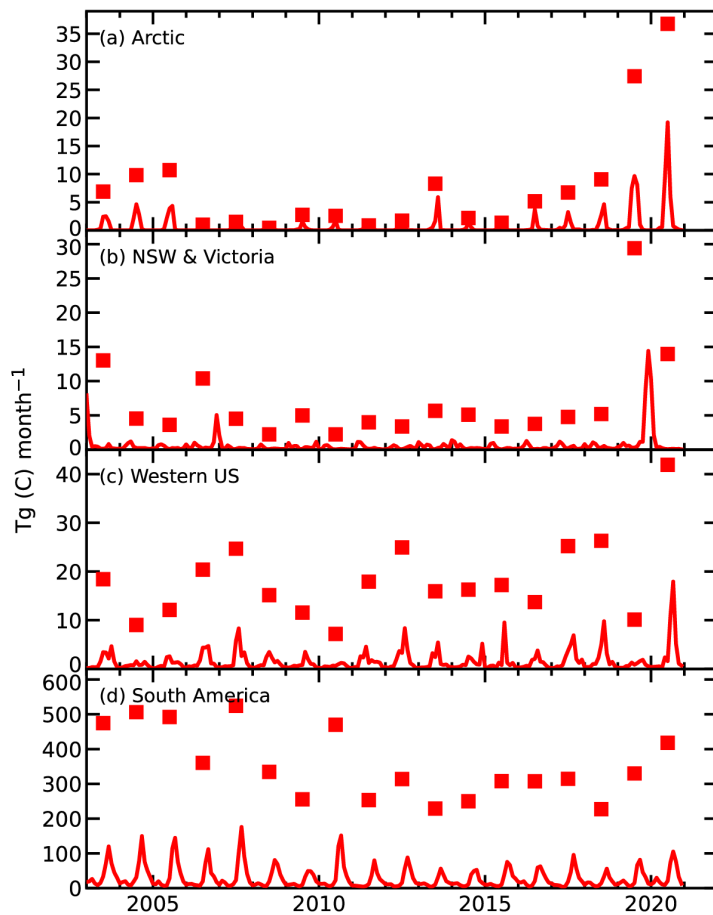


Fig. 2.74. Time series of annual (squares) and monthly (lines) regional fire activity in terms of carbon consumption: (a) Arctic, (b) New South Wales and Victoria, (c) western United States, and (d) South America. (Source: Global Fire Assimilation System GFASv1.4.)

Emissions Database, version 4 with small fires (GFED4s), which is mostly based on burnt area observation and dates back to 1997 (van der Werf et al. 2017). It shows that the global fire emissions during the 1997–98 El Niño remain unsurpassed.

Asia—including Indonesia—was one of the lowest on record, related to relatively wet conditions as La Niña started to evolve during the fire season.

At higher latitudes, 2020 was record breaking in both southeastern Australia and the western United States, where extreme heat and drought contributed to unprecedented fire conditions (Van Oldenborgh et al. 2020). While Australia as a whole did not exhibit anomalies (Table 2.11) due to the dominance of savanna fires in the northern part of the country and because the fire season in southeastern Australia started in 2019, the combined 2019–20 southeastern Australian fire season was unprecedented. For example, emissions were the highest since at least 2003 (Fig. 2.74), burnt area in New South Wales was the largest since at least 1968 with more than 5 million ha, and ~43% of the total Australian coverage of Eucalyptus forests and woodlands burned (Bowman et al. 2021). In the western United States, total fire emissions almost tripled compared to the 2003–10 mean and thus continued the recent upward trend (Fig. 2.74).

The Arctic experienced its highest fire year in 2020, surpassing the record set in 2019 (Kaiser et al. 2020; Sidebar 5.1) by 34%. Each of the last 5 years have thus seen more Arctic fires than the preceding year (Fig. 2.74). Most of the fires occurred in Arctic Asia, with Arctic America, and also all of Canada plus Alaska, experiencing their lowest fire year on record in 2020. While the fires burned within the Arctic circle and partly affected thawed permafrost, the largest fire complex was still in thinly forested regions and not in tundra, which leaves the long-term possibility of a partial uptake of the emitted carbon through re-growth.

The time series in Plate 1.1ac puts GFAS in the context of the Global Fire

GFAS produces global fire emission estimates in near real-time for the Copernicus Atmosphere Monitoring Service (Kaiser et al. 2012). Here, we used a consistent reprocessing of 2003–20 based on Collection 6 of the MODIS Fire Radiative Power product (Giglio et al. 2016). The 14% bias with respect to Collection 5 has been corrected and the satellite- and observation time-specific bias correction factors from Hüser et al. (2018) were applied for 17 August–2 September 2020 in order to compensate for the outage of observations from MODIS onboard the *Aqua* satellite.

4) *Phenology of primary producers*—D. L. Hemming, J. Garforth, J. O’Keefe, T. Park, A. D. Richardson, T. Rutishauser, T. H. Sparks, and S. J. Thackeray

During 2020, the satellite-derived (MODIS) normalized difference vegetation index (NDVI; Park et al. 2016) across the NH landmass (>30°N) revealed an earlier mean start of season (SOS_M), later end of season (EOS_M), and 1.8 days longer growing season, compared to the 2000–10 baseline (Fig. 2.75). These coincided with the second-warmest spring and warmest autumn on record across the NH (NOAA 2020). Regional differences resulted in 2.1 days earlier and 0.9 days later SOS_M in Eurasia (EA) and North America (NA), respectively. No clear signal in EOS_M was observed across NA, whereas, later EOS_M was dominant across EA (Fig. 2.75d). Overall, about 55% and 65% of the NH showed earlier SOS_M and later EOS_M in 2020. These spatial variations also correlate with spring and autumn surface temperature (section 2b1; NASA MERRA-2, Gelaro et al. 2017), which were 0.5°C (+1.2°C for EA, -0.95°C for NA) and 0.7°C (+1.0°C for EA, -0.05°C for NA) warmer in 2020 compared to the baseline. NH trends of earlier SOS_M and later (less significant) EOS_M over the last 21 years were noted in MODIS NDVI (SOS_M = -2.3 ± 0.7 days decade⁻¹, *p* = 0.01; EOS_M = 1.3 ± 0.9 days decade⁻¹, *p* = 0.18) while significant differences in magnitude were observed between

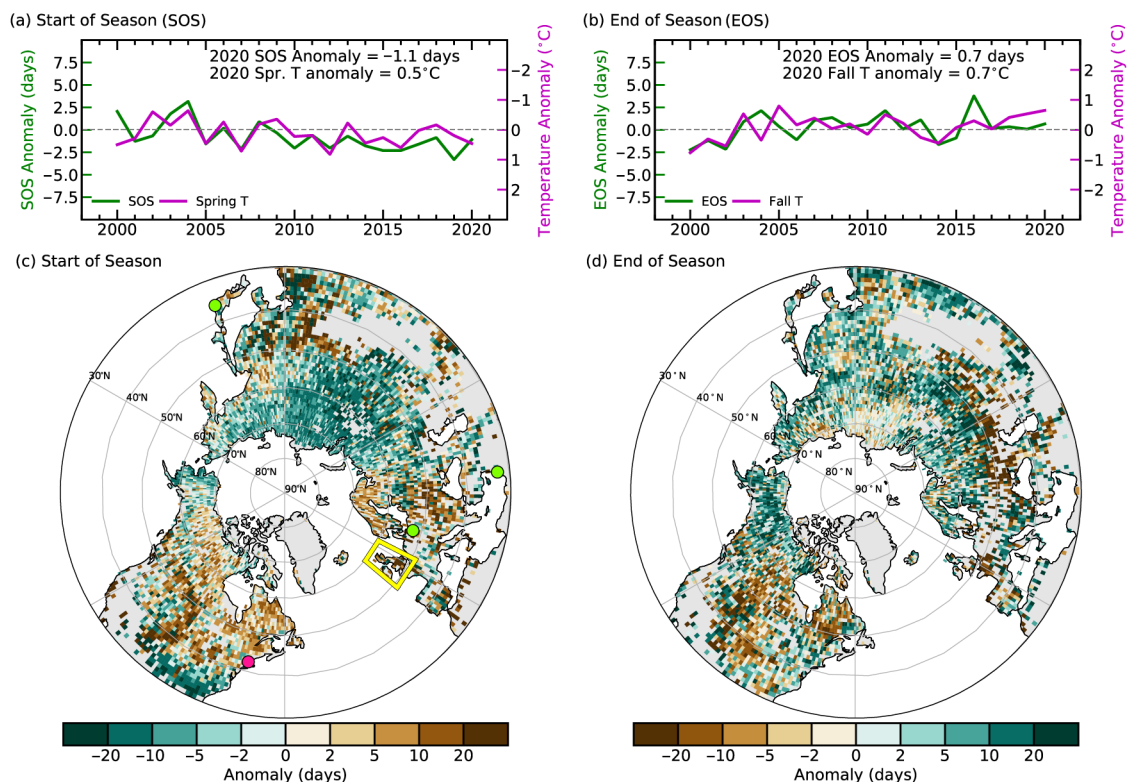


Fig. 2.75. (a) Time series of area-mean anomalies (days; base period 2000–10) in MODIS NDVI-based start of season (SOS) (green) and MERRA-2 spring (Mar–May, pink) temperature (°C) for Northern Hemisphere (>30°N). (b) Same as (a) but for end of season (EOS) (green) and autumn (Sep–Nov, pink) temperature. Note temperature scale reversal for (a). 2020 spatial pattern of (c) SOS and (d) EOS anomaly with respect to the baseline. Highlighted points and box identify the location of phenology sites shown in Fig. 2.76. (United States Harvard Forest, Massachusetts PhenoCam and Red oak [pink point]; United Kingdom mean Pedunculate oak [yellow box]; Lake Kasumigaura, Japan, Lake Kinneret, Israel and Müggelsee, Germany [green points]).

NA ($SOS_M = -0.05 \pm 0.5$ days decade⁻¹, $p = 0.24$; $EOS_M = 2.0 \pm 0.6$ days decade⁻¹, $p = 0.01$) and EA ($SOS_M = -1.7 \pm 0.6$ days decade⁻¹, $p = 0.02$; $EOS_M = 0.1 \pm 0.8$ days decade⁻¹, $p = 0.89$), indicating asymmetric extension of the growing season at the continental scale.

PhenoCam data across NA (Seyednasrollah et al. 2019) provide a link between the coarse and fine resolutions of satellite monitoring and site-level observations on individual organisms (Richardson et al. 2019). We compared PhenoCam-derived estimates (2008–20, $n = 13$) of start of season (SOS_{PC}) and end of season (EOS_{PC}) at Harvard Forest, a deciduous forest in Massachusetts, United States, with ground observations of Red oak (*Quercus rubra*) phenology ($SOS_{RO} = 50\%$ budburst and $EOS_{RO} = 50\%$ autumn color; Richardson and O’Keefe 2009, 2019), and MODIS SOS_M and EOS_M for the associated pixel (Figs. 2.76a,b). SOS_{PC} and EOS_{PC} were strongly correlated with SOS_{RO} and EOS_{RO} ($r = 0.90$ and 0.81 , respectively) and their timings were similar. Although SOS_{PC} and SOS_M were strongly correlated ($r = 0.79$), SOS_{PC} was later by 12 ± 3 days (Fig. 2.76a). The correlation between EOS_{PC} and EOS_M was weaker ($r = 0.48$), and EOS_{PC} was earlier on average by 48 ± 12 days (Fig. 2.76b). These differences may be explained in part by a mix of land cover types covered by the MODIS 5-km pixel. In 2020, SOS_{PC} (day 137, 16 May, ± 2 days) was 6 days later than in 2019, and consistent with the change for SOS_{RO} , which was 9 days later in 2020 than 2019. EOS_{PC} in 2020 (day 293, 19 October, ± 1 day) was unchanged, while EOS_{RO} was 4 days later than 2019. In comparison, SOS_M was 3 days earlier than 2019 and EOS_M remained unchanged (Figs. 2.76a,b). Later SOS_{PC} in 2020 was related to relatively cold spring temperatures and resulted in a growing season 5 days shorter than in 2019. 2020 had the shortest growing season observed at Harvard Forest in the last 13 years.

Dates of Pedunculate oak (*Quercus robur*) “first leaf” (SOS_{PO}) and “bare tree” (EOS_{PO}) recorded by citizen scientists across the United Kingdom have been collated by the Woodland Trust since 1999 (Collinson and Sparks 2008). The mean SOS_{PO} for the 2000–09 baseline was 26 April (day 116), and EOS_{PO} was 30 November (day 334), giving a 218-day growing season length (Figs. 2.76c,d). Both events were strongly influenced by temperature; SOS_{PO} advances by approximately 6 days for every 1°C increase in mean February–April temperature, and EOS_{PO} is delayed by approximately 3 days for every 1°C increase in October temperature. The year 2020, like 2019, had a very warm spring, and this resulted in the earliest United Kingdom SOS_{PO} in the 20-year series (10 days earlier than the in-situ baseline). October temperature was similar to recent years, and the EOS_{PO} date

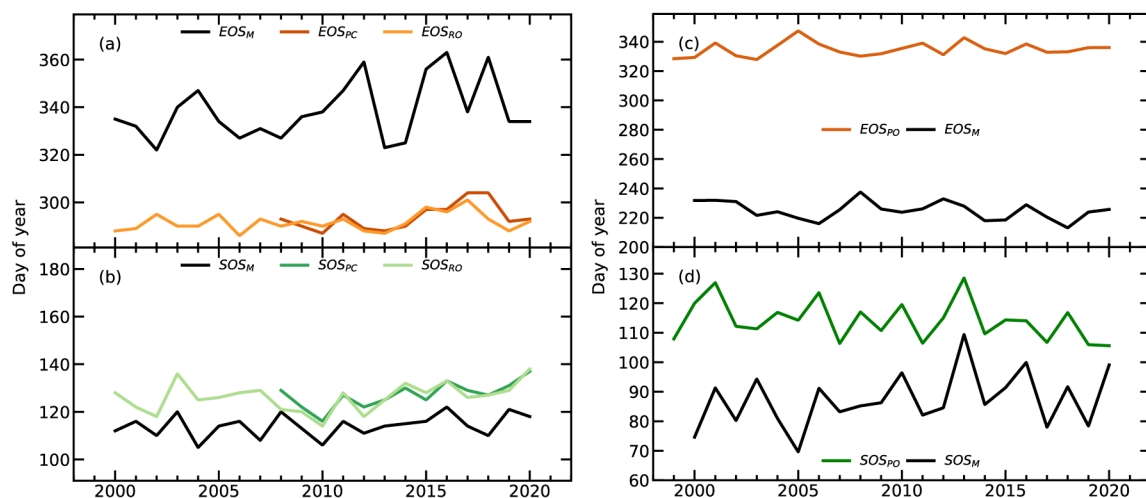


Fig. 2.76. Start of season (SOS) and end of season (EOS) phenology indicators derived from (a),(b) Harvard Forest, Massachusetts, United States, PhenoCam (SOS_{PC} and EOS_{PC}), Red oak ground observations (SOS_{RO} and EOS_{RO}), and MODIS remote sensing (SOS_M and EOS_M), and (c),(d) United Kingdom mean Pedunculate oak (SOS_{PO} and EOS_{PO}) and MODIS.

(note these were predicted from the temperature relationship due to COVID-19 monitoring restrictions) was approximately 2 days later than the baseline. The net result was a United Kingdom “oak season” 12 days longer than the baseline.

In 2020, monitoring data on lake water concentrations of the photosynthetic pigment chlorophyll-*a* were available to estimate the spring phytoplankton peak in three NH lake basins (Lake Kasumigaura in Japan, Lake Kinneret in Israel, and Müggelsee in Germany). Some in situ lake monitoring schemes were inactive in 2020 due to COVID-19 restrictions. The mean start of spring bloom during the 2000–10 baseline in these lakes ranged from 22 March (day 81, Lake Kasumigaura) to 21 April (day 111, Lake Kinneret). Spring peak was earlier in 2020 than the baseline in two lake basins (by 15 to 38 days), but later for Müggelsee (by 4 days). This variation between sites may relate to differences in climate or other factors that interact with climate to influence seasonal ecosystem behavior.

Sidebar 2.3. Long-term monitoring of vegetation state through passive microwave satellites—W. DORIGO, L. MOESINGER, R. VAN DER SCHALIE, R. M. ZOTTA, T. SCANLON, AND R. A. M. DE JEU

Microwave radiation emitted or reflected by the land surface is strongly affected by available water, including that stored in living biomass. The all-weather, sunlight-independent observing capacity of microwave satellites makes them complementary to satellites in the optical domain traditionally used to observe vegetation characteristics (Becker and Choudhury 1988; see section 2h2.). Particularly for areas with frequent cloud cover, such as the humid tropics, microwave satellites provide novel insights into vegetation dynamics, although with lower spatial detail (Rodriguez-Fernandez et al. 2018).

The portion of the radiance attenuated by the canopy is expressed by its vegetation optical depth (VOD), a parameter used in radiative transfer models to describe radiance interaction with vegetation. Long seen as a by-product of soil moisture retrievals (see section 2d10), VOD is increasingly proven to be a valuable indicator of land surface conditions itself. While VOD is not a biogeophysical variable per se, various studies have shown its close relationship to vegetation above-ground biomass (Mialon et al. 2020, Rodriguez-Fernandez et al. 2018), leaf area index (Vreugdenhil et al. 2017), gross primary production (Teubner et al. 2019), or canopy water content (Konings et al. 2017). Since VOD is wavelength-dependent and, with

increasing frequency, increasingly sensitive to the upper vegetation layer (Li et al. 2021), VOD estimates at low frequencies (L-band) are more closely related to forest biomass (Chaparro et al. 2019), while higher frequency observations (C-, X-, and Ku-band) show closer agreement with seasonal leaf dynamics and photosynthetic activity (Teubner et al. 2018; Fig. SB2.5) and, hence, are valuable phenological indicators (see section 2h4; Pfeil et al. 2020).

VOD products from various frequencies have been used to monitor global terrestrial carbon dynamics (Liu et al. 2015), assess the severity of agricultural droughts (Van Dijk et al. 2013; Crocetti et al. 2020), assess crop yield (Chaparro et al. 2018), model fire occurrence (Forkel et al. 2017, 2019) and terrestrial evaporation (Martens et al. 2017), and monitor land degradation (Liu et al. 2013) and deforestation (van Marle et al. 2015).

VOD observations from several available meteorological and Earth observation satellites, including SSM/I, TRMM, AMSR-E, and AMSR2, have been retrieved with the Land Parameter Retrieval Model (Meesters et al. 2005; Van der Schalie et al. 2018) and amalgamated into the long-term VOD Climate Archive (VODCA), which allows for studying variability and change at climatic time scales (Moesinger et al. 2020). VODCA contains individual

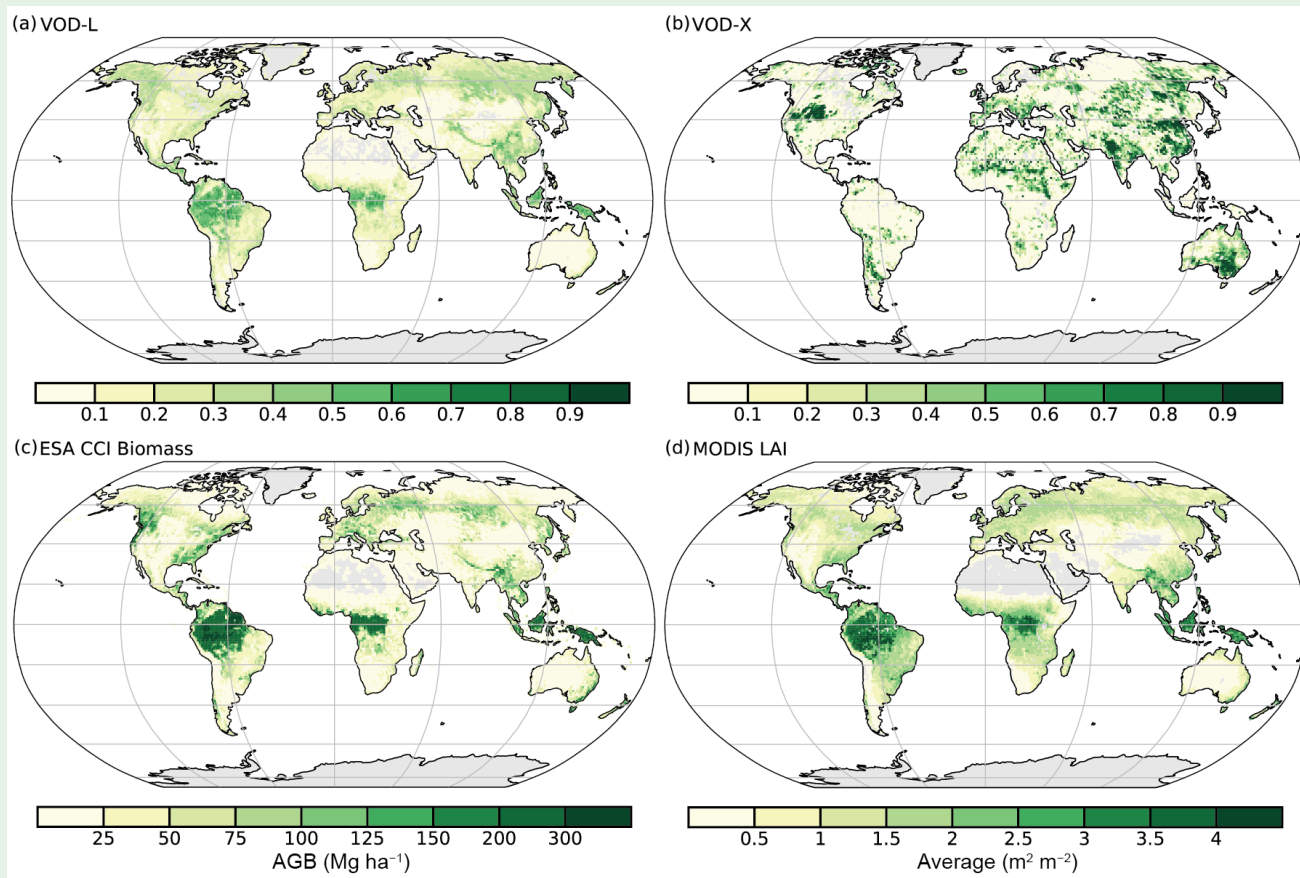


Fig. SB2.5. (a),(b) Global maps of average vertical optical depth (VOD; unitless) for the period 2010–20 for L- and X-band, respectively. Note that VOD is wavelength-dependent and hence has a different range for different bands. (c) ESA CCI above-ground biomass (Mg ha⁻¹) for 2017, (d) Average LAI (m² m⁻²) from MODIS for 2010–20.

datasets for Ku-band (covering the period 1987–2020), X-band (1997–2020), and C-band (2002–20) at 0.25° spatial and daily temporal resolutions. Because of the superior length of the data record, we used the VODCA Ku-band dataset to compute anomalies from the long-term (1991–2010) mean seasonal cycle. This frequency has a noted higher sensitivity to the upper canopy than the other frequencies and is thus a suitable indicator of foliage biomass and water content dynamics over space and time.

The year 2020 saw lower-than-usual VOD values (Appendix Fig. A2.12 in large parts of North and South America, central and southern Africa, most of Australia, and in a wide belt from eastern Europe, through Russia and Mongolia, to northern China and Korea. Some of these regions had to cope with strong agricultural droughts and crop yield losses, e.g., Argentina and Ukraine (see sections 7d3, 7f6). In early 2021, in southern Madagascar over one million people were at the brink of famine because of yield losses, according to the UN Global Disaster Alert and Coordination System. Above-normal vegetation activity was observed in the central United States, northeastern Brazil, the Sahel, eastern and central southern Africa, India, and large parts of Eurasia. Many of these regions were much

wetter than usual in 2020 (section 2d10). For example, eastern Africa was repeatedly struck by torrential rainfall, flooding, and landslides throughout the first half of the year (see sections 2d5, 7e4), while India received 109% of its typical rainfall during its monsoon season (see section 7g4).

Vegetation dynamics are not only driven by water availability, as they are the result of complex interactions of multiple drivers (e.g., precipitation, temperature, radiation, carbon dioxide fertilization), weather extremes, lagged effects due to deep rooting systems, and land management (Nemani et al. 2003; Reichstein et al. 2013). For example, in regions or seasons where plant growth is traditionally limited by low temperatures or radiation, plant growth may be anti-correlated with precipitation, as precipitation events are characterized by more cloud cover and, hence, lower temperatures. A good example is the dry, warm, and sunny April in Europe in 2019 (see section 7f; Appendix Fig. A.SB2.1d), which clearly boosted vegetation development in the same month. In May, while soil moisture conditions had returned to normal, VOD showed a lagged drought response to the soil water depletion in early spring for several consecutive months (Appendix Figs. A.SB2.1e,f).

Worldwide, but particularly in the global south, interannual VOD conditions can be linked to variations in the El Niño–Southern Oscillation (ENSO; Fig. SB2.6), which is characterized by predominantly dry conditions during El Niño and mostly wet conditions during La Niña episodes (see sections 2d4, 2d10). This connection between VOD and ENSO confirms previous studies based on optical data (e.g., Poulter et al. 2014) that, at the global scale, interannual vegetation activity is largely controlled by moisture supply. Although 2020 saw a transition from weak El Niño-like conditions at the start of the year to a moderate La Niña toward the end (see sections 2e1, 4b), this is not clearly reflected by the yearly and monthly VOD anomaly patterns (Appendix Fig. A.SB2.1), which show a mixture of typical El Niño-like patterns (e.g., wet and, hence, green conditions

in eastern Africa and dry conditions in southern Africa and Australia) and patterns typically observed during La Niña episodes (e.g., wetter conditions in northeastern Brazil and drier conditions in Argentina; see section 2e1).

Global long-term VOD trends are slightly positive (Fig. SB2.6; Moesinger et al. 2020) and in line with greening trends derived from observations in the optical domain (e.g., Forzieri et al. 2017; see section 2h2), thus affirming the usability of VOD for detecting and attributing long-term changes in vegetation activity (Liu et al. 2013). Through its multiple facets, long-term VOD observations perfectly complement the available suite of Earth observation tools to solve the complex puzzle of the effects of climate change on our biosphere.

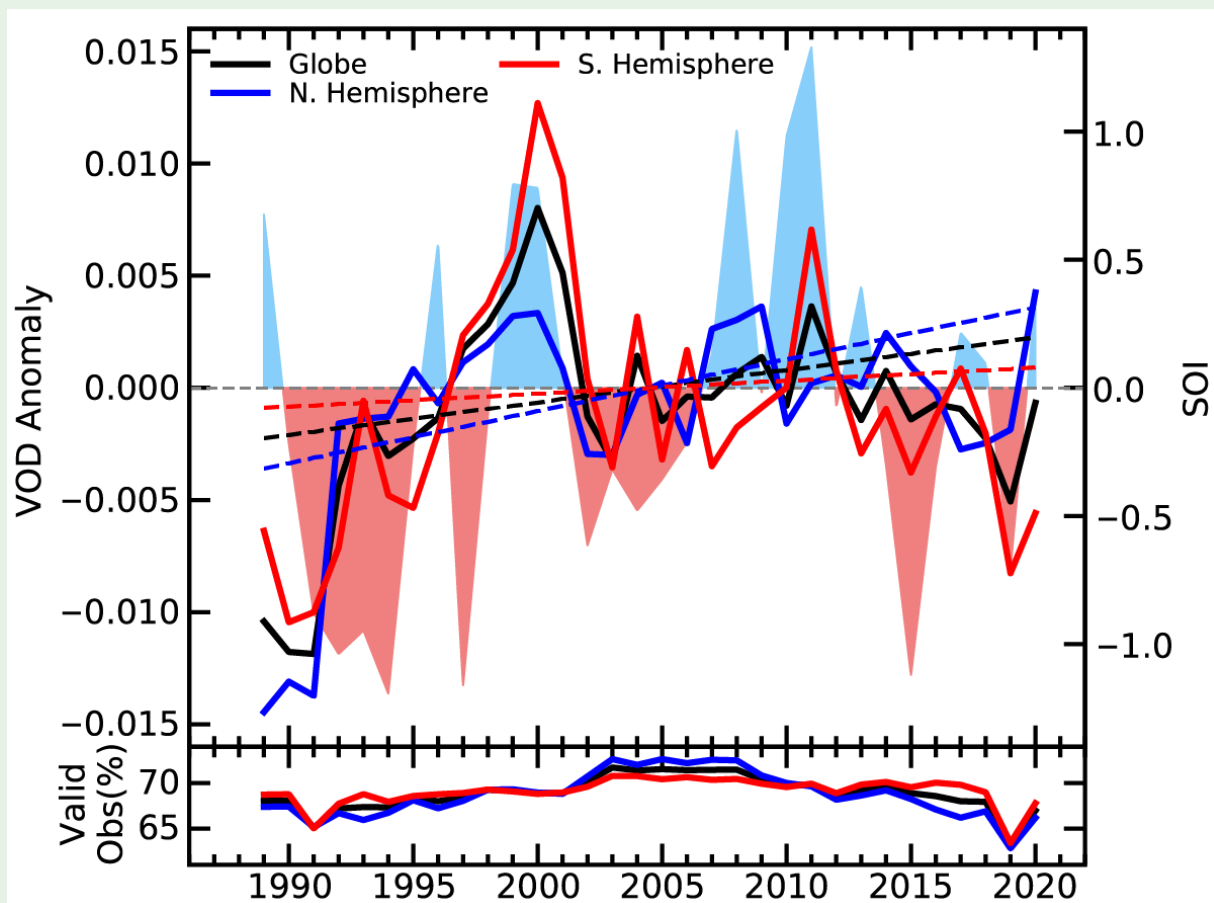


Fig. SB2.6. Yearly Ku-band virtual optical depth (VOD) anomalies juxtaposed with the Southern Oscillation Index Lines indicate the global and hemispheric VOD while the shading is the southern oscillation index (SOI) (red: La Niña, negative; blue: El Niño, positive). (Source: VODCA, <http://www.bom.gov.au/climate/current/soi2.shtml>.) The bottom plot shows the percentage of land pixels that provides valid data for each year.

Acknowledgments

2a1 (Overview)

Freya Aldred, Robert Dunn, and Kate Willett were supported by the Met Office Hadley Centre Climate Programme funded by BEIS and Defra.

We thank Rob Chadwick and David Parker, the five anonymous reviewers, and the BAMS Editor for their detailed comments when reviewing the chapter. We also thank Atsushi Goto (JMA), Julien Nicolas (ECMWF) and Mike Bosilovich (NASA) for the provision of the reanalysis data used in this chapter.

2b2 (Lake surface water temperature)

Lake surface water temperatures from satellite data have been generated within the GloboLakes project funded by the UK National Environment Research Council (NE/J023345/2) with extensions funded by the EU Copernicus Climate Change Service (C3S) programme. The in situ measurements used to validate the LSWT dataset have been kindly shared by Eugene Silow (Irkutsk State University, Russia); Merja Pulkkanen (SYKE, Helsinki, Finland); Antii Raike (SYKE, Helsinki, Finland); Eric Leibensperger (Department of Physics and Astronomy, Ithaca College, Ithaca, New York); Alo Laas (Estonian University of Life Sciences, Tartu, Estonia); Michela Rogora (CNR Institute for Water Research, Italy); Martin Dokulil (Austria); Shin-ichiro Matsuzaki (National Institute for Environmental Studies, Japan); Claudia Giardino (CNR IREA, Italy); Curtis DeGasperi (King County Water and Land Resources Division, Department of Natural Resources and Parks, Seattle, Washington); Martin Schmid (Eawag, Switzerland); and Don Pierson (Uppsala University, Sweden).

Lake Water Level timeseries are generated by LEGOS/CLS as part of the Theia Land programme supported by CNES with extensions funded by the EU Copernicus Climate Change Service (C3S) programme and by ESA through the Climate Change Initiative (CCI+) project. Valery Vuglinskii (SHI, Russia) provided water level in situ time series on 16 lakes in Russia allowing to validate the LWL products.

2b3 (Land and marine temperature extremes)

Robert J. H. Dunn was supported by the Hadley Centre Climate Programme funded by BEIS and Defra.

2b4 (Tropospheric temperature)

Work performed by Stephen Po-Chedley at Lawrence Livermore National Laboratory (LLNL) was performed under the auspices of the U.S. Department of Energy under Contract DE-AC52-07NA27344 with support from the Regional and Global Model Analysis Program of the Office of Science at the DOE.

2b5 (Stratospheric temperature and winds)

The National Center for Atmospheric Research is sponsored by the U.S. National Science Foundation.

Sidebar 2.1 (Night marine air temperature)

Richard Cornes, David Berry, and Elizabeth Kent were funded by the NERC CLASS programme (NE/R015953/1), the NERC GloSAT project (NE/S015647/2), and the Copernicus Climate Change Service (C3S_311a_Lot2). The UAHNMAV1 work was supported by the U.S. Department of Energy (DE-SC0005330 and DE-SC0019296). Nick Rayner was supported by the Met Office Hadley Centre Climate Programme funded by BEIS and Defra.

2c1 (Permafrost thermal state)

PERMOS is financially supported by MeteoSwiss in the framework of GCOS Switzerland, the Federal Office for the Environment, and the Swiss Academy of Sciences and acknowledges the important contribution of the partner institutions and principal investigators. The French Network PermaFRANCE is financially supported by OSUG (Observatoire des Sciences de l'Univers Grenoble) and the French Research Infrastructure OZCAR. Czech Antarctic Research Programme is supported by Czech Ministry of Education, Youth and Sport project VAN2020/1.

2c2 (Northern Hemisphere continental snow cover extent)

This work is funded in part by NOAA's Climate Data Record (CDR) Program located in Asheville, North Carolina, at the National Centers for Environmental Information.

2c4 (Lake ice)

We thank Kevin Blagrove, Nikolay Granin, Lars Rudstam, and Merja Pulkanen for providing updates to in situ lake ice phenology records.

Sidebar 2.2 (Rock glacier kinematics)

Rock glacier monitoring at Hinteres Langtalkar and Dösen rock glaciers (AT) was supported by different national and international projects during the last decades. The authority of the Hohe Tauern National Park is one of the most important supporters of this monitoring. Laurichard (FR) survey is supported by CryobsClim "long-term Observation and Experimentation System for Environmental Research" (SOERE/All'envi-OZCAR Research Infrastructure) and the PermaFrance observatory "monitoring the mountain permafrost in the French Alps." The Ecrins National Park helps field surveys since the early 2000's. The Swiss Permafrost Monitoring Network PERMOS is financially supported by MeteoSwiss in the framework of GCOS Switzerland, the Federal Office for the Environment and the Swiss Academy of Sciences. PERMOS acknowledges the important contribution of the partner institutions and principal investigators.

2d1 (Surface humidity)

Kate Willett and Alan Vance were supported by the Met Office Hadley Centre Climate Programme funded by BEIS and Defra. Adrian Simmons was supported by the Copernicus Climate Change Service implemented by ECMWF on behalf of the European Commission.

2d5 (Land-based precipitation extremes)

Mari Tye was supported by the National Center for Atmospheric Research, which is a major facility sponsored by the National Science Foundation under Cooperative Agreement No. 1852977.

2d6 (Lake water levels)

B. M. Kraemer received support from the 2017–2018 Belmont Forum and BiodivERsA joint call for research proposals, under the BiodivScen ERA-Net COFUND program, and with the funding organizations German Science Foundation (AD 91/22-1). This work benefited from B. M. Kraemer's participation in the Global Lake Ecological Observatory Network (GLEON).

2d8 (River discharge and runoff)

Hyungjun Kim was supported by the Japan Society for the Promotion of Science KAKENHI (16H06291 and 18KK0117) for this contribution.

2d10 (Soil moisture)

The ESA CCI SM datasets and the authors were supported by ESA's Climate Change Initiative for Soil Moisture (Contract No. 4000104814/11/I-NB and 4000112226/14/I-NB) and in addition the authors were supported by activities under provision of services to Copernicus Climate Change Service (Contract No. ECMWF/COPERNICUS/2018/C3S_312b_Lot4_EODC/SC2).

2d11 (Monitoring global drought using the self-calibrating Palmer Drought Severity Index)

J. Barichivich acknowledges the FONDECYT Grant 1181956. Tim Osborn received funding from UK NERC (NE/S015582/1). Ian Harris received funding from UK National Centre for Atmospheric Science (NCAS). The research presented in the drought section was carried out on the High Performance Computing Cluster supported by the Research and Specialist Computing Support service at the University of East Anglia.

2d12 (Land evaporation)

Diego G. Miralles acknowledges support from the European Research Council (ERC) under grant agreement no. 715254 (DRY-2-DRY). A. Koppa and D. Rains acknowledge support from the Belgian Science Policy Office (BELSPO) in the frame of the STEREO III program projects ALBERI (SR/00/373) and ET-Sense (SR/02/377). M. F. McCabe is supported by the King Abdullah University of Science and Technology.

2e2 (Land and ocean surface winds)

Robert J. H. Dunn was supported by the Hadley Centre Climate Programme funded by BEIS and Defra. L. Ricciardulli and Carl A. Mears are supported by the NASA Ocean Vector Wind Science Team (OVWST) program.

2f1 (Earth radiation budget at top-of-atmosphere)

This research has been supported by the NASA CERES project. The NASA Langley Atmospheric Sciences Data Center processed the instantaneous Single Scanner Footprint (SSF) data used as input to EBAF Ed4.1 and processes the FLASHFlux TISA version 4A.

2g4 (Stratospheric ozone)

Carlo Arosio, Melanie Coldewey-Egbers, Daan Hubert, Diego Loyola, Victoria Sofieva, Alexei Rozanov, and Mark Weber are grateful to ESA's Climate Change Initiative Ozone project and to the EU Copernicus Climate Change Service 312b Lot4 Ozone project for supporting the generation and extension of the GTO-ECV total ozone and SAGE-CCI-OMPS data records. Stacey M. Frith is supported by the NASA Long Term Measurement of Ozone program WBS 479717. Lucien Froidevaux's contribution, with the assistance of Ryan Fuller, was performed at the Jet Propulsion Laboratory, California Institute of Technology, under contract with NASA. Daan Hubert acknowledges the partial support by the EU/ERC Horizon 2020 project GAIA-CLIM.

2h1 (Land surface albedo dynamics)

The authors thank Monica Robustelli for her technical support and NASA's Land Processes Distributed Active Archive Center (LP DAAC) for providing access to the remote sensing data.

2h2 (Terrestrial vegetation dynamics)

The author thanks Monica Robustelli for her technical support and the providers of the remote sensing dataset needed to perform this research, i.e., the SeaWiFS Project (Code 970.2) and the Goddard Earth Sciences Data and Information Services Center/Distributed Active Archive Center (Code 902) at the Goddard Space Flight Center, Greenbelt, Maryland 20771. MERIS products were processed at the Grid On Demand facility of European Space Agency (ESA/ESRIN) using JRC software code.

2h4 (Phenology of primary producers)

Debbie Hemming acknowledges support from the Met Office Hadley Centre Climate Programme funded by BEIS and Defra, and thanks Robert Dunn for his expertise finalizing the figures. Taejin Park acknowledges support from the NASA Earth Science Directorate (grants NNX16AO34H and 80NSSC18K0173-CMS). Andrew Richardson acknowledges support from the National Science Foundation through the Macrosystems Biology (award 1702697) and LTER (award 1832210) programs. Nature's Calendar thanks all its volunteer recorders, without whom it could not function. Stephen Thackeray thanks Rita Adrian, Tamar Zohary, Kazuhiro Komatsu and Shin-Ichiro Matsuzaki for collecting and providing lake chlorophyll-*a* data.

Sidebar 2.3 (Long-term monitoring of vegetation state through passive microwave satellites)

Wouter A. Dorigo, L. Moesinger, and R. M. Zotta acknowledge the TU Wien Wissenschaftspreis 2015, a personal grant awarded to Wouter Dorigo.

Chapter 2 – Acronyms

AAO	Antarctic Oscillation
AATSR	Advanced Along Track Scanning Radiometer
ALEXI	Atmosphere–Land Exchange Inverse
ALT	active layer thickness
AMSRE-E	Advanced Microwave Scanning Radiometer
AO	Arctic Oscillation
AOD	aerosol optical depth
ATSR	Along Track Scanning Radiometer
AVHRR	Advanced Very High Resolution Radiometer
BDC	Brewer-Dobson circulation
BRW	Barrow Atmospheric Baseline Observatory
C3S	Copernicus Climate Change Service
CALIOP	Cloud-Aerosol Lidar with Orthogonal Polarization
CAMS	Copernicus Atmosphere Monitoring Service
CAMSRA	Copernicus Atmosphere Monitoring Service Reanalysis
CCMI	Chemistry Climate Model Initiative
CEI	Climate Extremes Index
CERES	Clouds and the Earth’s Radiant Energy System
CFC	chlorofluorocarbon
CH ₄	methane
Cl	chlorine
CO	carbon monoxide
CO ₂	carbon dioxide
CPT	cold-point tropopause
CRU TS	Climatic Research Unit gridded Time Series
DDM	drainage direction map
DU	Dobson unit
EA	Eurasia
ECV	essential climate variable
EESC	equivalent effective stratospheric chlorine
EESC-A	equivalent effective stratospheric chlorine-Antarctic
EESC-M	equivalent effective stratospheric chlorine-Midlatitude
ENSO	El Niño–Southern Oscillation
EOFs	empirical orthogonal functions
EOS	end of season
ERB	Earth’s radiation budget
ESA CCI SM	European Space Agency’s Climate Change Initiative for Soil Moisture
ET	evapotranspiration
ETCCDI	WMO Expert Team in Climate Change Detection and Indices
FAPAR	Fraction of Absorbed Photosynthetically Active Radiation
FF	fossil fuel
GCOS	Global Climate Observing System
GFAS	Global Fire Assimilation System
GFED	Global Fire Emissions Database
GGGRN	NOAA’s Global Greenhouse Gas ReferenceNetwork

GHCN	Global Historical Climatology Network
GHCNDEX	Global Historical Climatology Network-Daily database
GIN-P	Global Terrestrial Network for Permafrost
GLEAM	Global Land Evaporation Amsterdam Model
GMST	global mean surface temperature
GNSS	Global Navigation Satellite System
GPCC	Global Precipitation Climatology Centre
GPCP	Global Precipitation Climatology Project
GPS-RO	Global Positioning System-Radio Occultation
GRACE	Gravity Recovery and Climate Experiment
GRACE-FO	Gravity Recovery and Climate Experiment - Follow On
GTN-P	Global Terrestrial Network for Permafrost
HFCF	hydrochlorofluorocarbon
HFC	hydrofluorocarbon
HIRS	High Resolution Infra Red Radiation Sounder
HWF	heat wave frequency
HWM	heat wave magnitude
IOD	Indian Ocean dipole
IPA	International Permafrost Association
ITCZ	Intertropical Convergence Zone
LLGHG	long-lived greenhouse gases
LSA-SAF	Land Surface Analysis Satellite Applications Facility
LSWT	lake surface water temperature
LTT	lower tropospheric temperature
LWL	lake water level
MACC	Monitoring Atmospheric Composition and Climate
MAT	marine air temperature
MBL	marine boundary layer
MHW	marine heatwave
MLO	Mauna Loa, Hawaii
MLS	Microwave Limb Sounder
MODIS	Moderate Resolution Imaging Spectroradiometer
MOPITT	Measurement of Pollution in the Troposphere
MSU/AMSU	Microwave Sounding Unit/Advanced Microwave Sounding Unit
N ₂ O	nitrous oxide
NA	North America
NAO	North Atlantic Oscillation
NDVI	normalized difference vegetation index
NH	Northern Hemisphere
NMAT	night marine air temperature
O ₃	ozone
ODGI	Ozone Depleting Gas Index
ODGI-A	Ozone Depleting Gas Index-Antarctic
ODGI-M	Ozone Depleting Gas Index-Midlatitude
ODS	ozone-depleting substances
OH	hydroxyl radical
OLR	outgoing longwave radiation
OMI	Ozone Monitoring Instrument

PDO	Pacific Decadal Oscillation
PSC	polar stratospheric cloud
QBO	quasi-biennial oscillation
QTP	Qinghai-Tibetan Plateau
RFaci	radiative forcing resulting from aerosol–cloud interactions
RFari	radiative forcing resulting from aerosol–radiation
RGK	rock glacier kinematics
RH	relative humidity
RO	radio occultation
RSW	reflected shortwave
SAM	Southern Annular Mode
SAR	Synthetic Aperture Radar
SCE	snow cover extent
scPDSI	self-calibrating Palmer Drought Severity Index
SH	Southern Hemisphere
SLSTR	Sea and Land Surface Temperature Radiometer
SOI	Southern Oscillation Index
SORCE	Solar Radiation and Climate Experiment
SOS	start of season
SPO	South Pole Observatory
SSM/I	Special Sensor Microwave/Imager
SSMIS	Special Sensor Microwave Imager/Sounder
SSMIS	Special Sensor Microwave Imager/Sounder
SST	sea surface temperature
SSU	Stratospheric Sounding Unit
SW	shortwave
TCWV	total column water vapor
TIR	thermal infrared
TLS	lower stratospheric temperature
TOA	top of the atmosphere
TSI	total solar irradiance
TSIS-1	Total Solar and Spectral Irradiance Sensor-1
TTL	tropical tropopause layer
TTT	tropical tropospheric temperature
TWS	terrestrial water storage
UTH	upper tropospheric (relative) humidity
UV	ultraviolet
VOC	volatile organic compound
VOD	vegetation optical depth
VODCA	vegetation optical depth Climate Archive
WGMS	World Glacier Monitoring Service
WMO	World Meteorological Organization
WV	water vapor

APPENDIX 2: Supplemental Material

2b1 Surface air temperature

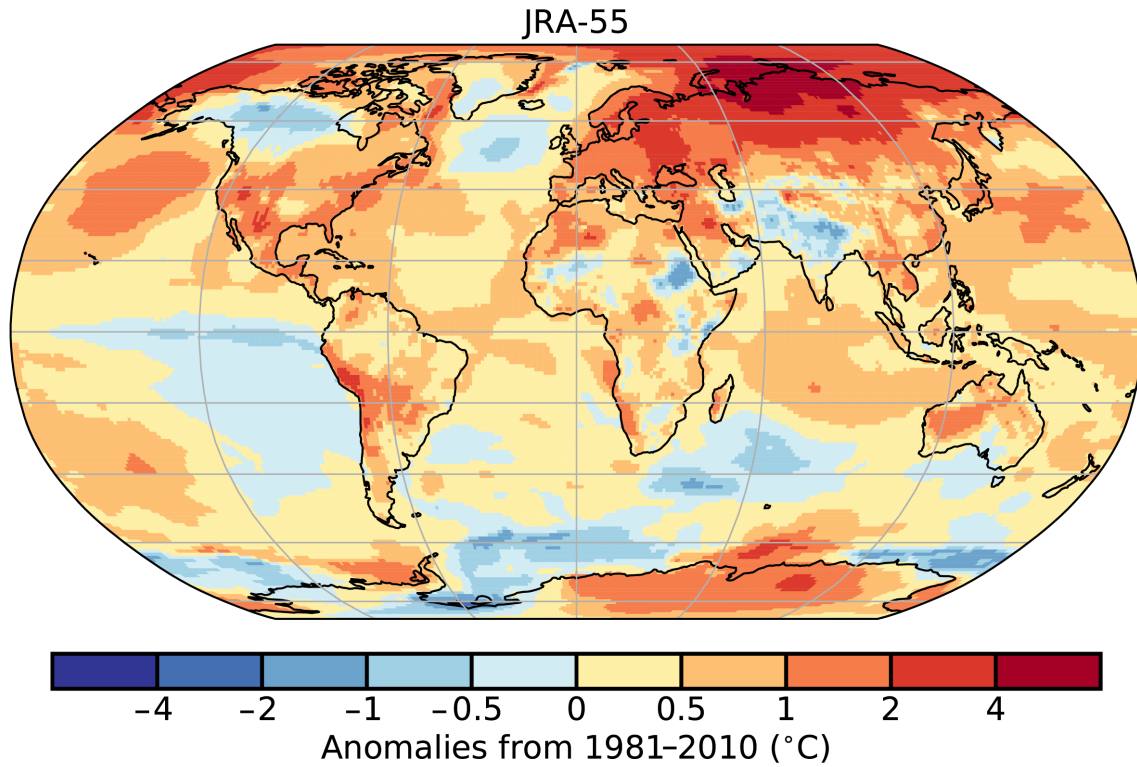


Fig. A2.1. Global 2-m surface temperature anomalies (°C; 1981–2010 base period).
(Source: JRA-55.)

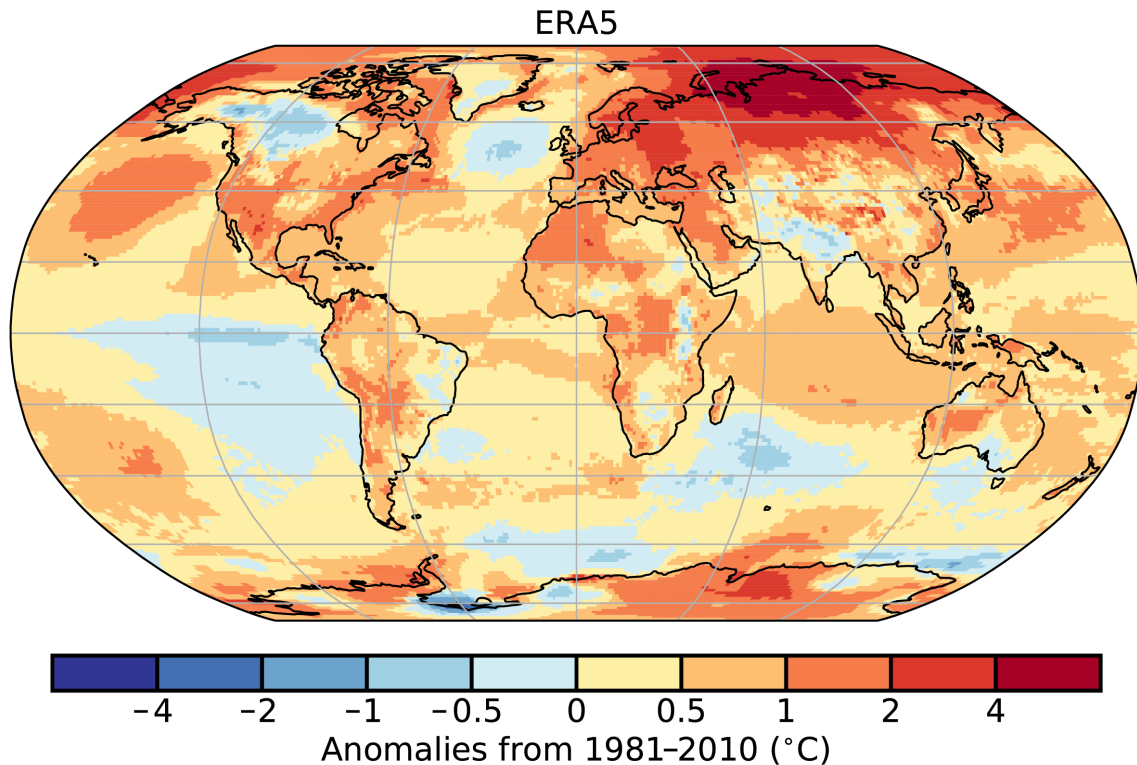


Fig. A2.2. Global 2-m surface temperature anomalies (°C; 1981–2010 base period).
(Source: ERA5.)

NASA GISS

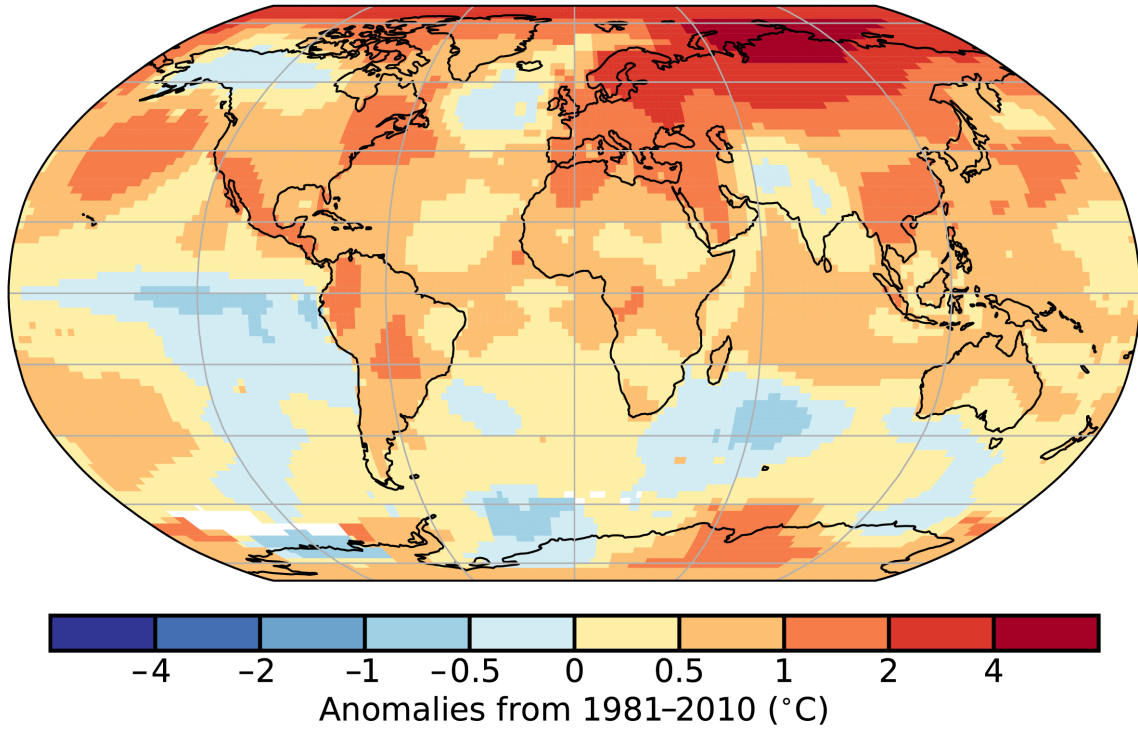


Fig. A2.3. Global surface temperature anomalies (°C; 1981–2010 base period).
(Source: NASA GISS.)

HadCRUT 5.0

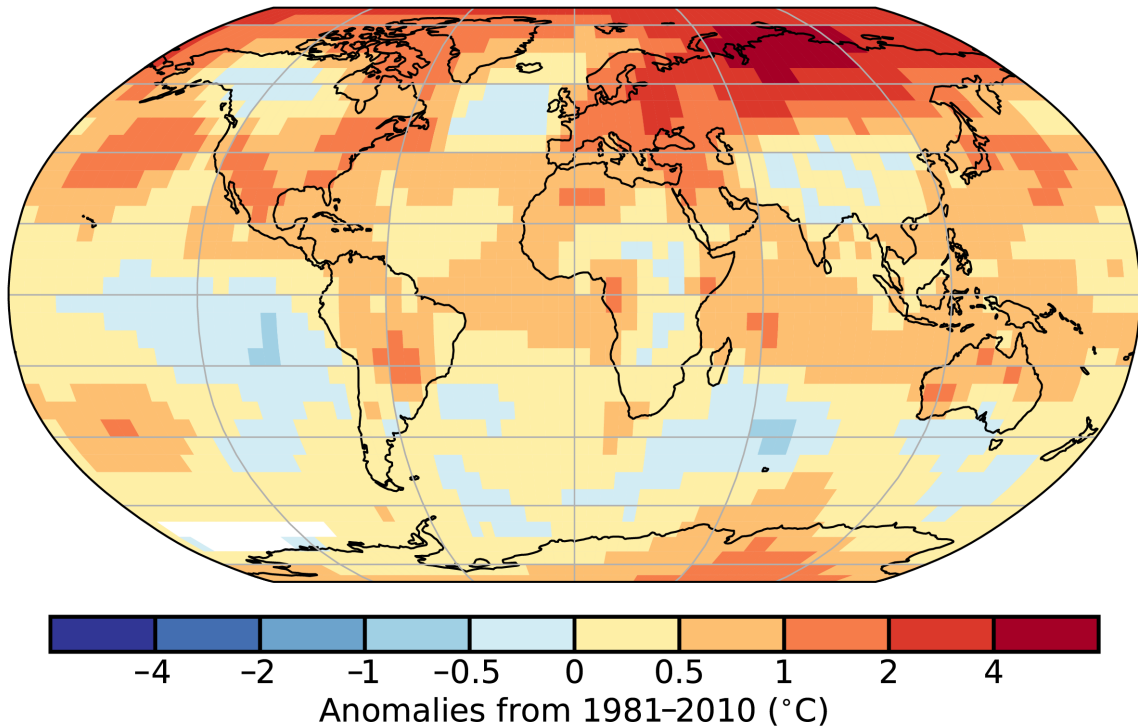


Fig. A2.4. Global surface temperature anomalies (°C; 1981–2010 base period).
(Source: HadCRUT5.)

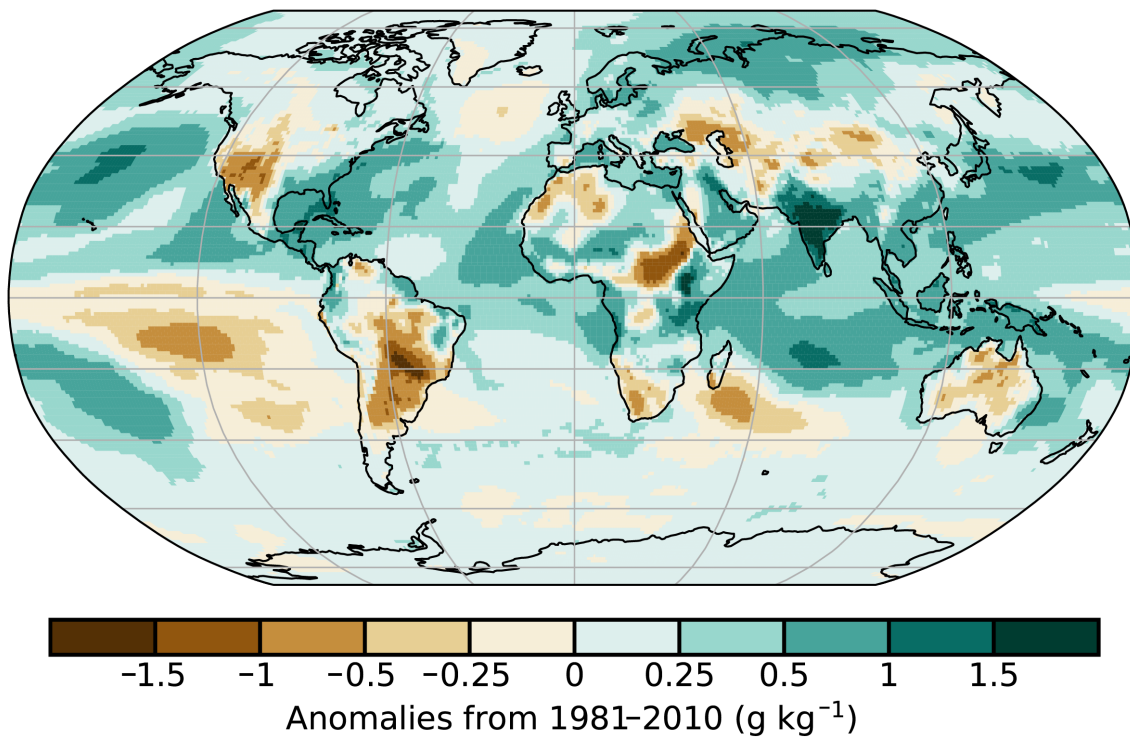


Fig. A2.5. Specific humidity annual average anomaly (g kg^{-1} ; base period 1981–2010)
(Source: ERA5.)

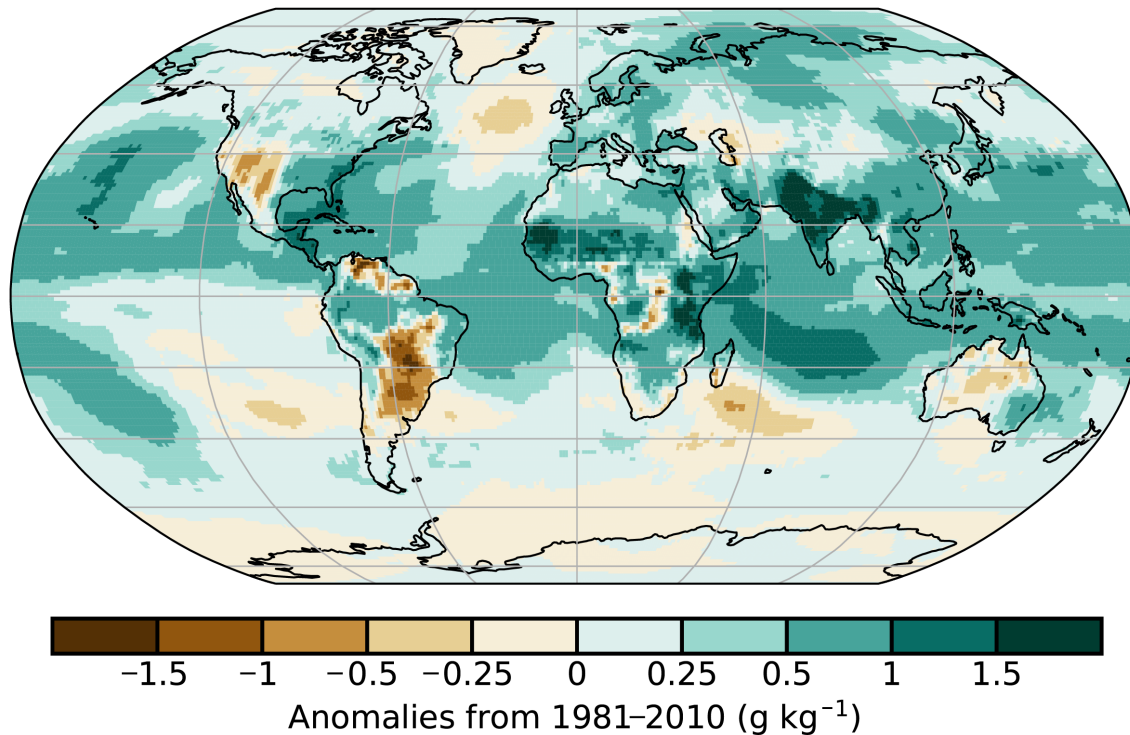


Fig. A2.6. Specific humidity annual average anomaly (g kg^{-1} ; base period 1981–2010)
(Source: MERRA-2.)

Section 2d2 Total column water vapor

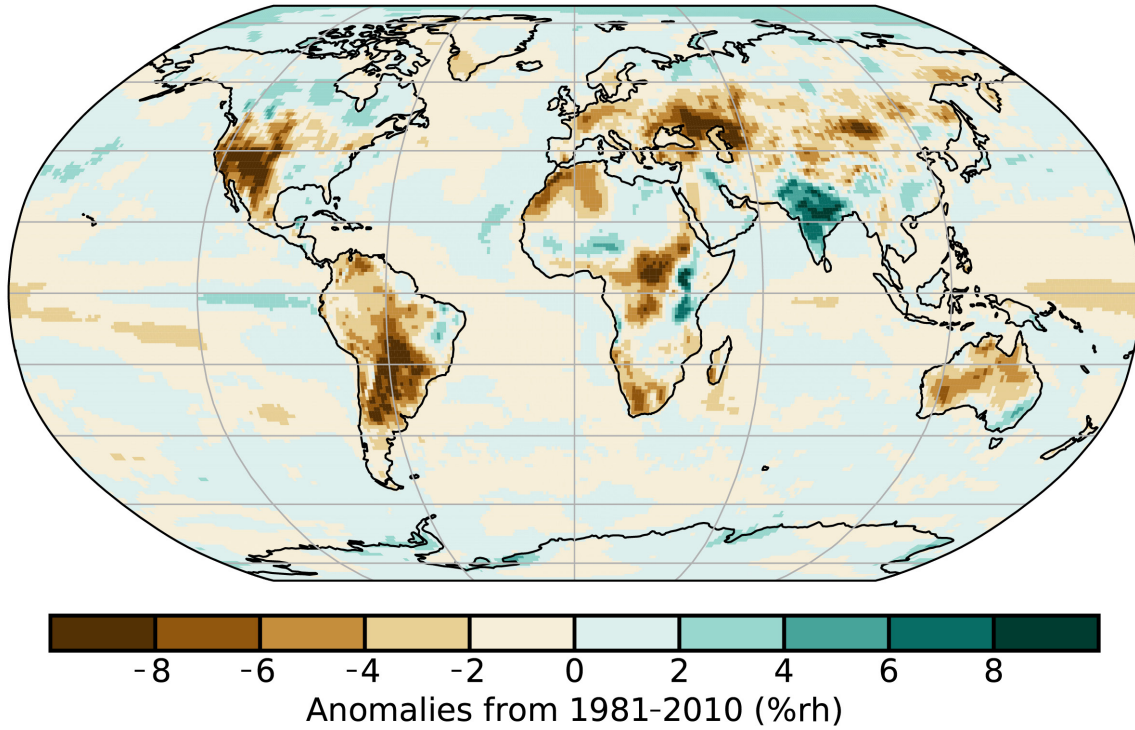


Fig. A2.7. Relative humidity annual average anomaly (%rh; base period 1981–2010)
(Source: ERA5.)

Section 2d3 Upper tropospheric humidity

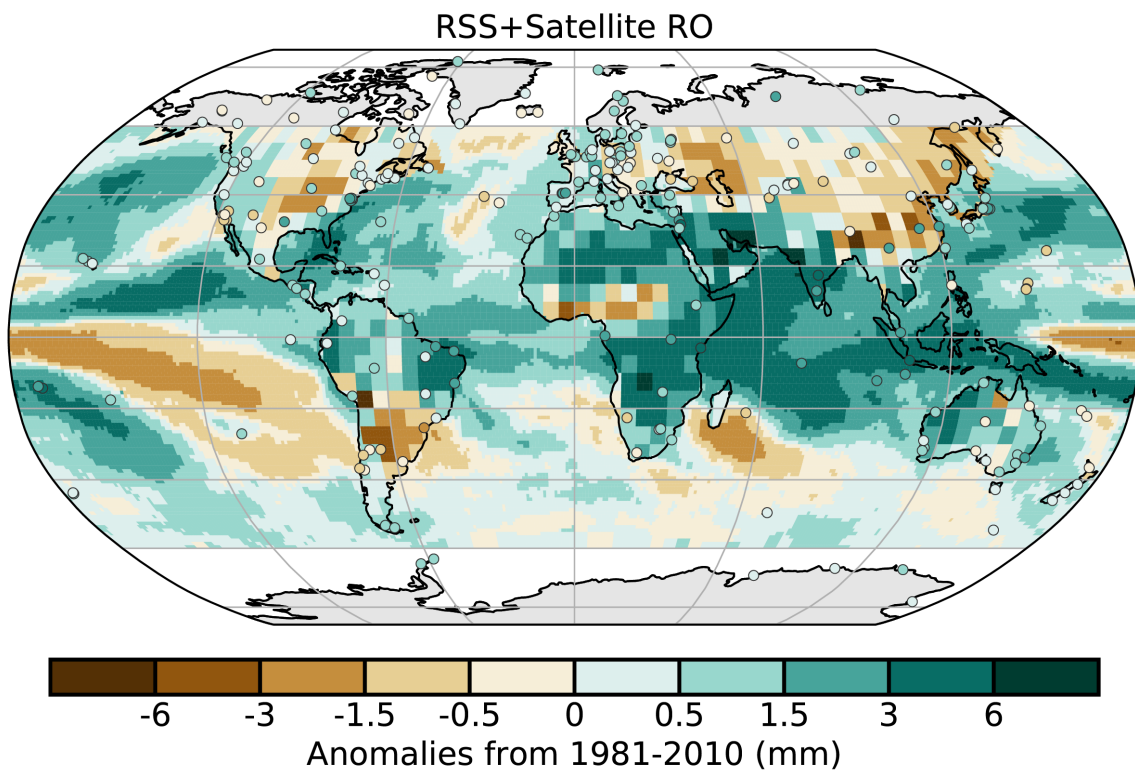


Fig. A2.8. Annual average TCWV anomalies (mm; 1981–2010 base period). The data are from satellite radiometers over the oceans (RSS) and from satellite RO over land. Data from GNSS stations are plotted as filled circles.

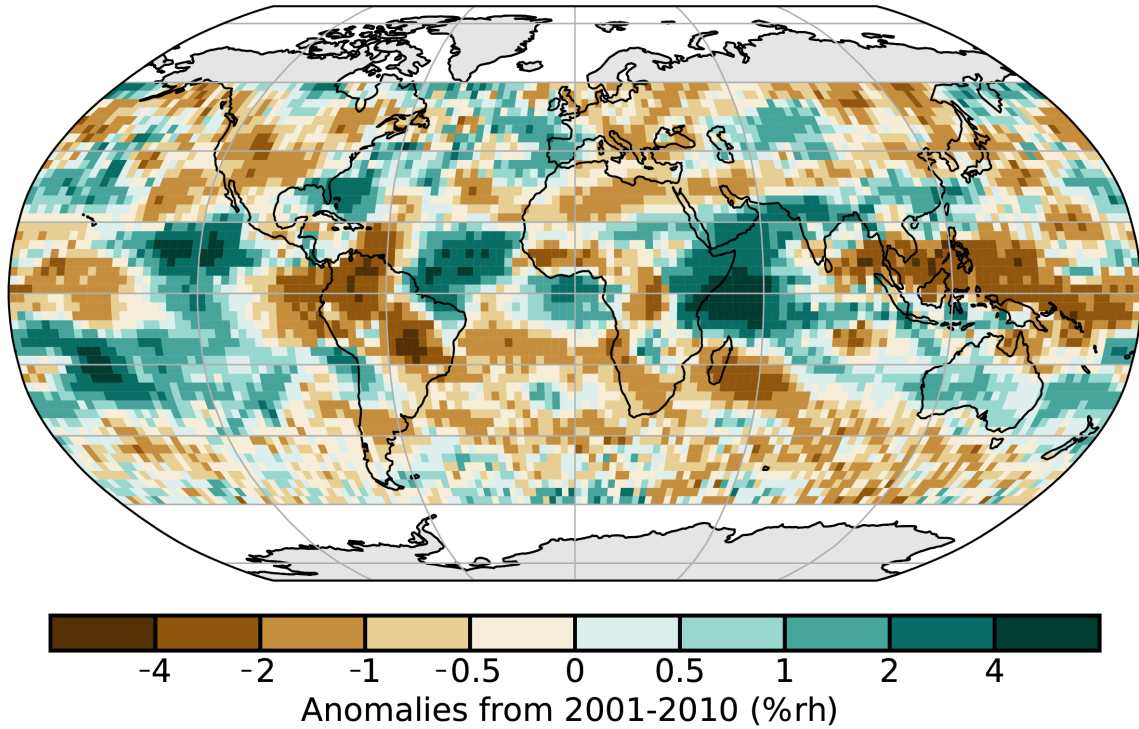


Fig. A2.9. Annual average UTH anomalies (%rh; 2001–10 base period)
(Source: HIRS UTH dataset.)

MERRA-2 R10mm - Number of heavy precipitation days

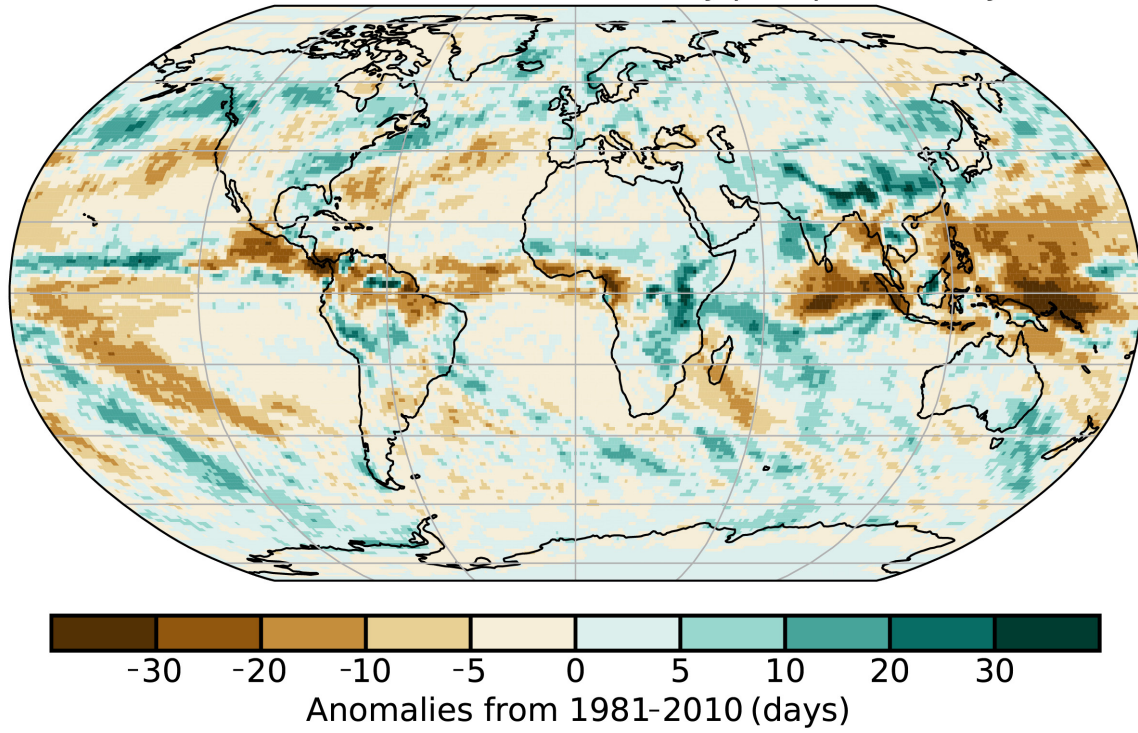


Fig. A2.10a.

ERA5 R10mm - Number of heavy precipitation days

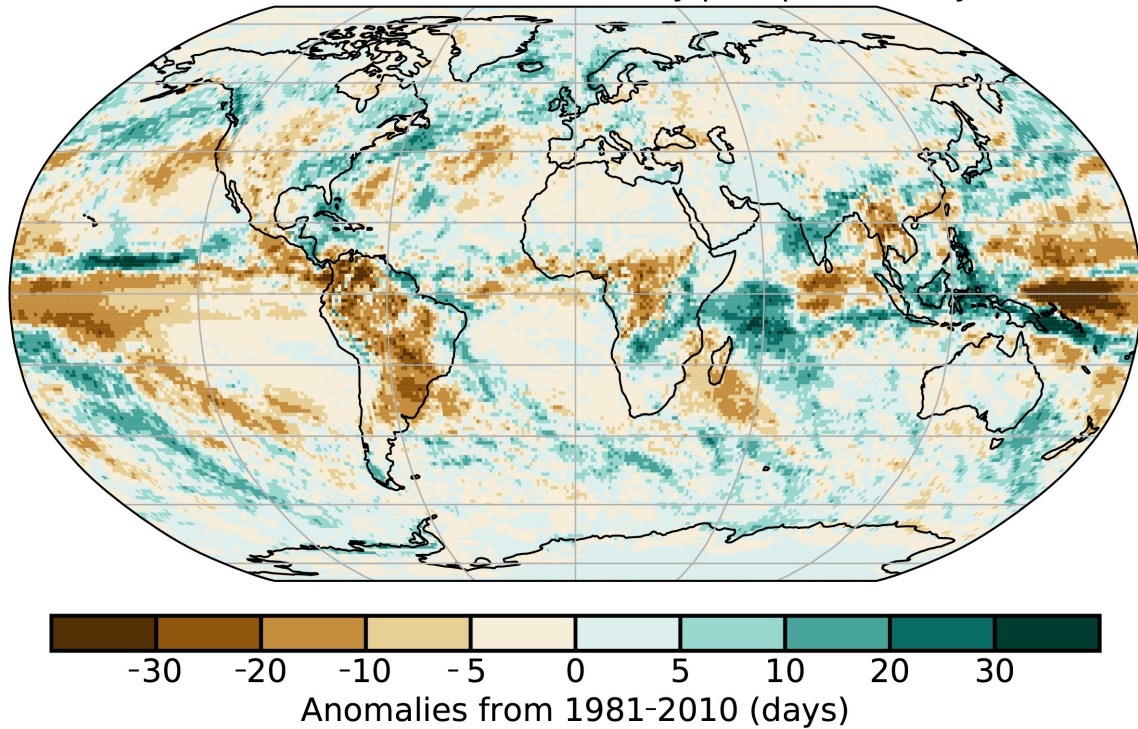


Fig. A2.10b.

GHCNDEX Rx5day - Maximum 5 day precipitation total

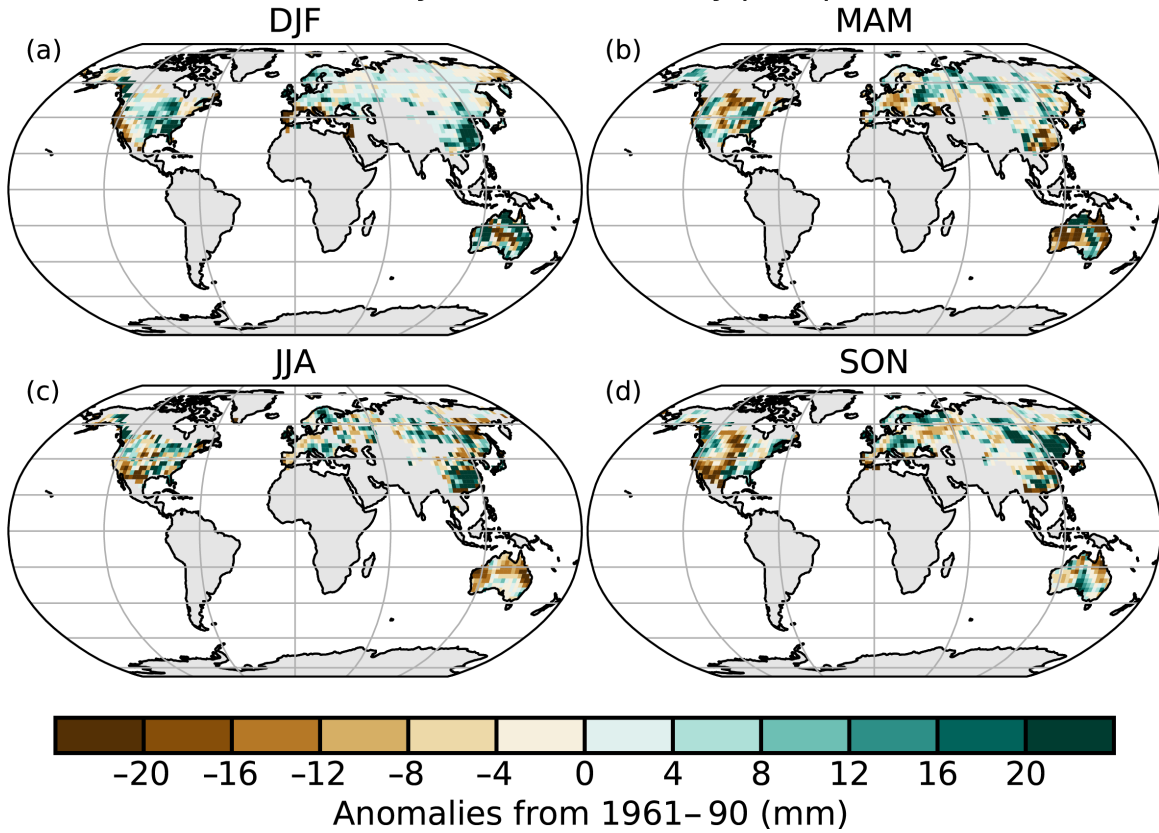


Fig. A2.10c.

GPCC Rx5day - Maximum 5 day precipitation total

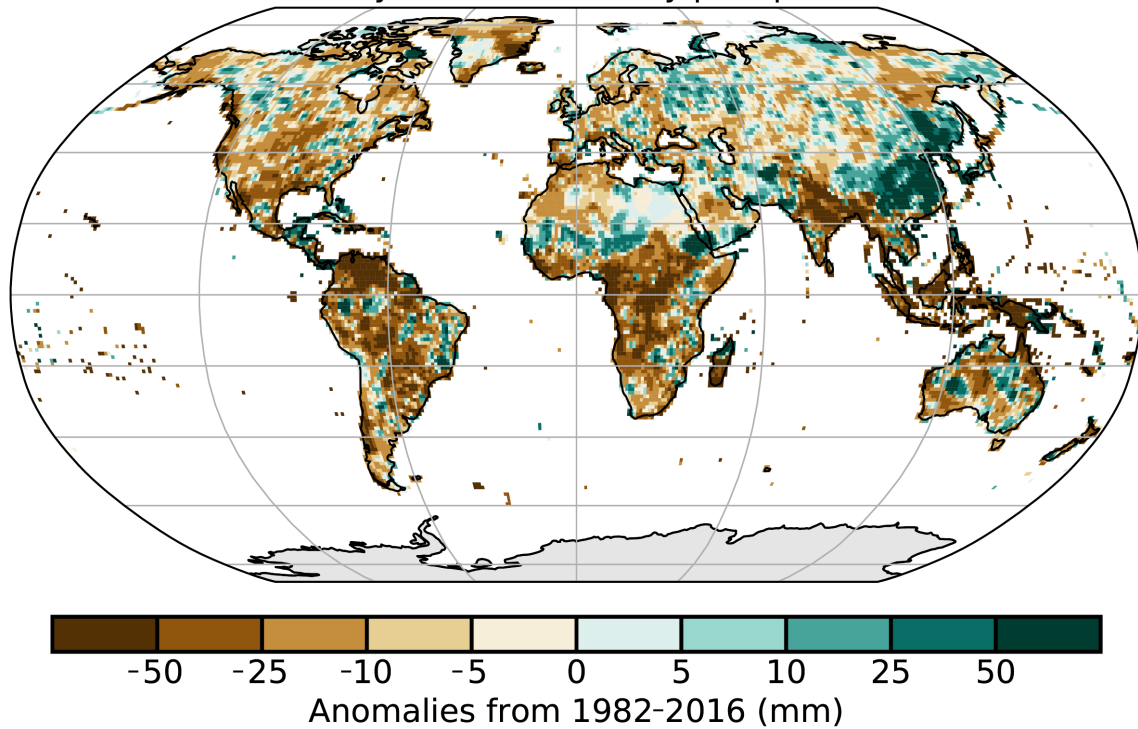


Fig. A2.10d. Anomalies of 2020 indices relative to a 1981–2010 base period for R10mm (days) derived from (a) MERRA-2 (Gelaro et al. 2017) and (b) ERA5 (Hersbach et al. 2020); Rx5day (mm) derived (c[a–d]) seasonally relative to a 1961–1990 base period from GHCNDEX (Donat et al. 2013) and (d) annually relative to a 1982–2016 base period from GPCC (Schamm et al. 2013).

Section 2d5 Land-based precipitation extremes

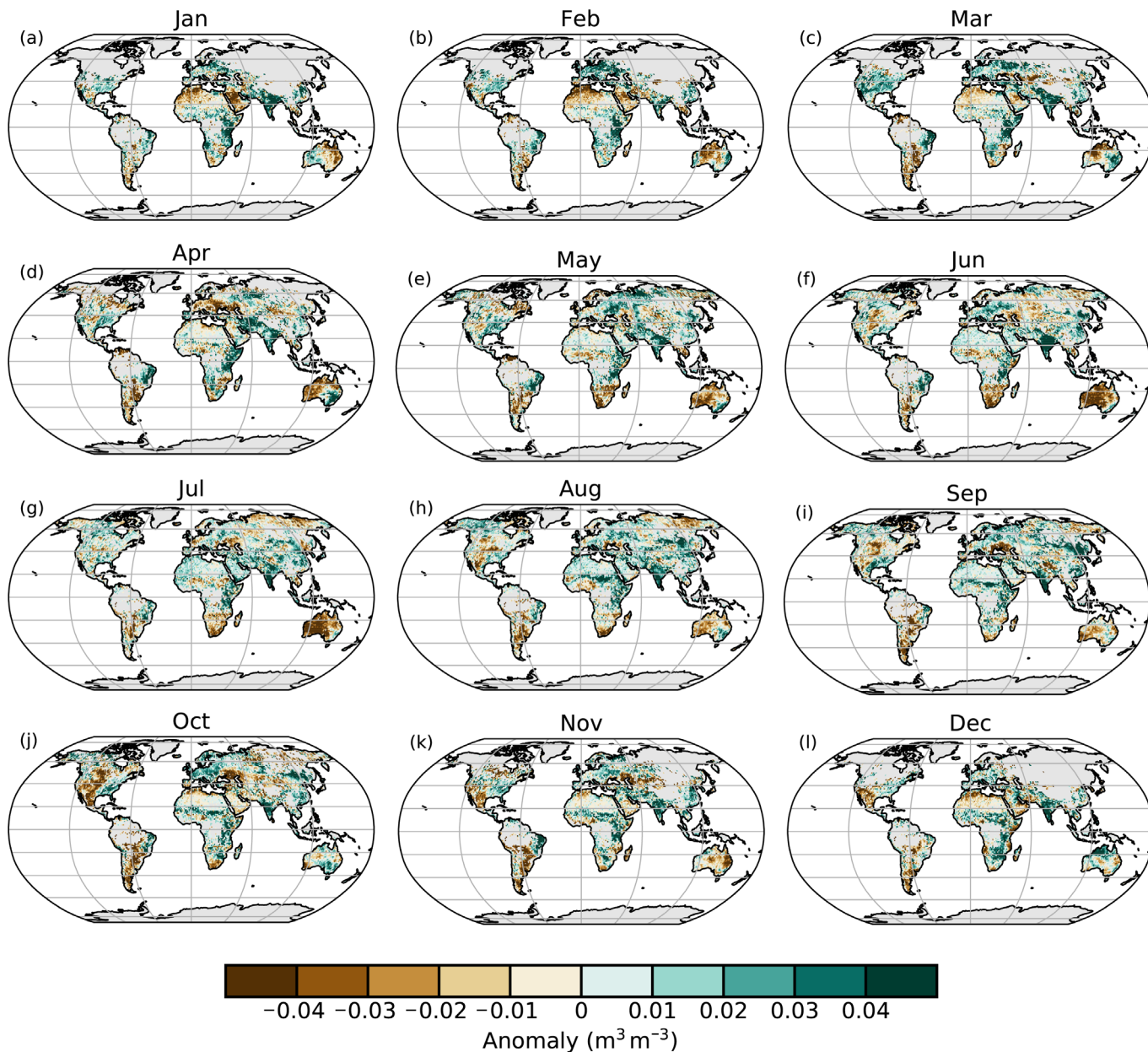


Fig. A2.11. (a–l) Monthly average soil moisture anomalies for 2020 ($\text{m}^3 \text{m}^{-3}$; 1991–2010 base period). Data are masked where no retrieval is possible or where the quality is not assured and flagged due to dense vegetation, frozen soil, radio frequency interference, etc. (Source: ESA CCI Soil Moisture.)

Section 2d10 Soil moisture

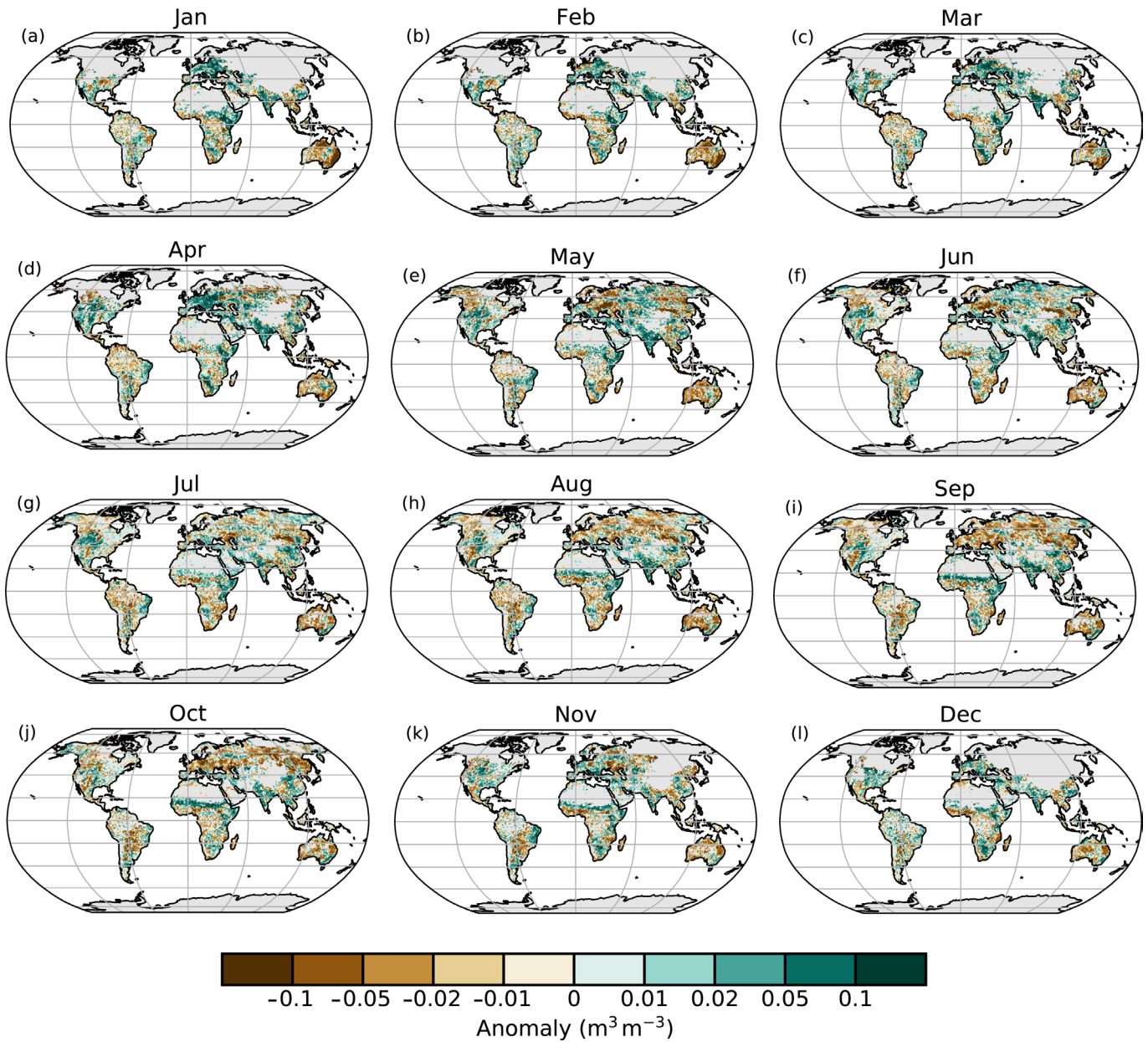


Fig. A2.12. (a–l) Monthly global Ku-band VOD anomalies (unitless; 1991–2010 reference period). High values indicate favorable vegetation conditions, and low values indicate lower vegetation activity than normal. Data are masked where no retrieval is possible due to sparse vegetation or frozen soils/snow cover. (Source: VODCA.)

References

- Adler, R., and Coauthors, 2018: The Global Precipitation Climatology Project (GPCP) monthly analysis (new version 2.3) and a review of 2017 global precipitation. *Atmosphere*, **9**, 138, <https://doi.org/10.3390/atmos9040138>.
- Alden, C. B., J. B. Miller, and J. W. C. White, 2010: Can bottom-up ocean CO₂ fluxes be reconciled with atmospheric ¹³C observations? *Tellus*, **62B**, 369–388, <https://doi.org/10.1111/j.1600-0889.2010.00481.x>.
- Alexander, L. V., M. Bador, R. Roca, S. Contractor, M. G. Donat, and P. L. Nguyen, 2020: Intercomparison of annual precipitation indices and extremes over global land areas from in situ, space-based and reanalysis products. *Environ. Res. Lett.*, **15**, 055002, <https://doi.org/10.1088/1748-9326/ab79e2>.
- Allan, R. J., and R. D. D'Arrigo, 1999: 'Persistent' ENSO sequences: How unusual was the 1990–1995 El Niño? *Holocene*, **9**, 101–118, <https://doi.org/10.1191/095968399669125102>.
- , J. Gergis, and R. D. D'Arrigo, 2019: Placing the 2014–2016 'protracted' El Niño episode into a long-term context. *Holocene*, **30**, 90–105, <https://doi.org/10.1177/0959683619875788>.
- Allan, R. P., K. P. Shine, A. Slingo, and J. A. Pamment, 1999: The dependence of clear-sky outgoing longwave radiation on surface temperature and relative humidity. *Quart. J. Roy. Meteor. Soc.*, **125**, 2103–2126, <https://doi.org/10.1002/qj.49712555809>.
- Allchin, M. I., and S. J. Dery, 2020: The climatologic context of trends in the onset of Northern Hemisphere seasonal snow cover, 1972–2017. *J. Geophys. Res. Atmos.*, **125**, e2019JD032367, <https://doi.org/10.1029/2019JD032367>.
- Alvarez-Garreton, C., J. P. Boisier, R. Garreaud, J. Seibert, and M. Vis, 2021: Progressive water deficits during multiyear droughts in basins with long hydrological memory in Chile. *Hydrol. Earth Syst. Sci.*, **25**, 429–446, <https://doi.org/10.5194/hess-25-429-2021>.
- Anabalón, A., and A. Sharma, 2017: On the divergence of potential and actual evapotranspiration trends: An assessment across alternate global datasets. *Earth's Future*, **5**, 905–917, <https://doi.org/10.1002/2016EF000499>.
- Andela, N., and Coauthors, 2017: A human-driven decline in global burned area. *Science*, **356**, 1356–1362, <https://doi.org/10.1126/science.aal4108>.
- Anderson, M. C., and Coauthors, 2011: Mapping daily evapotranspiration at field to continental scales using geostationary and polar orbiting satellite imagery. *Hydrol. Earth Syst. Sci.*, **15**, 223–239, <https://doi.org/10.5194/hess-15-223-2011>.
- Andersson, S. M., and Coauthors, 2015: Significant radiative impact of volcanic aerosol in the lowermost stratosphere. *Nat. Commun.*, **6**, 7692, <https://doi.org/10.1038/ncomms8692>.
- Andreassen, L., 2020: Glaciological investigations in Norway 2019. NVE Fakta 2/2020, 4 pp., http://publikasjoner.nve.no/faktaark/2020/faktaark2020_02.pdf.
- Anstey, J., T. Banyard, N. Butchart, L. Coy, P. Newman, S. Osprey, and C. Wright, 2020: Quasi-biennial oscillation disrupted by abnormal Southern Hemisphere stratosphere. Research Square, accessed 19 January 2021, <https://doi.org/10.21203/rs.3.rs-86860/v1>.
- , ———, ———, ———, ———, ———, and ———, 2021: Prospect of increased disruption to the QBO in a changing climate. *Geophys. Res. Lett.*, <https://doi.org/10.1029/2021GL093058>, in press.
- Archibald, A. T., and Coauthors, 2020: Tropospheric Ozone Assessment Report: A critical review of changes in the tropospheric ozone burden and budget from 1850 to 2100. *Elem. Sci. Anthropocene*, **8**, 034, <https://doi.org/10.1525/elementa.2020.034>.
- Arenson, L., M. Hoelzle, and S. Springman, 2002: Borehole deformation measurements and internal structure of some rock glaciers in Switzerland. *Permafrost Periglacial Processes*, **13**, 117–135, <https://doi.org/10.1002/ppp.414>.
- Arguez, A., and Coauthors, 2020: Should we expect each year in the next decade (2019–28) to be ranked among the top 10 warmest years globally? *Bull. Amer. Meteor. Soc.*, **101**, E655–E663, <https://doi.org/10.1175/BAMS-D-19-0215.1>.
- Arosio, C., A. Rozanov, E. Malinina, M. Weber, and J. P. Burrows, 2019: Merging of ozone profiles from SCIAMACHY, OMPS and SAGE II observations to study stratospheric ozone changes. *Atmos. Meas. Tech.*, **12**, 2423–2444, <https://doi.org/10.5194/amt-12-2423-2019>.
- Ashok, K., and T. Yamagata, 2009: The El Niño with a difference. *Nature*, **461**, 481–484, <https://doi.org/10.1038/461481a>.
- , S. K. Behera, S. A. Rao, H. Weng, and T. Yamagata, 2007: El Niño Modoki and its possible teleconnection. *J. Geophys. Res.*, **112**, C11007, <https://doi.org/10.1029/2006JC003798>.
- Augustine, J. A., K. O. Lantz, J.-P. Vernier, and H. Telg, 2020: Mauna Loa clear-sky "apparent" solar transmission [in "State of the Climate in 2019"]. *Bull. Amer. Meteor. Soc.*, **101** (8), S61–S62, <https://doi.org/10.1175/BAMS-D-20-0104.1>.
- Azorin-Molina, C., S. Rehman, J. A. Guijarro, T. R. McVicar, L. Minola, D. Chen, and S. M. Vicente-Serrano, 2018a: Recent trends in wind speed across Saudi Arabia, 1978–2013: A break in the stilling. *Int. J. Climatol.*, **38**, e966–e984, <https://doi.org/10.1002/joc.5423>.
- , J. Asin, T. R. McVicar, L. Minola, J. I. Lopez-Moreno, S. M. Vicente-Serrano, and D. Chen, 2018b: Evaluating anemometer drift: A statistical approach to correct biases in wind speed measurement. *Atmos. Res.*, **203**, 175–188, <https://doi.org/10.1016/j.atmosres.2017.12.010>.
- , R. J. H. Dunn, L. Ricciardulli, C. A. Mears, T. R. McVicar, J. P. Nicolas, G. P. Compo, and C. A. Smith, 2020: [Land and ocean surface winds [in "State of the Climate in 2019"]. *Bull. Amer. Meteor. Soc.*, **101** (8), S63–S65, <https://doi.org/10.1175/BAMS-D-20-0104.1>.
- Ball, W. T., and Coauthors, 2018: Evidence for a continuous decline in lower stratospheric ozone offsetting ozone layer recovery. *Atmos. Chem. Phys.*, **18**, 1379–1394, <https://doi.org/10.5194/acp-18-1379-2018>.
- Ballantyne, A. P., C. B. Alden, J. B. Miller, P. P. Tans, and J. W. C. White, 2012: Increase in observed net carbon dioxide uptake by land and oceans during the past 50 years. *Nature*, **488**, 70–72, <https://doi.org/10.1038/nature11299>.
- Banzon, V., T. M. Smith, M. Steele, B. Huang, and H.-M. Zhang, 2020: Improved estimation of proxy sea surface temperature in the arctic. *J. Atmos. Oceanic Technol.*, **37**, 341–349, <https://doi.org/10.1175/JTECH-D-19-0177.1>.
- Barichivich, J., T. J. Osborn, I. Harris, G. van der Schrier, and P. D. Jones, 2020: Global climate: Drought [in "State of the Climate in 2019"]. *Bull. Amer. Meteor. Soc.*, **101**, S59–S60, <https://doi.org/10.1175/BAMS-D-20-0104.1>.
- Barnes, E. A., A. M. Fiore, and L. W. Horowitz, 2016: Detection of trends in surface ozone in the presence of climate variability. *J. Geophys. Res. Atmos.*, **121**, 6112–6129, <https://doi.org/10.1002/2015JD024397>.
- Becker, A., P. Finger, A. Meyer-Christoffer, B. Rudolf, K. Schamm, U. Schneider, and M. Ziese, 2013: A description of the global land-surface precipitation data products of the Global Precipitation Climatology Centre with sample applications including centennial (trend) analysis from 1901–present. *Earth Syst. Sci. Data*, **5**, 71–99, <https://doi.org/10.5194/essd-5-71-2013>.
- Becker, F., and B. J. Choudhury, 1988: Relative sensitivity of normalized difference vegetation index (NDVI) and microwave polarization difference Index (MPDI) for vegetation and desertification monitoring. *Remote Sens. Environ.*, **24**, 297–311, [https://doi.org/10.1016/0034-4257\(88\)90031-4](https://doi.org/10.1016/0034-4257(88)90031-4).
- Bell, B., and Coauthors, 2020: ERA5 hourly data on pressure levels from 1950 to 1978 (preliminary version). Copernicus Climate Change Service (C3S) Climate Data Store (CDS), accessed 2 February 2021, <https://cds.climate.copernicus.eu/cdsapp#!/dataset/reanalysis-era5-pressure-levels-preliminary-back-extension?tab=overview>.
- Bellouin, N., and Coauthors, 2020: Radiative forcing of climate change from the Copernicus reanalysis of atmospheric composition. *Earth Syst. Sci. Data*, **12**, 1649–1677, <https://doi.org/10.5194/essd-12-1649-2020>.
- Benson, B., J. Magnuson, and S. Sharma, 2000: Global Lake and River Ice Phenology Database, Version 1. National Snow and Ice Data Center, accessed 8 January 2021, <https://doi.org/10.7265/N5W66HP8>.

- , and Coauthors, 2012: Extreme events, trends, and variability in Northern Hemisphere lake-ice phenology (1855–2005). *Climatic Change*, **112**, 299–323, <https://doi.org/10.1007/s10584-011-0212-8>.
- Berry, D. I., E. C. Kent, and P. K. Taylor, 2004: An analytical model of heating errors in marine air temperatures from ships. *J. Atmos. Oceanic Technol.*, **21**, 1198–1215, [https://doi.org/10.1175/1520-0426\(2004\)021<1198:AAMOHE>2.0.CO;2](https://doi.org/10.1175/1520-0426(2004)021<1198:AAMOHE>2.0.CO;2).
- Betts, R. A., C. D. Jones, J. R. Knight, R. F. Keeling, and J. J. Kennedy, 2016: El Niño and a record CO₂ rise. *Nat. Climate Change*, **6**, 806–810, <https://doi.org/10.1038/nclimate3063>.
- Biskaborn, B. K., and Coauthors, 2019: Permafrost is warming at a global scale. *Nat. Commun.*, **10**, 264, <https://doi.org/10.1038/s41467-018-08240-4>.
- Blenkinsop, S., M. R. Tye, M. Bosilovich, M. G. Donat, I. Durre, A. J. Simmons, and M. Ziese, 2020: Land surface precipitation extremes [in “State of the Climate in 2019”]. *Bull. Amer. Meteor. Soc.*, **101** (8), S47–S49, <https://doi.org/10.1175/BAMS-D-20-0104.1>.
- Bloom, A. A., and Coauthors, 2017: A global wetland methane emissions and uncertainty dataset for atmospheric chemical transport models (WetCHARTS version 1.0). *Geosci. Model Dev.*, **10**, 2141–2156, <https://doi.org/10.5194/gmd-10-2141-2017>.
- Blunden, J., and D. S. Arndt, 2019: State of the Climate in 2018. *Bull. Amer. Meteor. Soc.*, **100** (9), Si–S306, <https://doi.org/10.1175/2019BAMSStateoftheClimate.1>.
- Bock, O., 2020: Global GNSS integrated water vapour data, 1994–2020 [Data set]. AERIS, accessed 21 July 2021, <https://doi.org/10.25326/68>.
- Bodhaine, B. A., B. G. Mendonca, J. M. Harris, and J. M. Miller, 1981: Seasonal variations in aerosols and atmospheric transmission at Mauna Loa Observatory. *J. Geophys. Res.*, **86**, 7395–7398, <https://doi.org/10.1029/JC086iC08p07395>.
- Bodin, X., E. Thibert, D. Fabre, A. Ribolini, P. Schoeneich, B. Francou, and M. Fort, 2009: Two decades of responses (1986–2006) to climate by the Laurichard rock glacier, French Alps. *Permafrost Periglacial Processes*, **20**, 331–344, <https://doi.org/10.1002/ppp.665>.
- BoM, 2020a: Monthly Weather Review Australia. Bureau of Meteorology, www.bom.gov.au/climate/mwr/aus/mwr-aus-202001.pdf.
- , 2020b: Annual climate statement 2020. Bureau of Meteorology, 27 pp., www.bom.gov.au/climate/current/annual/aus/.
- , 2021a: Climate monitoring graphs. Bureau of Meteorology, www.bom.gov.au/climate/enso/indices.shtml?bookmark=ioid.
- , 2021b: Recent and historical rainfall maps. Bureau of Meteorology, www.bom.gov.au/climate/maps/rainfall/?variable=rainfall&map=anomaly&period=3month®ion=nat&year=2020&month=12&day=31.
- Bony, S., and Coauthors, 2015: Clouds, circulation and climate sensitivity. *Nat. Geosci.*, **8**, 261–268, <https://doi.org/10.1038/ngeo2398>.
- Boucher, O., and Coauthors: Clouds and aerosols. *Climate Change 2013: The Physical Science Basis*, T. F. Stocker et al., Eds., Cambridge University Press, 571–657, <https://doi.org/10.1017/CBO9781107415324.016>.
- Bowman, D. M. J. S., G. J. Williamson, O. F. Price, M. N. Ndalila, and R. A. Bradstock, 2021: Australian forests, megafires and the risk of dwindling carbon stocks. *Plant Cell Environ.*, **44**, 347–355, <https://doi.org/10.1111/pce.13916>.
- BP Statistical Review of the World Energy, 2021: <https://www.bp.com/content/dam/bp/business-sites/en/global/corporate/pdfs/energy-economics/statistical-review/bp-stats-review-2021-co2-emissions.pdf>
- Brohan, P., J. J. Kennedy, I. Harris, S. F. Tett, and P. D. Jones, 2006: Uncertainty estimates in regional and global observed temperature changes: A new data set from 1850. *J. Geophys. Res.*, **111**, D12106, <https://doi.org/10.1029/2005JD006548>.
- Broomandi, P., F. Karaca, A. Nikfal, A. Jahanbakhshi, M. Tamjidi, and J. R. Kim, 2020: Impact of COVID-19 event on the air quality in Iran. *Aerosol Air Qual. Res.*, **20**, 1793–1804, <https://doi.org/10.4209/aaqr.2020.05.0205>.
- Brutsaert, W., 2017: Global land surface evaporation trend during the past half century: Corroboration by Clausius-Clapeyron scaling. *Adv. Water Resour.*, **106**, 3–5, <https://doi.org/10.1016/j.advwatres.2016.08.014>.
- Buchli, T., A. Kos, P. Limpach, K. Merz, X. Zhou, and S. M. Springman, 2018: Kinematic investigations on the Furggwanghorn Rock Glacier, Switzerland. *Permafrost Periglacial Processes*, **29**, 3–20, <https://doi.org/10.1002/ppp.1968>.
- Byrne, M. P., and P. A. O’Gorman, 2013: Link between land-ocean warming contrast and surface relative humidities in simulations with coupled climate models. *Geophys. Res. Lett.*, **40**, 5223–5227, <https://doi.org/10.1002/grl.50971>.
- , and —, 2016: Understanding decreases in land relative humidity with global warming: Conceptual model and GCM simulations. *J. Climate*, **29**, 9045–9061, <https://doi.org/10.1175/JCLI-D-16-0351.1>.
- , and —, 2018: Trends in continental temperature and humidity directly linked to ocean warming. *Proc. Natl. Acad. Sci. USA*, **115**, 4863–4868, <https://doi.org/10.1073/pnas.1722312115>.
- Calvo, N., R. R. Garcia, W. J. Randel, and D. R. Marsh, 2010: Dynamical mechanism for the increase in tropical upwelling in the lowermost tropical stratosphere during warm ENSO events. *J. Atmos. Sci.*, **67**, 2331–2340, <https://doi.org/10.1175/2010JAS3433.1>.
- Capotondi, A., and Coauthors, 2015: Understanding ENSO diversity. *Bull. Amer. Meteor. Soc.*, **96**, 921–938, <https://doi.org/10.1175/BAMS-D-13-00117.1>.
- Carpenter, L. J., and Coauthors, 2018: Scenarios and information for policy makers. Scientific Assessment of Ozone Depletion: 2018, Global Ozone Research and Monitoring Project Rep. 58, 6.1–6.69, <https://ozone.unep.org/sites/default/files/2019-05/SAP-2018-Assessment-report.pdf>.
- Carrea, L., O. Embury, and C. J. Merchant, 2015: Datasets related to in-land water for limnology and remote sensing applications: Distance-to-land, distance-to-water, water-body identifier and lake-centre co-ordinates. *Geosci. Data J.*, **2**, 83–97, <https://doi.org/10.1002/gdj3.32>.
- , and Coauthors, 2019: Lake surface temperature [in “State of the Climate in 2018”]. *Bull. Amer. Meteor. Soc.*, **100**, S13–S14, <https://doi.org/10.1175/2019BAMSStateoftheClimate.1>.
- , and Coauthors, 2020: Lake surface temperature [in “State of the Climate in 2019”]. *Bull. Amer. Meteor. Soc.*, **101** (8), S26–S28, <https://doi.org/10.1175/BAMS-D-20-0104.1>.
- Cescatti, A., and Coauthors, 2012: Intercomparison of MODIS albedo retrievals and in situ measurements across the global FLUXNET network. *Remote Sens. Environ.*, **121**, 323–334, <https://doi.org/10.1016/j.rse.2012.02.019>.
- Chandra, S., J. R. Ziemke, W. Min, and W. G. Read, 1998: Effects of 1997–1998 El Niño on tropospheric ozone and water vapor. *Geophys. Res. Lett.*, **25**, 3867–3870, <https://doi.org/10.1029/98GL02695>.
- , —, B. N. Duncan, T. L. Diehl, N. Livesey, and L. Froidevaux, 2009: Effects of the 2006 El Niño on tropospheric ozone and carbon monoxide: Implications for dynamics and biomass burning. *Atmos. Chem. Phys.*, **9**, 4239–4249, <https://doi.org/10.5194/acp-9-4239-2009>.
- Chang, J., and Coauthors, 2019: Revisiting enteric methane emissions from domestic ruminants and their $\delta^{13}\text{C}_{\text{CH}_4}$ source signature. *Nat. Commun.*, **10**, 3420, <https://doi.org/10.1038/s41467-019-11066-3>.
- Chaparro, D., M. Piles, M. Vall-llossera, A. Camps, A. G. Konings, and D. Entekhabi, 2018: L-band vegetation optical depth seasonal metrics for crop yield assessment. *Remote Sens. Environ.*, **212**, 249–259, <https://doi.org/10.1016/j.rse.2018.04.049>.
- , G. Duveiller, M. Piles, A. Cescatti, M. Vall-llossera, A. Camps, and D. Entekhabi, 2019: Sensitivity of L-band vegetation optical depth to carbon stocks in tropical forests: A comparison to higher frequencies and optical indices. *Remote Sens. Environ.*, **232**, 111303, <https://doi.org/10.1016/j.rse.2019.111303>.
- Chen, C., and Coauthors, 2019: China and India lead in greening of the world through land-use management. *Nat. Sustainability*, **2**, 122–129, <https://doi.org/10.1038/s41893-019-0220-7>.
- Chen, X., S. Jeong, H. Park, J. Kim, and C.-R. Park, 2020: Urbanization has stronger impacts than regional climate change on wind stilling: A lesson from South Korea. *Environ. Res. Lett.*, **15**, 054016, <https://doi.org/10.1088/1748-9326/ab7e51>.

- Cheng, L., and Coauthors, 2017: Recent increases in terrestrial carbon uptake at little cost to the water cycle. *Nat. Commun.*, **8**, 110, <https://doi.org/10.1038/s41467-017-00114-5>.
- Chipperfield, M. P., and Coauthors, 2018: On the cause of recent variations in lower stratospheric ozone. *Geophys. Res. Lett.*, **45**, 5718–5726, <https://doi.org/10.1029/2018GL078071>.
- Christiansen, H. H., G. L. Gilbert, U. Neumann, N. Demidov, M. Guglielmin, K. Isaksen, M. Osuch, and J. Boike, 2021: Ground ice content, drilling methods and equipment and permafrost dynamics in Svalbard 2016–2019 (PermaSval). SESS Report 2020, M. Moreno-Ibáñez et al., Eds., Svalbard Integrated Arctic Earth Observing System, 259–275.
- Christy, J. R., and R. T. McNider, 2017: Satellite bulk tropospheric temperatures as a metric for climate sensitivity. *Asia-Pacific J. Atmos. Sci.*, **53**, 511–518, <https://doi.org/10.1007/s13143-017-0070-z>.
- , D. E. Parker, S. J. Brown, I. Macadam, M. Stendel, and W. B. Norris, 2001: Differential trends in tropical sea surface and atmospheric temperatures since 1979. *Geophys. Res. Lett.*, **28**, 183–186, <https://doi.org/10.1029/2000GL011167>.
- , R. W. Spencer, W. D. Braswell, and R. Junod, 2018: Examination of space-based bulk atmospheric temperatures for climate research. *Yaogan Xuebao*, **39**, 3580–3607, <https://doi.org/10.1080/01431161.2018.1444293>.
- , C. A. Mears, S. Po-Chedley, and L. Haimberger, 2020: Tropospheric temperature [in “State of the Climate in 2019”]. *Bull. Amer. Meteor. Soc.*, **101** (8), S30–S31, <https://doi.org/10.1175/BAMS-D-20-0104.1>.
- Chung, E.-S., B. Soden, and V. O. John, 2013: Intercalibrating microwave satellite observations for monitoring long-term variations in upper- and midtropospheric water vapor. *J. Atmos. Oceanic Technol.*, **30**, 2303–2319, <https://doi.org/10.1175/JTECH-D-13-00001.1>.
- , B. J. Soden, B. J. Sohn, and L. Shi, 2014: Upper-tropospheric moistening in response to anthropogenic warming. *Proc. Natl. Acad. Sci. USA*, **111**, 11 636–11 641, <https://doi.org/10.1073/pnas.1409659111>.
- , X. Huang, L. Shi, and V. O. John, 2016: An assessment of the consistency between satellite measurements of upper tropospheric water vapor. *J. Geophys. Res. Atmos.*, **121**, 2874–2887, <https://doi.org/10.1002/2015JD024496>.
- Cicoira, A., J. Beutel, J. Faillietaz, and A. Vieli, 2019: Water controls the seasonal rhythm of rock glacier flow. *Earth Planet. Sci. Lett.*, **528**, 115844, <https://doi.org/10.1016/j.epsl.2019.115844>.
- City of Cape Town, 2021: Weekly water dashboard, 12 July 2021. 5 pp., <https://resource.capetown.gov.za/documentcentre/Documents/City%20research%20reports%20and%20review/damlevels.pdf>.
- Coddington, O. M., 2017: TSIS Algorithm Theoretical Basis Document. Laboratory for Atmospheres and Space Physics (LASP) Doc. No. 151430 RevA, 108 pp., https://docserver.gesdisc.eosdis.nasa.gov/public/project/TSIS/TSIS_Algorithm_Theoretical_Basis_Document_151430RevA.pdf.
- Cohen, Y., and Coauthors, 2018: Climatology and long-term evolution of ozone and carbon monoxide in the upper troposphere–lower stratosphere (UTLS) at northern midlatitudes, as seen by IAGOS from 1995 to 2013. *Atmos. Chem. Phys.*, **18**, 5415–5453, <https://doi.org/10.5194/acp-18-5415-2018>.
- Coldewey-Egbers, M., and Coauthors, 2015: The GOME-type Total Ozone Essential Climate Variable (GTO-ECV) data record from the ESA Climate Change Initiative. *Atmos. Meas. Tech.*, **8**, 3923–3940, <https://doi.org/10.5194/amt-8-3923-2015>.
- Collinson, N., and T. Sparks, 2008: Phenology – nature’s calendar: An overview of results from the UK phenology network. *Arboric. J.*, **30**, 271–278, <https://doi.org/10.1080/03071375.2008.9747506>.
- Collow, A., M. Bosilovich, A. Dezfuli, and R. Lucchesi, 2020: File specification for MERRA-2 climate statistics products. GMAO Office Note 19 (Version 1.0), 15 pp., http://gmao.gsfc.nasa.gov/pubs/office_notes.
- Cooper, O. R., and Coauthors, 2014: Global distribution and trends of tropospheric ozone: An observation-based review. *Elementa*, **2**, 000029, <https://doi.org/10.12952/journal.elementa.000029>.
- , and Coauthors, 2020: Multi-decadal surface ozone trends at globally distributed remote locations. *Elem. Sci. Anthropocene*, **8**, 23, <https://doi.org/10.1525/elementa.420>.
- Copernicus Climate Change Service, 2021: Copernicus: 2020 warmest year on record for Europe; globally, 2020 ties with 2016 for warmest year recorded. 8 January, <https://climate.copernicus.eu/2020-warmest-year-record-europe-globally-2020-ties-2016-warmest-year-recorded>.
- Cornes, R. C., E. C. Kent, D. I. Berry, and J. J. Kennedy, 2020: CLASSmat: A global night marine air temperature data set, 1880–2019. *Geosci. Data J.*, **7**, 170–184, <https://doi.org/10.1002/gdj3.100>.
- Cowtan, K., and Coauthors, 2015: Robust comparison of climate models with observations using blended land air and ocean sea surface temperatures. *Geophys. Res. Lett.*, **42**, 6526–6534, <https://doi.org/10.1002/2015GL064888>.
- Cox, P. M., D. Pearson, B. B. Booth, P. Friedlingstein, C. Huntingford, C. D. Jones, and C. M. Luke, 2013: Sensitivity of tropical carbon to climate change constrained by carbon dioxide variability. *Nature*, **494**, 341–344, <https://doi.org/10.1038/nature11882>.
- Coy, L., P. A. Newman, S. Pawson, and L. R. Lait, 2017: Dynamics of the disrupted 2015/16 Quasi-biennial oscillation. *J. Climate*, **30**, 5661–5674, <https://doi.org/10.1175/JCLI-D-16-0663.1>.
- Crétaux, J.-F., and Coauthors, 2011: SOLS: A Lake database to monitor in Near Real Time water level and storage variations from remote sensing data. *J. Adv. Space Res.*, **47**, 1497–1507, <https://doi.org/10.1016/j.asr.2011.01.004>.
- , and Coauthors, 2018: Absolute calibration/validation of the altimeters on Sentinel-3A and Jason-3 over the Lake Issykkul. *Remote Sens.*, **10**, 1679, <https://doi.org/10.3390/rs10111679>.
- Crocetti, L., and Coauthors, 2020: Earth observation for agricultural drought monitoring in the Pannonian Basin (southeastern Europe): Current state and future directions. *Reg. Environ. Change*, **20**, 123, <https://doi.org/10.1007/s10113-020-01710-w>.
- Dameris, M., D. G. Loyola, M. Nützel, M. Coldewey-Egbers, C. Lerot, F. Romahn, and M. van Roozendaal, 2021: Record low ozone values over the Arctic in boreal spring 2020. *Atmos. Chem. Phys.*, **21**, 617–633, <https://doi.org/10.5194/acp-21-617-2021>.
- Daniel, J. S., S. Solomon, and D. L. Albritton, 1995: On the evaluation of halocarbon radiative forcing and global warming potentials. *J. Geophys. Res.*, **100**, 1271–1285, <https://doi.org/10.1029/94JD02516>.
- Davidson, E. A., 2009: The contribution of manure and fertilizer nitrogen to atmospheric nitrous oxide since 1860. *Nat. Geosci.*, **2**, 659–662, <https://doi.org/10.1038/ngeo608>.
- Davis, S. M., and Coauthors, 2016: The Stratospheric Water and Ozone Satellite Homogenized (SWOOSH) database: A long-term database for climate studies. *Earth Syst. Sci. Data*, **8**, 461–490, <https://doi.org/10.5194/essd-8-461-2016>.
- Deeter, M. N., and Coauthors, 2014: The MOPITT Version 6 product: Algorithm enhancements and validation. *Atmos. Meas. Tech.*, **7**, 3623–3632, <https://doi.org/10.5194/amt-7-3623-2014>.
- Delaloye, R., and Coauthors, 2008: Recent interannual variations of rock glacier creep in the European Alps. *Proc. of the 9th Int. Conf. on Permafrost*, Fairbanks, AK, University of Alaska Fairbanks, 343–348.
- , C. Lambiel, and I. Gärtner-Roer, 2010: Overview of rock glacier kinematics research in the Swiss Alps. *Geogr. Helv.*, **65**, 135–145, <https://doi.org/10.5194/gh-65-135-2010>.
- , C. Barboux, X. Bodin, A. Brenning, L. Hartl, Y. Hu, and A. Ikeda, 2018: Rock glacier inventories and kinematics: A new IPA Action Group. *5th European Conf. on Permafrost, Book of Abstracts*, Chamonix, France, Laboratoire EDYTEM, 392–393.
- Deng, K., C. Azorin-Molina, L. Minola, G. Zhang, and D. Chen, 2021: Global near-surface wind speed changes over the last decades revealed by reanalyses and CMIP6 model simulations. *J. Climate*, **34**, 2219–2234, <https://doi.org/10.1175/JCLI-D-20-0310.1>.
- Dewitte, S., D. Crommelynck, and A. Joukof, 2004: Total solar irradiance observations from DIARAD/VIRGO. *J. Geophys. Res.*, **109**, A02102, <https://doi.org/10.1029/2002JA009694>.

- Di Girolamo, L., A. Menzies, G. Zhao, K. Mueller, C. Moroney, and D. J. Diner, 2010: Multi-angle imaging SpectroRadiometer level 3 cloud fraction by altitude algorithm theoretical basis document. JPL Publ., D-62358, 23 pp., https://eosps.nasa.gov/sites/default/files/atbd/MISR_CFBA_ATBD.pdf.
- Dlugokencky, E. J., L. P. Steele, P. M. Lang, and K. A. Masarie, 1994: The growth rate and distribution of atmospheric methane. *J. Geophys. Res.*, **99**, 17 021–17 043, <https://doi.org/10.1029/94JD01245>.
- , S. Houweling, L. Bruhwiler, K. A. Masarie, P. M. Lang, J. B. Miller, and P. P. Tans, 2003: Atmospheric methane levels off: Temporary pause or a new steady-state? *Geophys. Res. Lett.*, **30**, 1992, <https://doi.org/10.1029/2003GL018126>.
- Döll, P., and B. Lehner, 2002: Validation of a new global 30-min drainage direction map. *J. Hydrol.*, **258**, 214–231, [https://doi.org/10.1016/S0022-1694\(01\)00565-0](https://doi.org/10.1016/S0022-1694(01)00565-0).
- Donat, M., L. Alexander, H. Yang, I. Durre, R. Vose, and J. Caesar, 2013: Global land-based datasets for monitoring climatic extremes. *Bull. Amer. Meteor. Soc.*, **94**, 997–1006, <https://doi.org/10.1175/BAMS-D-12-00109.1>.
- Dorigo, W. A., and Coauthors, 2017: ESA CCI Soil Moisture for improved Earth system understanding: State-of-the art and future directions. *Remote Sens. Environ.*, **203**, 185–215, <https://doi.org/10.1016/j.rse.2017.07.001>.
- , and Coauthors, 2021: Closing the water cycle from observations across scales: Where do we stand? *Bull. Amer. Meteor. Soc.*, <https://doi.org/10.1175/BAMS-D-19-0316.1>, in press.
- Doumbia, T., and Coauthors, 2021: Changes in global air pollutant emissions during the COVID-19 pandemic: A dataset for atmospheric chemistry modeling. *Earth Syst. Sci. Data Discuss.*, <https://doi.org/10.5194/essd-2020-348>.
- Du, H., and Coauthors, 2019: Precipitation from persistent extremes is increasing in most regions and globally. *Geophys. Res. Lett.*, **46**, 6041–6049, <https://doi.org/10.1029/2019GL081898>.
- Dunn, R. J. H., 2019: HadISD version 3: Monthly updates. Hadley Centre Tech. Note 103, 10 pp., www.metoffice.gov.uk/research/library-and-archive/publications/science/climate-science-technical-notes.
- , K. M. Willett, P. W. Thorne, E. V. Woolley, I. Durre, A. Dai, D. E. Parker, and R. S. Vose, 2012: HadISD: A quality-controlled global synoptic report database for selected variables at long-term stations from 1973–2011. *Climate Past*, **8**, 1649–1679, <https://doi.org/10.5194/cp-8-1649-2012>.
- , —, D. E. Parker, and L. Mitchell, 2016: Expanding HadISD: Quality-controlled, sub-daily station data from 1931. *Geosci. Instrum. Methods Data Syst.*, **5**, 473–491, <https://doi.org/10.5194/gi-5-473-2016>.
- , and Coauthors, 2020a: Development of an updated global land in-situ-based data set of temperature and precipitation extremes: HadEX3. *J. Geophys. Res. Atmos.*, **125**, e2019JD032263, <https://doi.org/10.1029/2019JD032263>.
- Dussaillant, I., and Coauthors, 2019: Two decades of glacier mass loss along the Andes. *Nat. Geosci.*, **12**, 802–808, <https://doi.org/10.1038/s41561-019-0432-5>.
- Dvortsov, V., and S. Solomon, 2001: Response of the stratospheric temperatures and ozone to past and future increases in stratospheric humidity. *J. Geophys. Res.*, **106**, 7505–7514, <https://doi.org/10.1029/2000JD900637>.
- Ellis, H. T., and R. F. Pueschel, 1971: Solar radiation: Absence of air pollution trends at Mauna Loa. *Science*, **172**, 845–846, <https://doi.org/10.1126/science.172.3985.845>.
- Engel, A., and M. Rigby, 2018: Update on ozone-depleting substances (ODS) and other gases of interest to the Montreal protocol. Scientific Assessment of Ozone Depletion: 2018, Global Ozone Research and Monitoring Project Rep. 58, 1.1–1.66, <https://ozone.unep.org/sites/default/files/2019-05/SAP-2018-Assessment-report.pdf>.
- Eriksen, H. Ø., L. Rouyet, T. R. Lauknes, I. Berthling, K. Isaksen, H. Hindberg, Y. Larsen, and G. D. Corner, 2018: Recent acceleration of a rock glacier complex, Ådjet, Norway, Documented by 62 years of remote sensing observations. *Geophys. Res. Lett.*, **45**, 8314–8323, <https://doi.org/10.1029/2018GL077605>.
- Estilow, T. W., A. H. Young, and D. A. Robinson, 2015: A long-term Northern Hemisphere snow cover extent data record for climate studies and monitoring. *Earth Syst. Sci. Data*, **7**, 137–142, <https://doi.org/10.5194/essd-7-137-2015>.
- Etheridge, D. M., L. P. Steele, R. L. Langenfelds, R. J. Francey, J. M. Barnola, and V. I. Morgan, 1996: Natural and anthropogenic changes in atmospheric CO₂ over the last 1000 years from air in Antarctic ice and firn. *J. Geophys. Res.*, **101**, 4115–4128, <https://doi.org/10.1029/95JD03410>.
- Etzelmüller, B., and Coauthors, 2020: Twenty years of European mountain permafrost dynamics – The PACE legacy. *Environ. Res. Lett.*, **15**, 104070, <https://doi.org/10.1088/1748-9326/abae9d>.
- Feng, W., S. Dhomse, C. Arosio, M. Weber, J. P. Burrows, M. L. Santee, and M. P. Chipperfield, 2021: Arctic ozone depletion in 2019/20: Roles of chemistry, dynamics and the Montreal Protocol. *Geophys. Res. Lett.*, **48**, e2020GL091911, <https://doi.org/10.1029/2020GL091911>.
- Fioletov, V. E., G. E. Bodeker, A. J. Miller, R. D. McPeters, and R. Stolarski, 2002: Global and zonal total ozone variations estimated from ground-based and satellite measurements: 1964–2000. *J. Geophys. Res.*, **107**, 4647, <https://doi.org/10.1029/2001JD001350>.
- , and Coauthors, 2008: The performance of the ground-based total ozone network assessed using satellite data. *J. Geophys. Res.*, **113**, D14313, <https://doi.org/10.1029/2008JD009809>.
- Fisher, J. B., and Coauthors, 2017: The future of evapotranspiration: Global requirements for ecosystem functioning, carbon and climate feedbacks, agricultural management, and water resources. *Water Resour. Res.*, **53**, 2618–2626, <https://doi.org/10.1002/2016WR020175>.
- , and Coauthors, 2020: ECOSTRESS: NASA's next generation mission to measure evapotranspiration from the international space station. *Water Resour. Res.*, **56**, <https://doi.org/10.1029/2019WR026058>.
- Flato, G., and Coauthors, 2013: Evaluation of climate models. *Climate Change 2013: The Physical Science Basis*, T. F. Stocker et al., Eds., Cambridge University Press, 741–866.
- Fleming, Z. L., and Coauthors, 2018: Tropospheric Ozone Assessment Report: Present-day ozone distribution and trends relevant to human health. *Elem. Sci. Anthropocene*, **6**, 12, <https://doi.org/10.1525/elementa.273>.
- Flemming, J., and A. Inness, 2019: Carbon monoxide [in “State of the Climate in 2018”]. *Bull. Amer. Meteor. Soc.*, **100**, S181–S185, <https://doi.org/10.1175/2019BAMSStateoftheClimate.1>.
- , and Coauthors, 2017: The CAMS interim reanalysis of carbon monoxide, ozone and aerosol for 2003–2015. *Atmos. Chem. Phys.*, **17**, 1945–1983, <https://doi.org/10.5194/acp-17-1945-2017>.
- Floodlist, 2020a: India and Bangladesh – Torrential rain from Cyclone Amphan triggers flooding. 21 May, accessed 11 February 2021, <http://floodlist.com/asia/india-bangladesh-cyclone-amphan-floods-may-2020>.
- , 2020b: Somalia – Floods after Tropical Storm Gati dumps year's worth of rain. 24 November, accessed 8 February 2021, <http://floodlist.com/africa/somalia-floods-storm-gati-november-2020>.
- , 2020c: Italy - 200 rescued from floods in Calabria after 450mm in 48 hours. 23 November, accessed 11 February 2021, <http://floodlist.com/europe/italy-floods-calabria-november-2020>.
- , 2020d: New Zealand – Record rainfall causes flooding in Napier. 10 November, accessed 11 February 2021, <http://floodlist.com/australia/new-zealand-flood-napier-november-2020>.
- Folland, C. K., and T. R. Karl, 2001: Recent rates of warming in marine environment meet controversy. *Eos, Trans. Amer. Geophys. Union*, **82**, 453–461, <https://doi.org/10.1029/01EO00270>.
- Forkel, M., W. Dorigo, G. Lasslop, I. Teubner, E. Chuvieco, and K. Thonicke, 2017: A data-driven approach to identify controls on global fire activity from satellite and climate observations (SOFIA V1). *Geosci. Model Dev.*, **10**, 4443–4476, <https://doi.org/10.5194/gmd-10-4443-2017>.
- , and Coauthors, 2019: Recent global and regional trends in burned area and their compensating environmental controls. *Environ. Res. Commun.*, **1**, 051005, <https://doi.org/10.1088/2515-7620/ab25d2>.
- Forster, P. M., and Coauthors, 2020: Current and future global climate impacts resulting from COVID-19. *Nat. Climate Change*, **10**, 913–919, <https://doi.org/10.1038/s41558-020-0883-0>.

- Forzieri, G., R. Alkama, D. G. Miralles, and A. Cescatti, 2017: Satellites reveal contrasting responses of regional climate to the widespread greening of Earth. *Science*, **356**, 1180–1184, <https://doi.org/10.1126/science.aal1727>.
- Francis, D., R. Fonseca, N. Nelli, J. Cuesta, M. Weston, A. Evan, and M. Temimi, 2020: The atmospheric drivers of the major Saharan dust storm in June 2020. *Geophys. Res. Lett.*, **47**, e2020GL090102, <https://doi.org/10.1029/2020GL090102>.
- Frauenfelder, R., W. Haeberli, and M. Hoelzle, 2003: Rock glacier occurrence and related terrain parameters in a study area of the Eastern Swiss Alps. *Permafrost: Proceedings of the 8th International Conference on Permafrost*, M. Phillips, S. M. Springman, and L. U. Arenson, Eds., A. A. Balkema, 253–258.
- Free, M., D. J. Seidel, J. K. Angel, J. Lanzante, I. Durre, and T. C. Peterson, 2005: Radiosonde Atmospheric Temperature Products for Assessing Climate (RATPAC): A new dataset of large-area anomaly time series. *J. Geophys. Res.*, **110**, D22101, <https://doi.org/10.1029/2005JD006169>.
- Freie Universität Berlin, 2021: Die Quasi-Biennial-Oszillation (QBO) Datenreihe. Accessed 19 January 2021, www.geo.fu-berlin.de/met/ag/strat/produkte/qbo/index.html.
- Friedlingstein, P., and Coauthors, 2020: Global carbon budget 2020. *Earth Syst. Sci. Data*, **12**, 3269–3340, <https://doi.org/10.5194/essd-12-3269-2020>.
- Frith, S. M., N. A. Kramarova, R. S. Stolarski, R. D. McPeters, P. K. Bhartia, and G. J. Labov, 2014: Recent changes in total column ozone based on the SBUV Version 8.6 Merged Ozone Data Set. *J. Geophys. Res.*, **119**, 9735–9751, <https://doi.org/10.1002/2014JD021889>.
- , R. S. Stolarski, N. A. Kramarova, and R. D. McPeters, 2017: Estimating uncertainties in the SBUV Version 8.6 merged profile ozone data set. *Atmos. Chem. Phys.*, **17**, 14695–14707, <https://doi.org/10.5194/acp-17-14695-2017>.
- Fujita, R., S. Morimoto, S. Maksyutov, H. S. Kim, M. Arshinov, G. Brailsford, S. Aoki, and T. Nakazawa, 2020: Global and regional CH₄ emissions for 1995–2013 derived from atmospheric CH₄, δ¹³C-CH₄, and δD-CH₄ observations and a chemical transport model. *J. Geophys. Res. Atmos.*, **125**, e2020JD032903, <https://doi.org/10.1029/2020JD032903>.
- Garane, K., and Coauthors, 2018: Quality assessment of the Ozone_cci Climate Research Data Package (release 2017): 1. Ground-based validation of total ozone column data products. *Atmos. Meas. Tech.*, **11**, 1385–1402, <https://doi.org/10.5194/amt-11-1385-2018>.
- Garcia, H. E., and Coauthors, 2019: World Ocean Atlas 2018: Product documentation. NOAA, 20 pp., www.ncei.noaa.gov/sites/default/files/2020-04/woa18documentation.pdf.
- Garfinkel, C. I., A. Gordon, L. D. Oman, F. Li, S. Davis, and S. Pawson, 2018: Non-linear response of tropical lower-stratospheric temperature and water vapor to ENSO. *Atmos. Chem. Phys.*, **18**, 4597–4615, <https://doi.org/10.5194/acp-18-4597-2018>.
- Garreaud, R. D., and Coauthors, 2017: The 2010–2015 megadrought in central Chile: Impacts on regional hydroclimate and vegetation. *Hydrol. Earth Syst. Sci.*, **21**, 6307–6327, <https://doi.org/10.5194/hess-21-6307-2017>.
- Gaudel, A., and Coauthors, 2018: Tropospheric Ozone Assessment Report: Present-day distribution and trends of tropospheric ozone relevant to climate and global atmospheric chemistry model evaluation. *Elementa*, **6**, 39, <https://doi.org/10.1525/elementa.291>.
- , and Coauthors, 2020: Aircraft observations since the 1990s reveal increases of tropospheric ozone at multiple locations across the Northern Hemisphere. *Sci. Adv.*, **6**, eaba8272, <https://doi.org/10.1126/sciadv.aba8272>.
- GCOS, 2016: The Global Observing System for Climate: Implementation needs. Tech. Rep. GCOS-200, World Meteorological Organization, 315 pp., https://library.wmo.int/doc_num.php?explnum_id=3417.
- Gelaro, R., and Coauthors, 2017: The Modern-Era Retrospective Analysis for Research and Applications, Version 2 (MERRA-2). *J. Climate*, **30**, 5419–5454, <https://doi.org/10.1175/JCLI-D-16-0758.1>.
- Getirana, A., S. Kumar, M. Girotto, and M. Rodell, 2017: Rivers and floodplains as key components of global terrestrial water storage variability. *Geophys. Res. Lett.*, **44**, 10359–10368, <https://doi.org/10.1002/2017GL074684>.
- Ghilain, N., A. Arboleda, and F. Gellens-Meulenberghs, 2011: Evapotranspiration modelling at large scale using near-real time MSG SEVIRI derived data. *Hydrol. Earth Syst. Sci.*, **15**, 771–786, <https://doi.org/10.5194/hess-15-771-2011>.
- Giglio, L., W. Schroeder, and C. O. Justice, 2016: The collection 6 MODIS active fire detection algorithm and fire products. *Remote Sens. Environ.*, **178**, 31–41, <https://doi.org/10.1016/j.rse.2016.02.054>.
- Gleason, K. L., J. H. Lawrimore, D. H. Levinson, T. R. Karl, and D. J. Karoly, 2008: A revised U.S. Climate Extremes Index. *J. Climate*, **21**, 2124–2137, <https://doi.org/10.1175/2007JCLI1883.1>.
- Gobron, N., 2019: Terrestrial vegetation activity [in “State of the Climate in 2018”]. *Bull. Amer. Meteor. Soc.*, **100** (9), S63–S64, <https://doi.org/10.1175/2019BAMSStateoftheClimate.1>.
- , and M. Robustelli, 2013: Monitoring the state of the global terrestrial surfaces. *Proc. 2013 ESA Living Planet Symp.*, Edinburgh, United Kingdom, European Space Agency, JRC84937, <https://publications.jrc.ec.europa.eu/repository/handle/JRC84937>.
- , A. S. Belward, B. Pinty, and W. Knorr, 2010: Monitoring biosphere vegetation 1998–2009. *Geophys. Res. Lett.*, **37**, L15402, <https://doi.org/10.1029/2010GL043870>.
- Goss, M., D. L. Swain, J. T. Abatzoglou, A. Sarhadi, C. A. Kolden, A. P. Williams, and N. S. Diffenbaugh, 2020: Climate change is increasing the likelihood of extreme autumn wildfire conditions across California. *Environ. Res. Lett.*, **15**, 094016, <https://doi.org/10.1088/1748-9326/ab83a7>.
- Granier, C., and Coauthors, 2011: Evolution of anthropogenic and biomass burning emissions of air pollutants at global and regional scales during the 1980–2010 period. *Climatic Change*, **109**, 163–190, <https://doi.org/10.1007/s10584-011-0154-1>.
- Gromov, S., C. A. Brenninkmeijer, and P. Jöckel, 2018: A very limited role of tropospheric chlorine as a sink of the greenhouse gas methane. *Atmos. Chem. Phys.*, **18**, 9831–9843, <https://doi.org/10.5194/acp-18-9831-2018>.
- Gruber, A., W. A. Dorigo, W. Crow, and W. Wagner, 2017: Triple collocation-based merging of satellite soil moisture retrievals. *IEEE Trans. Geosci. Remote Sens.*, **55**, 6780–6792, <https://doi.org/10.1109/TGRS.2017.2734070>.
- , T. Scanlon, R. van der Schalie, W. Wagner, and W. Dorigo, 2019: Evolution of the ESA CCI Soil Moisture Climate Data Records and their underlying merging methodology. *Earth Syst. Sci. Data*, **11**, 717–739, <https://doi.org/10.5194/essd-11-717-2019>.
- Haeberli, W., 1985: Creep of mountain permafrost: Internal structure and flow of alpine rock glaciers. *Mitteilungen der Versuchsanstalt für Wasserbau, Hydrologie und Glaziologie* **77**, 142 pp., <https://ethz.ch/content/dam/ethz/special-interest/baug/vaw/vaw-dam/documents/das-institut/mitteilungen/1980-1989/077.pdf>.
- Haimberger, L., C. Tavalato, and S. Sperka, 2012: Homogenization of the Global Radiosonde Temperature dataset through combined comparison with reanalysis background series and neighboring stations. *J. Climate*, **25**, 8108–8131, <https://doi.org/10.1175/JCLI-D-11-00668.1>.
- Hamilton, D. S., and Coauthors, 2019: Improved methodologies for Earth system modelling of atmospheric soluble iron and observation comparisons using the Mechanism of Intermediate complexity for Modelling Iron (MIMI v1.0). *Geosci. Model Dev.*, **12**, 3835–3862, <https://doi.org/10.5194/gmd-12-3835-2019>.
- Hansen, J., R. Ruedy, M. Sato, and K. Lo, 2010: Global surface temperature change. *Rev. Geophys.*, **48**, RG4004, <https://doi.org/10.1029/2010RG000345>.
- Harris, C., and Coauthors, 2009: Permafrost and climate in Europe: Monitoring and modelling thermal, geomorphological and geotechnical responses. *Earth-Sci. Rev.*, **92**, 117–171, <https://doi.org/10.1016/j.earscirev.2008.12.002>.
- Harris, I., T. J. Osborn, P. D. Jones, and D. H. Lister, 2020: Version 4 of the CRU TS monthly high-resolution gridded multivariate climate dataset. *Sci. Data*, **7**, 109, <https://doi.org/10.1038/s41597-020-0453-3>.
- Hartmann, D. L., and Coauthors, 2013: Observations: Atmosphere and surface. *Climate Change 2013: The Physical Science Basis*, T. F. Stocker et al., Eds., Cambridge University Press, 159–254.

- Heidinger, A. K., M. J. Foster, A. Walther, and X. Zhao, 2013: The pathfinder atmospheres extended AVHRR climate dataset. *Bull. Amer. Meteor. Soc.*, **95**, 909–922, <https://doi.org/10.1175/BAMS-D-12-00246.1>.
- Held, I. M., and B. J. Soden, 2000: Water vapor feedback and global warming. *Annu. Rev. Energy Environ.*, **25**, 441–475, <https://doi.org/10.1146/annurev.energy.25.1.441>.
- , and —, 2006: Robust responses of the hydrological cycle to global warming. *J. Climate*, **19**, 5686–5699, <https://doi.org/10.1175/JCLI3990.1>.
- Hersbach, H., and Coauthors, 2019: Global reanalysis: Goodbye ERA-Interim, hello ERA5. ECMWF Newsletter, No. 159, ECMWF, Reading, United Kingdom, 17–24, <https://doi.org/10.21957/vf291hehd7>.
- , and Coauthors, 2020: The ERA5 global reanalysis. *Quart. J. Roy. Meteor. Soc.*, **146**, 1999–2049, <https://doi.org/10.1002/qj.3803>.
- Hirahara, S., M. A. Balmaseda, E. de Boisseson, and H. Hersbach, 2016: Sea surface temperature and sea ice concentration for ERA5. ERA Rep. Series 26, 25 pp, www.ecmwf.int/node/16555.
- Hirsch, E., and I. Koren, 2021: Record-breaking aerosol levels explained by smoke injection into the stratosphere. *Science*, **371**, 1269–1274, <https://doi.org/10.1126/science.abe1415>.
- Ho, S.-P., X. Zhou, Y.-H. Kuo, D. Hunt, and J.-H. Wang, 2010a: Global evaluation of radiosonde water vapor systematic biases using GPS radio occultation from COSMIC and ECMWF analysis. *Remote Sens.*, **2**, 1320–1330, <https://doi.org/10.3390/rs2051320>.
- , Y.-H. Kuo, W. Schreiner, and X. Zhou, 2010b: Using SI-traceable global positioning system radio occultation measurements for climate monitoring [in “State of the Climate in 2009”]. *Bull. Amer. Meteor. Soc.*, **91** (7), S36–S37, <https://doi.org/10.1175/BAMS-91-7-StateoftheClimate>.
- , and Coauthors, 2020a: The COSMIC/FORMOSAT-3 radio occultation mission after 12 years: Accomplishments, remaining challenges, and potential impacts of COSMIC-2. *Bull. Amer. Meteor. Soc.*, **101**, E1107–E1136, <https://doi.org/10.1175/BAMS-D-18-0290.1>.
- , and Coauthors, 2020b: Initial assessment of the COSMIC-2/FORMOSAT-7 neutral atmosphere data quality in NESDIS/STAR using in situ and satellite data. *Remote Sens.*, **12**, 4099, <https://doi.org/10.3390/rs12244099>.
- Hobday, A.J., and Coauthors, 2016: A hierarchical approach to defining marine heatwaves. *Prog. Oceanogr.*, **141**, 227–238, <https://doi.org/10.1016/j.pocan.2015.12.014>.
- , and Coauthors, 2018: Categorizing and naming marine heatwaves. *Oceanography*, **31**, 162–173, <https://doi.org/10.5670/oceanog.2018.205>.
- Hock, R., and Coauthors, 2019: High mountain areas. *IPCC Special Report on the Ocean and Cryosphere in a Changing Climate*, H.-O. Pörtner, Eds., IPCC, 131–202, www.ipcc.ch/srocc/.
- Hofmann, D. J., and S. A. Montzka, 2009: Recovery of the ozone layer: The ozone depleting gas index. *Eos, Trans. Amer. Geophys. Union*, **90**, 1–2, <https://doi.org/10.1029/2009EO010001>.
- , J. H. Butler, E. J. Dlugokencky, J. W. Elkins, K. Masarie, S. A. Montzka, and P. Tans, 2006: The role of carbon dioxide in climate forcing from 1979 to 2004: Introduction of the annual greenhouse gas index. *Tellus*, **58B**, 614–619, <https://doi.org/10.1111/j.1600-0889.2006.00201.x>.
- Hossaini, R., and Coauthors, 2016: A global model of tropospheric chlorine chemistry: Organic versus inorganic sources and impact on methane oxidation. *J. Geophys. Res. Atmos.*, **121**, 14271–14297, <https://doi.org/10.1002/2016JD025756>.
- Hrbáček, F., Z. Engel, M. Kňázková, and J. Smolíková, 2021: Effect of summer snow cover on the active layer thermal regime and thickness on CALM-5 JGM site, James Ross Island, eastern Antarctic Peninsula. *Catena*, <https://doi.org/10.1016/j.catena.2021.105608>.
- Hu, L., and Coauthors, 2019: Enhanced North American carbon uptake associated with El Niño. *Sci. Adv.*, **5**, eaaw0076, <https://doi.org/10.1126/sciadv.aaw0076>.
- Huang, B., and Coauthors, 2015: Extended reconstructed sea surface temperature version 4 (ERSST.v4). Part I: Upgrades and intercomparisons. *J. Climate*, **28**, 911–930, <https://doi.org/10.1175/JCLI-D-14-00006.1>.
- Huang, C.-Y., W.-H. Teng, S.-P. Ho, and Y. H. Kuo, 2013: Global variation of COSMIC precipitable water over land: Comparisons with ground-based GPS measurements and NCEP reanalyses. *Geophys. Res. Lett.*, **40**, 5327–5331, <https://doi.org/10.1002/grl.50885>.
- Huijnen, V., and Coauthors, 2016: Fire carbon emissions over maritime southeast Asia in 2015 largest since 1997. *Sci. Rep.*, **6**, 26886, <https://doi.org/10.1038/srep26886>.
- Humphrey, V., J. Zscheischler, P. Ciaia, L. Gudmundsson, S. Sitch, and S. I. Seneviratne, 2018: Sensitivity of atmospheric CO₂ growth rate to observed changes in terrestrial water storage. *Nature*, **560**, 628–631, <https://doi.org/10.1038/s41586-018-0424-4>.
- Hüser, I., B. Gehrke, and J. W. Kaiser, 2018: Methodology to correct biases in individual satellite FRP products. CAMS Rep. CAMS44-2016SC3-D44.3.3.1-2018-20187, ECMWF, Reading, United Kingdom, 20 pp., Available upon request from <http://support.ecmwf.int>.
- Inness, A., and Coauthors, 2013: The MACC reanalysis: An 8-year data set of atmospheric composition. *Atmos. Chem. Phys.*, **13**, 4073–4109, <https://doi.org/10.5194/acp-13-4073-2013>.
- , and Coauthors, 2019: The CAMS reanalysis of atmospheric composition. *Atmos. Chem. Phys.*, **19**, 3515–3556, <https://doi.org/10.5194/acp-19-3515-2019>.
- , S. Chabrillat, J. Flemming, V. Huijnen, B. Langenrock, J. Nicolas, I. Polichtchouk, and M. Razinger, 2020: Exceptionally low Arctic stratospheric ozone in Spring 2020 as seen in the CAMS reanalysis. *J. Geophys. Res.*, **125**, e2020JD033563, <https://doi.org/10.1029/2020JD033563>.
- IPCC, 2013: *Climate Change 2013: The Physical Science Basis*. Cambridge University Press, 1535 pp., <https://doi.org/10.1017/CBO9781107415324>.
- John, V. O., and B. J. Soden, 2007: Temperature and humidity biases in global climate models and their impact on climate feedbacks. *Geophys. Res. Lett.*, **34**, L18704, <https://doi.org/10.1029/2007GL030429>.
- , G. Holl, R. P. Allan, S. A. Buehler, D. E. Parker, and B. J. Soden, 2011: Clear-sky biases in satellite infra-red estimates of upper tropospheric humidity and its trends. *J. Geophys. Res.*, **116**, D14108, <https://doi.org/10.1029/2010JD015355>.
- Jones, G. S., 2020: “Apples and oranges”: On comparing simulated historic near-surface temperature changes with observations. *Quart. J. Roy. Meteor. Soc.*, **146**, 3747–3771, <https://doi.org/10.1002/qj.3871>.
- Junod, R. A., and J. R. Christy, 2020: A new compilation of globally gridded nighttime marine air temperatures: The UAHNMATv1 dataset. *Int. J. Climatol.*, **40**, 2609–2623, <https://doi.org/10.1002/joc.6354>.
- Kääb, A., and M. Vollmer, 2000: Surface geometry, thickness changes and flow fields on creeping mountain permafrost: Automatic extraction by digital image analysis. *Permafrost Periglacial Processes*, **11**, 315–326, [https://doi.org/10.1002/1099-1530\(200012\)11:4<315::AID-PPP365>3.0.CO;2-J](https://doi.org/10.1002/1099-1530(200012)11:4<315::AID-PPP365>3.0.CO;2-J).
- , R. Frauenfelder, and I. Roer, 2007: On the response of rock glacier creep to surface temperature increase. *Global Planet. Change*, **56**, 172–187, <https://doi.org/10.1016/j.gloplacha.2006.07.005>.
- , T. Strozzi, T. Bolch, R. Caduff, H. Trefall, M. Stoffel, and A. Kokarev, 2021: Inventory and changes of rock glacier creep speeds in Ile Alatau and Kungöy Ala-Too, northern Tien Shan, since the 1950s. *Cryosphere*, **15**, 927–949, <https://doi.org/10.5194/tc-15-927-2021>.
- Kablick, G. P., D. R. Allen, M. D. Fromm, and G. E. Nedoluha, 2020: Australian PyroCb smoke generates synoptic-scale stratospheric anticyclones. *Geophys. Res. Lett.*, **47**, e2020GL088101, <https://doi.org/10.1029/2020GL088101>.
- Kaiser, J. W., and Coauthors, 2012: Biomass burning emissions estimated with a global fire assimilation system based on observed fire radiative power. *Biogeosciences*, **9**, 527–554, <https://doi.org/10.5194/bg-9-527-2012>.
- , G. R. van der Werf, and I. Hüser, 2020: Biomass burning [in “State of the Climate in 2019”]. *Bull. Amer. Meteor. Soc.*, **101** (8), S93–S95, <https://doi.org/10.1175/BAMS-D-20-0104.1>.
- Kannan, K., and K. R. Rajagopal, 2013: A model for the flow of rock glaciers. *Int. J. Non-linear Mech.*, **48**, 59–64, <https://doi.org/10.1016/j.ijnonlinmec.2012.06.002>.

- Kaplan, A., 2011: Patterns and indices of climate variability [in "State of the Climate in 2010"]. *Bull. Amer. Meteor. Soc.*, **92** (6), S20–S25, <https://doi.org/10.1175/1520-0477-92.6.S1>.
- Karlsson, K.-G., and Coauthors, 2017: CLARA-A2: The second edition of the CM SAF cloud and radiation data record from 34 years of global AVHRR data. *Atmos. Chem. Phys.*, **17**, 5809–5828, <https://doi.org/10.5194/ACP-17-5809-2017>.
- Karpechko, A. Y., and A. C. Maycock, 2018: Stratospheric ozone changes and climate. Scientific Assessment of Ozone Depletion: 2018, Global Ozone Research and Monitoring Project Rep. 58, 5.1–5.50, <https://ozone.unep.org/sites/default/files/2019-05/SAP-2018-Assessment-report.pdf>.
- Keeling, C. D., and R. Revelle, 1985: Effects of El-Niño Southern Oscillation on the atmospheric content of carbon-dioxide. *Meteoritics*, **20**, 437–450.
- Kellerer-Pirklbauer, A., and V. Kaufmann, 2012: About the relationship between rock glacier velocity and climate parameters in central Austria. *Aust. J. Earth Sci.*, **105**, 94–112.
- , and —, 2018: Deglaciation and its impact on permafrost and rock glacier evolution: New insight from two adjacent cirques in Austria. *Sci. Total Environ.*, **621**, 1397–1414, <https://doi.org/10.1016/j.scitotenv.2017.10.087>.
- Kennedy, J. J., and Coauthors, 2010: How do we know the world has warmed? [in "State of the Climate in 2009"]. *Bull. Amer. Meteor. Soc.*, **91** (7), S26–S27, <https://doi.org/10.1175/BAMS-91-7-StateoftheClimate>.
- , N. A. Rayner, C. P. Atkinson, and R. E. Killick, 2019: An ensemble data set of sea surface temperature change from 1850: The Met Office Hadley Centre HadSST4.0.0.0 data set. *J. Geophys. Res. Atmos.*, **124**, 7719–7763, <https://doi.org/10.1029/2018JD029867>.
- Kent, E. C., N. A. Rayner, D. I. Berry, M. Saunby, B. I. Moat, J. J. Kennedy, and D. E. Parker, 2013: Global analysis of night marine air temperature and its uncertainty since 1880: The HadNMAT2 data set. *J. Geophys. Res. Atmos.*, **118**, 1281–1298, <https://doi.org/10.1002/jgrd.50152>.
- Khaykin, S., and Coauthors, 2020: The 2019/20 Australian wildfires generated a persistent smoke-charged vortex rising up to 352km altitude. *Commun. Earth Environ.*, **1**, 22, <https://doi.org/10.1038/s43247-020-00022-5>.
- Kim, H., 2020: River discharge and runoff [in "State of the Climate in 2019"]. *Bull. Amer. Meteor.*, **101**, S53–S55, <https://doi.org/10.1175/BAMS-D-20-0104.1>.
- , P. J.-F. Yeh, T. Oki, and S. Kanae, 2009: Role of rivers in the seasonal variations of terrestrial water storage over global basins. *Geophys. Res. Lett.*, **36**, L17402, <https://doi.org/10.1029/2009GL039006>.
- Kim, J., and K. Paik, 2015: Recent recovery of surface wind speed after decadal decrease: A focus on South Korea. *Climate Dyn.*, **45**, 1699–1712, <https://doi.org/10.1007/s00382-015-2546-9>.
- King, O., and Coauthors, 2019: Six decades of glacier mass changes around mount everest are revealed by historical and contemporary images. *One Earth*, **3**, 608–620, <https://doi.org/10.1016/j.oneear.2020.10.019>.
- Klein Tank, A. M. G., and Coauthors, 2002: Daily dataset of 20th-century surface air temperature and precipitation series for the European Climate Assessment. *Int. J. Climatol.*, **22**, 1441–1453, <https://doi.org/10.1002/joc.773>.
- Kobayashi, S., and Coauthors, 2015: The JRA-55 reanalysis: General specifications and basic characteristics. *J. Meteorol. Soc. Japan*, **93**, 5–48, <https://doi.org/10.2151/jmsj.2015-001>.
- Konings, A. G., Y. Yu, L. Xu, Y. Yang, D. S. Schimel, and S. S. Saatchi, 2017: Active microwave observations of diurnal and seasonal variations of canopy water content across the humid African tropical forests. *Geophys. Res. Lett.*, **44**, 2290–2299, <https://doi.org/10.1002/2016GL072388>.
- Kopp, G., and J. L. Lean, 2011: A new, lower value of total solar irradiance: Evidence and climate significance. *Geophys. Res. Lett.*, **38**, L01706, <https://doi.org/10.1029/2010GL045777>.
- Kratz, D. P., P. W. Stackhouse Jr., S. K. Gupta, A. C. Wilber, P. Sawaengphokhai, and G. R. McGarragh, 2014: The Fast Longwave and Shortwave Flux (FLASHFlux) data product: Single scanner footprint fluxes. *J. Appl. Meteor. Climatol.*, **53**, 1059–1079, <https://doi.org/10.1175/JAMC-D-13-061.1>.
- Kummert, M., R. Delaloye, and L. Braillard, 2018: Erosion and sediment transfer processes at the front of rapidly moving rock glaciers: Systematic observations with automatic cameras in the western Swiss Alps. *Permafrost Periglacial Processes*, **29**, 21–33, <https://doi.org/10.1002/ppp.1960>.
- Lagouarde, J.-P., and Coauthors, 2018: The Indian-French Trishna Mission: Earth observation in the thermal infrared with high spatio-temporal resolution. *IGARSS 2018—2018 IEEE Int. Geoscience and Remote Sensing Symp.*, Valencia, Spain, IEEE, 4078–4081, <https://doi.org/10.1109/IGARSS.2018.8518720>.
- Lan, X., and Coauthors, 2021: Improved constraints on global methane emissions and sinks using $\delta^{13}\text{C}-\text{CH}_4$. *Global Biogeochem. Cycles*, **35**, e2021GB007000, <https://doi.org/10.1029/2021GB007000>.
- Landerer, F. W., and Coauthors, 2020: Extending the global mass change data record: GRACE follow-on instrument and science data performance. *Geophys. Res. Lett.*, **47**, e2020GL088306, <https://doi.org/10.1029/2020GL088306>.
- Lassey, K. R., D. M. Etheridge, D. C. Lowe, A. M. Smith, and D. F. Ferretti, 2007: Centennial evolution of the atmospheric methane budget: What do the carbon isotopes tell us? *Atmos. Chem. Phys.*, **7**, 2119–2139, <https://doi.org/10.5194/acp-7-2119-2007>.
- Lawrence, Z. D., J. Perlwitz, A. H. Butler, G. L. Manney, P. A. Newman, S. H. Lee, and E. R. Nash, 2020: The remarkably strong Arctic stratospheric polar vortex of winter 2020: Links to record-breaking Arctic oscillation and ozone loss. *J. Geophys. Res. Atmos.*, **125**, e2020JD033271, <https://doi.org/10.1029/2020JD033271>.
- Lee, H.-T., and NOAA CDR Program, 2011: NOAA Climate Data Record (CDR) of Monthly Outgoing Longwave Radiation (OLR), Version 2.2-1. NOAA National Climatic Data Center, accessed 2 February 2021, <https://doi.org/10.7289/V5222RQP>.
- Lenssen, N. J. L., G. A. Schmidt, J. E. Hansen, M. J. Menne, A. Persin, R. Ruedy, and D. Zyss, 2019: Improvements in the GISTEMP uncertainty model. *J. Geophys. Res. Atmos.*, **124**, 6307–6326, <https://doi.org/10.1029/2018JD029522>.
- Le Quére, C., and Coauthors, 2020: Temporary reduction in daily global CO₂ emissions during the COVID-19 forced confinement. *Nat. Climate Change*, **10**, 647–653, <https://doi.org/10.1038/s41558-020-0797-x>.
- Levy, R. C., and Coauthors, 2013: The collection 6 MODIS aerosol products over land and ocean. *Atmos. Meas. Tech.*, **6**, 2989–3034, <https://doi.org/10.5194/amt-6-2989-2013>.
- L'Heureux, M. L., and Coauthors, 2016: Observing and predicting the 2015/16 El Niño. *Bull. Amer. Meteor. Soc.*, **98**, 1363–1382, <https://doi.org/10.1175/BAMS-D-16-0009.1>.
- Li, M., and Coauthors, 2017: Anthropogenic emission inventories in China: A review. *Nat. Sci. Rev.*, **4**, 834–866, <https://doi.org/10.1093/nsr/nwx150>.
- Li, X., and Coauthors, 2021: Global-scale assessment and inter-comparison of recently developed/reprocessed microwave satellite vegetation optical depth products. *Remote Sens. Environ.*, **253**, 112208, <https://doi.org/10.1016/j.rse.2020.112208>.
- Lieb, G. K., and A. Kellerer-Pirklbauer, 2020: Sammelbericht über die Gletschermessungen des Österreichischen Alpenvereins im Jahr 2019. Letzter Bericht: Bergauf 2/2019, Jg. 74 (144), S. 20–29, www.alpenverein.at/portal_wAssets/docs/service/bergauf/Lieb_Kellerer_Gletscherbericht_2_20.pdf.
- Lin, M., L. W. Horowitz, S. J. Oltmans, A. M. Fiore, and S. Fan, 2014: Tropospheric ozone trends at Mauna Loa Observatory tied to decadal climate variability. *Nat. Geosci.*, **7**, 136–143, <https://doi.org/10.1038/ngeo2066>.
- Liu, Y. Y., A. I. J. M. van Dijk, M. F. McCabe, J. P. Evans, and R. A. M. de Jeu, 2013: Global vegetation biomass change (1988–2008) and attribution to environmental and human drivers. *Global Ecol. Biogeogr.*, **22**, 692–705, <https://doi.org/10.1111/geb.12024>.
- , and Coauthors, 2015: Recent reversal in loss of global terrestrial biomass. *Nat. Climate Change*, **5**, 470–474, <https://doi.org/10.1038/nclimate2581>.
- , and Coauthors, 2017: Enhanced canopy growth precedes senescence in 2005 and 2010 Amazonian droughts. *Remote Sens. Environ.*, **211**, 26–37, <https://doi.org/10.1016/j.rse.2018.03.035>.

- Loeb, N. G., B. A. Wielicki, D. R. Doelling, G. L. Smith, D. F. Keyes, S. Kato, N. Manalo-Smith, and T. Wong, 2009: Toward optimal closure of the Earth's top-of-atmosphere radiation budget. *J. Climate*, **22**, 748–766, <https://doi.org/10.1175/2008JCLI2637.1>.
- , S. Kato, W. Su, T. Wong, F. Rose, D. R. Doelling, and J. Norris, 2012: Advances in understanding top-of-atmosphere radiation variability from satellite observations. *Surv. Geophys.*, **33**, 359–385, <https://doi.org/10.1007/s10712-012-9175-1>.
- , and Coauthors, 2018: Clouds and the Earth's Radiant Energy System (CERES) Energy Balanced and Filled (EBAF) Top-of-Atmosphere (TOA) Edition-4.0 data product. *J. Climate*, **31**, 895–918, <https://doi.org/10.1175/JCLI-D-17-0208.1>.
- Lu, X., and Coauthors, 2018a: Surface and tropospheric ozone trends in the Southern Hemisphere since 1990: Possible linkages to poleward expansion of the Hadley circulation. *Sci. Bull.*, **64**, 400–409, <https://doi.org/10.1016/j.scib.2018.12.021>.
- , and Coauthors, 2018b: Severe surface ozone pollution in China: A global perspective. *Environ. Sci. Technol. Lett.*, **5**, 487–494, <https://doi.org/10.1021/acs.estlett.8b00366>.
- MacCallum, S. N., and C. J. Merchant, 2012: Surface water temperature observations of large lakes by optimal estimation. *Can. J. Remote Sens.*, **38**, 25–45, <https://doi.org/10.5589/m12-010>.
- MacFarling Meure, C., and Coauthors, 2006: Law dome CO₂, CH₄ and N₂O ice core records extended to 2000 years BP. *Geophys. Res. Lett.*, **33**, L14810, <https://doi.org/10.1029/2006GL026152>.
- Mafaranga, H., 2020: Heavy rains, human activity, and rising waters at Lake Victoria. *Eos, Trans. Amer. Geophys. Union*, **101**, <https://doi.org/10.1029/2020E0146582>.
- Magnin, F., P. Deline, L. Ravanel, J. Noetzi, and P. Pogliotti, 2015: Thermal characteristics of permafrost in the steep alpine rock walls of the Aiguille du Midi (Mont Blanc Massif, 3842 m a.s.l.). *Cryosphere*, **9**, 109–121, <https://doi.org/10.5194/tc-9-109-2015>.
- Magnuson, J. J., and Coauthors, 2000: Historical trends in lake and river ice cover in the Northern Hemisphere. *Science*, **289**, 1743–1746, <https://doi.org/10.1126/science.289.5485>.
- Manabe, S., and R. Wetherald, 1967: Thermal equilibrium of the atmosphere with a given distribution of relative humidity. *J. Atmos. Sci.*, **24**, 241–259, [https://doi.org/10.1175/1520-0469\(1967\)024<0241:TEOTAW>2.0.CO;2](https://doi.org/10.1175/1520-0469(1967)024<0241:TEOTAW>2.0.CO;2).
- Mann, M., and Coauthors, 2017: Influence of anthropogenic climate change on planetary wave resonance and extreme weather events. *Sci. Rep.*, **7**, 452242, <https://doi.org/10.1038/srep45242>.
- Manney, G. L., and Coauthors, 2020: Record-low Arctic stratospheric ozone in 2020: MLS observations of chemical processes and comparisons with previous extreme winters. *Geophys. Res. Lett.*, **47**, e2020GL089063, <https://doi.org/10.1029/2020GL089063>.
- Martens, B., and Coauthors, 2017: GLEAM v3: Satellite-based land evaporation and root-zone soil moisture. *Geosci. Model Dev.*, **10**, 1903–1925, <https://doi.org/10.5194/gmd-10-1903-2017>.
- , W. Waegeman, W. A. Dorigo, N. E. C. Verhoest, and D. G. Miralles, 2018: Terrestrial evaporation response to modes of climate variability. *npj Climate Atmos. Sci.*, **1**, 43, <https://doi.org/10.1038/s41612-018-0053-5>.
- Maycock, A. C., and Coauthors, 2018: Revisiting the mystery of recent stratospheric temperature trends. *Geophys. Res. Lett.*, **45**, 9919–9933, <https://doi.org/10.1029/2018GL078035>.
- McCabe, M. F., A. Ershadi, C. Jiménez, D. G. Miralles, D. Michel, and E. F. Wood, 2016: The GEWEX LandFlux project: Evaluation of model evaporation using tower-based and globally-gridded forcing data. *Geosci. Model Dev.*, **9**, 283–305, <https://doi.org/10.5194/gmd-9-283-2016>.
- , and Coauthors, 2017a: The future of Earth observation in hydrology. *Hydrol. Earth Syst. Sci.*, **21**, 3879–3914, <https://doi.org/10.5194/hess-21-3879-2017>.
- , B. Aragon, R. Houborg, and J. Mascaro, 2017b: CubeSats in hydrology: Ultra-high-resolution insights into vegetation dynamics and terrestrial evaporation. *Water Resour. Res.*, **53**, 10017–10024, <https://doi.org/10.1002/2017WR022240>.
- McDonald, B. C., and Coauthors, 2018: Volatile chemical products emerging as largest petrochemical source of urban organic emissions. *Science*, **359**, 760–764, <https://doi.org/10.1126/science.aag0524>.
- McKittrick, R., and J. Christy, 2018: A test of the tropical 200- to 300-hPa warming rate in climate models. *Earth Space Sci.*, **5**, 529–536, <https://doi.org/10.1029/2018EA000401>.
- , and J. Christy, 2020: Pervasive warming bias in CMIP6 tropospheric layers. *Earth Space Sci.*, **7**, e2020EA001281, <https://doi.org/10.1029/2020EA001281>.
- McVicar, T. R., and Coauthors, 2012: Global review and synthesis of trends in observed terrestrial near-surface wind speeds: Implications for evaporation. *J. Hydrol.*, **416–417**, 182–205, <https://doi.org/10.1016/j.jhydrol.2011.10.024>.
- Mears, C. A., and F. J. Wentz, 2016: Sensitivity of satellite-derived tropospheric temperature trends to the diurnal cycle adjustment. *J. Climate*, **29**, 3629–3646, <https://doi.org/10.1175/JCLI-D-15-0744.1>.
- , ———, P. Thorne, and D. Bernie, 2011: Assessing uncertainty in estimates of atmospheric temperature changes from MSU and AMSU using a Monte-Carlo estimation technique. *J. Geophys. Res.*, **116**, D08112, <https://doi.org/10.1029/2010JD014954>.
- , D. K. Smith, L. Ricciardulli, J. Wang, H. Huelsing, and F. J. Wentz, 2018: Construction and uncertainty estimation of a satellite-derived total precipitable water data record over the world's oceans. *Earth Space Sci.*, **5**, 197–210, <https://doi.org/10.1002/2018EA000363>.
- Meesters, A. G. C. A., R. A. M. De Jeu, and M. Owe, 2005: Analytical derivation of the vegetation optical depth from the microwave polarization difference index. *IEEE Trans. Geosci. Remote Sens.*, **2**, 121–123, <https://doi.org/10.1109/LGRS.2005.843983>.
- Menne, M. J., I. Durre, R. S. Vose, B. E. Gleason, and T. G. Houston, 2012: An overview of the global historical climatology network-daily database. *J. Atmos. Oceanic Technol.*, **29**, 897–910, <https://doi.org/10.1175/JTECH-D-11-00103.1>.
- Menzel, W. P., R. A. Frey, E. E. Borbas, B. A. Baum, G. Cureton, and N. Bearson, 2016: Reprocessing of HIRS satellite measurements from 1980–2015: Development towards a consistent decadal cloud record. *J. Appl. Meteor. Climatol.*, **55**, 2397–2410, <https://doi.org/10.1175/JAMC-D-16-0129.1>.
- Met Office, 2020: A look back at 2020. 30 December, www.metoffice.gov.uk/about-us/press-office/news/weather-and-climate/2020/2020-round-up.
- Mialon, A., N. Rodriguez-Fernandez, M. Santoro, S. Saatchi, S. Mermoz, E. Bousquet, and Y. Kerr, 2020: Evaluation of the sensitivity of SMOS L-VOD to forest above-ground biomass at global scale. *Remote Sens.*, **12**, 1450, <https://doi.org/10.3390/rs12091450>.
- Miller, B. R., and Coauthors, 2010: HFC-23 (CHF₃) emission trend response to HCFC-22 (CHClF₂) production and recent HFC-23 emission abatement measures. *Atmos. Chem. Phys.*, **10**, 7875–7890, <https://doi.org/10.5194/acp-10-7875-2010>.
- Mills, G., and Coauthors, 2018: Tropospheric Ozone Assessment Report: Present-day tropospheric ozone distribution and trends relevant to vegetation. *Elem. Sci. Anthropocene*, **6**, 47, <https://doi.org/10.1525/elementa.302>.
- Ming, Y., and Coauthors, 2020: Assessing the influence of COVID-19 on the short-wave radiative fluxes over the East Asian marginal seas. *Geophys. Res. Lett.*, **48**, e2020GL091699, <https://doi.org/10.1029/2020GL091699>.
- Minnis, P., and Coauthors, 2008: Cloud detection in nonpolar regions for CERES using TRMM VIRS and Terra and Aqua MODIS data. *IEEE Trans. Geosci. Remote Sens.*, **46**, 3857–3884, <https://doi.org/10.1109/TGRS.2008.2001351>.
- , K. Bedka, Q. Trepte, C. R. Yost, S. T. Bedka, B. Scarino, K. Khlopenkov, and M. M. Khaiyer, 2016: A consistent long-term cloud and clear-sky radiation property dataset from the Advanced Very High Resolution Radiometer (AVHRR). Climate Algorithm Theoretical Basis Document (C-ATBD), CDRP-ATBD-0826 Rev 1, 159 pp., [www.ncdc.noaa.gov/sites/default/files/cdr-documentation/CDRP-ATBD-0826%20AVHRR%20Cloud%20Properties%20-%20NASA%20C-ATBD%20\(01B-30b\)%20\(DSR-1051\).pdf](http://www.ncdc.noaa.gov/sites/default/files/cdr-documentation/CDRP-ATBD-0826%20AVHRR%20Cloud%20Properties%20-%20NASA%20C-ATBD%20(01B-30b)%20(DSR-1051).pdf).
- Miralles, D. G., T. R. H. Holmes, R. A. M. De Jeu, J. H. Gash, A. G. C. A. Meesters, and A. J. Dolman, 2011: Global land-surface evaporation estimated from satellite-based observations. *Hydrol. Earth Syst. Sci.*, **15**, 453–469, <https://doi.org/10.5194/hess-15-453-2011>.

- , and Coauthors, 2014: El Niño–La Niña cycle and recent trends in continental evaporation. *Nat. Climate Change*, **4**, 122–126, <https://doi.org/10.1038/nclimate2068>.
- , and Coauthors, 2016: The WACMOS-ET project – Part 2: Evaluation of global terrestrial evaporation data sets. *Hydrol. Earth Syst. Sci.*, **20**, 823–842, <https://doi.org/10.5194/hess-20-823-2016>.
- Moesinger, L., W. Dorigo, R. de Jeu, R. van der Schalie, T. Scanlon, I. Teubner, and M. Forkel, 2020: The global long-term microwave Vegetation Optical Depth Climate Archive (VODCA). *Earth Syst. Sci. Data*, **12**, 177–196, <https://doi.org/10.5194/essd-12-177-2020>.
- Monks, P. S., and Coauthors, 2015: Tropospheric ozone and its precursors from the urban to the global scale from air quality to short-lived climate forcer. *Atmos. Chem. Phys.*, **15**, 8889–8973, <https://doi.org/10.5194/acp-15-8889-2015>.
- Montzka, S. A., and Coauthors, 1996: Decline in the tropospheric abundance of halogen from halocarbons: Implications for stratospheric ozone depletion. *Science*, **272**, 1318–1322, <https://doi.org/10.1126/science.272.5266.1318>.
- , and Coauthors, 2011: Ozone-depleting substances (ODSs) and related chemicals. Scientific Assessment of Ozone Depletion: 2010, Global Ozone Research and Monitoring Project Rep. 52, World Meteorological Organization, Ch. 1, https://tsapps.nist.gov/publication/get_pdf.cfm?pub_id=909747.
- , and Coauthors, 2018: An unexpected and persistent increase in global emissions of ozone-depleting CFC-11. *Nature*, **557**, 413–417, <https://doi.org/10.1038/s41586-018-0106-2>.
- , and Coauthors, 2021: A decline in global CFC-11 emissions during 2018–2019. *Nature*, **590**, 428–432, <https://doi.org/10.1038/s41586-021-03260-5>.
- Morice, C. P., and Coauthors, 2021: An updated assessment of near-surface temperature change from 1850: The HadCRUT5 data set. *J. Geophys. Res. Atmos.*, **126**, e2019JD032361, <https://doi.org/10.1029/2019JD032361>.
- Mühle, J., and Coauthors, 2010: Perfluorocarbons in the global atmosphere: Tetrafluoromethane, hexafluoroethane, and octafluoropropane. *Atmos. Chem. Phys.*, **10**, 5145–5164, <https://doi.org/10.5194/acp-10-5145-2010>.
- Myhre, G., and Coauthors, 2013: Anthropogenic and natural radiative forcing. *Climate Change 2013: The Physical Science Basis*, T. F. Stocker et al., Eds., Cambridge University Press, 659–740.
- Nemani, R. R., C. D. Keeling, H. Hashimoto, W. M. Jolly, S. C. Piper, C. Tucker, R. B. Myneni, and S. W. Running, 2003: Climate-driven increases in global terrestrial net primary production from 1982 to 1999. *Science*, **300**, 1560–1563, <https://doi.org/10.1126/science.1082750>.
- NESDIS, 2020: Powerful “dragon” storm hits Egypt while Israel prepares for impact. 13 March, accessed 11 February 2021, www.nesdis.noaa.gov/content/powerful-%E2%80%9Cdragon%20hits-egypt-while-israel-prepares-impact.
- Neu, J., and Coauthors, 2014: Tropospheric ozone variations governed by changes in stratospheric circulation. *Nat. Geosci.*, **7**, 340–344, <https://doi.org/10.1038/ngeo2138>.
- Newman, P. A., J. S. Daniel, D. W. Waugh, and E. R. Nash, 2007: A new formulation of equivalent effective stratospheric chlorine (EESC). *Atmos. Chem. Phys.*, **7**, 4537–4552, <https://doi.org/10.5194/acp-7-4537-2007>.
- Ni, X., and P. M. Groffman, 2018: Declines in methane uptake in forest soils. *Proc. Natl. Acad. Sci. USA*, **115**, 8587–8590, <https://doi.org/10.1073/pnas.1807377115>.
- Nisbet, E. G., and Coauthors, 2019: Very strong atmospheric methane growth in the 4 years 2014–2017: Implications for the Paris Agreement. *Global Biogeochem. Cycles*, **33**, 318–342, <https://doi.org/10.1029/2018GB006009>.
- NIWA, 2020: Auckland’s drought most extreme in modern times. <https://niwa.co.nz/news/aucklands-drought-most-extreme-in-modern-times>.
- , 2021: Aotearoa New Zealand Climate Summary: Summer 2020–21. <https://niwa.co.nz/climate/summaries/seasonal/summer-2020-21>.
- NOAA, 2020: State of the Climate. www.ncdc.noaa.gov/sotcl/.
- , 2021a: State of the Climate: National Climate Report for Annual 2020. Accessed 5 February 2021, www.ncdc.noaa.gov/sotc/national/202013.
- , 2021b: State of the Climate: Global Climate Report for Annual 2020. Accessed 21 March 2021, www.ncdc.noaa.gov/sotc/global/202013.
- , 2021c: US Climate Extremes Index (CEI). Accessed 25 February 2021, www.ncdc.noaa.gov/extremes/cei/graph/us/01-12/4.
- Noetzli, J., and Coauthors, 2018: Permafrost thermal state [in “State of the Climate in 2017”]. *Bull. Amer. Meteor. Soc.*, **99** (8), S20–S22, <https://doi.org/10.1175/2018BAMSStateoftheClimate.1>.
- , and Coauthors, 2019: Permafrost thermal state [in “State of the Climate in 2018”]. *Bull. Amer. Meteor. Soc.*, **100** (9), S21–S22, <https://doi.org/10.1175/2019BAMSStateoftheClimate.1>.
- , H. H. Christiansen, K. Isaksen, S. Smith, L. Zhao, and D. A. Streltsov, 2020: Permafrost thermal state [in “State of the Climate in 2019”]. *Bull. Amer. Meteor. Soc.*, **101** (8), S34–S36, <https://doi.org/10.1175/BAMS-D-20-0104.1>.
- Novelli, P. C., K. A. Masarie, P. M. Lang, B. D. Hall, R. C. Myers, and J. W. Elkins, 2003: Reanalysis of tropospheric CO trends: Effects of the 1997–1998 wildfires. *J. Geophys. Res.*, **108**, 4464, <https://doi.org/10.1029/2002JD003031>.
- O’Keefe, J., 2019: Phenology of Woody Species at Harvard Forest since 1990. Harvard Forest Data Archive: HF003, Environmental Data Initiative: <https://doi.org/10.6073/pasta/6b0a6e266e06ab52148af3e5cd942159>.
- O’Neil, S., and Coauthors, 2019: Reanalysis of the US Geological Survey Benchmark Glaciers: Long-term insight into climate forcing of glacier mass balance. *J. Glaciol.*, **65**, 850–866, <https://doi.org/10.1017/jog.2019.66>.
- Osborn, T. J., J. Barichivich, I. Harris, G. van der Schrier, and P. D. Jones, 2018: Monitoring global drought using the self-calibrating Palmer Drought Severity Index [in “State of the Climate in 2017”]. *Bull. Amer. Meteor. Soc.*, **99**, S36–S37, <https://doi.org/10.1175/2018BAMSStateoftheClimate.1>.
- , and Coauthors, 2021: Land surface air temperature variations across the globe updated to 2019: The CRUTEM5 dataset. *J. Geophys. Res. Atmos.*, **126**, e2019JD032352, <https://doi.org/10.1029/2019JD032352>.
- Osprey, S. M., and Coauthors, 2016: An unexpected disruption of the atmospheric quasi-biennial oscillation. *Science*, **353**, 1424–1427, <https://doi.org/10.1126/science.aah4156>.
- Otto, F. E. L., and Coauthors, 2018: Anthropogenic influence on the drivers of the Western Cape drought 2015–2017. *Environ. Res. Lett.*, **13**, 124010, <https://doi.org/10.1088/1748-9326/aae9f9>.
- Overland, J. E., and M. Wang, 2020: The 2020 Siberian heat wave. *Int. J. Climatol.*, **41**, E2341–E2346, <https://doi.org/10.1002/joc.6850>.
- Park, J., and H. Kim, S.-Y. Wang, J.-H. Jeong, K.-S. Lim, and J.-H. Yoon, 2020: Intensification of the East Asian summer monsoon lifecycle based on observation and CMIP6. *Environ. Res. Lett.*, **15**, 0940b9, <https://doi.org/10.1088/1748-9326/ab9b3f>.
- Park, S., and Coauthors, 2021: A decline in emissions of CFC-11 and related chemicals from eastern China. *Nature*, **590**, 433–437, <https://doi.org/10.1038/s41586-021-03277-w>.
- Park, T., and Coauthors, 2016: Changes in growing season duration and productivity of northern vegetation inferred from long-term remote sensing data. *Environ. Res. Lett.*, **11**, 084001, <https://doi.org/10.1088/1748-9326/11/8/084001>.
- Patel, K., 2021: Snow free glaciers in winter. NASA Earth Observatory, <https://earthobservatory.nasa.gov/images/147840/snow-free-glaciers-in-winter>.
- Pekel, J.-F., A. Cottam, N. Gorelick, and A. S. Belward, 2016: High-resolution mapping of global surface water and its long-term changes. *Nature*, **540**, 418–422, <https://doi.org/10.1038/nature20584>.
- Penalba, O. C., and J. A. Rivera, 2016: Precipitation response to El Niño/La Niña events in Southern South America – Emphasis in regional drought occurrences. *Adv. Geosci.*, **42**, 1–14, <https://doi.org/10.5194/adgeo-42-1-2016>.
- Pendergrass, A. G., and R. Knutti, 2018: The uneven nature of daily precipitation and its change. *Geophys. Res. Lett.*, **45**, 11980–11988, <https://doi.org/10.1029/2018GL080298>.
- Perkins, S. E., and L. V. Alexander, 2013: On the measurement of heat waves. *J. Climate*, **26**, 4500–4517, <https://doi.org/10.1175/JCLI-D-12-00383.1>.
- PERMOS, 2019: Permafrost in Switzerland 2014/2015 to 2017/2018. Glaciological Rep. (Permafrost) 16–19, Cryospheric Commission of the Swiss Academy of Sciences, 104 pp., <https://doi.org/10.13093/permos-rep-2019-16-19>.

- Peterson, T. C., and R. S. Vose, 1997: An overview of the global historical climatology network temperature database. *Bull. Amer. Meteor. Soc.*, **78**, 2837–2849, [https://doi.org/10.1175/1520-0477\(1997\)078<2837:A00TGH>2.0.CO;2](https://doi.org/10.1175/1520-0477(1997)078<2837:A00TGH>2.0.CO;2).
- Petoukhov, V., S. Rahmstorf, S. Petri, and H. J. Schellnhuber, 2013: Quasiresonant amplification of planetary waves and recent Northern Hemisphere weather extremes. *Proc. Natl. Acad. Sci. USA*, **110**, 5336–5341, <https://doi.org/10.1073/pnas.1222000110>.
- Pétron, G., and Coauthors, 2020: Atmospheric Carbon Monoxide dry air mole fractions from the NOAA GML Carbon Cycle Cooperative Global Air Sampling Network, 1988–2020, Version: 2020-08. NOAA, <https://doi.org/10.15138/33bv-s284>.
- Pfeil, I., W. Wagner, M. Forkel, W. Dorigo, and M. Vreugdenhil, 2020: Does ASCAT observe the spring reactivation in temperate deciduous broadleaf forests? *Remote Sens. Environ.*, **250**, 112042, <https://doi.org/10.1016/j.rse.2020.112042>.
- Pinty, B., and Coauthors, 2011: Exploiting the MODIS albedos with the Two-stream Inversion Package (JRC-TIP): 2. Fractions of transmitted and absorbed fluxes in the vegetation and soil layers. *J. Geophys. Res.*, **116**, D09106, <https://doi.org/10.1029/2010JD015373>.
- Platnick, S., P. Hubanks, K. Meyer, and M. D. King, 2015: MODIS Atmosphere L3 Monthly Product (08_L3). NASA MODIS Adaptive Processing System, Goddard Space Flight Center, accessed 21 January 2021, https://doi.org/10.5067/MODIS/MOD08_M3.006 (Terra), https://doi.org/10.5067/MODIS/MYD08_M3.006 (Aqua).
- Po-Chedley, S., T. J. Thorsen, and Q. Fu, 2015: Removing diurnal cycle contamination in satellite-derived tropospheric temperatures: Understanding tropical tropospheric trend discrepancies. *J. Climate*, **28**, 2274–2290, <https://doi.org/10.1175/JCLI-D-13-00767.1>.
- , B. D. Santer, S. Fueglistaler, M. D. Zelinka, P. J. Cameron-Smith, J. Painter, and Q. Fu, 2021: Natural variability contributes to model-satellite differences in tropical tropospheric warming. *Proc. Natl. Acad. Sci. USA*, **118**, e2020962118, <https://doi.org/10.1073/pnas.2020962118>.
- Pogliotti, P., M. Guglielmin, E. Cremonese, U. M. di Cella, G. Filippa, C. Pellet, and C. Hauck, 2015: Warming permafrost and active layer variability at Cime Bianche, Western European Alps. *Cryosphere*, **9**, 647–661, <https://doi.org/10.5194/tc-9-647-2015>.
- Popp, T., and Coauthors, 2016: Development, production and evaluation of aerosol climate data records from European satellite observations (Aerosol_cci). *Remote Sens.*, **8**, 421, <https://doi.org/10.3390/rs8050421>.
- Poulter, B., and Coauthors, 2014: Contribution of semi-arid ecosystems to interannual variability of the global carbon cycle. *Nature*, **509**, 600–603, <https://doi.org/10.1038/nature13376>.
- Prather, M. J., C. D. Holmes, and J. Hsu, 2012: Reactive greenhouse gas scenarios: Systematic exploration of uncertainties and the role of atmospheric chemistry. *Geophys. Res. Lett.*, **39**, L09803, <https://doi.org/10.1029/2012GL051440>.
- Preimesberger, W., A. Pasik, R. van der Schalie, T. Scanlon, R. Kidd, R. A. M. De Jeu, and W. A. Dorigo, 2020: Soil moisture [in “State of the Climate in 2019”]. *Bull. Amer. Meteor.*, **101** (8), S81–S83, <https://doi.org/10.1175/BAMS-D-20-0104.1>.
- Quarty, G. D., and Coauthors, 2020: The roles of the S3MPC: Monitoring, validation and evolution of Sentinel-3 altimetry observations. *Remote Sens.*, **12**, 1763, <https://doi.org/10.3390/rs12111763>.
- Ramon, J., L. Lledó, V. Torralba, A. Soret, and F. J. Doblas-Reyes, 2019: What global reanalysis best represents near-surface winds? *Quart. J. Roy. Meteor. Soc.*, **145**, 3236–3251, <https://doi.org/10.1002/qj.3616>.
- Randel, W. J., and J. B. Cobb, 1994: Coherent variations of monthly mean total ozone and lower stratospheric temperature. *J. Atmos. Sci.*, **99**, 5433–5447, <https://doi.org/10.1029/93JD03454>.
- , A. K. Smith, F. Wu, C.-Z. Zou, and H. Qian, 2016: Stratospheric temperature trends over 1979–2015 derived from combined SSU, MLS and SABER satellite observations. *J. Climate*, **29**, 4843–4859, <https://doi.org/10.1175/JCLI-D-15-0629.1>.
- , C. Covey, and L. Polvani, 2020: Stratospheric temperature [in “State of the Climate in 2019”]. *Bull. Amer. Meteor. Soc.*, **101** (8) S32–S34, <https://doi.org/10.1175/BAMS-D-20-0104.1>.
- Ravishankara, A. R., J. S. Daniel, and R. W. Portmann, 2009: Nitrous oxide (N₂O): The dominant ozone-depleting substance emitted in the 21st century. *Science*, **326**, 123–125, <https://doi.org/10.1126/science.1176985>.
- Ray, E. A., and Coauthors, 2017: Quantification of the SF6 lifetime based on mesospheric loss measured in the stratospheric polar vortex. *J. Geophys. Res. Atmos.*, **122**, 4626–4638, <https://doi.org/10.1002/2016JD026198>.
- Reichstein, M., and Coauthors, 2013: Climate extremes and the carbon cycle. *Nature*, **500**, 287–295, <https://doi.org/10.1038/nature12350>.
- Ricciardulli, L., 2016: ASCAT on MetOp-A data product update notes: V2.1 Data Release. Tech. Rep. 040416, Remote Sensing Systems, Santa Rosa, CA, 5 pp., http://images.remss.com/papers/rsstech/2016_040416_RSS_ASCAT_V2_update.pdf.
- , and F. J. Wentz, 2015: A scatterometer geophysical model function for climate-quality winds: QuikSCAT Ku-2011. *J. Atmos. Oceanic Technol.*, **32**, 1829–1846, <https://doi.org/10.1175/JTECH-D-15-0008.1>.
- Richardson, A. D., 2018: Tracking seasonal rhythms of plants in diverse ecosystems with digital camera imagery. *New Phytol.*, **222**, 1742–1750, <https://doi.org/10.1111/nph.15591>.
- , and J. O’Keefe, 2009: Phenological differences between understory and overstory. *Phenology of Ecosystem Processes*, A. Noormets, Eds., Springer, 87–117, https://doi.org/10.1007/978-1-4419-0026-5_4.
- Richardson, M., K. Cowtan, and R. J. Millar, 2018: Global temperature definition affects achievement of long-term climate goals. *Environ. Res. Lett.*, **13**, 054004, <https://doi.org/10.1088/1748-9326/aab305>.
- Ričko, M., and Coauthors, 2012: Intercomparison and validation of continental water level products derived from satellite radar altimetry. *J. Appl. Remote Sens.*, **6**, 061710, <https://doi.org/10.1117/1.JRS.6.061710>.
- Rigby, M., and Coauthors, 2019: Increase in CFC-11 emissions from eastern China based on atmospheric observations. *Nature*, **569**, 546–550, <https://doi.org/10.1038/s41586-019-1193-4>.
- Roderick, M. L., L. D. Rotstayn, G. D. Farquhar, and M. T. Hobbins, 2007: On the attribution of changing pan evaporation. *Geophys. Res. Lett.*, **34**, L17403, <https://doi.org/10.1029/2007GL031166>.
- Rodríguez, E., 2020: ‘Apocalyptic’ fires are ravaging the world’s largest tropical wetland. *Nature*, **586**, 20–21, <https://doi.org/10.1038/d41586-020-02716-4>.
- Rodríguez-Fernández, N. J., and Coauthors, 2018: An evaluation of SMOS L-band vegetation optical depth (L-VOD) data sets: High sensitivity of L-VOD to above-ground biomass in Africa. *Biogeosciences*, **15**, 4627–4645, <https://doi.org/10.5194/bg-15-4627-2018>.
- Romanovsky, V. E., T. S. Sazonova, V. T. Balobaev, N. I. Shender, and D. O. Sergueev, 2007: Past and recent changes in air and permafrost temperatures in eastern Siberia. *Global Planet. Change*, **56**, 399–413, <https://doi.org/10.1016/j.gloplacha.2006.07.022>.
- Romanovsky, V. E., and Coauthors, 2010: Thermal state of permafrost in Russia. *Permafrost Periglacial Processes*, **21**, 136–155, <https://doi.org/10.1002/ppp.683>.
- Rubino, A., D. Zanchettin, F. De Rovere, and M. J. McPhaden, 2020: On the interchangeability of sea-surface and near-surface air temperature anomalies in climatologies. *Sci. Rep.*, **10**, 7433, <https://doi.org/10.1038/s41598-020-64167-1>.
- Sanchez-Lugo, A., C. Morice, P. Berrisford, and A. Arguez, 2017: Global surface temperatures [in “State of the Climate in 2016”]. *Bull. Amer. Meteor. Soc.*, **90** (8), S11–S13, <https://doi.org/10.1175/2017BAMSStateoftheClimate.1>.
- Santer, B. D., and Coauthors, 2008: Consistency of modelled and observed temperature trends in the tropical troposphere. *Int. J. Climatol.*, **28**, 1703–1722, <https://doi.org/10.1002/joc.1756>.
- , and Coauthors, 2014: Volcanic contribution to decadal changes in tropospheric temperature. *Nat. Geosci.*, **7**, 185–189, <https://doi.org/10.1038/ngeo2098>.
- , and Coauthors, 2017: Tropospheric warming over the past two decades. *Sci. Rep.*, **7**, 2336, <https://doi.org/10.1038/s41598-017-02520-7>.

- Santos, A., and Coauthors, 2019: Dynamics and predictability of the El Niño–Southern Oscillation: An Australian perspective on progress and challenges. *Bull. Amer. Meteor. Soc.*, **100**, 403–420, <https://doi.org/10.1175/BAMS-D-18-0057.1>.
- Satheesh, S. K., and Coauthors, 2017: Variability of atmospheric aerosols over India. Observed Climate Variability and Change over the Indian Region, M. Rajeevan and S. Nayak, Springer, 221–248, https://doi.org/10.1007/978-981-10-2531-0_13.
- Saunois, M., and Coauthors, 2020: The global methane budget 2000–2017. *Earth Syst. Sci. Data*, **12**, 1561–1623, <https://doi.org/10.5194/essd-12-1561-2020>.
- Schaaf, C. B., and Coauthors, 2002: First operational BRDF, albedo nadir reflectance products from MODIS. *Remote Sens. Environ.*, **83**, 135–148, [https://doi.org/10.1016/S0034-4257\(02\)00091-3](https://doi.org/10.1016/S0034-4257(02)00091-3).
- Schaefer, H., and Coauthors, 2016: A 21st-century shift from fossil-fuel to biogenic methane emissions indicated by $^{13}\text{CH}_4$. *Science*, **352**, 80–84, <https://doi.org/10.1126/science.aad2705>.
- Schamm, K., M. Ziese, A. Becker, P. Finger, A. Meyer-Christoffer, B. Rudolf, and U. Schneider, 2013: GPCP First Guess Daily Product at 1.0°: Near Real-Time First Guess Daily Land-Surface Precipitation from Rain-Gauges Based on SYN-OP Data. Global Precipitation Climatology Centre, accessed 18 January 2021, https://doi.org/10.5676/DWD_GPCP/FG_D_100.
- Schneider, T., P. A. O’Gorman, and X. J. Levine, 2010: Water vapor and the dynamics of climate changes. *Rev. Geophys.*, **48**, RG3001, <https://doi.org/10.1029/2009RG000302>.
- Schneider, U., A. Becker, P. Finger, R. Elke, and M. Ziese, 2020: GPCP Monitoring Product: Near Real-Time Monthly Land-Surface Precipitation from Rain-Gauges based on SYNOP and CLIMAT Data, Global Precipitation Climatology Centre Global Precipitation Climatology Centre, accessed 2 March 2021, https://doi.org/10.5676/DWD_GPCP/MP_M_V2020_100.
- Schroeder, W., P. Oliva, L. Giglio, and I. A. Csiszar, 2014: The new VIIRS 375m active fire detection data product: Algorithm description and initial assessment. *Remote Sens. Environ.*, **143**, 85–96, <https://doi.org/10.1016/j.rse.2013.12.008>.
- Schwartz, M. J., and Coauthors, 2020: Australian New Year’s PyroCb impact on stratospheric composition. *Geophys. Res. Lett.*, **47**, e2020GL090831, <https://doi.org/10.1029/2020GL090831>.
- Schwietzke, S., and Coauthors, 2016: Upward revision of global fossil fuel methane emissions based on isotope database. *Nature*, **538**, 88–91, <https://doi.org/10.1038/nature19797>.
- Seyednasrollah, B., and Coauthors, 2019: Tracking vegetation phenology across diverse biomes using Version 2.0 of the PhenoCam Dataset. *Sci. Data*, **6**, 261, <https://doi.org/10.1038/s41597-019-0270-8>.
- Sharma, S., and R. I. Woolway, 2020: Lake ice [in “State of the Climate in 2019”]. *Bull. Amer. Meteor. Soc.*, **101** (8), S39–S41, <https://doi.org/10.1175/BAMS-D-20-0104.1>.
- Shi, L., and J. J. Bates, 2011: Three decades of intersatellite-calibrated high-resolution infrared radiation sounder upper tropospheric water vapor. *J. Geophys. Res.*, **116**, D04108, <https://doi.org/10.1029/2010JD014847>.
- Simmons, A., and Coauthors, 2021: Low frequency variability and trends in surface air temperature and humidity from ERA5 and other datasets. ECMWF Tech. Memo. 881, 97 pp., <https://doi.org/10.21957/ly5vbtbfld>.
- Simmons, A. J., P. Berrisford, D. P. Dee, H. Hersbach, S. Hirahara, and J. N. Thepaut, 2017: A reassessment of temperature variations and trends from global reanalyses and monthly surface climatological datasets. *Quart. J. Roy. Meteor. Soc.*, **143**, 101–119, <https://doi.org/10.1002/qj.2949>.
- Simpson, I. R., T. G. Shepherd, and M. Sigmond, 2011: Dynamics of the lower stratospheric circulation response to ENSO. *J. Atmos. Sci.*, **68**, 2537–2556, <https://doi.org/10.1175/JAS-D-11-05.1>.
- Slater, T., and Coauthors, 2021: Review article: Earth’s ice imbalance. *Cryosphere*, **15**, 233–246, <https://doi.org/10.5194/tc-15-233-2021>.
- Slivinski, L. C., and Coauthors, 2019: Towards a more reliable historical reanalysis: Improvements for version 3 of the twentieth century reanalysis system. *Quart. J. Roy. Meteor. Soc.*, **145**, 2876–2908, <https://doi.org/10.1002/qj.3598>.
- Solomon, S., 1999: Stratospheric ozone depletion: A review of concepts and history. *Rev. Geophys.*, **37**, 275–316, <https://doi.org/10.1029/1999RG900008>.
- , K. H. Rosenlof, R. W. Portmann, J. S. Daniel, S. M. Davis, T. J. Sanford, and G.-K. Plattner, 2010: Contributions of stratospheric water vapor to decadal changes in the rate of global warming. *Science*, **327**, 1219–1223, <https://doi.org/10.1126/science.1182488>.
- , D. Kinnison, J. Bandoro, and R. Garcia, 2015: Simulation of polar ozone depletion: An update. *J. Geophys. Res.*, **120**, 7958–7974, <https://doi.org/10.1002/2015JD023365>.
- SPARC/IO3C/GAW, 2019: SPARC/IO3C/GAW report on long-term ozone trends and uncertainties in the stratosphere. SPARC Rep. No. 9, WCRP-17/2018, GAW Rep. 241, 99 pp., <https://doi.org/10.17874/f899e57a20b>.
- Spencer, R. W., J. R. Christy, and W. D. Braswell, 2017: UAH Version 6 global satellite temperature products: Methodology and results. *Asia-Pac. J. Atmos. Sci.*, **53**, 121–130, <https://doi.org/10.1007/s13143-017-0010-y>.
- Stackhouse, P. W., T. Wong, D. P. Kratz, P. Sawaengphokhai, A. C. Wiber, S. K. Gupta, and N. G. Loeb, 2016: Earth radiation budget at top-of-atmosphere [in “State of the Climate in 2015”]. *Bull. Amer. Meteor. Soc.*, **97** (8), S41–S43, <https://doi.org/10.1175/2016BAMSStateoftheClimate.1>.
- Staub, B., C. Lambiel, and R. Delaloye, 2016: Rock glacier creep as a thermally-driven phenomenon: A decade of inter-annual observation from the Swiss Alps. XI Int. Conf. on Permafrost, Potsdam, Germany, Alfred Wegener Institute Helmholtz Center for Polar and Marine Research, 96–97, <https://doi.org/10.2312/GFZ.LIS.2016.001>.
- Steinbrecht, W., and Coauthors, 2017: An update on ozone profile trends for the period 2000 to 2016. *Atmos. Chem. Phys.*, **17**, 10675–10690, <https://doi.org/10.5194/acp-17-10675-2017>.
- Stengel, M., and Coauthors, 2017: Cloud property datasets retrieved from AVHRR, MODIS, AATSR and MERIS in the framework of the Cloud_cci project. *Earth Syst. Sci. Data*, **9**, 881–904, <https://doi.org/10.5194/essd-9-881-2017>.
- Strode, S. A., J. R. Ziemke, L. D. Oman, L. N. Lamsal, M. A. Olsen, and J. Liu, 2019: Global changes in the diurnal cycle of surface ozone. *Atmos. Environ.*, **199**, 323–333, <https://doi.org/10.1016/j.atmosenv.2018.11.028>.
- Stroeve, J., J. E. Box, Z. Wang, C. Schaaf, and A. Barrett, 2013: Re-evaluation of MODIS MCD43 Greenland albedo accuracy and trends. *Remote Sens. Environ.*, **138**, 199–214, <https://doi.org/10.1016/j.rse.2013.07.023>.
- Strozzi, T., and Coauthors, 2020: Monitoring rock glacier kinematics with satellite synthetic aperture radar. *Remote Sens.*, **12**, 559, <https://doi.org/10.3390/rs12030559>.
- Sun, W., P. Hess, and B. Tian, 2014: The response of the equatorial tropospheric ozone to the Madden-Julian Oscillation in TES satellite observations and CAM-chem model simulation. *Atmos. Chem. Phys.*, **14**, 11775–11790, <https://doi.org/10.5194/acp-14-11775-2014>.
- Susskind, J., G. Molnar, L. Iredell, and N. G. Loeb, 2012: Interannual variability of outgoing longwave radiation as observed by AIRS and CERES. *J. Geophys. Res.*, **117**, D23107, <https://doi.org/10.1029/2012JD017997>.
- Swiss Re, 2020: Swiss Re Institute estimates USD 83 billion global insured catastrophe losses in 2020, the fifth-costliest on record. 15 December, accessed 9 February 2021, www.swissre.com/media/news-releases/nr-20201215-sigma-full-year-2020-preliminary-natcat-loss-estimates.html.
- Takaya, Y., I. Ishikawa, C. Kobayashi, H. Endo, and T. Ose, 2020: Enhanced Meiyu-Baiu rainfall in early summer 2020: Aftermath of the 2019 super IOD event. *Geophys. Res. Lett.*, **47**, e2020GL090671, <https://doi.org/10.1029/2020GL090671>.
- Talsma, C. J., S. P. Good, C. Jiménez, B. Martens, J. B. Fisher, D. G. Miralles, M. F. McCabe, and A. J. Purdy, 2018: Partitioning of evapotranspiration in remote sensing-based models. *Agric. For. Meteorol.*, **260–261**, 131–143, <https://doi.org/10.1016/j.agrformet.2018.05.010>.
- Tapley, B. D., S. Bettadpur, J. C. Ries, P. F. Thompson, and M. M. Watkins, 2004: GRACE measurements of mass variability in the Earth system. *Science*, **305**, 503–505, <https://doi.org/10.1126/science.1099192>.

- Tarasick, D. W., and Coauthors, 2019: Tropospheric Ozone Assessment Report: Tropospheric ozone from 1877 to 2016, observed levels, trends and uncertainties. *Elem. Sci. Anthropocene*, **7**, 39, <https://doi.org/10.1525/elementa.376>.
- Teng, W.-H., C.-Y. Huang, S.-P. Ho, Y.-H. Kuo, and X.-J. Zhou, 2013: Characteristics of global precipitable water in ENSO events revealed by COSMIC measurements. *J. Geophys. Res. Atmos.*, **118**, 8411–8425, <https://doi.org/10.1002/jgrd.50371>.
- Teubner, I. E., and Coauthors, 2018: Assessing the relationship between microwave vegetation optical depth and gross primary production. *Int. J. Appl. Earth Obs. Geoinf.*, **65**, 79–91, <https://doi.org/10.1016/j.jag.2017.10.006>.
- , and Coauthors, 2019: A carbon sink-driven approach to estimate gross primary production from microwave satellite observations. *Remote Sens. Environ.*, **229**, 100–113, <https://doi.org/10.1016/j.rse.2019.04.022>.
- The Watchers, 2020: Very rare cyclone over the Middle East, state of emergency declared in Egypt. 12 March, accessed 11 February 2021, <https://watchers.news/2020/03/12/very-rare-cyclone-over-the-middle-east-state-of-emergency-declared-in-egypt/>.
- Thibert, E., M. Bonnefoy-Demongeot, F. Finance, and X. Bodin, 2018: Extracting the time signal in surface velocity changes along 3 decades at Laurichard rock glacier (French Alps). *5th European Conf. Permafrost, Book of Abstracts*, Chamonix, France, Laboratoire EDYTEM, 615–616.
- Thompson, R. L., and Coauthors, 2019: Acceleration of global N₂O emissions seen from two decades of atmospheric inversion. *Nat. Climate Change*, **9**, 993–998, <https://doi.org/10.1038/s41558-019-0613-7>.
- Tian, H., and Coauthors, 2020: A comprehensive quantification of global nitrous oxide sources and sinks. *Nature*, **586**, 248–256, <https://doi.org/10.1038/s41586-020-2780-0>.
- Timmermann, A., and Coauthors, 2018: El Niño–Southern Oscillation complexity. *Nature*, **559**, 535–545, <https://doi.org/10.1038/s41586-018-0252-6>.
- Torralba, V., F. J. Doblas-Reyes, and N. Gonzalez-Reviriegol, 2017: Uncertainty in recent near-surface wind speed trends: A global reanalysis intercomparison. *Environ. Res. Lett.*, **12**, 114019, <https://doi.org/10.1088/1748-9326/aa8a58>.
- Trepte, Q. Z., P. Minnis, C. R. Trepte, S. Sun-Mack, and R. Brown, 2010: Improved cloud detection in CERES Edition 3 algorithm and comparison with the CALIPSO Vertical Feature Mask. *13th Conf. on Atmospheric Radiation and Cloud Physics*, Portland, OR, Amer. Meteor. Soc., JP1.32, <https://ams.confex.com/lams/13CldPhy13AtRad/webprogram/Paper171785.html>.
- Turner, A. J., and Coauthors, 2020: Observed impacts of COVID-19 on urban CO₂ emissions. *Geophys. Res. Lett.*, **47**, e2020GL090037, <https://doi.org/10.1029/2020GL090037>.
- Turner, J., G. J. Marshall, K. Clem, S. Colwell, T. Phillips, and H. Lu, 2020: Antarctic temperature variability and change from station data. *Int. J. Climatol.*, **40**, 2986–3007, <https://doi.org/10.1002/joc.6378>.
- van der A, R. J., M. A. F. Allaart, and H. J. Eskes, 2015: Extended and refined multi sensor reanalysis of total ozone for the period 1970–2012. *Atmos. Meas. Tech.*, **8**, 3021–3035, <https://doi.org/10.5194/amt-8-3021-2015>.
- van der Schalie, R., and Coauthors, 2017: The merging of radiative transfer based surface soil moisture data from SMOS and AMSR-E. *Remote Sens. Environ.*, **189**, 180–193, <https://doi.org/10.1016/j.rse.2016.11.026>.
- , R. De Jeu, R. Parinussa, N. Rodríguez-Fernández, Y. Kerr, A. Al-Yaari, J.-P. Wigneron, and M. Drusch, 2018: The effect of three different data fusion approaches on the quality of soil moisture retrievals from multiple passive microwave sensors. *Remote Sens.*, **10**, 107, <https://doi.org/10.3390/rs10010107>.
- van der Schrier, G., J. Barichivich, K. R. Briffa, and P. D. Jones, 2013: A scPDSI-based global dataset of dry and wet spells for 1901–2009. *J. Geophys. Res. Atmos.*, **118**, 4025–4048, <https://doi.org/10.1002/jgrd.50355>.
- van der Werf, G. R., and Coauthors, 2017: Global fire emissions estimates during 1997–2016. *Earth Syst. Sci. Data*, **9**, 697–720, <https://doi.org/10.5194/essd-9-697-2017>.
- van Dijk, A. I. J. M., H. E. Beck, R. S. Crosbie, R. A. M. de Jeu, Y. Y. Liu, G. M. Podger, B. Timbal, and N. R. Viney, 2013: The Millennium Drought in south-east Australia (2001–2009): Natural and human causes and implications for water resources, ecosystems, economy, and society. *Water Resour. Res.*, **49**, 1040–1057, <https://doi.org/10.1002/wrcr.20123>.
- van Heerwaarden, C. C., and Coauthors, 2021: Record high solar irradiance in Western Europe during first COVID-19 lockdown largely due to unusual weather. *Commun. Earth Environ.*, **2**, 37, <https://doi.org/10.1038/s43247-021-00110-0>.
- van Marle, M. J. E., R. D. Field, G. R. van der Werf, I. A. Estrada de Wagt, R. A. Houghton, L. V. Rizzo, P. Artaxo, and K. Tsigaridis, 2016: Fire and deforestation dynamics in Amazonia (1973–2014). *Global Biogeochem. Cycles*, **31**, 24–38, <https://doi.org/10.1002/2016GB005445>.
- van Oldenborgh, G. J., and Coauthors, 2020: Attribution of the Australian bushfire risk to anthropogenic climate change. *Nat. Hazards Earth Syst. Sci.*, **21**, 941–960, <https://doi.org/10.5194/nhess-2020-69>.
- Vautard, R., J. Cattiaux, P. Yiou, J. N. Thépaut, and P. Ciais, 2010: Northern Hemisphere atmospheric stilling partly attributed to an increase in surface roughness. *Nat. Geosci.*, **3**, 756–761, <https://doi.org/10.1038/ngeo979>.
- Vernier, J.-P., and Coauthors, 2011: Major influence of tropical volcanic eruptions on the stratospheric aerosol layer during the last decade. *Geophys. Res. Lett.*, **38**, L12807, <https://doi.org/10.1029/2011GL047563>.
- Vose, R. S., and Coauthors, 2012: NOAA's merged land–ocean surface temperature analysis. *Bull. Amer. Meteor. Soc.*, **93**, 1677–1685, <https://doi.org/10.1175/BAMS-D-11-00241.1>.
- Vreugdenhil, M., S. Hahn, T. Melzer, B. Bauer-Marschallinger, C. Reimer, W. Dorigo, and W. Wagner, 2017: Assessing vegetation dynamics over Mainland Australia with Metop ASCAT. *IEEE J. Sel. Top. Appl. Earth Obs. Remote Sens.*, **10**, 2240–2248, <https://doi.org/10.1109/JSTARS.2016.2618838>.
- Wagner, W., and Coauthors, 2013: The ASCAT soil moisture product: A review of its specifications, validation results, and emerging applications. *Meteor. Z.*, **22**, 5–33, <https://doi.org/10.1127/0941-2948/2013/0399>.
- Wainwright, C. M., D. L. Finney, M. Kilavi, E. Black, and J. H. Marsham, 2020: Extreme rainfall in East Africa October 2019–January 2020 and context under future climate change. *Weather*, **76**, 26–31, <https://doi.org/10.1002/wea.3824>.
- Wang, C., C. Deser, J. Y. Yu, P. DiNezio, and A. Clement, 2017: El Niño and Southern Oscillation (ENSO): A Review. *Coral Reefs of the Eastern Tropical Pacific*, P. Glynn, D. Manzello, and I. Enochs, Eds., Coral Reefs of the World, Vol. 8, Springer, 85–106, https://doi.org/10.1007/978-94-017-7499-4_4.
- Wang, G., and W. Cai, 2020: Two-year consecutive concurrences of positive Indian Ocean Dipole and Central Pacific El Niño preconditioned the 2019/2020 Australian “black summer” bushfires. *Geosci. Lett.*, **7**, 19, <https://doi.org/10.1186/s40562-020-00168-2>.
- Wang, S.-Y., H. Kim, D. Coumou, J.-H. Yoon, L. Zhao and R. Gillies, 2019: Consecutive extreme flood and heat wave events in Japan: Are they becoming a norm? *Atmos. Sci. Lett.*, **20**, e933, <https://doi.org/10.1002/asl.933>.
- Wang, Z., and Coauthors, 2012: The isotopic record of Northern Hemisphere atmospheric carbon monoxide since 1950: Implications for the CO budget. *Atmos. Chem. Phys.*, **12**, 4365–4377, <https://doi.org/10.5194/acp-12-4365-2012>.
- Weatherhead, E. C., and Coauthors, 1998: Factors affecting the detection of trends: Statistical considerations and applications to environmental data. *J. Geophys. Res.*, **103**, 17 149–17 161, <https://doi.org/10.1029/98JD00995>.
- Weber, M., and Coauthors, 2018: Total ozone trends from 1979 to 2016 derived from five merged observational datasets – The emergence into ozone recovery. *Atmos. Chem. Phys.*, **18**, 2097–2117, <https://doi.org/10.5194/acp-18-2097-2018>.
- , and Coauthors, 2021: The unusual stratospheric Arctic winter 2019/20: Chemical ozone loss from satellite observations and TOMCAT chemical transport model. *J. Geophys. Res. Atmos.*, **126**, e2020JD034386, <https://doi.org/10.1029/2020JD034386>.

- Wells, N., S. Goddard, and M. J. Hayes, 2004: A self-calibrating palmer drought severity index. *J. Climate*, **17**, 2335–2351, [https://doi.org/10.1175/1520-0442\(2004\)017<2335:ASPDSI>2.0.CO;2](https://doi.org/10.1175/1520-0442(2004)017<2335:ASPDSI>2.0.CO;2).
- Weng, H. Y., K. Ashok, S. Behera, A. S. Rao, and T. Yamagata, 2007: Impacts of recent El Niño Modoki on dry/wet conditions in the Pacific rim during boreal summer. *Climate Dyn.*, **29**, 113–129, <https://doi.org/10.1007/s00382-007-0234-0>.
- Wentz, F. J., 1997: A well calibrated ocean algorithm for Special Sensor Microwave/Imager. *J. Geophys. Res.*, **102**, 8703–8718, <https://doi.org/10.1029/96JC01751>.
- , 2015: A 17-year climate record of environmental parameters derived from the Tropical Rainfall Measuring Mission (TRMM) microwave imager. *J. Climate*, **28**, 6882–6902, <https://doi.org/10.1175/JCLI-D-15-0155.1>.
- , L. Ricciardulli, K. Hilburn, and C. Mears, 2007: How much more rain will global warming bring? *Science*, **317**, 233–235, <https://doi.org/10.1126/science.1140746>.
- WGMS, 2017: Global Glacier Change Bulletin No. 2 (2014–2015). M. Zemp et al., Eds., World Glacier Monitoring Service, 244 pp., <https://wgms.ch/ggcb/>.
- , 2018: Glacier Map Collection (GMC), World Glacier Monitoring Service, <https://doi.org/10.5904/wgms-maps-2018-02>
- , 2020: Global Glacier Change Bulletin No. 3 (2016–2017). M. Zemp et al., Eds., World Glacier Monitoring Service, 274 pp., <https://wgms.ch/ggcb/>.
- Wielicki, B. A., B. R. Barkstrom, E. F. Harrison, R. B. Lee III., G. L. Smith, and J. E. Cooper, 1996: Clouds and the Earth’s Radiant Energy System (CERES): An Earth observing system experiment. *Bull. Amer. Meteor. Soc.*, **77**, 853–868, [https://doi.org/10.1175/1520-0477\(1996\)077<0853:CATERE>2.0.CO;2](https://doi.org/10.1175/1520-0477(1996)077<0853:CATERE>2.0.CO;2).
- , and Coauthors, 1998: Clouds and the Earth’s Radiant Energy System (CERES): Algorithm overview. *IEEE Trans. Geosci. Remote Sens.*, **36**, 1127–1141, <https://doi.org/10.1109/36.701020>.
- Wiese, D. N., F. W. Landerer, and M. M. Watkins, 2016: Quantifying and reducing leakage errors in the JPL RL05M GRACE mascon solution. *Water Resour. Res.*, **52**, 7490–7502, <https://doi.org/10.1002/2016WR019344>.
- Willett, K. M., C. N. Williams Jr., R. J. H. Dunn, P. W. Thorne, S. Bell, M. de Podesta, P. D. Jones, and D. E. Parker, 2013: HadISDH: An updated land surface specific humidity product for climate monitoring. *Climate Past*, **9**, 657–677, <https://doi.org/10.5194/cp-9-657-2013>.
- , R. J. H. Dunn, P. W. Thorne, S. Bell, M. de Podesta, D. E. Parker, P. D. Jones, and C. N. Williams Jr., 2014: HadISDH land surface multi-variable humidity and temperature record for climate monitoring. *Climate Past*, **10**, 1983–2006, <https://doi.org/10.5194/cp-10-1983-2014>.
- , R. J. H. Dunn, J. Kennedy, and D. Berry, 2020: Development of the HadISDH marine humidity climate monitoring dataset. *Earth Syst. Sci. Data*, **12**, 2853–2880, <https://doi.org/10.5194/essd-12-2853-2020>.
- Wills, R. C. J., R. H. White, and X. J. Levine, 2019: Northern Hemisphere stationary waves in a changing climate. *Curr. Climate Change Rep.*, **5**, 372–389, <https://doi.org/10.1007/s40641-019-00147-6>.
- Winker, D. M., W. Hunt, and M. J. McGill, 2007: Initial performance assessment of CALIOP. *Geophys. Res. Lett.*, **34**, L19803, <https://doi.org/10.1029/2007GL030135>.
- WMO, 2018: Scientific assessment of ozone depletion, 2018. Global Ozone Research and Monitoring Project Rep. 58, 588 pp., <https://csl.noaa.gov/assessments/ozone/2018/>.
- , 2021: State of the Global Climate 2020. Provisional Rep., 38 pp., accessed 11 February 2021, https://library.wmo.int/doc_num.php?explnum_id=10444.
- Wohland, J., N.-E. Omrani, D. Witthaut, and N.-S. Keenlyside, 2019: Inconsistent wind speed trends in current twentieth century reanalyses. *J. Geophys. Res. Atmos.*, **124**, 1931–1940, <https://doi.org/10.1029/2018JD030083>.
- Woolway, R. I., and C. J. Merchant, 2018: Intralake heterogeneity of thermal responses to climate change: A study of large Northern Hemisphere lakes. *J. Geophys. Res. Atmos.*, **123**, 3087–3098, <https://doi.org/10.1002/2017JD027661>.
- , and Coauthors, 2017: Lake surface temperature [in “State of the Climate in 2016”]. *Bull. Amer. Meteor. Soc.*, **98** (8), S13–S14, <https://doi.org/10.1175/2017BAMSStateoftheClimate.1>.
- , and Coauthors, 2018: Lake surface temperature [in “State of the Climate in 2017”]. *Bull. Amer. Meteor. Soc.*, **99** (8), S13–S15, <https://doi.org/10.1175/2018BAMSStateoftheClimate.1>.
- , B. M. Kraemer, J. D. Lenters, C. J. Merchant, C. M. O’Reilly, and S. Sharma, 2020: Global lake responses to climate change. *Nat. Rev. Earth Environ.*, **1**, 388–403, <https://doi.org/10.1038/s43017-020-0067-5>.
- Worden, J. R., and Coauthors, 2017: Reduced biomass burning emissions reconcile conflicting estimates of the post-2006 atmospheric methane budget. *Nat. Commun.*, **8**, 2227, <https://doi.org/10.1038/s41467-017-02246-0>.
- Wu, Q., and T. Zhang, 2008: Recent permafrost warming on the Qinghai–Tibetan Plateau. *J. Geophys. Res. Atmos.*, **113**, 1–22, <https://doi.org/10.1029/2007JD009539>.
- Wylie, D. P., D. L. Jackson, W. P. Menzel, and J. J. Bates, 2005: Trends in Global cloud cover in two decades of HIRS observations. *J. Climate*, **18**, 3021–3031, <https://doi.org/10.1175/JCLI3461.1>.
- Yamazaki, D., S. Kanae, H. Kim, and T. Oki, 2011: A physically-based description of floodplain elevation dynamics in a global river routing model. *Water Resour. Res.*, **47**, W04501, <https://doi.org/10.1029/2010WR009726>.
- Yang, J., Q. Liu, S.-P. Xie, Z. Liu, and L. Wu, 2007: Impact of the Indian Ocean SST basin mode on the Asian summer monsoon. *Geophys. Res. Lett.*, **34**, L02708, <https://doi.org/10.1029/2006GL028571>.
- Yin, Y., and Coauthors, 2020: Accelerating methane growth rate from 2010 to 2017: Leading contributions from the tropics and East Asia. *Atmos. Chem. Phys. Discuss.*, <https://doi.org/10.5194/acp-2020-649>.
- Yosef, Y., E. Aguilar, and P. Alpert, 2021: Is it possible to fit extreme climate change indices together seamlessly in the era of accelerated warming? *Int. J. Climatol.*, **41**, E952–E963, <https://doi.org/10.1002/joc.6740>.
- Young, I., and A. Ribal, 2019: Multiplatform evaluation of global trends in wind speed and wave height. *Science*, **364**, 548–552, <https://doi.org/10.1126/science.aav9527>.
- Young, P. J., and Coauthors, 2013: Pre-industrial to end 21st century projections of tropospheric ozone from the Atmospheric Chemistry and Climate Model Inter-comparison Project (ACCMIP). *Atmos. Chem. Phys.*, **13**, 2063–2090, <https://doi.org/10.5194/acp-13-2063-2013>.
- , and Coauthors, 2018: Tropospheric Ozone Assessment Report: Assessment of global-scale model performance for global and regional ozone distributions, variability, and trends. *Elem. Sci. Anthropocene*, **6**, 10, <https://doi.org/10.1525/elementa.265>.
- Yu, P., and Coauthors, 2021: Persistent stratospheric warming due to 2019–2020 Australian wildfire smoke. *Geophys. Res. Lett.*, **48**, e2021GL092609, <https://doi.org/10.1029/2021GL092609>.
- Zemp, M., and Coauthors, 2019: Global glacier mass changes and their contributions to sea-level rise from 1961 to 2016. *Nature*, **568**, 382–386, <https://doi.org/10.1038/s41586-019-1071-0>.
- Zeng, Z., and Coauthors, 2019: A reversal in global terrestrial stilling and its implications for wind energy production. *Nat. Climate Change*, **9**, 979–985, <https://doi.org/10.1038/s41558-019-0622-6>.
- Zhang, H.-M., and Coauthors, 2019: Updated temperature data give a sharper view of climate trends. *Eos*, **100**, <https://doi.org/10.1029/2019EO12822>.
- Zhang, X., and Coauthors, 2011: Indices for monitoring changes in extremes based on daily temperature and precipitation data. *Wiley Interdiscip. Rev.: Climate Change*, **2**, 851–870, <https://doi.org/10.1002/wcc.147>.
- Zhang, Y., J. M. Wallace, and D. S. Battisti, 1997: ENSO-like interdecadal variability: 1900–93. *J. Climate*, **10**, 1004–1020, [https://doi.org/10.1175/1520-0442\(1997\)010<1004:ELIV>2.0.CO;2](https://doi.org/10.1175/1520-0442(1997)010<1004:ELIV>2.0.CO;2).
- Zhang, Y., and Coauthors, 2016a: Multi-decadal trends in global terrestrial evapotranspiration and its components. *Sci. Rep.*, **6**, 19124, <https://doi.org/10.1038/srep19124>.
- , O. R. Cooper, A. Gaudel, A. M. Thompson, P. Nédélec, S.-Y. Ogino, and J. J. West, 2016b: Tropospheric ozone change from 1980 to 2010 dominated by equatorward redistribution of emissions. *Nat. Geosci.*, **9**, 875–879, <https://doi.org/10.1038/ngeo2827>.

- Zhang, Y., and Coauthors, 2020: Contributions of world regions to the global tropospheric ozone burden change from 1980 to 2010. *Geophys. Res. Lett.*, **47**, e2020GL089184, <https://doi.org/10.1029/2020GL089184>.
- Zhang, W., W. Mao, F. Jiang, M. F. Stuecker, F-F. Jin, and L. Qi, 2021: Tropical Indo-Pacific compounding thermal conditions drive the 2019 Australian extreme drought. *Geophys. Res. Lett.*, **48**, e2020GL090323. <https://doi.org/10.1029/2020GL090323>.
- Zhao, L., and Coauthors, 2020: Changing climate and the permafrost environment on the Qinghai–Tibet (Xizang) plateau. *Permafrost Periglacial Processes*, **31**, 396–405, <https://doi.org/10.1002/ppp.2056>.
- , and Coauthors, 2021: A synthesis dataset of permafrost thermal state for the Qinghai–Xizang (Tibet) plateau, China. *Earth Syst. Sci. Data Discuss.*, <https://doi.org/10.5194/essd-2021-1>.
- Ziemke, J. R., and O. R. Cooper, 2019: Tropospheric ozone [in “State of the Climate in 2019”]. *Bull. Amer. Meteor. Soc.*, **101** (8), S83–S85, <https://doi.org/10.1175/BAMS-D-20-0104.1>.
- , A. R. Douglass, L. D. Oman, S. E. Strahan, and B. N. Duncan, 2015: Tropospheric ozone variability in the tropical Pacific from ENSO to MJO and shorter timescales. *Atmos. Chem. Phys.*, **15**, 8037–8049, <https://doi.org/10.5194/acp-15-8037-2015>.
- , and Coauthors, 2019: Trends in global tropospheric ozone inferred from a composite record of TOMS/OMI/MLS/OMPS satellite measurements and the MERRA-2 GMI simulation. *Atmos. Chem. Phys.*, **19**, 3257–3269, <https://doi.org/10.5194/acp-19-3257-2019>.
- Zou, C.-Z., and H. Qian, 2016: Stratospheric temperature climate data record from merged SSU and AMSU-A observations. *J. Atmos. Oceanic Technol.*, **33**, 1967–1984, <https://doi.org/10.1175/JTECH-D-16-0018.1>.

